UNIVERSITY OF SOUTHAMPTON

FACULTY OF ENGINEERING AND THE ENVIRONMENT

ENGINEERING MATERIALS

SUSTAINED MACROSCOPIC DEFLECTED CRACKING IN NICKEL BASED SUPERALLOYS: MECHANISM AND DESIGN CRITERIA

by

Christian Schoettle

Thesis for the degree of Doctor of Engineering

June 2013

UNIVERSITY OF SOUTHAMPTON

ABSTRACT

FACULTY OF ENGINEERING AND THE ENVIRONMENT

ENGINEERING MATERIALS

Doctor of Engineering

SUSTAINED MACROSCOPIC DEFLECTED CRACKING IN NICKEL BASED SUPERALLOYS: MECHANISM AND DESIGN CRITERIA

by Christian Schoettle

In this EngD thesis the phenomenon of sustained macroscopic deflected crack growth (SMDCG) during fatigue in Nickel based Superalloys is discussed, also referred to as 'teardrop' cracking in previous work. In a corner notched bend (CNB) specimen a fatigue crack usually grows in a quarter-circular plane perpendicular to the stress axis, the SMDCG however exhibits considerable deflection from this plane at the free surfaces, so that a central planar region is enclosed by large shear terraces (thus forming the 'teardrop'). This is difficult to characterise in terms of component lifing (both in terms of crack path and crack growth rates), and this thesis aims to further understanding of the underlying mechanisms and to develop assessment methodologies for lifing of such cracks in aeroengine components. The SMDCG effect has been observed under externally applied mode I loading in Udimet 720Li with relatively fine grain sizes of 6-18µm, which are candidate materials for aero engine turbine discs. CNB and single edge bend notch bend (SENB) fatigue tests have been carried out on cast and wrought and powder metallurgy variants of Udimet 720Li and SMDCG was observed at 300°C in air and at 300, 600 and 650°C in vacuum. A consistent measure of the onset of deflection has been defined; this is the crack tip stress intensity factor range ΔK at which the sustained deflection from the free surface exceeds the expected shear lip area, which is estimated as the distance of the monotonic plane stress plastic zone size from the free surface. This has been used to characterise samples from other research programmes and aeroengine components from rigtests, that have shown some form of deflected crack growth, to assess whether they exhibit SMDCG or whether the apparent deflection was caused by the expected plane stress region, or other factors such as tunnelling due to creep effects or complex overall loading conditions. Fracture surfaces exhibiting SMDCG have been studied via SEM and the fractographic analysis shows a competition between local shear crack growth and mode I crack growth occurs in both the macroscopically deflected and planar regions. This indicates that the *macroscopic* deflection is triggered by the stress state at the free surface. Further detailed analysis of the deflected crack tip with focussed ion beam (FIB) serial sectioning combined with EBSD analysis has allowed a detailed 3D reconstruction of the crack tip interaction with local microstructure. This, together with TEM foils extracted via FIB in the same region, have confirmed that the SMDCG in these systems is not linked to any local texture effects or surface microstructural differences. Lifetime predictions for the CNB samples have been carried out based on Paris law coefficients from the SENB tests, and showed shorter lifetimes than the actual samples with deflected crack growth. Whilst this could be partially due to unaccounted for initiation effects, it could also indicate that significant extrinsic shielding caused by the deflected crack growth may actually increase fatigue lifetimes. To assess the driving force evolving during SMDCG, an Alicona Infinite Focus profilometre has been used to map the complex 3D crack shapes, from where tilt angles could be measured to define a mixed mode plane stress SENB test, with the aim of replicating the stress state that had given rise to the locally deflected shear growth and to explicitly measure crack growth behaviour in the deflected regions. However this was not achieved with this test set-up, as the achievable ΔK_{eff} was not high enough to trigger the deflection throughout the sample. As a result the 3D map was next used to define Finite Element model to assess the local crack tip stress state of the complex deflected crack path. Crack driving forces that have been identified at the point the deflected crack path becomes self-sustaining, could be used in a lifing model to predict crack paths in aeroengine components, together with the measured onset of deflection.

Table of Contents

List of Figures

List of Tables

Declaration of Authorship

I, Christian Schoettle,

declare that the thesis entitled

Sustained Macroscopic Deflected Cracking In Nickel Based Superalloys: Mechanism And Design Criteria

and the work presented in the thesis are both my own, and have been generated by me as the result of my original research. I confirm that:

- this work was done wholly or mainly while in candidature for a research degree at this University;
- where any part of this thesis has previously been submitted for a degree or any other qualification at this University or any other institution, it has been clearly stated;
- where I have consulted the published work of others, it has been clearly attributed;
- where the thesis is based on work done by myself jointly with others, I have made clear exactly what was done by others and what I have contributed myself;
- parts of this work have been published as:

Schoettle, C., Reed, P.A.S., Starink, M.J., Sinclair, I., Child, D., West, G.D., Thomson, R.C. (2011) Mechanism of Sustained Macroscopic Deflected Fatigue Crack Growth in the Nickel Based Superalloy Udimet 720, *Proceedings of Materials Science and Technology Conference and Exhibition 2011, MS and T'11*, pp.781-788 [1]

Schoettle, C., Sinclair, I., Starink, M.J., Reed, P.A.S. (2012) Deflected 'Teardrop Cracking' in Nickel based Superalloys: Sustained Macroscopic Deflected Fatigue Crack Growth, International Journal of Fatigue, Volume 44, November 2012, Pages 188–201, http://dx.doi.org/10.1016/j.ijfatigue.2012.04.017 [2]

Schoettle, C., Reed, P.A.S., Starink, M.J., Sinclair, I., Child, D.J., West, G.D. and Thomson, R.C. (2012) Sustained Macroscopic Deflected Fatigue Crack Growth in Nickel Based Superalloy 720Li, in Superalloys 2012 (eds E. S. Huron, R. C. Reed, M. C. Hardy, M. J. Mills, R. E. Montero, P. D. Portella and J. Telesman), John Wiley & Sons, Inc., Hoboken, NJ, USA. doi: 10.1002/9781118516430.ch43 [3]

Signed:

Date: 21st June 2013

Acknowledgements

Despite this thesis having my name on the cover, a number of people have supported me and helped me to get this far:

I could have not made it without the guidance, advice and motivation of my supervisor Professor Philippa Reed, and her support with any issues of the EngD and beyond.

I would also like to thank my co-supervisors Professor Marco Starink and Professor Ian Sinclair, who supported me in particular during my first year.

I am grateful to Rolls Royce plc. for funding and support, in particular my industrial supervisors, Adam Coles (from Critical Parts Lifing) and Dr Mutz Ganesan (from Materials), and also Dr Mark Hardy, Steve Williams and Dr Richard Corran for a number of useful discussions.

I would also like to acknowledge further funding from Engineering and Physical Sciences Research Council, the University of Southampton and the University of Birmingham.

I would like to thank all my colleagues in the Engineering Materials Research Group, who made my time at the University enjoyable by giving me welcome distractions from work, but of course also for helping me out with my research, in particular Dr Stewart Everitt for teaching me everything about fatigue testing and metallography, Dr Tom Mbuya and Dr Kath Soady for sharing the struggles of lab work, and also Dr Terry Harvey for his help with the Alicona Infinite Focus profilometre and Dr Shuncai Wang for help with the FEG SEM.

I also would like to thank the technicians Rob Barnes, Chris Williams and Dave Beckett for their help and assistance in the lab.

I am also grateful for the help of Professor Rachel Thomson and her group at Loughborough University, in particular Dr Geoff West for the extraction and sectioning of a crack tip, Dr Daniel Child for help with the 3D reconstructions, Dr Zhaoxia Zhou for the TEM work.

Thanks also to Dr Hangyue Li from the University of Birmingham for letting me examine her samples.

I would like to thank my parents for their continuous support and the inspiration they have given me to never stop learning. They will however be pleased that I am finally finished studying.

Finally, I would like to thank my partner Sonia for putting up with my long hours of research and writing, my daughter Sofia for being a great motivation in my life, and both of them for giving me reasons to get away from my desk.

1 Introduction

This EngD has been sponsored and supported by Rolls Royce plc. (R-R). R-R is a world-leading provider of power systems and services for civil and defence aerospace, marine and energy sectors, supplying more than 500 airlines, 4,000 corporate and utility aircraft and helicopter operators, 160 armed forces, more than 4,000 marine customers, including 70 navies, and energy customers in more than 80 countries. Annual underlying revenues were £11.3 billion in 2011, of which more than half came from the provision of services, which includes leasing aeroengines to airlines, and servicing them. It is therefore important to the company to ensure good, well-characterised lifetimes of their products. Improved lifing methodologies will allow greater confidence in allowing longer operating lifetimes for their components, which makes products more competitive and also reduces the cost of servicing.

Nickel based Superalloys are used for high temperature applications, such as aeroengine turbine discs and blades, due to their high temperature strength and oxidation resistance. In service the materials experience variations of loads and temperatures. Turbine disc are safety critical components and their failure could impair the ability of the aircraft to operate safely. It is therefore important to take these take safety critical components out of service before significant defects appear. It is therefore crucial to be able to predict fatigue crack growth behaviour so that catastrophic failure can be avoided.

Current lifing approaches at Rolls Royce plc. for turbine discs are based on macroscopically flat mode I (tensile) crack growth, however an unusual crack growth mode has been observed in the polycrystalline Nickel base Superalloy Udimet 720 (U720), which shows significant deflection from this plane.

In previous work [4, 5] this 'sustained deflected fatigue crack growth' has also been referred to as 'Tear Drop' Cracking (TDC), which is derived from the specific fracture surface that can be observed in a Corner Notch (CN) specimen under mode I loading where in the centre a flat elliptical or 'teardrop' shaped region is surrounded by sharply deflected shear regions at the surrounding free surfaces, where mode I and mode II (shear) are alternating giving rise to a three dimensional deflected crack. In such a specimen a crack is usually expected to grow in a planar 'quarter circular' shape perpendicular to the loading direction.

The effect has not only been observed on lab coupons, a number of cracks of complex morphology have been observed on actual turbine discs in spin tests. This highly deflected crack morphology is difficult to explain in terms of conventional fatigue mechanics and leads to concerns about the accuracy of crack growth rate data and predictions of crack trajectories in components.

Traditional fatigue crack propagation assessments are based on assumptions of macroscopic mode I failure and R-R use crack growth rates that are determined from fatigue testing on CN samples. These may have been affected by deflection, but are assumed to be rates for planar cracks. There is a risk that the crack growth behaviour for these deflected cracks could be different, and cracks exhibiting such behaviour in components could grow at unexpected rates, but more importantly a deflected crack could grow out of the expected plane into a different (increasing) stress field and cause potentially unexpected catastrophic failure.

It is therefore necessary to understand the occurrence of this phenomenon and to develop criteria allowing the assessment of likelihood of teardrop cracking and its effect on component fatigue life.

Past work [4, 5] has established certain dependencies between the degree of 'teardrop formation' and the material and loading parameters, e.g. grain size, test temperature and environment, specimen geometry etc., but no clear mechanism has been unambiguously determined.

Hence the aim of this project is to develop an understanding of the mechanism of 'teardrop' cracking and deliver assessment methodologies that can be incorporated into the component design and lifing process.

1.1 Aims of this work

The aim of this work is to identify the mechanism that causes this sustained deflection and to deliver assessment methodologies that can be incorporated into the component design and lifing process. Subsidiary aims can be further defined as:

- Review of available fractures (test-pieces and components from Rolls Royce and from previous researchers)
- Produce a working definition of macroscopically sustained mixed mode cracking to enable the categorisation of fractures, that can be used for different specimen types (e.g. CN and SEN in tension-tension and bend loading).
- From the above propose microstructures and test conditions susceptible to teardrop cracking.
- Define an experimental programme to confirm the above considering the different temperatures and environments established in previous work as well as using different specimen types to compare the effect of constraint conditions.
- Postulate mechanism (Mechanism map)
- Experimental programme (mechanical testing and deformation mode study) to confirm mechanism.
- Determine overall crack growth rates from tests and local crack growth rates of deflected regions and effect on macroscopic crack growth rates. This can be used as an input for a lifing model to predict crack growth for different regimes.
- Analytic modelling of growth of deflected cracks: Crack Shape Mapping and strategic Finite Element Analysis (FEA)of mixed mode crack in 2D and 3D, to be able to predict crack path
- Model validation using service experience

2 Literature Review

2.1 Nickel based Superalloys

Superalloys are metallic materials based on iron, nickel or cobalt developed for applications at high temperature and applied stress. They usually show a good long-term strength at elevated temperature, fatigue resistance, creep resistance and resistance to high temperature corrosion and erosion. Their applications are usually in the hot sections of gas power turbines in aircraft and in land-based power generation facilities.

2.1.1 Composition

Nickel-base superalloys have an austenitic face-centred cubic (FCC) phase, commonly known as the gamma (γ) phase, which does not change its structure up to the melting point. The main strengthening precipitate (particularly at high temperatures) is the ordered fcc nickel-rich $Ni_3(Ti,Al)$ precipitate, generally referred to as gamma-prime (γ') precipitate, which is usually coherent with the γ matrix . Depending on the alloying elements present, various other precipitates may also be formed in the alloy. [6]

In order to form the γ' phase, Aluminium (Al) and Titanium (Ti) typically up to about 8 wt % (in total) are present in the alloy. The γ' volume fraction is directly related to the amount of Al and Ti that the alloy contains. [7] Niobium (Nb) and Tantalum (Ta) can substitute Al in forming γ' and may increase the solution temperature of γ' permitting strengthening effects to persist to higher temperatures. High additions (greater than 4 wt %) of Nb can lead to the precipitation of another hardening phase, gamma double prime, γ'', Ni_3Nb, which can be seen in some Ni superalloys, such as Inconel 718. [8]

Chromium (Cr) is one of the main alloying elements in nickel-base superalloys in the range of 10-20 wt % and is added to the alloy to increase resistance to corrosion and oxidation due to formation of an adherent and non-porous, and hence protective Cr_2O_3 oxide layer. [8] However higher Cr levels can lead to lower volume fractions of γ', as Cr preferentially forms the γ phase with Ni, which reduces the amount of Ni available to form the γ' phase. Too high chromium contents in nickel-base superalloys have been associated with an increased propensity to formation of the deleterious sigma (σ) phase.

Cobalt (Co) is added to nickel-base superalloys to reduce the solubility of Al and Ti in the γ matrix, hence favouring formation of the γ' phase and maintaining the strength of the alloy at high temperatures. The presence of cobalt also reduces creep deformation by lowering stacking fault energy (SFE) between partial dislocations, thus reducing dislocation cross-slip and climb. The presence of 15 wt % cobalt has been indicated to generate a minimum SFE which promotes planar slip and potentially improves fatigue crack propagation (FCP) resistance.[9]

At higher temperatures, diffusion and dislocation cross-slip are important in determining material strength. Slowly diffusing elements such as Molybdenum (Mo) and Tungsten (W) are useful as solid-solution additions and can help reduce creep deformation. Mo, W and Tantalum (Ta) also dissolve to some extent in the γ' phase and affect the γ' solvus temperature,

γ' volume fraction and the matrix/precipitate lattice mismatch. In addition, these elements also form complex carbides with each other and with other elements, such as chromium and iron. [6]

Addition of Ta has been shown to increase the tensile strength but segregates to form very stable tantalum carbide (MC carbide). The Ta concentration can be controlled to allow the MC carbide to breakdown and promote formation of grain boundary carbides [9]. Addition of Ta has also been associated with enhanced oxidation resistance and contribution to γ' strengthening (increased hardness of the γ' phase). [10]

Addition of B and C was found to reduce creep rates. Addition of these elements is believed to significantly reduce dislocation mobility by pinning of the dislocations. This impedance to dislocation motion gives rise to high activation energy for creep. [11]

2.1.1.1 Strengthening Precipitates

$Ni_3(Al,Ti)$ precipitates, i.e. the γ' phase, gives the main form of strengthening in nickel-base superalloys. The γ' phase has an ordered FCC crystal structure which is coherent with the FCC γ matrix. The γ' phase can have a range of composition depending especially on the Al and Ti contents in the alloy. The γ' phase is also a 'reasonably ductile' phase, this is useful since it will not cause embrittlement when formed along grain boundaries in the alloy. The strength of γ' increases with temperature due to Kears-Wilsdorf locking, thermally activated locking of dislocations within the γ'. [12, 13]

Primary γ' precipitates, which are incoherent with the γ matrix, as they are not dissolved during a sub-solvus solution treatment, are present at grain boundaries and their size and volume fraction are controlled during the solution treatment stage in powder metallurgy (PM) alloys. The heat treatments of Nickel superalloys and the effect on the precipitates are discussed in more detail in Section 2.1.3. Within the grains, there are finer secondary and tertiary γ' precipitates which are coherent with the γ matrix. The main difference between secondary and tertiary γ' precipitates is in the size and shape, where secondary γ' are larger and usually cuboidal in shape (due to larger lattice mismatch), and tertiary γ' are finer and spherical in shape. [14]

2.1.1.2 Carbides

Primary carbides are usually in the form MC, where M is Ti, Nb, Ta, Hf, Th or Zr. MC carbides have a B1 (NaCl) crystal structure. They are generally very stable and form during solidification of the material. Primary carbides are difficult to dissolve in the solid phase and they play an important part in restricting grain growth during the solution treatment stage. Lower carbides which can be dissolved by solution treatment in the range 1050°C to 1200°C have the general formula M_6C or $M_{23}C_6$ where M stands for the metallic constituent.

During heat treatment or service, primary carbides may react with the γ matrix to form lower carbides. Lower carbides are formed from primary carbides according to the following equations:

$MC + \gamma \rightarrow M_6C + \gamma'$ Equation 2-1

$MC + \gamma \rightarrow M_{23}C_6 + \gamma'$ Equation 2-2

Carbides in commercial alloys can form both at grain boundaries and within grains. In nickel-base superalloys, the effects of coherent γ' precipitates within the grains generally dominate over the effect of any carbides in these regions, so only intergranular carbides are considered important to the mechanical properties.

Carbides are generally harder and more brittle than the alloy matrix, hence their distribution along the grain boundaries is important. When the carbide is present as a continuous film along the grain boundaries it tends to delineate grain boundaries, giving a continuous fracture path and is therefore detrimental to the alloy. During creep deformation, a continuous film of carbide also restricts grain boundary sliding, leading to stress build-up and early fracture. On the other hand if there are no grain boundary carbides present, excessive grain boundary sliding and growth of voids along grain boundaries occur during high temperature deformation. An optimum amount and distribution of carbide is therefore necessary to limit grain boundary movement for best high temperature performance. [8]

Although blocky MC and M_6C carbides may be formed in nickel alloys, the beneficial effect of carbon has been attributed primarily to the fine intergranular $M_{23}C_6$ carbides which are formed during heat treatment giving improved high temperature strength by inhibiting grain boundary sliding. The increase in strength is however offset by a concomitant reduction in fracture ductility. [15]

2.1.1.3 Other Phases

Ni_3Nb, generally designated as the γ'' phase, is a less frequently occurring hardening phase. The γ'' phase has an ordered body-centred-tetragonal crystal structure and is coherent with the γ matrix. It usually forms as discs in the γ matrix.[8]

The δ phase is the stable orthorhombic form of Ni_3Nb. It can be found in some nickel-base superalloys at grain boundaries, at primary carbides or inside grains during ageing treatments or after prolonged thermal exposure. It gives additional strengthening when present in optimum condition.[16]

Other intermetallic phases, such as the Laves phase and Sigma (σ) phase, which are topologically-closed-packed (TCP), can also form within the complex alloy systems of nickel-base superalloys. Precipitation of the σ phase has been found to be deleterious to the strength and ductility of the alloy, as well as giving poorer creep and fatigue resistance. The formation of these intermetallic phases is generally avoided for two reasons. Firstly these intermetallic phases themselves are brittle and hard, hence liable to fracture. When formed as needles, large platelets or continuous intergranular film, these phases facilitate propagation of cracks through the matrix. The hard σ phase, especially in a plate-like or needle morphology at grain boundaries, also offer ideal sites for crack initiation. Secondly the formation of these phases is not desired as they remove useful strengthening elements from the matrix; they are rich in refractory elements such as Cr, Co, Mo and W. Precipitation of these phases will result in solute depletion in the surrounding γ matrix leading to localised compositional weakening. The

alloy can be more susceptible to environmental attack if formation of the protective Cr_2O_3 scale is inhibited through chromium depletion.

Numerous other phases are also present in nickel-base superalloys; these include nitrides, borides, sulphides and phosphides. [8]

2.1.2 Processing route

Turbine discs may be produced by one of two manufacturing processes, i.e. either by a cast and wrought (C&W) route or through powder metallurgy (PM) techniques. In the cast and wrought process, melting is usually carried out in vacuum, to avoid contamination, followed by pouring into moulds and various final forging processes. However, increased difficulties in forgeability due to increases in alloy high temperature strength, as well as problems associated with shrinkage and grain size control have been reported [12, 13]. Powder metallurgy (PM) techniques were used to overcome some of these problems during manufacture caused by using the cast and wrought technique. Highly alloyed atomised powder particles can be compacted and sintered usually through hot extrusion or hot isostatic pressing allowing formation of these high strength alloys with minimal segregation [12, 13]. Although powder metallurgy fabricated alloys are usually associated with improved properties, they are usually expensive to manufacture. [8]

2.1.3 Heat Treatments

To create an optimal microstructure for the material to provide good high temperature properties, typically a solution heat treatment followed by one or more ageing treatments are applied.

Solution treatment of superalloy discs is usually done between 1040 and 1230°C, below the γ' solvus temperature (temperature at which γ' is completely dissolved in γ matrix). Some γ' precipitates (primary) are therefore retained to control the grain size. The higher the solution treatment temperature the more γ' will dissolve and the lower the volume fraction of primary γ' which will cause larger grains. Also there will be more γ' forming elements in the solution which will cause more secondary and tertiary γ' (which usually causes an increase in hardness). [17]

Secondary and tertiary γ' precipitates are formed uniformly throughout the γ matrix during cooling from solution temperature, which can be described in the following way. Early on during cooling, nucleation of secondary γ' precipitates occurs in the supersaturated γ matrix. As temperature decreases further, growth of secondary γ' precipitates occurs with partitioning of solutes into surrounding matrix. Eventually, diffusion rates of the solutes decrease and the γ' precipitates cannot grow fast enough to keep supersaturation of the matrix low. Eventually, at a critical undercooling, the driving force is sufficient to allow nucleation of tertiary γ' precipitates to occur. [17, 18]

Nucleation and growth kinetics of γ' precipitates strongly depend on the cooling rate from solution temperature, hence this cooling rate can be manipulated to change the frequency of nucleation as well as the distribution of precipitates in the matrix. During cooling from solution temperature, the size and volume fraction of secondary γ' precipitates formed were noted to

decrease with higher cooling rates [18], while the size of tertiary γ' precipitates formed appear to be relatively insensitive to the cooling rate [17]. Higher cooling rates result in more undercooling and subsequently more supersaturation build-up, leading to larger numbers of small secondary γ' nuclei with small interparticle spacing [18, 19]. Since growth of γ' precipitates is essentially a diffusion-controlled process, growth of secondary γ' precipitates is suppressed during fast cooling due to rapid temperature drop and limited time for diffusion, i.e. higher cooling rates result in larger numbers of small secondary γ' precipitates with small interparticle spacing, and vice versa for slower cooling rates. The volume fraction of secondary γ' precipitates decreases with increasing cooling rates as fast cooling suppresses growth of secondary γ' precipitates. When nucleation of tertiary γ' precipitates is expected, the temperature is likely to be relatively low to allow intensive solute diffusion, and growth of tertiary γ' precipitates is restricted[18]. The size of tertiary γ' precipitates is therefore relatively insensitive to the cooling rate.

Ageing treatments are carried out below the γ' solvus temperature to allow precipitation and growth of the γ' hardening phase. Higher cooling rates from solution temperature exhibit more ageing strengthening than a lower cooling rate, as faster cooling results in lower volume fraction of secondary γ' precipitates and retains a higher amount of γ'-forming elements in solution for precipitation of tertiary γ' during ageing [18]. It was noted that ageing treatment does not cause secondary γ' precipitates to grow significantly, and the main microstructural activity during ageing is the continuous growth of the very fine tertiary γ' precipitates nucleated during cooling from solution temperature [17, 18]. The full equilibrium volume fraction of γ' is formed very early in the ageing treatment and any subsequent change in the γ' precipitates during ageing treatment or during service involves only precipitate coarsening [14].

For many turbine disc alloys, double ageing treatments are usually carried out to give a duplex γ' distribution to provide a combination of high strength and good creep resistance [20, 21]. A duplex γ' distribution has been indicated to arise during cooling from solution temperature anyway for U720Li [17, 18]. High ageing temperatures produce high creep extensions before fracture, and lower ageing temperatures reduce creep rate, combining the two, i.e. a two stage ageing treatment, gives better creep characteristics than are obtained by a simple precipitation treatment.

Table 1 shows the different heat treatments and the corresponding grain size for different microstructures of U720 and U720Li, as used in this and previous work.

Previous worker	Loo-Morrey [4]	Brooks [22]		Pang[23]	
Material	U720	U720	U720 CG (Coarse Grain)	U720Li	U720Li-LG (large grain)
Grain Size	~11µm	10±5µm	48±29µm	6.4µm (range 2.1-13.1)	15.4µm (range 4.8-41.3)
Solution heat treatment	4h 1080°C	4h 1105°C	4h 1170°C	4h 1105°C	4h 1135°C
	oil quench	oil quench	air cool	oil quench	air cool
			4h 1080°C		
			air cool		
Ageing heat treatment	24h 650°C	24h 650°C	24h 650°C	24h 650°C	24h 650°C
	air cool	air cool	air cool	air cool	air cool
	16h 760°C	16h 760°C	16h 760°C	16h 760°C	16h 760°C
	air cool	air cool	air cool	air cool	air cool

Table 1: Heat treatments of U720 and U720Li for different microstructures

2.1.4 Deformation behaviour

2.1.4.1 Dislocation - γ′ interaction

During deformation in nickel-base superalloys, there are three processes in which dislocations can interact with precipitates: precipitate cutting, Orowan looping/bowing between precipitates, or by glide and climb around precipitates [24]. The first two processes are relatively athermal. Dislocation glide and climb around precipitates is dependent on diffusion, and is hence thermally activated and will generally dominate over athermal mechanisms at high temperatures and relatively low applied stresses.

In the precipitate shearing process, build-up of dislocation density within planar deformation bands (known as slip bands) occurs initially. In the process, the dislocation density becomes high enough that the effective stress is sufficient for a dislocation to penetrate a precipitate (e.g. coherent γ' precipitates). Due to the ordered structure of the γ' precipitate, a dislocation cutting through it forms a high energy antiphase boundary (APB). To minimise this energy a second dislocation will follow (Dislocation pairing). The final precipitate offset is two Burgers vectors and the reduced cross-section of the precipitate in the slip plane makes it easier for the next dislocation pair to go through the precipitate at a lower stress level, leading to softening in a preferential slip direction and hence concentration of slip in that particular slip direction and therefore planar slip. [25]

When dislocations bypass precipitates by Orowan bowing mechanism, dislocation loops are left around the precipitates. Formation of loops around precipitates increases the internal resistance to succeeding dislocations in the same slip plane owing to a decrease in the effective spacing between precipitates [26]. This forces dislocations to move out to adjacent planes in the same slip system when the strain amplitude is small or to cross-slip on to other systems when the strain amplitude is large, with both processes leading to a more homogeneous distribution of dislocations in the matrix, and an increased rate of work hardening [27].

2.1.4.2 Planarity of slip

Nickel-base superalloys tend to show planar or heterogeneous slip, i.e. dislocation motion is concentrated in well-defined planar bands. It occurs in the {111} plane at low temperatures. This is due to their low stacking fault energy (SFE) and the formation of APBs on shearing of ordered γ' precipitates [28, 29]. Low SFE promotes dissociation of screw dislocations into partial dislocations separated by a low energy stacking fault. The mixed screw and edge character of the partial dislocations means that they are not able to cross-slip. The pairing of dislocations favoured by minimising the APB caused on shearing of ordered γ' precipitates and the low SFE makes cross-slip difficult and encourages planar deformation in nickel-base superalloys.

At temperatures above 760°C slip can now occur on the {100} planes. This permits the long trailing partial dislocations to cross slip to this plane which causes extremely efficient tangling that makes dislocations immobile. This phenomenon is known as Kears Wilsdorf locking and is responsible for the high temperature strength of Nickel-based Superalloys . It occurs only due

to the ordered structure of the γ' precipitate which allows the formation of APB. Hence it is dependent on the γ' volume fraction. If the temperature is further increased slip on the {100} planes becomes easier, which reduces the effect of Kears-Wilsdorf locking. [12, 13]

The homogeneity of slip in the material can be characterised by the density of the slip bands or the average spacing of the slip bands [27]. Wider spaced but more intense slip bands indicate more heterogeneous slip behaviour. Higher density of less intense slip bands implies a more homogeneous slip. Homogeneity of slip is promoted by high temperatures and high loading frequencies. Increased heterogeneity of slip is also promoted in vacuum as there is less gas absorption and oxide formation, hence giving rise to more reversible slip. [4]

2.1.4.3 Effect of slip behaviour on mechanical properties

Strain localisation or heterogeneous slip does not have an effect on yield strength but generally has a deleterious effect on the toughness [30-32]. The influence of slip characteristics on fatigue and creep-fatigue behaviour varies in different fatigue regimes. In the fatigue crack initiation and short crack growth regime, the effects of slip behaviour are of major importance. Where environmental interactions are important during crack growth, the effects of slip behaviour on crack growth are extremely complex.

In general, the impingement of intense slip bands associated with heterogeneous deformation may act as stress concentrators across grain boundaries, leading to premature intergranular failure [33], or premature transgranular failure in coarser slip bands [30]. Dislocations pile up at grain boundaries at isolated points, and the large associated tensions across the grain boundaries open intergranular cracks that propagate without absorbing much energy [33]. A more homogeneous deformation would reduce the localised stress concentration and minimise the chances of intergranular cracking due to relaxation of the stress generated between a grain boundary and an impinging slip band [34]. Impingement of slip bands can also cause decohesion of the matrix/carbide interface, leading to intergranular cracking [27].

In fatigue crack growth experiments, strain localisation in slip bands may also enhance extrinsic shielding mechanisms, such as roughness-induced closure, crack branching and crack deflection [30]. In addition, heterogeneous slip increases the reversibility of slip, which reduces the extent of fatigue damage, thereby increasing the intrinsic fatigue crack growth resistance [30].

2.1.4.4 Dynamic Strain Aging (DSA)

DSA also known as Portevin-Le Chatelier effect results in a serrated stress-strain curve during plastic deformation [35]. It is common in Nickel based superalloys at intermediate temperatures and was observed in U720 at temperatures above 300°C, but was most intense at temperatures between 500 and 600 °C. [22] The exact cause for DSA is still under debate, but there are a number of possible explanations in the literature.

Most commonly it is assumed that DSA occurs when solute interstitial atoms are able to diffuse faster than dislocations travel through the lattice and are hence able to catch up with them and repeatedly pin them. The stress must increase to tear the dislocations away from the pinning atoms, and subsequently the dislocations can move at a lower stress (until a solute atom catches up again). This occurs many times, which causes serrations in the stress-strain curve. [36] Another possible explanation for DSA in nickel based superalloys is that a carbon atmosphere is created around the dislocation line. Carbon atoms can diffuse along that line to the γ' precipitates on which dislocations are arrested [37]. However it was also claimed that at 650°C interstitial solute atoms such as carbon are too mobile to create a sufficient drag force on the dislocations [38].

DSA has not only been seen in nickel based Superalloys, but also for example in steels, where there are no γ' particles. This suggests that the presence of γ' may not be required for DSA to occur. [39] Other theories state that DSA could be related to interstitial solute atoms. It is stated that carbon only causes drag at temperatures below 300°C [40], however drag effects were seen between 450 and 700°C due to chromium in an iron-nickel-chromium alloy with less than 10 ppm carbon. [41]

A relationship between DSA and an increase in work hardening is widely accepted. While DSA is pinning the mobile dislocations, new dislocations are created to maintain the plastic deformation rate. The density of dislocations is thus increased, which causes work hardening [36]. The disappearance of DSA with increased temperature and strain has been related to a precipitation mechanism, for example the precipitation of carbides that reduces the amount of interstitial carbon available to cause DSA. [37]

2.2 Fatigue

Fatigue of materials refers to failure of material due to repeated load cycling or fluctuating stresses. Under these circumstances, it is possible that failure occurs at maximum stress levels much lower than the tensile or yield strength for static loading. In engineering applications, this form of failure constitutes a majority of all the failures in structural and mechanical systems, final failure sometimes occurring very suddenly and without warning due to gradual growth of an unobserved crack to a critical length [42]. It is important to be able to quantify fatigue, and various approaches to safe-life prediction have been developed over the years.

The overall fatigue life of a component is characterised by three distinct regimes, i.e. the crack initiation period, followed by subsequent short and long crack growth, and finally followed by final fracture after the flaw has reached a critical size. Cracks will initiate at the most favourable sites, usually at points of high stress concentrations, i.e. at defects or discontinuities in the components, and in smooth components, microcracks can initiate at the surface, e.g. at persistent slip bands. This is followed by rapid growth in the early stages of the short crack under local stress/strain conditions which caused the initiation, until some type of microstructural barrier is encountered [43]. The short crack growth may then undergo acceleration and/or deceleration due to various intrinsic and extrinsic factors. As the crack length increases, the crack will propagate more steadily as the crack tip process zone also increases and starts to sample a larger volume of material, i.e. the crack grows under conditions nearer to the material's average properties. At this point, crack growth behaviour will approximate to what is known as the long crack growth or more averaged behaviour. The relative time spent in each regime depends on various factors, such as the material, initial defect size, loading conditions and environment.

2.2.1 Linear Elastic Fracture Mechanics

Various fracture mechanics approaches have been developed over the years to characterise fatigue crack growth with loading conditions, the most widely used being the Linear Elastic Fracture Mechanics (LEFM) approach.

2.2.1.1 Macroscopic modes of fracture

The crack surface displacements in the three macroscopic modes of fracture are schematically shown in Figure 2-1.

Mode I in the tensile/opening mode, in which the crack opens normal to the crack plane, mode II is the shearing or in plane sliding mode, where the crack faces shear in a direction normal to the crack front, and mode III is the tearing or twisting mode where the crack faces are sheared parallel to the crack front. [44]

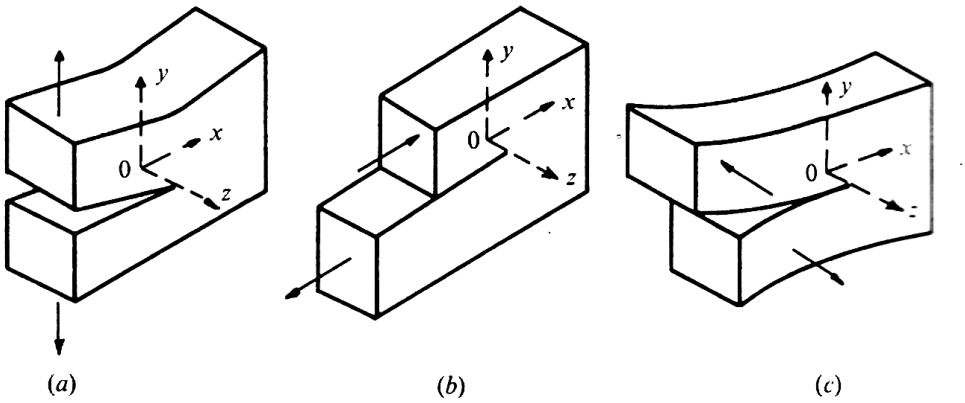

Figure 2-1: Macroscopic modes of fracture (a) mode I (opening) (b) mode II (shearing) (c) mode III (twisting) [44]

2.2.1.2 The Griffith Energy Balance Relationship

According to Griffith [45, 46], a crack can form or an existing crack can grow if the surface energy W_S created through the extension of a crack is equal to the potential energy Π (due to displacement and including the stored elastic energy)

Hence the critical condition for fracture is, if the total energy is constant or decreased:

$$\frac{dW_{Total}}{dA} = \frac{d\Pi}{dA} + \frac{dW_s}{dA} = 0 \qquad \text{Equation 2-3}$$

where A is the surface area of the crack.

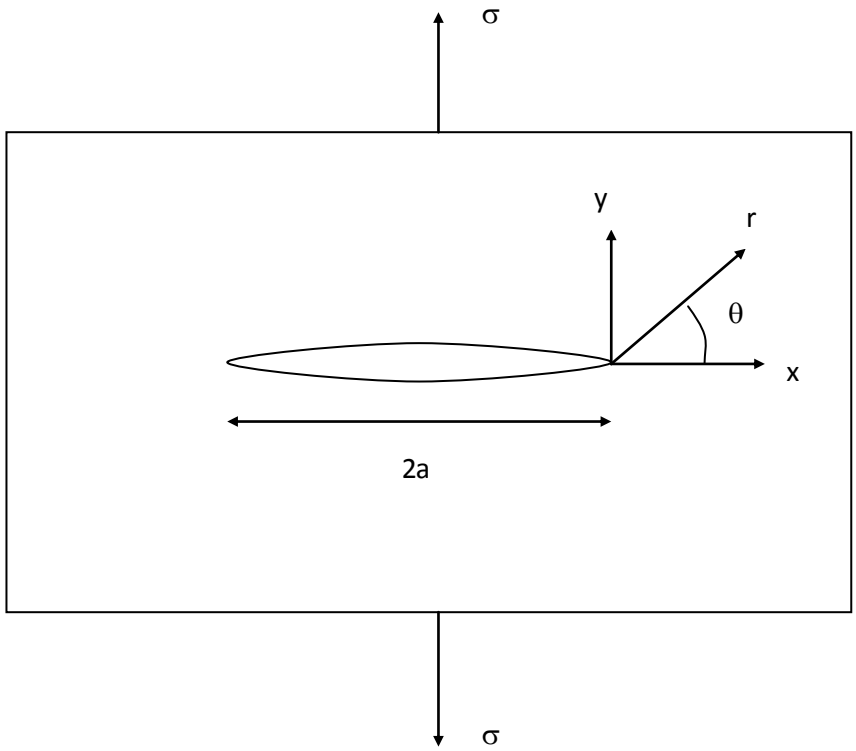

Figure 2-2: Sharp crack length 2*a* in a thin elastic plate, with a nominal applied stress σ [47]

For a sharp through thickness crack of length 2*a* in an infinitely wide plate with a remote tensile stress σ, as shown in Figure 2-2, Griffith showed that

$$\Pi = \Pi_o - \frac{\pi\sigma^2 a^2 B}{E} \qquad \text{Equation 2-4}$$

Π_0 is the potential energy of an uncracked plate, *B* thickness of the plate, and *E* is the Young's modulus. Since the formation of the crack requires two surfaces,

$$W_S = 4aB\gamma_S \qquad \text{Equation 2-5}$$

where γ_S is the surface energy of the material. Thus

$$-\frac{d\Pi}{dA} = \frac{\pi\sigma^2 a}{E} \qquad \text{Equation 2-6}$$

and

$$\frac{dW_S}{dA} = 2\gamma_S \qquad \text{Equation 2-7}$$

Equating Equation 2-6 and Equation 2-7 gives the fracture stress

$$\sigma_f = \left(\frac{2E\gamma_S}{\pi a} \right)^{\frac{1}{2}}$$ Equation 2-8

This is valid for sharp cracks in brittle materials.

2.2.1.3 The Strain Energy Release Rate

Irwin [48] proposed an energy approach similar to Griffith's, more convenient for solving engineering problems. The crack driving force or energy release rate *G* is the energy available for one increment of crack extension:

$$G = -\frac{d\Pi}{dA}$$ Equation 2-9

G is the rate of change in potential energy with crack area *A*. For a wide plate in plane stress with a crack of the length 2*a* (Figure 2-2), G can be derived from Equation 2-6:

$$G = \frac{\pi\sigma^2 a}{E}$$ Equation 2-10

Crack extension occurs if *G* reaches a critical value G_C (the fracture toughness of the material)

$$G_C = \frac{W_S}{dA} = 2w_f$$ Equation 2-11

where

$$w_f = \gamma_S$$ Equation 2-12

for an ideal brittle material and

$$w_f = \gamma_S + \gamma_P$$ Equation 2-13

for an elastic plastic material, where γ_P is the plastic work per unit of surface area created.

2.2.1.4 The Stress Intensity Factor

Irwin quantified the near tip stress field for linear elastic cracks in terms of the stress intensity factor, using the analytical methods of Westergaard. In this approach, local stresses ahead and near the crack tip are correlated to the far-field applied stress and the flaw length.

Consider a sharp, through thickness crack of length 2*a* in a thin elastic plate of an isotropic homogenous solid (see Figure 2-2). For the plane problem (i.e. mode I and II), the local near crack tip stresses for mode I at co-ordinates (r, θ) are given, to a first approximation, by [44]:

$$\sigma_{xx} = \sigma\left(\frac{a}{2r}\right)^{1/2}\left[\cos\frac{\theta}{2}\left(1-\sin\frac{\theta}{2}\sin\frac{3\theta}{2}\right)\right]$$ Equation 2-14

$$\sigma_{yy} = \sigma\left(\frac{a}{2r}\right)^{1/2}\left[\cos\frac{\theta}{2}\left(1+\sin\frac{\theta}{2}\sin\frac{3\theta}{2}\right)\right]$$ Equation 2-15

$$\sigma_{xy} = \sigma\left(\frac{a}{2r}\right)^{1/2}\left[\sin\frac{\theta}{2}\cos\frac{\theta}{2}\cos\frac{3\theta}{2}\right]$$ Equation 2-16

Note that the stresses tend to infinity as *r* tends to zero. In reality this does not occur due to plastic yielding.

Similar calculation can be done for mode II and III.

The term stress intensity factor, denoted *K*, was introduced to describe the elastic stress field near the crack tip. The general form of equation relating *K* to the load and flaw size is given by:

$$\mathrm{K} = \sigma_f \sqrt{\pi a}\ f\left(\frac{a}{W}\right)$$ Equation 2-17

where σ_f is the far-field applied stress, a is the flaw size and f(*a/W*) is the compliance function to accommodate different component geometry and shape, where *W* refers to the width of the specimen. *K* is very useful as it describes the local crack tip stress state (and strains). If two cracks of different size and shape have similar values of *K*, in theory the stress fields around the two flaws are identical. The use of *K* is convenient as it can be calculated from specimen and crack dimensions and external loading conditions.

2.2.1.5 *K* and *G* equivalence

Energy release rate *G* is a global parameter, while the stress intensity factor K is a local parameter. For linear elastic materials *K* and *G* are uniquely related. Combining Equation 2-10 and Equation 2-17, both for behaviour for a through crack in an infinite plate, leads to the following relationship between *G* and K_I (for mode I loading) for plane stress:

$$G = \frac{K_I{}^2}{E}$$ Equation 2-18

For plane strain, this is adjusted to:

$$G = \frac{K_I{}^2}{\left(\frac{E}{1-\nu^2}\right)}$$ Equation 2-19

When all three modes of fracture are present, the energy release rate is given as:

$$G = \frac{K_I^{\,2} + K_{II}^{\,2}}{E} \qquad \text{Equation 2-20}$$

for plane stress and

$$G = \frac{(K_I^{\,2} + K_{II}^{\,2})}{\frac{E}{1-\nu^2}} + \frac{K_{III}^{\,2}}{\frac{E}{1+\nu}} \qquad \text{Equation 2-21}$$

for plane strain.

2.2.2 Fatigue

Instead of the stress range $\Delta\sigma$, the stress intensity factor range ΔK has been adopted widely to characterise fatigue crack growth as it describes the range of crack tip stress field. Plots of the crack growth rate per cycle, *da/dN* vs. ΔK (on a logarithmic scale) generally show a sigmoidal relationship divided into three distinct regimes, as shown in Figure 2-3.

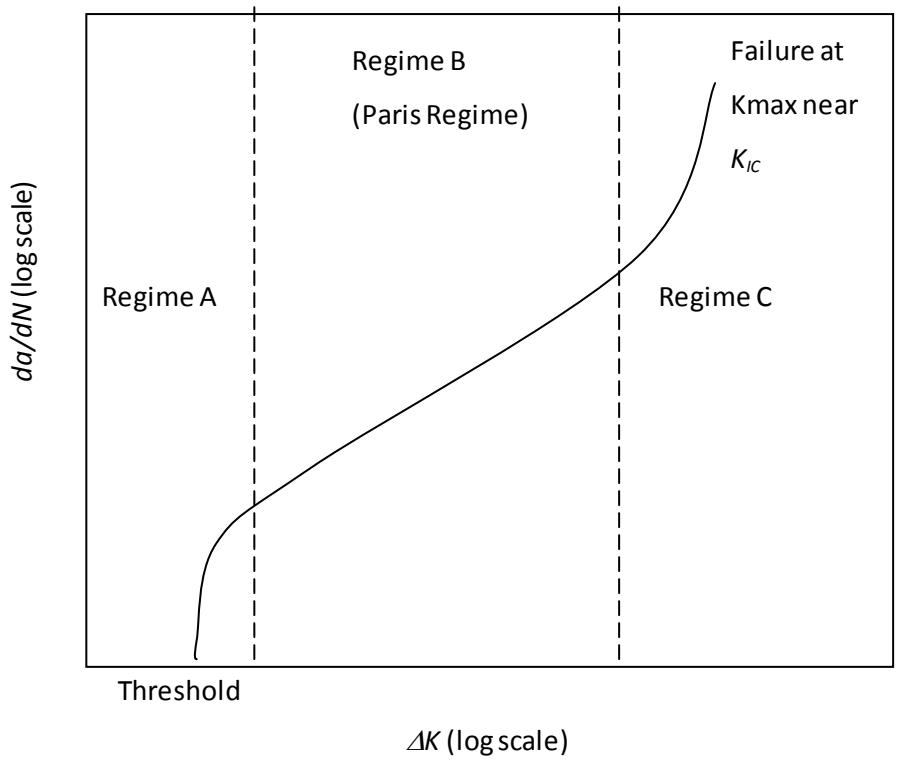

Figure 2-3: Typical *da/dN* vs. ΔK curve [47]

Regime A describes the low ΔK region where non-continuum behaviour is observed. Below the threshold stress intensity factor range ΔK_{th}, crack growth is considered arrested [44]. A large influence of microstructure, environment and mean stress on crack growth is generally observed in this region. Regime *B* denotes the region of stable crack growth which can generally be described by the Paris Equation:

$$\frac{da}{dN} = C\Delta K^m \qquad \text{Equation 2-22}$$

where *C* and *m* are material constants, which are generally less microstructurally sensitive. Regime *C* is the region of high ΔK where the crack growth accelerates rapidly to final failure and static failure modes increasingly come into play.

The ΔK parameter however is an elastic assumption, and when a significant amount of plastic deformation is taking place, alternative parameters such as the J-integral are more appropriate to characterise fatigue crack growth. When plastic deformation is occurring at the crack tip, the use of ΔK is still valid provided there is sufficient material around the plastic zone which is behaving elastically to provide true constraint. Other factors, such as microstructural effects, crack deflection and crack closure can also alter the effective value of local ΔK relative to the global ΔK calculated from the crack geometry and loading. These effects are discussed further in subsequent sections of the literature review.

There are also some uncertainties in extending linear elastic concepts to high temperature crack growth where plastic flow near the crack tip could be more extensive [49]. In addition, there could also be superimposed non-linear effects at these high temperatures such as time-dependent creep effects and environmental effects, which could alter the characteristics of the crack tip.

2.2.3 Crack Closure

The term crack closure describes load transfer in the wake of a growing crack, due to contact between the crack faces. Crack closure could arise due to surface roughness, oxide debris or plastic wake due to prior plasticity ahead of the crack tip. Very often more than one of these mechanisms is in operation during the event of crack closure. All these mechanisms can cause contact of the crack surfaces at a stress intensity greater than the applied minimum stress intensity, hence the crack tip experiences an effective ΔK that is less than the applied ΔK, i.e. a lower crack tip driving force, causing a reduced *da/dN*. [44]

2.2.4 Crack tip plastic zones

Within the vicinity ahead of the crack tip, there is a zone in which the local crack tip stresses will exceed the yield strength of the material, in this region the material yields and local plastic processes are expected to operate. This process zone is likely to be important in controlling crack tip failure mechanisms.

In monotonic loading, for a maximum stress intensity factor K_{max} the size of this plastic zone can be generally described by

$$r_{p,monotonic} = \alpha\left(\frac{K_{\max}}{\sigma_y}\right)^2$$ Equation 2-23

Where σ_y is the yield stress and α is a constant factor that depends on the approximations used in allowing for this local plasticity within a *K*-dominated stress field.

However in cyclic loading, the material at the crack tip, which has already yielded in tensile loading, on unloading must both unload from the tensile yield state and re-yield in compression. Thus the reversed plastic zone size (PZS) ahead of a fatigue crack depends on ΔK and the effective yield stress is $2\sigma_y$ (assuming no Bauschinger effects on unloading) and so is considerably smaller than the monotonic PZS. It can be described as:

$$r_{p,cyclic} = \alpha\left(\frac{\Delta K}{2\sigma_y}\right)^2$$ Equation 2-24

For plane strain conditions the added physical constraint of the surrounding material results in an increase in the local stress values required to cause yielding of the material, which causes the plane strain PZS to be smaller than the plane stress PZS. [50]

A number of approximations are detailed below, which give a variety of values for α:

The Rice model has been developed from Griffith's energy balance relationship. [51]

For the plane stress region:

$$\alpha = \frac{1}{2\pi}$$ Equation 2-25

In the plane strain region, the added physical constraint of the surrounding material results in an increase in the local stress values required to cause yielding of the material. The extend of plasticity at the crack tip is therefore smaller, and can be described by:

$$\alpha = \frac{1}{6\pi}$$ Equation 2-26

The Irwin approximation estimates the plastic zone in a ductile solid by considering the crack tip zone ahead of a crack within which the von Mises equivalent stress exceeds the tensile flow stress. [52]

For the plane stress region:

$$\alpha = \frac{1}{\pi}$$ Equation 2-27

For the plane strain region

$$\alpha = \frac{1}{3\pi}$$ Equation 2-28

The Dugdale approximation considers the shape of the plastic zone size. The model based on the assumption that yielding takes place in a narrow strip ahead of the crack, and is

particularly appropriate for use during faceted Stage I crack growth (slip band crack growth) for materials which exhibit highly planar slip. [53]

For the plane stress region:

$$\alpha = \frac{\pi}{8}$$ Equation 2-29

For the plane strain region

$$\alpha = \frac{\pi}{24}$$ Equation 2-30

2.2.5 Initiation and Short Crack Behaviour

Fatigue crack initiation and short crack growth are important as a majority of turbine disc fatigue life is spent in these fatigue regimes during service [54-57]. High component stresses result in a relatively small extent of fatigue crack propagation prior to fast fracture, limiting a large proportion of the usable fatigue life to the short crack growth regime [58, 59]. The influence of microstructure and environment on fatigue crack initiation and short crack growth has been shown to play a dominant role, especially on cracks which are of a size comparable to the scale of characteristic microstructural features [57, 60]. Different authors have different definitions of the length which corresponds to a short crack, but in general this corresponds to the length at which non-continuum mechanics are operating. The definition of short cracks, according to Suresh [44], is as follows:

a) microstructurally short crack: where the crack size is comparable to the scale of a characteristic microstructural dimension such as the grain size for monolithic materials.

b) mechanically short crack: small fatigue cracks in smooth specimens where the near-tip plasticity is comparable to the crack size, or cracks which are engulfed by the plastic strain field of a notch.

c) physically short crack: where the flaws are significantly larger than the characteristic microstructural dimension and the scale of local plasticity, but are merely physically small with length typically smaller than a millimetre or two.

d) chemically short cracks, which are nominally amenable to linear elastic fracture mechanics analyses, but exhibit apparent anomalies in propagation rates when below a certain crack size as a consequence of the dependence of local crack tip environmental interactions on crack size.

The first definition represents a limitation as to the relevance of continuum mechanics, while the second represents a limitation on current LEFM descriptions of the crack driving force.

2.2.5.1 Crack initiation in Nickel base Superalloys

Naturally initiated cracks will form at the least resistant point in the microstructure, i.e. at pre-existing defects or in slip bands in favourably oriented groups of grains. The number of cycles required to initiate a crack will decrease as the amplitude of the cyclic load is raised, while the number of appearing cracks will increase with the amplitude of the cyclic load. [55, 61]

A variety of crack initiation mechanisms is possible in nickel-base superalloys. The mechanisms of crack initiation in nickel-base superalloys will depend strongly on various factors including microstructure, environment and temperature. At room temperature, fatigue cracks initiate predominately from slip bands, this is promoted by heterogeneous slip [21, 62], but also from twin boundaries [56], grain boundaries[61], at carbides[62, 63], due to cracking of inclusions/precipitates [21] or at defects [63]. At elevated temperatures, crack initiation has been observed to occur from slip bands [62], grain boundaries [20], twin boundaries [59],or at inclusions [63] or at defects [64].

2.2.5.2 Short Crack growth

Short crack growth is the regime of crack growth bridging the crack initiation process and the long crack growth process. Non-continuum mechanics are at work during short crack growth, hence the application of LEFM to characterise small crack growth may be inappropriate.

The general characteristics of short crack growth include:

i) Short cracks exhibit anomalously high, irregular growth rates when compared to larger cracks at the same ΔK [57, 62].

ii) Short cracks can also grow below the ΔK_{th} found for long cracks.[43]

iii) Considerable fluctuations and scatter are seen in short crack growth data. [43]

The application of the conventional method of life prediction, i.e. using integration of the *da/dN* vs. ΔK relationship with an initial flaw size and a critical flaw size may le ad to non-conservative estimates of component life, if the characteristics of short crack growth are not taken into account [65].

The anomalous short crack growth behaviour is attributed to the invalidity of using ΔK to characterise short crack growth due to the non-continuum behaviour of the cracks, due to local microstructural effects and to the absence of crack closure [54, 61]. Accelerated chemical attack due to relative ease of access to the short crack tips has also been cited to cause anomalous short crack growth behaviour [61]. The ΔK is unable to correctly describe the magnitude of crack tip stress-strain field for the case of short cracks. The crack tip driving force for short crack growth is noted to be significantly higher than that described by ΔK and LEFM predictions [65].

Short crack or stage I crack propagation generally occurs by single shear in the direction of the primary slip system and when the crack and its surrounding plastic zone are less than a few grain diameters in length[44]. A combination of this and the concentration of deformation into

intense slip bands leads to short cracks growing in a highly crystallographic manner, often parallel to the {111} planes [61]. This single slip mechanism results in a zig-zag crack path and predominantly faceted fracture surface at low temperature.

The fluctuations and scatter observed in short crack growth data are associated with interactions between the crack tip and microstructural features [61]. When the crack tip encounters a microstructural barrier, such as a grain boundary, inclusion, precipitate or twin boundary, the crack path might be altered, deceleration of the crack growth may occur, and may even lead to total arrest of the crack [59]. Furthermore the crack may also be deflected when overcoming this microstructural barrier. Each individual crack might show a different behaviour since it is affected by different local microstructures [43].

The high values of applied stress at which short crack studies are normally performed also result in extensive overall plasticity levels and hence growth at an effectively high value of R [29]. The lack of crack closure has also been associated with the anomalous high mean growth rates of small cracks [29]. At short crack lengths where the 'wake' behind the crack tip is limited, a small closure contribution is experienced [7]. Also, the greater plastic strain experienced at the tip of the short crack (as the crack is in plane stress state) results in greater crack opening displacements at the same nominal ΔK compared to a through-thickness long crack (which is in plane strain state), resulting in the loss of closure [29].

2.2.5.3 Convergence with long crack behaviour

As the short crack increases in size and more grains are encountered, deformation within the plastic zone is constrained by the need to maintain compatibility between randomly oriented grains, and the small crack growth rates will be expected to gradually merge with long crack growth data [66]. Convergence of short and long crack behaviour is generally assumed to occur when the short crack begins to sample the material as a continuum [62], i.e. when the constraints are sufficient to compel the microcrack to grow like a large crack, i.e. at a slower, 'average' rate. The general indication of convergence of short and long crack behaviour is the transition from stage I structure-sensitive crack growth (faceted) to stage II structure-insensitive crack growth (striated). Many studies have noted convergence of short and long crack data when the crack length has spanned as many as eight to ten microstructural elements [60]. Other researchers have noted convergence of short and long crack data when the crack tip plastic zone size exceeds the grain size of the materials [7]. These two are essentially similar conditions as the crack tip plastic zone size often exceeds the grain size when the crack has grown across approximately 8-10 grains [67] at the stress levels typically used in these studies.

2.2.5.4 Effect of temperature

With increasing temperature, the time required for crack initiation may be reduced or increased depending on the mechanisms in operation. As slip becomes more homogenous with higher temperature, cracking along slip bands may be suppressed. If the temperature is further increased, oxidation can reduce crack initiation resistance [63, 68]. Higher short crack growth rates have been observed at higher temperatures when compared with room

temperature. This increase can usually be associated with a change in slip character indicated by the fracture surface changing from a highly faceted to flatter surfaces. [62]

2.2.5.5 Effect of Environment

Increased crack initiation periods and reduced short crack growth rates have been observed during vacuum tests, in particular at elevated temperatures when testing Nickel alloys [27, 63]. Oxygen penetration along persistent slip bands has been cited to enhance stage I crack initiation and Stage II crack growth and penetration of oxygen along grain boundaries was associated with increased intergranular crack growth in Rene 80, MAR-M-200, IN738 and IN718. [27]

2.2.6 Threshold and near threshold long crack growth

Threshold or near-threshold crack growth is essentially the early portion of long crack growth regime, where under certain circumstances, e.g. low ΔK, the crack is unable to propagate or propagates very slowly. Crack propagation typically occurs in a very crystallographic manner in this crack growth regime, giving rise to a facetted fracture surface. In this regime, microstructure, temperature and environment have been shown to have significant effects on crack propagation behaviour.

Non-continuum failure processes are at work in the near-threshold crack growth regime. However, as the crack length is much larger than both the microstructural element size and the crack tip plastic zone size, stress intensity solutions can be applied to characterise crack growth in this regime. In many ways, the near-threshold crack growth regime and the short crack growth regime are similar. In both cases, the crack tip plastic zone is typically confined to a single grain causing the crack to propagate in stage I crack growth mode. However, in the near-threshold crack growth regime, the crack samples the material's average properties due to its larger crack dimensions, whereas in the short crack growth regime the crack samples only the material local to the crack.

A transition from structure-sensitive near-threshold crack growth to structure-insensitive long crack growth is found to occur when the crack tip plastic zone size exceeds the grain size of the materials [29]. Beyond the transition, a much flatter fracture surface is observed. The transition was observed to be independent of R-ratio (the ratio of $\sigma_{min}/\sigma_{max}$) and the change from an air to vacuum environment[69]. Some studies have also noted a discontinuity in the crack growth rates da/dN vs. ΔK plot to correspond to the transition [69].

2.2.7 Long crack growth in Paris regime

Long crack growth corresponds to crack growth where the flaw size is large compared to the scale of plasticity or microstructural elements. Continuum mechanics are at work in this crack growth regime and the crack growth behaviour can be described by the Paris equation (Equation 2-22).

The fatigue crack growth process is a complicated function of a number of variables, including stress intensity, load ratio, temperature, frequency, hold time and environment. In general, the crack growth process can be grouped into two categories, i.e. cycle-dependent crack growth and time-dependent crack growth. Generally, cycle-dependent behaviour is favoured

by low temperatures, high cycling frequencies and inert environment, whereas time-dependent behaviour is prevalent at high temperatures, low cycling frequencies, and detrimental environments [70, 71].

In the cycle-dependent regime, the crack growth rate per cycle, *da/dN*, is controlled by the characteristics of the loading cycle, i.e. ΔK and the load ratio. Temperature has little effect on the crack propagation process except as they affect the yield strength and modulus of the material. Other factors, e.g. frequency, hold-time and environment, which are essentially time-dependent parameters will also have little effect on cycle-dependent crack growth processes. Crack propagation in the cycle-dependent regime is characterised by a transgranular crack path with evidence of striations in many cases.

Creep and environmental effects are the main processes giving rise to time-dependent behaviour in fatigue of superalloys. Creep is defined as the time-dependent deformation of a material under an applied load at elevated temperatures. It is an inherent characteristic of the material and occurs even in the absence of any environmental effects. Contribution of creep to overall deformation increases with temperature until it dominates material behaviour. Environmental effects include oxidation and corrosion, which are time-dependent due to the kinetics of the chemical reactions involved. The thermally activated processes of environmental degradation and creep produce a temperature and time-dependent crack growth. In the time-dependent regime, crack growth is characterised by an intergranular crack path (as observed in Nickel based superalloys) [72].

At some intermediate temperatures and frequencies, cycle-dependent and time-dependent components contribute to crack growth, i.e. the cycle-dependent and time-dependent regimes are not mutually exclusive. This regime is known as the mixed cycle and time-dependent crack growth regime, where creep-fatigue-environmental interactions may be taking place. Crack propagation in this regime is characterised by mixed transgranular and intergranular crack growth.

It is possible to separate the various effects on fatigue crack growth by testing under different conditions. Testing in air and in high vacuum will enable the effects of environment to be separated from those of fatigue and/or creep-fatigue as vacuum suppresses oxidation which takes place in the air environment. When testing in vacuum, any time-dependent behaviour present is principally due to creep alone. The interactions of creep and fatigue can be further assessed by testing using high frequencies in vacuum, which will reveal the pure fatigue crack growth behaviour, or by imposition of hold times at maximum load in vacuum to quantify the creep-fatigue interactions. The growth of cracks under service conditions is usually due to a combination of fatigue, creep and environmental effects. The complex interaction of all these effects is not usually a straightforward summation of the individual effects, and this makes the characterisation of fatigue crack growth even more complicated under these conditions. Depending on the load, creep and environmental effects can augment one another thus accelerating crack growth or oppose each other thereby retarding crack growth and sometimes even contributing to crack arrest. [70]

Creep is an inelastic deformation, hence the standard LEFM parameter ΔK used to characterise fatigue becomes invalid. Attempts to characterise creep-fatigue are based on partitioning

crack growth rates into fatigue and creep components, or by partitioning crack growth driving forces into elastic and inelastic components. Various attempts have been made to characterise crack growth in the mixed cycle and time-dependent regime, the most simplistic being the summation of the individual effects of fatigue and creep component of the crack growth [71], i.e.

$$\frac{da}{dN} = \left(\frac{da}{dN}\right)_c + \left(\frac{da}{dN}\right)_f \qquad \text{Equation 2-31}$$

where $(da/dN)_c$ and $(da/dN)_f$ are the crack growth rates due to the creep and fatigue components respectively. Good correlation between calculated and experimental results was found only in a limited number of studies [71]. Apparently this approach only works if there is no interaction between creep and fatigue crack growth, giving a total crack growth rate equal to the sum of the individual fatigue and creep components of the crack growth. When creep-fatigue interactions occur at the crack tip, acceleration of crack growth due to creep crack growth or retardation of crack growth due to stress relief from creep deformation may occur. Environmental effects, if any are present, are also not considered in this simple approach. Linear superposition would generally underestimate crack growth rates in the mixed crack growth mode regime as creep and environment effects tend to accelerate crack growth. The applicability of this simple cumulative damage concept at lower R-ratios where crack closure effects might be important is also questionable [71].

Another approach initially proposed by Saxena and used by Gayda et al. [73] with higher degree of success is the time integration method. The general form of the equation is:

$$da/dN = (da/dN)_f + \int (da/dt)dt \qquad \text{Equation 2-32}$$

where the term $(da/dN)_f$ is the crack growth rates due to "pure" fatigue unaffected by creep or environment effects. This can be obtained experimentally by testing at high frequencies in vacuum. The integral term corresponds to any time-dependent contribution to crack growth, and to calculate this portion of the equation, data from sustained load tests under conditions similar to the creep-fatigue tests are required. Effects of waveform used in the creep-fatigue tests are taken into account when calculating the integral term. This method has been used by Gayda et al. [73] to account for the effects of dwell time during creep-fatigue cycling in their tests, and good correlation was found in regions where environmental effects are not significant. In the time integration scheme, any effects of environment are clearly not taken into account except as they affect creep crack growth. Any interactive effects between the air environment and fatigue loading are also not considered.

2.2.7.1 Effect of temperature

An increase in temperature will generally lead to an increase in crack growth rates, when testing in air [74]. Smaller effects of temperature on crack growth rates were noted in vacuum tests compared to testing in air [72].

In the cycle-dependent crack growth regime, the increase in crack growth rates with temperature was found to be minimal [43]. In most cases, the variation in crack growth rates

can be rationalised in terms of changes in yield strength and modulus of the material with temperature. A change in slip character might also be responsible for the higher crack growth rates. An increase in temperature giving a more homogeneous slip would enable strain accommodation and hence reduce the localised stress concentrations, but at the same time the reduced degree of slip heterogeneity may lead to more irreversible slip and greater damage accumulation, which may be detrimental to crack growth resistance.

In the time-dependent crack growth regime, an increase in temperature will lead to a more pronounced increase in crack growth rates. In addition to changing slip deformation characteristics, changes in temperature also change the degree of time-dependent phenomena, i.e. creep and environmental degradation. The degree of creep and environment damage increases with temperature as both processes are thermally activated [72]. As temperature is increased, a transition from transgranular crack growth indicative of cycle-dependent crack growth to a mixed transgranular and intergranular crack growth or a predominantly intergranular crack growth will occur, indicating increasing contribution of creep and/or environmental damage to the crack growth process [25].

In tests involving hold times at maximum load, some studies [74]have noted that the crack growth rates increase with an initial increase in temperature, but with further increase in temperature, a decrease in crack growth rates was observed. This was attributed to crack tip blunting at the elevated temperature, or due to coarsening of shearable precipitates [74] leading to a more homogeneous slip process. As mentioned previously this will reduce the localised stress concentration and minimise the chance of intergranular cracking due to relaxation of the stresses generated between a grain boundary and an impinging slip band. This may also increase the intergranular crack tip resistance to environmental damage.

2.2.7.2 Effect of Environment

In the time-dependent regime, testing in an air environment has been associated with higher crack growth rates compared to testing in vacuum or an inert environment. Testing in air resulted in oxidation-dominated intergranular fracture in a study by Hide et al. [75] on U720. The effect of air as an oxidising environment was more marked in lower frequency and/or longer hold time tests, or at higher temperatures.

It has also been noted that the m-values, i.e. the slope of the da/dN vs. ΔK plot remained almost constant under various temperatures and imposed dwell time for tests carried out on U720 in an air environment [75]. Oxidation embrittlement along grain boundaries which dominates crack growth under the various test conditions could explain the similar m-values observed.

In the long crack growth regime, the effect of environment on crack growth rates is generally more marked in fine grain microstructures [76]. This is due to the larger amount of grain boundaries in the fine grain microstructure, which increases the influence of environment on the crack growth process. The intergranular crack growth process usually associated with environment interactions in fine grain microstructure is usually suppressed when the material is tested in vacuum, further supporting that environmental attack is predominant in air tests for fine grain microstructures.

2.3 Crack deflection

As a sustained macroscopic crack deflection is discussed in this work, it is important to consider the driving forces that have been found to control deflected crack growth in this and other alloy systems.

For a crack with a kink of length *b* at an angle α, as shown in Figure 2-4, where b is much smaller than the total crack length *a*, the local stress intensity factors k_1 for mode 1 (opening) and k_2 (shearing) describe the behaviour at the crack tip under plane strain conditions.

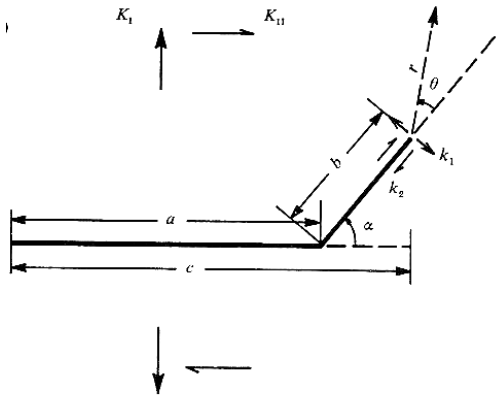

Figure 2-4: A schematic presentation of a kinked crack geometry and the associated nomenclature [77]

Suresh and Shih [77] have presented available stress intensity factor solutions for local k_1 and k_2 as functions of the kink angle α for a line crack containing a kink of the length b=0.1a that is subjected to a far field stress intensity factor K_I, as shown in the diagram in Figure 2-5.

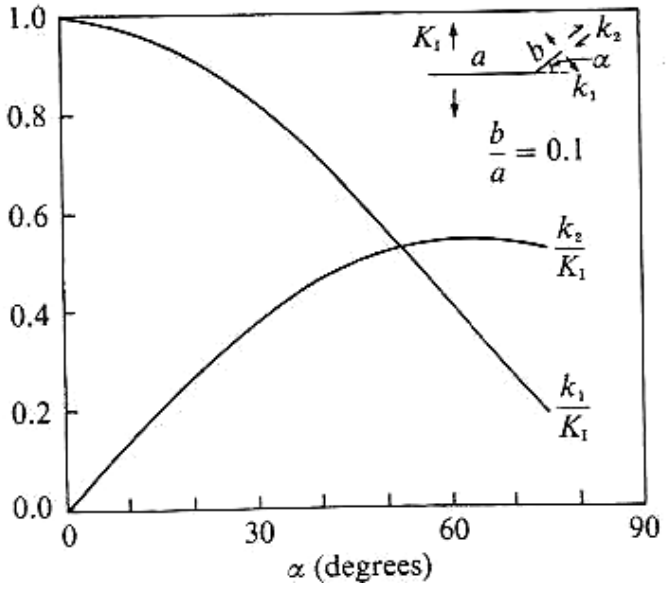

Figure 2-5: Variation of normalised k_1 and k_2 for b/a=0.1as a function of a kink angle α [77]

Prediction of the mixed mode behaviour of a crack is complicated, as the crack may not grow co-planar with the original crack. Past work on prediction of mixed mode failure can be divided into 3 categories. The first approach states that crack behaviour is controlled by some component of the crack tip stress or strain field – e.g. the Maximum Tangential Stress (MTS) [78]. The second extends Griffith's elastic energy release rate concept to mixed mode loading conditions – fracture is controlled by G_{max} [78]. The third suggests that a "strain energy density" may be evaluated in the vicinity of the crack tip and that this quantity controls crack behaviour, with the crack following the direction of minimum strain energy density S_{min} [79].

In the following sections a prediction of mixed mode fracture behaviour based on these three methods is reviewed in more detail.

2.3.1 Maximum Tangential Stress

For a central crack at an angle β with respect to the loading axis of the crack under a uniaxial far field tensile stress σ_a as shown in Figure 2-6. [78]

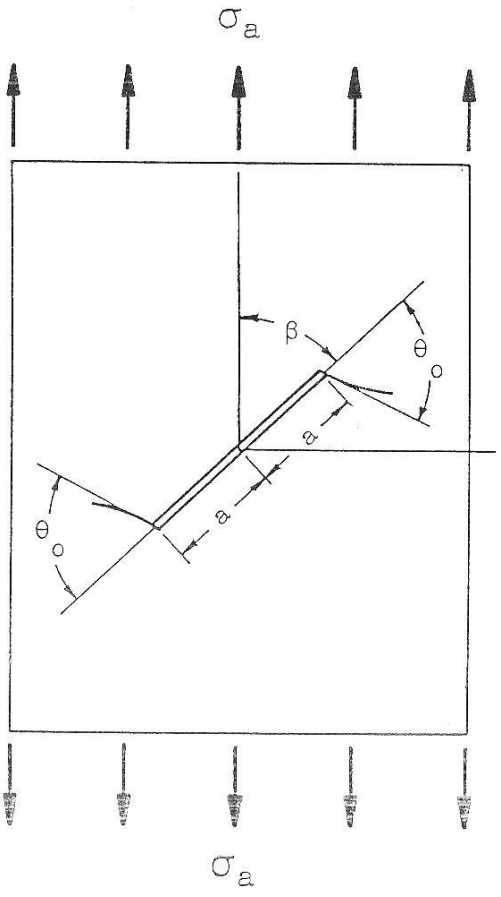

Figure 2-6: Inclined central crack subjected to uniaxial loading [80]

A Stage II crack is predicted to grow at an angle Θ_0 along which the resolved tangential tensile stress $\sigma_{\theta\theta}$ is a maximum, and the resolved shear stress $\sigma_{r\theta}$ is 0. It is always the direction of the resolved tangential stress, not the largest principle stress ($\sigma_{\theta\theta}$ or σ_{rr}).

For the example shown in Figure 2-6, the resolved tensile stresses are perpendicular (σ_y) and parallel (σ_x) to the crack, and the resolved shear stress τ_{xy} will develop parallel to the crack.

$$\sigma_x = \sigma_a \cos^2 \beta$$ Equation 2-33

$$\tau_{xy} = \sigma_a \sin \beta \cos \beta$$ Equation 2-34

The stress intensity factors for opening K_I and shear K_{II} can be described (for a large plate) as:

$$K_I = \sigma_a \sqrt{\pi a} \sin^2 \beta$$ Equation 2-35

$$K_{II} = \sigma_a \sqrt{\pi a} \sin \beta \cos \beta$$ Equation 2-36

For values of β between 0 and 90°, combinations of mode I and mode II are obtained, with pure mode I conditions for β = 90°.

The stresses $\sigma_{\Theta\Theta}$ and $\sigma_{r\Theta}$ near the crack tip can be described by:

$$\sigma_{\theta\theta} = \frac{K_I \cos(\theta/2)}{\sqrt{2\pi r}} \cos^2(\theta/2) + \frac{K_{II} \cos(\theta/2)}{\sqrt{2\pi r}} (-\frac{3}{2} \sin\theta)$$ Equation 2-37

$$\sigma_{r\theta} = \frac{K_I \cos(\theta/2)}{\sqrt{2\pi r}} \sin\theta + \frac{K_{II} \cos(\theta/2)}{\sqrt{2\pi r}} (3\cos\theta - 1)$$ Equation 2-38

The angle of the crack propagation Θ_0 can be determined for any K_I and K_{II} by differentiation of $\sigma_{\Theta\Theta}$ with respect to 0, setting the derivative to 0 and Θ to Θ_0:

$$K_I (\sin\theta_0) + K_{II} (3\cos\theta_0 - 1) = 0$$ Equation 2-39

The criterion for failure can be expressed as:

$$\frac{K_{If}}{\sqrt{2\pi r}} (\cos^3(\theta_0/2)) + \frac{K_{IIf}}{\sqrt{2\pi r}} (\frac{3}{2} \cos(\theta_0/2) \sin\theta_0) = \sigma_{\theta\theta c}$$ Equation 2-40

2.3.2 Analyses based on *G*

Erdogan and Sih [78] noted that the overall energy release rate G is:

$$G = G_I + G_{II}$$ Equation 2-41

and this could be used as an energy criterion for crack growth under mixed mode, when G exceeds a critical G_c. G_I ans G_{II} can be calculated from K_I and K_{II} using Equation 2-18

$$G_I = \frac{K_I^2}{E}$$ Equation 2-42

$$G_{II} = \frac{K_{II}^{\ 2}}{E}$$ Equation 2-43

K_I and K_{II} can be calculated from applied stress and crack length, which makes this approach appealing, however this is only valid if the increment of crack extension used to determine G_I and G_{II} is coplanar with the original crack. In reality mixed mode fractures do not occur in the direction of the original crack and to apply the Griffith energy criterion correctly, G must be calculated for an increment of crack propagation in an arbitrary direction. The criterion for crack extension would then be that the crack will propagate in the direction of the maximum energy release rate G_{max}, when G_{max} exceeds G_c. [78]

2.3.3 Analyses based on Strain Density

Sih [79] proposed the incremental strain energy dW stored in a volume dV of an elastic body at some position near the tip of the crack as:

$$\frac{dW}{dV} = \frac{1}{r}S + \text{ higher order terms in } r$$ Equation 2-44

S is the strain energy density factor, a function of θ, K_I, K_{II}, shear modulus μ and Poisson's ratio, v for a mode I and II situation.

The first term of the equations dominate for small r, S then characterises the magnitude of the energy field at the crack tip and can be used in fracture predictions. Crack propagation will be in direction of maximum potential energy, since this is equal to the negative strain energy. Crack propagation will be in the radial direction along which the strain energy is a minimum.

However several situations have been presented in the literature [81-83] under which no minimum in dW/dV is found at the crack tip, which does not support the S minimum hypothesis.

2.3.4 Crack Tip Shielding

Crack path deflection can cause crack tip shielding, i.e. the local reduction in effective crack driving force. A complex (deflected or branched) crack path can give rise to intrinsic shielding i.e. inherent to the crack path, that reduces the effective diving force at the crack tip and hence the crack growth rate, when the deflection of crack is following a certain k_i/k_{ii}. [50]

The size of the deflected crack segment, rather than just the angle can have an effect as it dictates the extent of the crack that experiences the reduced driving force. [84]

Suresh makes estimations of the deflected crack growth rate da/dN for a 2D case [85]:

$$\Delta K_{effective} = \frac{b\cos^2\left(\frac{\theta}{2}\right) + c}{b + c}\Delta K_{Nominal}$$ Equation 2-45

$$\frac{da}{dN} = \frac{b\cos\theta + c}{b + c}\left(\frac{da}{dN}\right)_{Nominal}$$ Equation 2-46

Where b is the deflected distance, c is the undeflected distance and θ is the deflection angle.

Suresh also confirms that periodic changes in the crack path on a microscopic scale may actually cause slower fatigue crack growth rates [77]. It is further suggested that the twist component k_{iii} might further reduce the crack tip driving force as compared to an in plane deflection (k_i and k_{ii} only). [84]

Extrinsic shielding can also be caused by roughness induced crack closure in deflected crack paths, as mentioned in section 2.2.3, which can slow down the crack growth. This contact shielding is caused by wedging of fracture surface asperities due to mismatch from the irreversible nature of inelastic crack tip displacements.

It depends on the degree of fracture surface roughness and frequent deflection, and it occurs usually at low stress intensity factor ranges and small crack tip opening displacements. It can be promoted by planar slip, e.g. in Nickel based Superalloys, and can be beneficial in reducing near threshold crack growth rates. [84]

Reed et al. [86] observed intrinsic shielding in single crystal U720 caused by greater reversibility of slip in vacuum, leading to less damage accumulation and highly planar slip, while in polycrystalline U720 studied by Loo Morrey [50] a higher crack growth threshold in vacuum is linked to both intrinsically lower crack growth and extrinsic shielding arising for the complex crack path.

2.3.5 Crack deflections in different alloy systems

An apparently similar deflection behaviour has been observed in U720 by Tong [87] in quasi static tests, with very low frequency and long dwells at 650°C in compact tension (CT) specimens, where deflected and planar cracking occurred. Stress intensity factors have been evaluated using FE software ANSYS, where K_I and K_{II} were calculated from the crack tip opening displacement. This showed an increase in K_{II}/K_I for the growing crack. No obvious explanation has been found to explain the deflection, however Tong made links to work by Cotterell [88], which proposes that mixed mode fracture can be caused by crack path instability. A crack deflects on a microscopic scale due to local inhomogeneity, the local mode I and mode II condition may then influence whether a crack is unstable and deflects further or is stable and returns to the original crack path.

The actual occurrence of the unstable crack growth may also depend on other factors such as the crack growth mechanism or grain size. Pook [89] summarised some work on deflected crack paths. He describes crack deflection in a similar way: The crack path is described as chaotic, with initial deviations from the crack path occurring due to microstructural variation, which can cause the crack to either follow a stable or unstable crack path.

Sustained deflected crack growth in fatigue has been reported in other alloy systems: Strongly deflected crack growth has also been reported in Udimet 720 single crystal systems in mixed mode loading and under vacuum conditions, where fatigue behaviour is more controlled by planar slip processes. The direction of the Stage I deflected crack growth was found to be dependent on the crystallographic primary and secondary orientations as well as loading conditions. Consideration of the local resolved shear-stress intensity and local resolved

normal-stress intensity for each slip system as it intersected the nominal crack-growth plane allowed the prediction of stage I crack paths. A *combination* of both opening and shearing were found to promote stage I crack growth, and boundary conditions were established within which stage I cracking was promoted. Highly deflected stage I cracking gave rise to significant shielding effects, but under suitable mixed-mode loading (described in more detail in Chapter 8.2.1), highly oriented, coplanar stage I crack growth was produced. Intrinsic stage I cracking under mixed-mode loading appeared to be greatly accelerated compared with mode I-dominated stage II crack growth for comparable stress-intensity levels [86]

Deflected crack growth behaviour has also been observed in aluminium alloys tested under mixed mode loading in fatigue, where crack propagation occurs along grain boundaries[90]. The deflection from the expected nominal crack plane has been linked to either strongly textured alloys with high volume fractions of shearable δ' (Al_3Li) precipitates where slip band crack growth has been promoted or specific alignments where grain boundary failure processes (principally shear controlled) have dominated fatigue failure. For the alloy AA7050, for a number of mixity conditions and initial $K_{eq,\,max}$ values the fracture deflection angles were measured and compared to predictions using conventional mixed mode analyses such as maximum tangential stress (MTS), G_{max} and S_{min}. It was found that the deflection angle decreased from the predicted angle (assuming MTS, G_{max} or S_{min} controls crack growth) at a $K_{eff,max}$ above 10MPa√m and that for increased K_{II}/K_I mixed mode grain boundary failure seems to be sustained. Results show variation from these predictions as shown in Figure 2-7. [90]

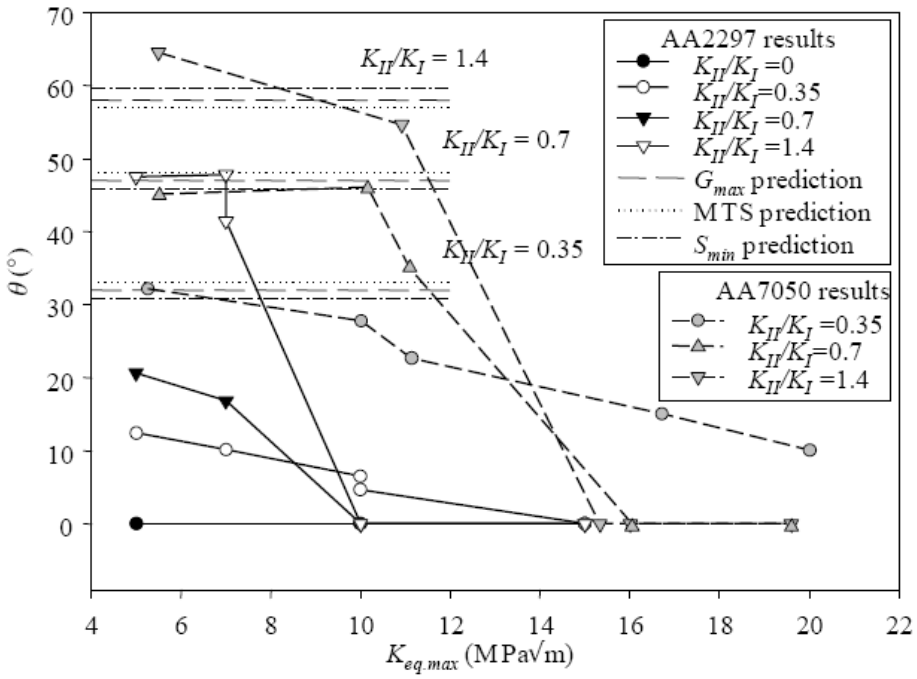

Figure 2-7: Initial crack propagation angle as a function of initial $K_{eq,max}$ for AA2297 and AA97 and predictions for MTS, S_{min} and G_{max} [90]

2.3.6 Previous work on Sustained Macroscopic Deflected Fatigue Crack Growth ('Tear Drop Cracking')

The sustained deflected fatigue crack growth discussed in this work, has previously been observed by Brooks [91]and Loo-Morrey [50]. It has been referred to as 'teardrop' cracking (TDC). Under mode I (tensile) loading a crack would usually be expected to grow in a plane perpendicular to the stress axis; however this unusual deflected crack growth has been observed in the superalloys Udimet 720 and RR1000 [23]. This fatigue crack exhibits considerable deflection from this plane. In tests performed with corner notch (CN) specimens at intermediate temperatures of 200 to 500°C, a central planar region (or teardrop) is found to be surrounded by sharply deflected shear regions at the surrounding free surfaces, where mode I and mode II (shear) are alternating. The term 'teardrop cracking' derives from the specific crack shape in this specimen. The specimen finally failed with a largely deflected shear fracture. The fracture surface of a TDC is shown in Figure 2-8.

Previous fractography [5] has shown that crack growth in the planar teardrop regions take place by Stage II crack growth, as well as the flat terraces in the shear regions. Loo Morrey observed some secondary cracks between the shear and planar region in the terraces, this could cause further shielding affecting the crack driving force of the deflected region. [50]

Fatigue tests done by Loo-Morrey [4] on U720 using Beachmarking (with an alternating R-Ratio of 0.1 and 0.5, see Figure 2-9) showed that the crack front advances in a projected quarter circular shape, so the crack is not tunnelling, due to creep as described by Antunes et al. [92], to form the tear drop and shear regions are forming progressively due to fatigue crack growth.

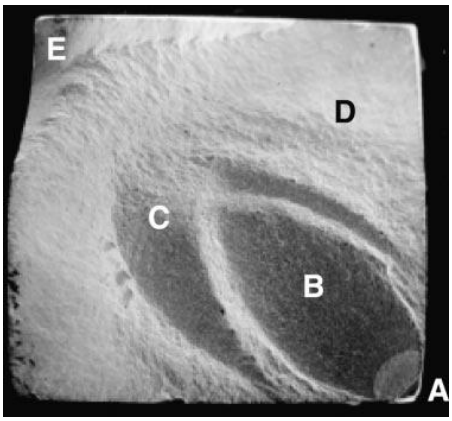

Figure 2-8: Tear Drop Crack Fracture Surface in U720 at 300 in air with A: Initial Notch, B: Flat Tear Drop region, C: Terraced region, D: Shear region, E: Final Shear Fracture [5]

Figure 2-9: TDC fracture surface with Beachmarking showing shear lips form progressively during fatigue [4]

2.3.6.1 Effect of Temperature and Environment

Teardrop Cracking was observed in fatigue tests between 200 and 500°C in air, while tests at room temperature (20°C) and higher temperatures (600°C) in air showed a macroscopically flat fracture surface. In fatigue tests that were performed in vacuum TDC was retained up to higher temperatures of 600°C. The fracture surfaces for the different environments and temperatures as tested by Loo-Morrey are shown in Figure 2-10. [4]

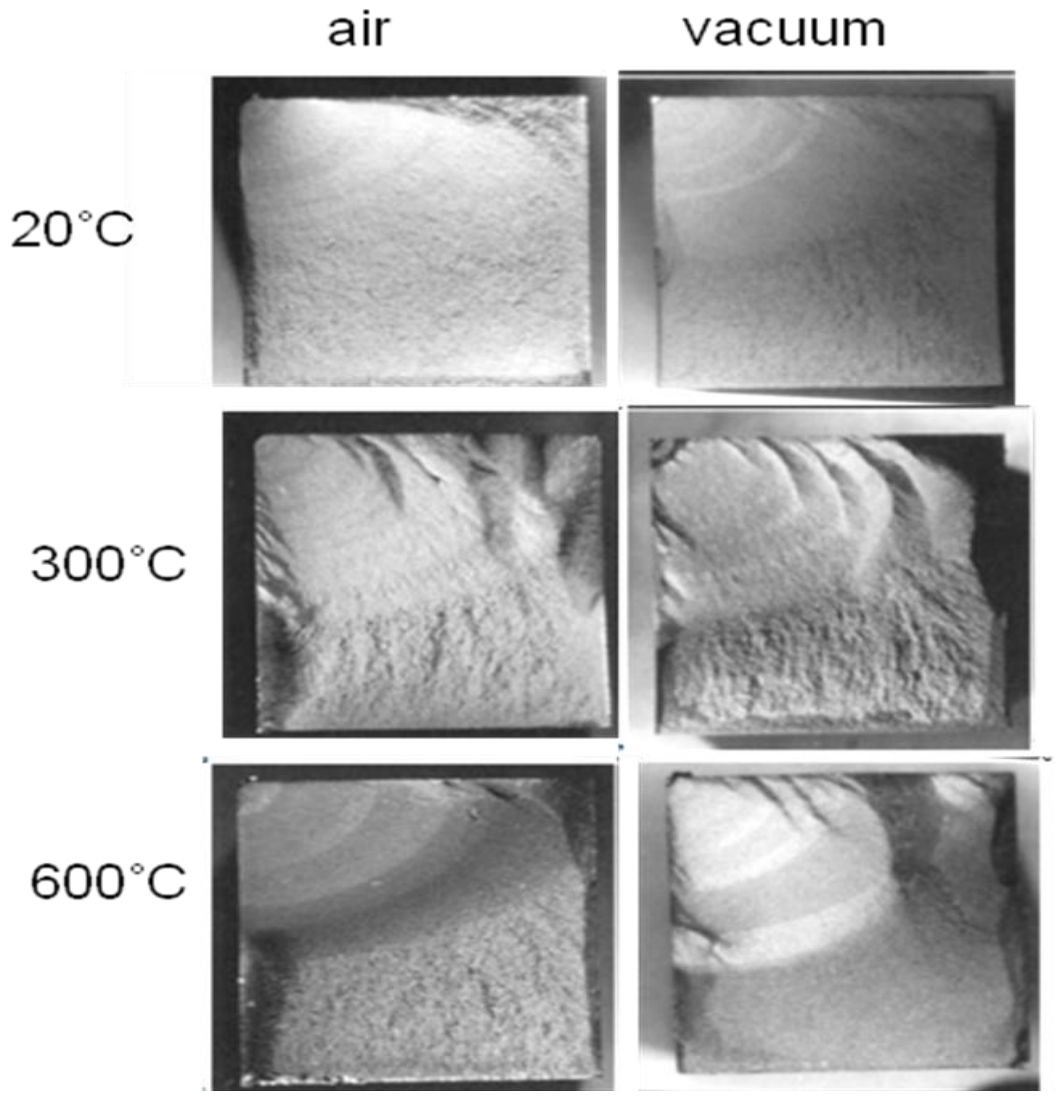

Figure 2-10: Fracture Surfaces at 20, 300, 600°C in air and Vacuum [4]

2.3.6.2 Applied Stress and Crack Tip Stress Intensity Factor

The shape of the TDC can be related to the initial crack tip stress intensity factor range ΔK_i and the overall applied stress and stress range $\Delta\sigma$. Higher ΔK_i, σ and $\Delta\sigma$ caused larger deflected terraced regions. Loo-Morrey et al. [4] found that TDC is influenced by the crack tip stress intensity factor range ΔK rather than the maximum stress intensity factor, which shows that TDC is evidently a fatigue phenomenon. Figure 2-11 shows TDC at different stress levels, where the shear regions completely enclose the teardrop region at an initial stress intensity factor range of ΔK_i=18MPa√m (c), a so called closed tear drop, while lower stress intensity

factor ranges, such as (a) initial ΔK_i=8MPa√m or (b) initial ΔK_i=12MPa√m result in smaller deflected regions and larger tear drop regions (open tear drop).

Moreover the onset of the terracing effect was observed to start around a ΔK of 29-33 MPa√m, while the largest shear lips were seen usually seen between 53-89MPa√m.

a: initial ΔK_i=8MPa√m b: initial ΔK_i=12MPa√m c: initial ΔK_i=18MPa√m

Figure 2-11: TDC Fracture surfaces from CNB samples tested at 300°C in vacuum at R=0.1 at given initial ΔK_i [4]

2.3.6.3 Effect of the Microstructure and Processing Route

TDC has been observed only in certain microstructures of U720:

- It was seen in fine grained materials, with grain sizes of approx. 10µm, while a flat fracture surface was observed in tests on materials with a grain size of about 48 µm. [5]
- The γ' size of the material, where TDC was observed, was ca. 2µm for the primary, 80-100 nm for the secondary and 10-20nm for the tertiary γ'. The phenomenon was suppressed by larger γ' (410nm [5]). Secondary and tertiary γ' have the most effect on the slip character of the material, which may be contributing to the deflected crack growth, however a direct influence on TDC was hard to establish.

Tests performed with Cast and wrought (C&W) and powder metallurgical (PM) materials with a similar composition and microstructure (effectively a fine grain size) have both shown the occurrence of TDC in the relevant temperature range [22]. Tests performed with the materials U720 and U720Li (low interstitial) showed TDC for both materials at the same conditions and microstructures, therefore it seems that the content of interstitial atoms, such as Boron, has no clear influence on the occurrence of TDC. [5]

Table 2 summarizes the previous findings on factors that influence teardrop cracking.

Test Conditions		Microstructure	
Temperature	200°C to 500°C in air	Grain size	Fine Grains (ca. 10µm)
Environment	In vacuum up to higher temperatures (600°C)	γ' size	γ' sizes of ca. 2µm (primary), 80-100 nm (secondary) and 10-20nm (tertiary)
Stress Intensity	ΔK controlled (not K_{max}) Onset of terracing: 29-33MPa√m for CNB and CDB, 20-22MPa√m for SENB	Interstitial content (C, B)	No effect
Frequency	No effect (between 0.25 and 145Hz)	Processing route (Powder Metallurgy or Cast & Wrought)	No effect

Table 2: Previous tear drop cracking (TDC) findings from Loo-Morrey [50] and Brooks [35]

2.3.6.4 Possible explanations

Based on the review of previous work TDC can therefore be described as a periodic, macroscopically mixed mode crack growth, which is 'initiated' at free surfaces. The slip character of Nickel based superalloys could be a possible explanation for TDC. Nickel based superalloys show inhomogeneous slip behaviour, which favours shear crack growth. Firstly this could be caused by the shearing of coherent γ' precipitates, which occurs at temperatures below 600˚C. At higher temperatures γ' strengthens and cross-slip can occur, hence slip becomes more homogenous and can occur predominantly in γ channels (particularly in high γ' volume fractions such as turbine blade materials). However this cannot be the full explanation, as no TDC is seen at room temperature, where the most planar slip behaviour is expected. The phenomenon cannot be explained by dislocation mechanics alone, meso- and macro fracture mechanics also need to be considered. Dynamic strain aging (DSA) does occur in nickel based superalloys at the relevant temperature range, however TDC was observed in U720Li (low interstitial) to the same extent as in U720, hence DSA, which is thought to be caused by the interstitial solute atoms, cannot be the sole cause of TDC.

2.4 Summary of Literature review

- Nickel based superalloys, such as Udimet 720Li are used in aero engine turbines, due to their good high temperature strength creep and fatigue resistance and resistance against high temperature corrosion. They gain their high temperature strength in particular due to the coherent γ' precipitates.
- Nickel based superalloys exhibit planar slip, due to the shearable coherent γ' precipitates.
- Material composition can be used to optimise the material in terms of e.g. high temperature strength or corrosion resistance
- Through heat treatments of the material, the microstructure can be varied to be optimised for the application. The grain size is controlled through solution heat treatment, which is usually below the γ' solvus so primary γ' are retained to a greater or lesser extent to pin grain size. Coherent γ' is formed during cooling from solution temperature.
- Processing route: PM has improved properties (e.g. grain size control) over C&W, but at increased cost
- Fatigue occurs in three different regimes: initiation and short crack behaviour, Paris regime, and final failure. For this work the long crack growth where the Paris regime is valid is most important.
- The crack tip stress intensity factor *K* is a useful parameter for linear elastic fracture mechanics and is used in this work to characterise the crack tip stress state.
- The occurrence of sustained macroscopic deflected crack, previously referred to as 'teardrop' cracking, in fatigue tests under intermediate temperatures in air and vacuum and at high temperatures in vacuum has been observed. No clear mechanism has yet been identified and this deflection is not considered in current lifing approaches for aeroengine components and could hence cause catastrophic failure.
- Moreover some of the literature on crack deflection has been studied, to help understand the mechanism and origins of deflections, and ways to predict the growth of deflected cracks under mixed mode, such as the Maximum Tangential Stress.
- Nickel based superalloys (and other alloy systems) have shown mixed mode cracking and deflection, which could in some cases be linked to shearable precipitates and growth along slip plane
- Deflection may slow down the fatigue crack growth due to crack tip shielding or roughness induced closure.

2.5 Aims of this work

As no clear mechanism has yet been identified by previous workers, the aim of this work is to identify the mechanism that causes this sustained deflection and to deliver assessment methodologies that can be incorporated into the component design and lifing process. Subsidiary aims to achieve these aims have been defined as:

- Review of available fractures (test-pieces and components from Rolls Royce and from previous researchers)
- Produce a working definition of macroscopically sustained mixed mode cracking to enable the categorisation of fractures, that can be used for different specimen types in which it was observed (CN and SEN in tension-tension and bend).
- From above propose microstructures and test conditions susceptible to teardrop cracking.
- Define experimental programme to confirm above considering the different temperatures and environments established in previous work as well as using different specimen types to compare the effect of constraint conditions.
- Postulate mechanism (Mechanism map)
- Experimental programme (mechanical testing and deformation mode study) to confirm mechanism.
- Determine overall crack growth rates from tests and local crack growth rates of deflected regions and effect on macroscopic crack growth rates. This can be used as an input for a lifing model to predict crack growth for different regimes.
- Analytic modelling of growth of deflected cracks: Crack Shape Mapping and strategic Finite Element Analysis (FEA) of mixed mode crack in 2D and 3D, to be able to predict crack path
- Model validation using service experience

3 Materials

3.1 Introduction

The material studied in this project is Udimet 720Li (U720Li), where Li (low interstitial) indicates the reduced content of interstitial atoms, such as Boron, and is compared in Table 5 with the composition of powder metallurgy (PM) Udimet 720 (U720), originally studied by Loo-Morrey [50] and U720Li in a cast and wrought variant as studied by Brooks [91]. The U720Li materials studied in preliminary work comprise: PM U720 in a fine grain (FG) and coarse grain (LG) variant (designated U720Li PM FG and LG respectively) which were previously also studied by Pang [23]. The majority of testing in this EngD has however been carried out on cast and wrought (C&W) U720Li supplied by Rolls Royce. Samples of the U720 PM material tested by Loo-Morrey were available and have been re-examined in Chapter 6, hence this material was also cut up and studied for comparison.

The U720 tested in previous work have a higher Cr content than the U720Li variants, i.e. expected to have better resistance to oxidation and corrosion. The PM material tested by Loo-Morrey has the lowest content of γ' formers Al and Ti, which might mean that this alloy has a lower high temperature strength. Brook's U720 PM FG has high Al and Ti contents, compared to the other alloys, so it should have comparatively good high temperature strength. However this material is also high in Co (ca. 17wt.%), which may increase high temperature strength, as it reduces solubility of γ' formers. The other materials have ca. 15wt.% cobalt, which also minimises Stacking Fault Energy. The U720Li variants are lower in B, i.e. boride former and the C&W variant used in this work is also lower in C, i.e. carbide former. Reduced C and B content might also reduce creep resistance, as they might cause dislocation pinning [11]. The heat treatments for these materials are described in Table 3 which has given rise to the variation of grain sizes reported in this and previous work.

The reported Yield strength (0.2% proof stress) of the materials over a range of test temperatures is given in Table 4, estimates for U720Li PM FG and LG are made based on comparison of the Vickers Hardness at room temperature, this is also done for the U720 PM material, where yield strength values are also available for some temperatures.

Material	U720 PM [4]	U720 PM FG [22]	U720 PM CG [22]	U720Li PM FG [23]	U720Li PM LG [23]	U720Li C&W [93]
Solution heat treatment	4h 1080°C	4h 1105°C	4h 1170°C	4h 1105°C	4h 1135°C	4h 1080 to 1100°C
	oil quench	oil quench	air cool	oil quench	air cool	oil quench
			4h 1080°C			
			air cool			
Ageing heat treatment	24h 650°C	24h 650°C	24h 650°C	24h 650°C	24h 650°C	16h 760°C
	air cool	air cool	air cool	air cool	air cool	air cool
	16h 760°C	16h 760°C	16h 760°C	16h 760°C	16h 760°C	
	air cool	air cool	air cool	air cool	air cool	

Table 3: Heat treatments of U720Li and U720

Material	U720 PM measure by Loo-Morrey	U720 PM Estimate for comparison	U720Li PM FG	U720Li PM LG	U720Li C&W
HV10 at room temperature	**461**	**461**	**477.5**	**433.5**	**434**
Ratio of HV10 compared to U720Li C&W	1.06	1.06	1.10	1.00	1.00
Yield strength at *T*	From [64]	Estimate	Estimate	Estimate	From[66]
20°C	1227	*1210*	*1253*	*1138*	1139
300°C	1141	*1151*	*1193*	*1083*	1084
600°C	1118	*1133*	*1174*	*1066*	1067
650°C		*1121*	*1161*	*1054*	1055

Table 4: Yield Strength in MPa of materials at different temperatures (Estimates based on U720Li C&W printed in italics, measurements done in this work printed in bold)

Alloy	Cr	Co	Ti	Mo	Al	W	Fe	Zr	B	C	Ni
U720Li PM FG and LG (as tested by H.T. Pang [23])	15.92	14.57	5.18	2.98	2.44	1.35	0.08	0.042	0.016	0.023	Bal.
U720 PM (as tested by M. Loo Morrey [50])	17.5	14	4.75	2.75	2.25	1	-	0.04	0.03	0.02	Bal.
U720 PM FG (as tested by R.R. Brooks [91])	18.2	17.1	5.27	3.29	3.02	1.28	-	0.043	0.031	0.022	Bal.
U720 PM CG (as tested by R.R. Brooks [91])	18.6	14.9	5.66	3	3.12	1.23	-	0.120	0.020	0.019	Bal.
U720Li C&W (as tested by R.R. Brooks [91])	16	14.3	5	2.98	2.54	1.34	-	0.039	0.011	0.021	Bal.
U720Li C&W [93]	15.74	14.50	4.98	3.00	2.56	1.24	0.17	0.037	0.016	0.014	Bal.

Table 5: Respective compositions in wt.% of U720Li and U720

3.2 Metallography

The microstructure was assessed to characterise grain size and γ' size and distributions in the material. The mounted samples were ground with 600 and 1200 grit SiC paper and then polished with a DP Plan Cloth with 9µm diamond suspension, then a DP Dac cloth with a 3µm diamond suspension and finally an OP Chem cloth with OP-S.

Etching was carried out on the polished samples with Nimonic Etch (40ml H_2O, 10ml HNO_3, 50ml HCl, 2.5g $CuCl_2$). Typical etching times were 10 to 15 seconds.

As the nimonic etch showed poor results for U720Li PM samples, further etching of the material was carried out through electrolytic etching using 10% orthophosphoric acid in H_2O. This etch preferentially removes the γ' on the surface. Stainless steel wires were used as electrodes and a voltage of about 2 volts was employed. The specimen was made anodic by spot welding the electrode to one corner of the specimen and the cathode (stainless steel washer spotwelded to electrode) was moved to a close distance (about 1mm) from the specimen surface covering the entire surface for about 5-6 seconds.

The etched samples were observed with an optical Microscope Olympus BH2 and in a Field Emission Gun Scanning Electron Microscope (FEG-SEM) Jeol JSM6500F. Secondary electron images were obtained at an acceleration voltage of 10kV.

To overcome the poor contrast for grain size analysis, a binary image of the grain structure and the primary γ' was produced manually by carefully tracing over enlarged SEM micrographs leaving out the primary γ′. For primary and secondary γ′ respectively, the precipitates are traced over from SEM micrographs. The binary images were then scanned and saved into the computer for further analysis.

To measure grain and precipitate size and distribution, the automatic image analysis software ImageJ was used. The pictures are scaled and parameters such as perimeter, area and feret diameters of the grain and primary and secondary γ' binary images were measured. Incomplete objects at the edge of the binary were removed using the image analysis software. The number of objects analysed for the grain size was no less than 100 in each case and no less than 500 objects were analysed for the primary γ' and no less 200 for secondary γ'.

Electron back scatter diffraction (EBSD) scans were also carried out on unetched mechanically polished samples of all 4 materials. EBSD data were collected using a Hikari EBSD camera, attached to an FEI Nova 600 Nanolab Dual-Beam FEG SEM/FIB system. Data collection speeds of 260 points per second were performed over a scan area of approximately 200 µm x 200 µm. Both γ and γ′ phases were indexed to a nickel structure file with a lattice parameter of 3.52Å. Between 2500 and 6500 grains were measured in the area, depending on the grain size.

3.3 Results

3.3.1 Udimet 720Li C&W

Figure 3-1 shows the microstructure etched with nimonic etch for 10 seconds observed in the SEM, where the primary γ′ is etched out and the grain boundaries are more clearly visible. Secondary γ′ can be observed at higher magnifications.

Figure 3-1 a shows variability in grain size in the C&W material (grain banding), which is linked to the processing route (cast and wrought). Figure 3-1 b and c show that twin boundaries can be seen in the material. Grain and precipitate measurements from these graphs are summarised in Table 6.

Figure 3-7 shows the EBSD grain orientation map and Figure 3-11 shows the image quality (IQ) map from the EBSD which shows the grain size. From the orientation map, it can be seen that this material has a no clear texture. The maps also confirm the large variation in grain size and evidence of twinning. The primary γ′ can be identified, as they are typically smaller than the γ grains and are principally located at grain boundaries.

Figure 3-15 shows the misorientation angle measured in the EBSD. Most grain boundaries have a high angle and a large number of twin boundaries (coincident site lattices) can be observed within the grains, so there is little apparent texture in this material.

3.3.2 Udimet 720 PM (studied by M. Loo-Morrey [50])

Figure 3-2 shows the microstructure etched with nimonic etch for 10 seconds in SEM, where the primary γ′ is etched out and the grain boundaries are visible. Secondary γ′ are shown at higher magnifications.

The EBSD map in Figure 3-8 shows the EBSD grain orientation and Figure 3-12 the grain size. From the orientation map, again little or no texture is evident in this material. The smaller grains surrounding larger grains can be identified as primary γ′ again. Figure 3-16 shows the misorientation angle measured in the EBSD. Most grain boundaries have a high angle and a large number of twin boundaries can again be observed within the grains.

3.3.3 Udimet 720Li PM (preliminary work, also studied by H.T. Pang [23])

For comparison detailed information on the microstructure of U720Li PM LG and FG have been taken from previous research [23] and compared with metallographic assessment conducted as part of this project on available samples. Figure 3-3 shows the γ matrix and primary γ′ in the PM U720Li Fine Grain (FG), etched with 10% orthophosphoric acid, which are again located on the grain boundaries.

Figure 3-4 shows a TEM image of a carbon replica; the larger particles are the secondary γ′ and the small ones the tertiary γ′. In Figure 3-5 the primary γ′ and the grain boundaries of PM U720Li Large Grain (LG) are visible. The grains are larger than in the both previous materials. Figure 3-6 shows the carbon replica of the secondary and tertiary γ′, where the secondary γ′ is larger than in the previous materials.

For the FG variant in considering the EBSD map in Figure 3-9, and the IQ map in Figure 3-13, it is difficult to distinguish between γ grains and primary γ′, as the sizes are quite similar. For the LG variant in Figure 3-10 for the EBSD map and Figure 3-14 for the IQ map, a large variation in grain size can be observed, and also some twins. Both alloys show little or no apparent texture. Figure 3-17 and Figure 3-18 show the misorientation angle measured in the EBSD for the FG and LG respectively. Most grain boundaries have a high angle and a large number of twin boundaries can be observed within the grains.

3.3.4 Comparison of grain and precipitate sizes

A summary of the sizes of grains, incoherent and coherent γ' estimations for the current materials assessed in this work and those in comparable previous work (from the etched microstructures) is shown in Table 6.

Histograms showing the relative frequency of the grain sizes (Figure 3-19), primary (Figure 3-20) and secondary (Figure 3-21) γ′ sizes have been created, from the measurements of binarised SEM graphs of the etched U720Li C&W and U720 PM, and measurements for the U720Li PM FG and LG from Pang [23] to show in more detail how grain sizes are distributed. From the EBSD a histogram is also created showing the relative frequency and the area fractions of the different grain sizes. This information combines the γ grains and primary γ′, as they cannot be distinguished in the EBSD. The primary γ′ can be clearly recognised in the histograms as the lower peak. Comparing the two histograms clearly shows that the larger grains make up much of the area fraction, but only a small number of the grains.

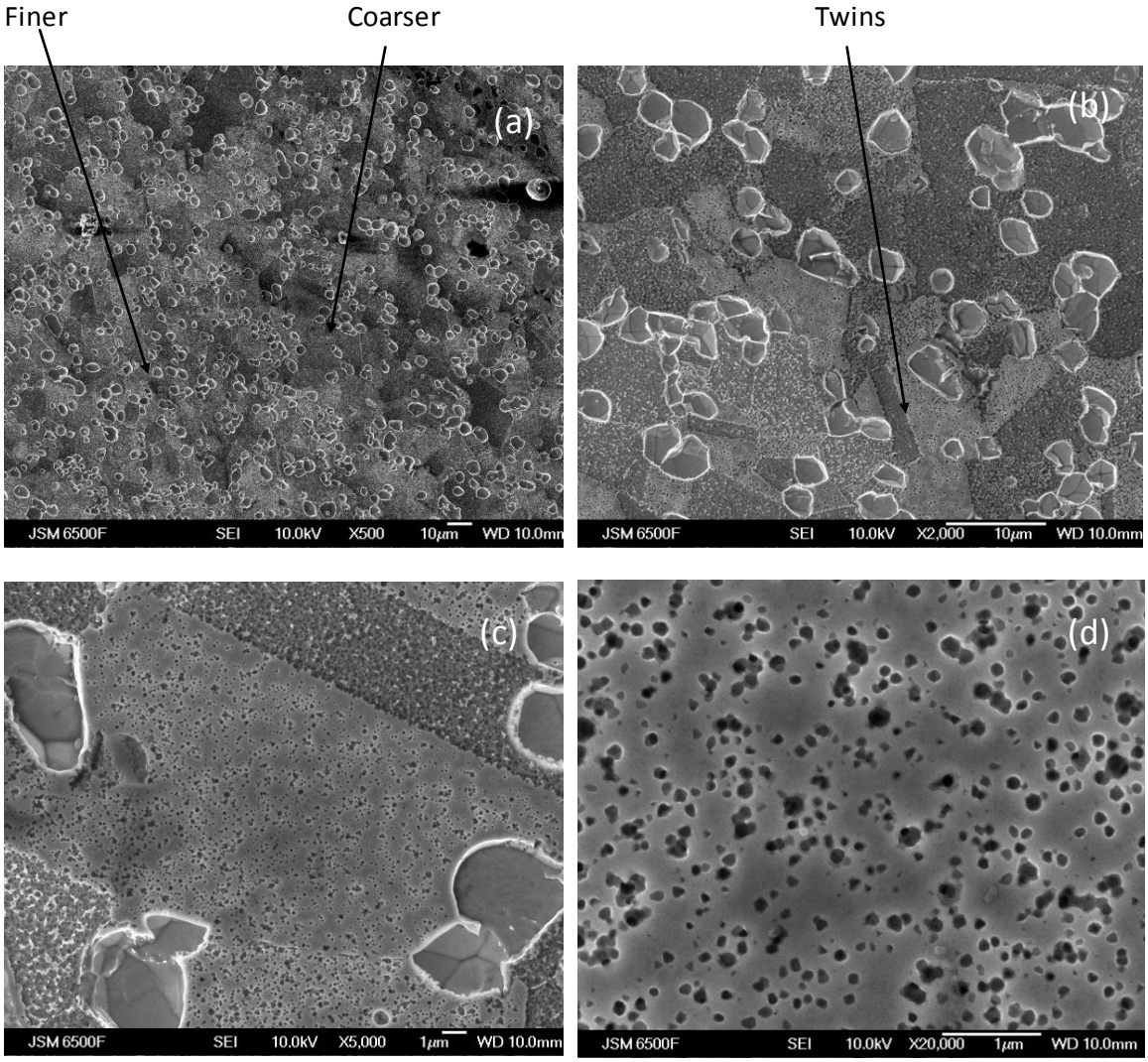

Figure 3-1: Microstructure of U720Li C&W (SEM micrograph with Nimonic etch (applied for 10 sec)) (a) Overview at low magnification (b) Higher magnification picture showing grain structure (c) Close-up showing etched out primary γ′, twin boundaries and secondary γ′ (d) Close-up of secondary γ′

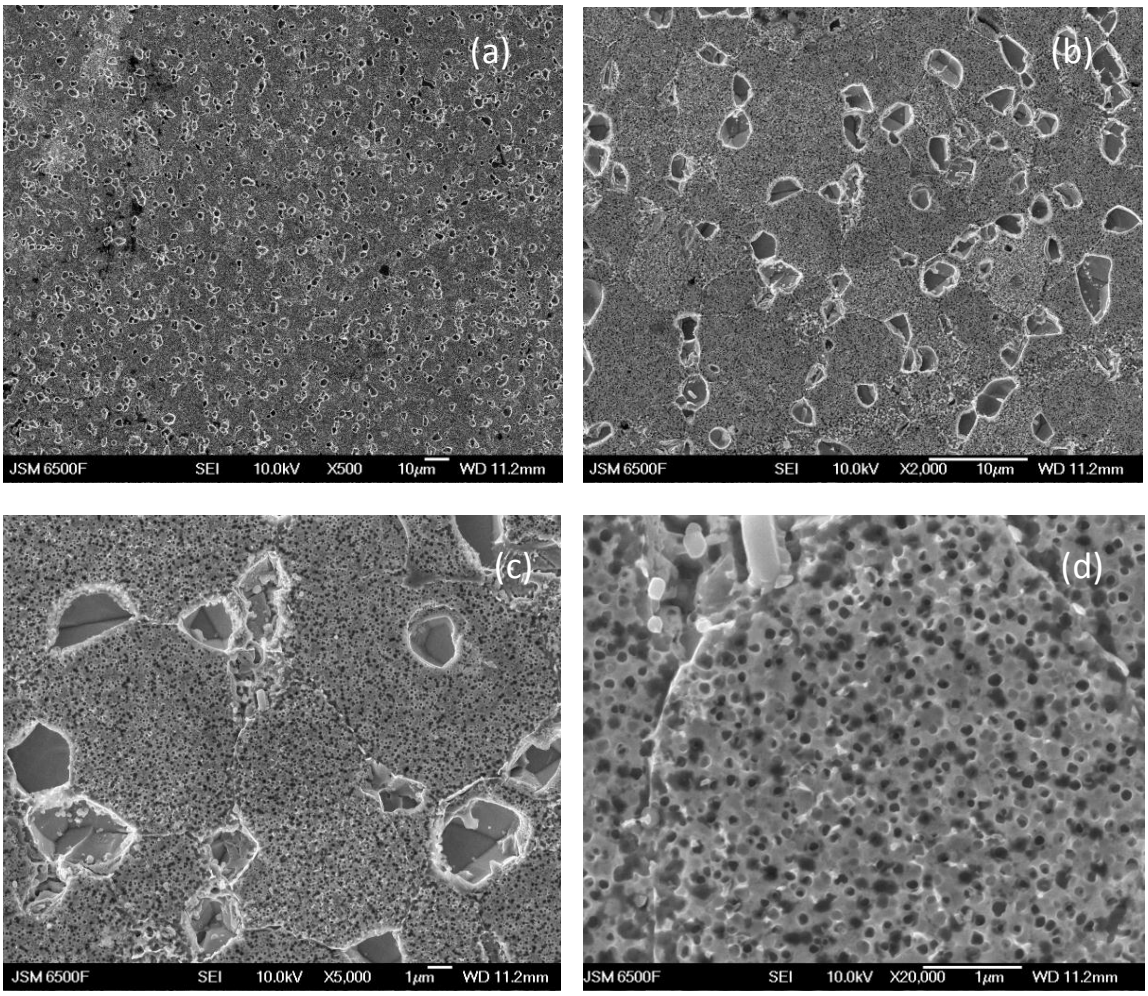

Figure 3-2: Microstructure of U720 PM (SEM micrograph with Nimonic etch (applied for 15 sec)) (a) Overview at low magnification (b) Higher magnification picture showing grain structure (c) Close-up showing etched out primary γ′ and secondary γ′ (d) Close-up of secondary γ′

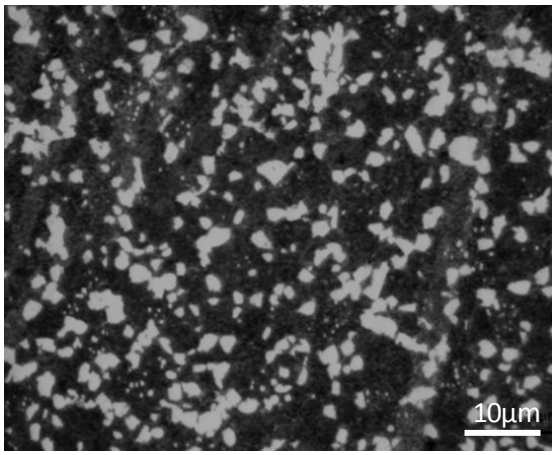

Figure 3-3: Microstructure of U720Li FG (optical micrograph with orthophosphoric etch)

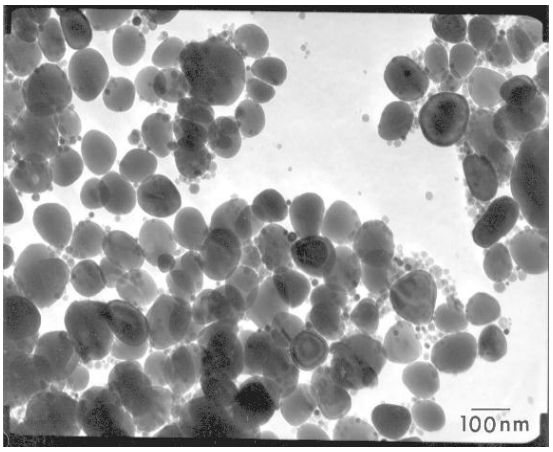

Figure 3-4: Microstructure of U720Li FG (Carbon replica in TEM) [23]

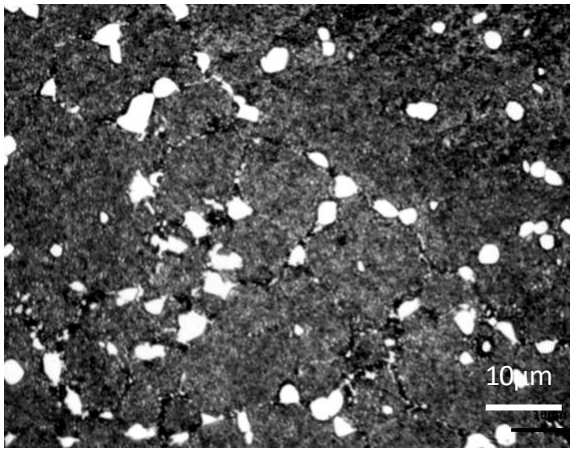

Figure 3-5: Microstructure of U720Li LG (optical micrograph with orthophosphoric etch)

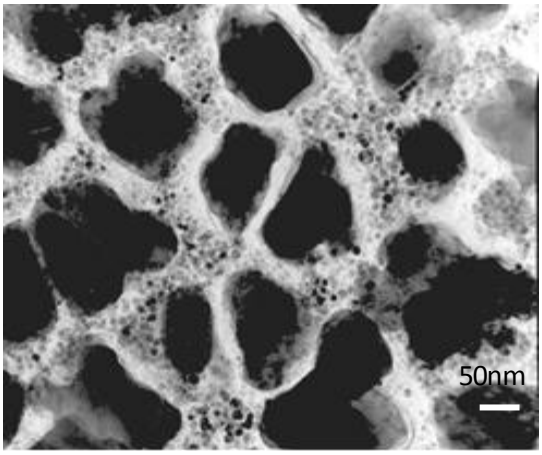

Figure 3-6: Microstructure of U720Li (LG) (Carbon replica in TEM) [23]

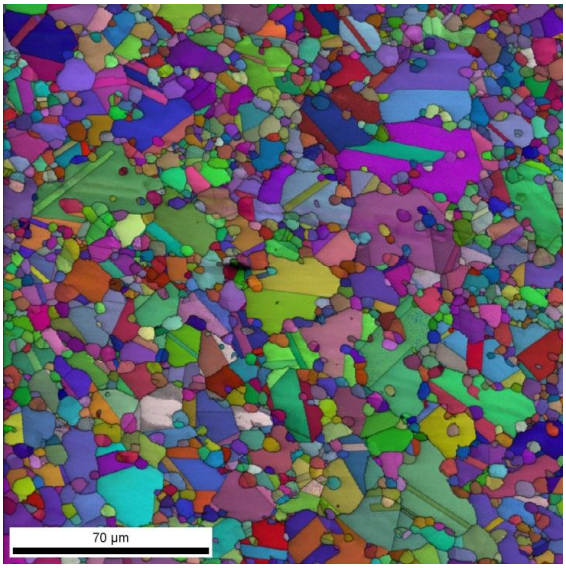

Figure 3-7: Microstructure of U720Li C&W EBSD image from plain polished sample showing variation in grain size (banding of finer and coarser grains) and location of primary γ′ (sometimes within grains as well as at grain boundaries). The colours represent different orientations of the grains.

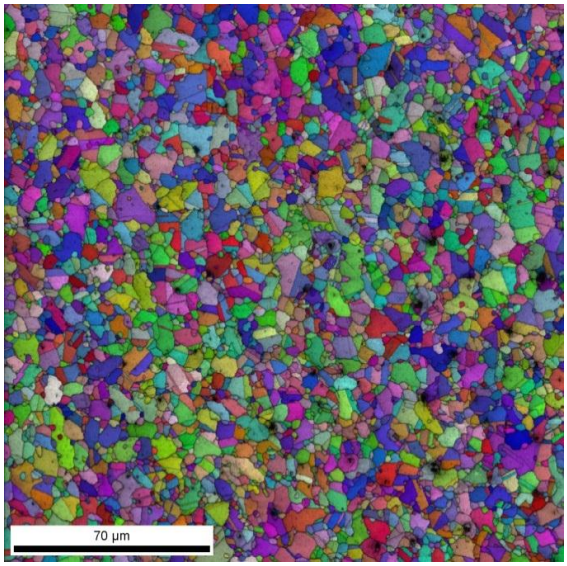

Figure 3-8: Microstructure of U720 PM EBSD image from plain polished sample showing grain size and location of primary γ′. The colours represent different orientations of the grains.

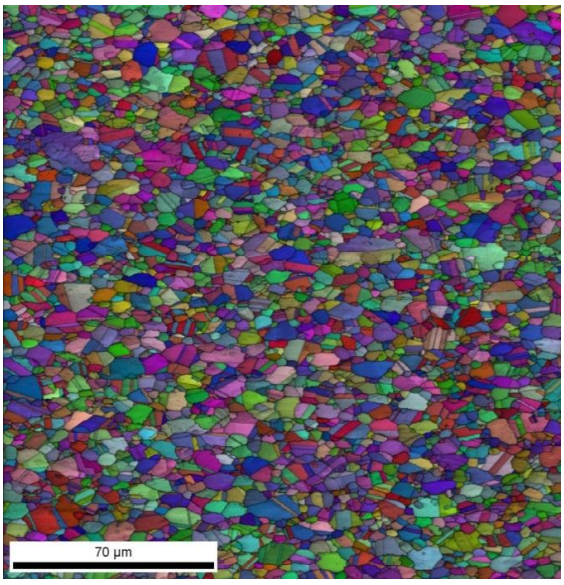

Figure 3-9: Microstructure of U720Li PM FG EBSD image from plain polished sample showing grain size and location of primary γ′. The colours represent different orientations of the grains.

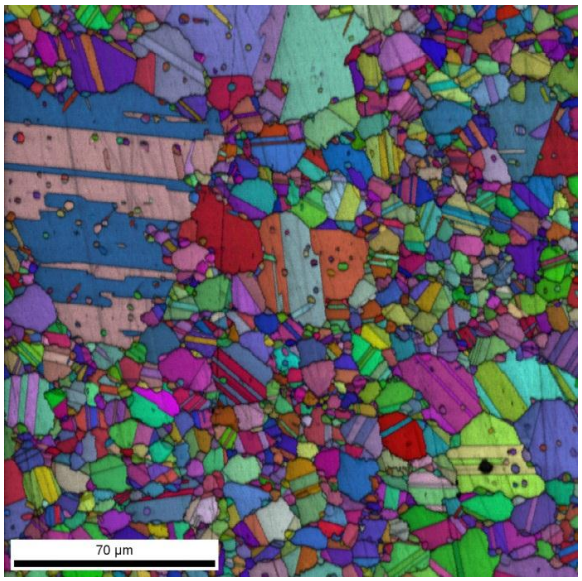

Figure 3-10: Microstructure of U720Li PM LG EBSD image from plain polished sample showing grain size (banding of finer and coarser grains) and location of primary γ′ at grain boundaries. The colours represent different orientations of the grains.

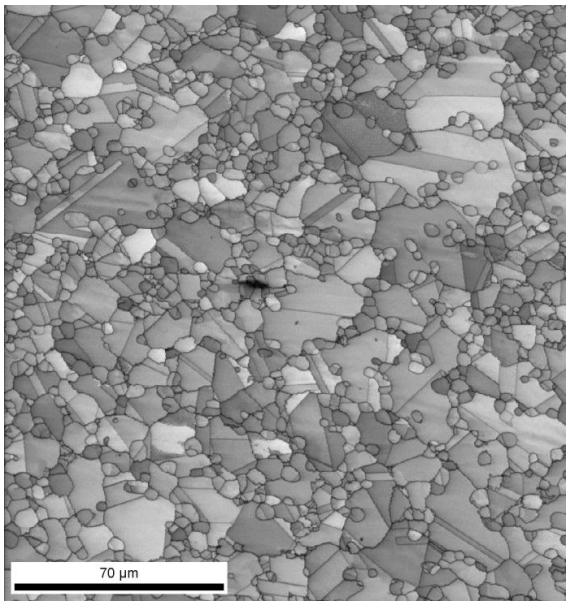

Figure 3-11: Microstructure of U720Li C&W EBSD image quality picture from plain polished sample showing variation in grain size (banding of finer and coarser grains) and location of primary γ′ (sometimes within grains as well as at grain boundaries)

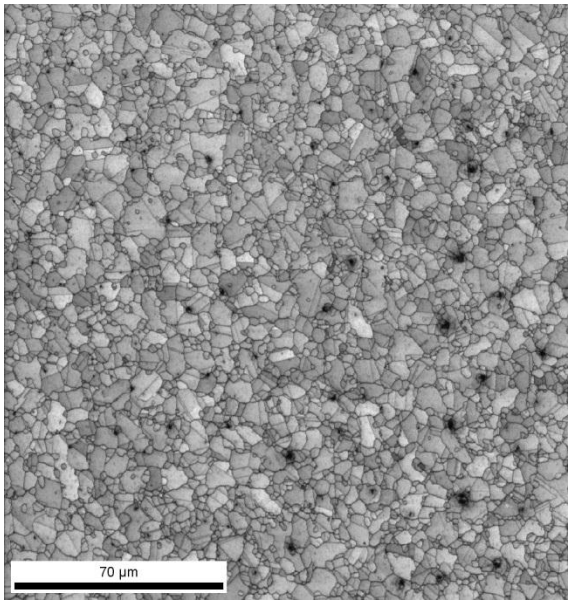

Figure 3-12: Microstructure of U720 PM EBSD image quality picture from plain polished sample showing grain and primary γ′ size and distribution

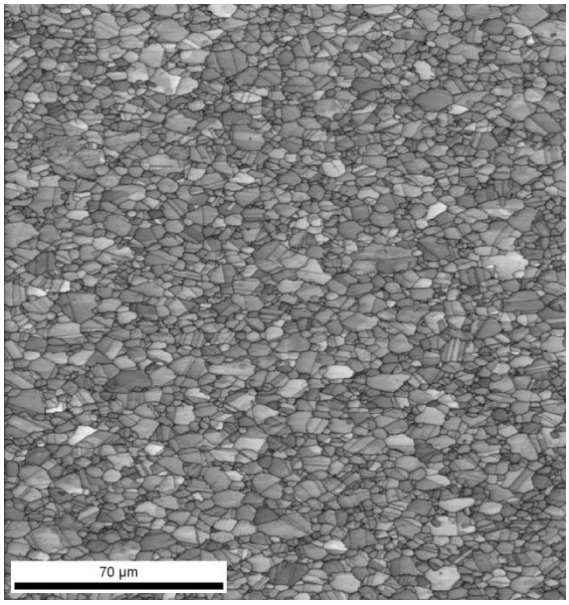

Figure 3-13: Microstructure of U720Li PM FG EBSD image quality picture from plain polished sample showing grain and primary γ′ size and distribution

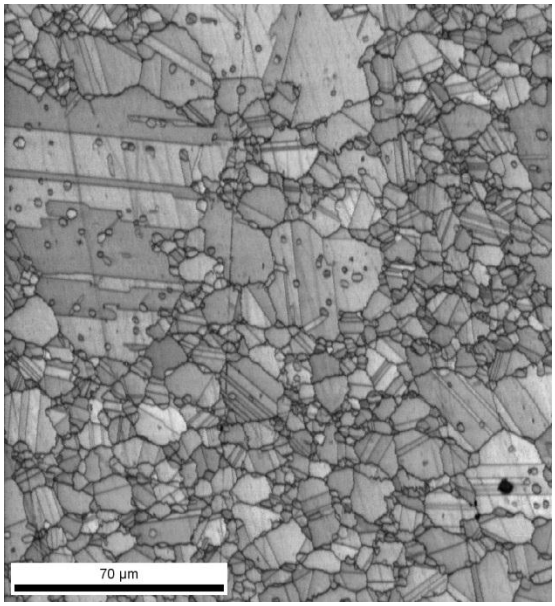

Figure 3-14: Microstructure of U720Li PM LG EBSD image quality picture from plain polished sample showing grain and primary γ′ size and distribution

2 – 5°
5 – 15°
15 – 180°
Coincident site lattice

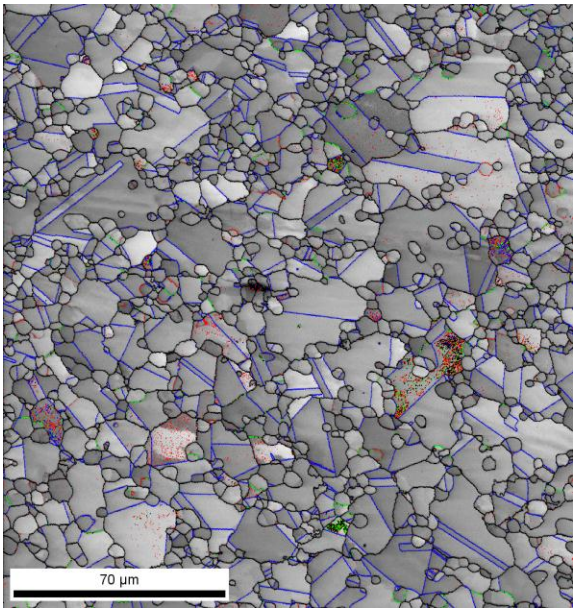

Figure 3-15: Misorientation Angles of U720Li C&W (colours indicate angles of boundaries as shown above)

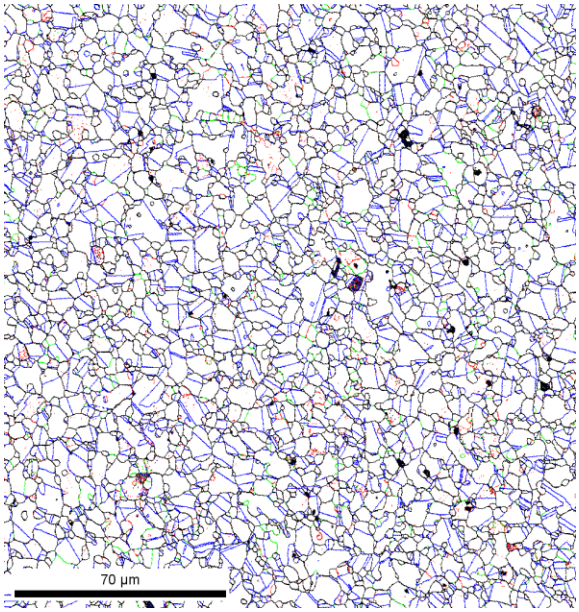

Figure 3-16: Misorientation Angles of U720 PM(colours indicate angles of boundaries as shown above)

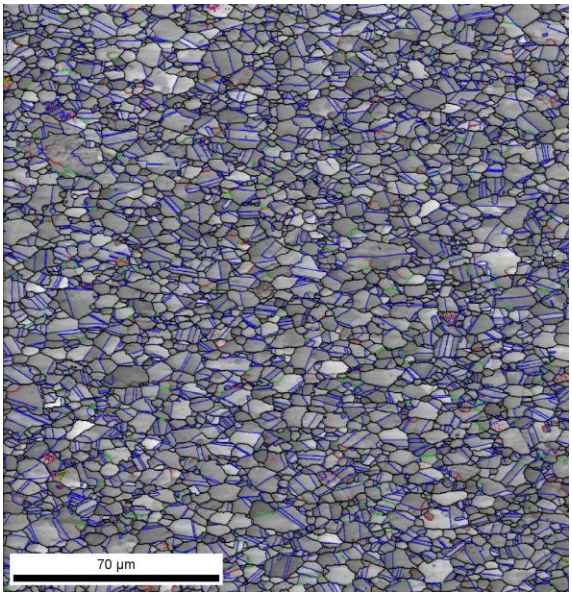

Figure 3-17: Misorientation Angles of U720Li PM FG (colours indicate angles of boundaries as shown above)

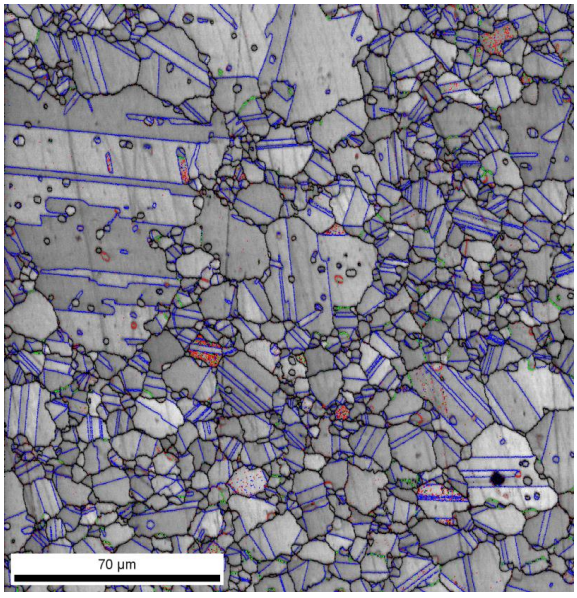

Figure 3-18: Misorientation Angles of U720Li PM LG (colours indicate angles of boundaries as shown above)

Material	U720 (as tested by Loo-Morrey [50])	U720	U720 CG	U720Li C&W	U720Li FG [23]	U720Li LG (large grain) [23]	U720Li C&W
		As tested by Brooks (using linear intercept method [91])					
Grain Size	**18.1 µm (Range 4.8 – 62.6µm)** *11 µm (Loo Morrey [50])*	*10±5µm*	*48±29µm*	*15±9µm*	6.4µm (range 2.1-13.1 µm) [23]	15.4µm (range 4.8-41.3 µm) [23]	**16.7µm (Range4.5-45.3 m)(Image J)** ***10.7 (linear intercept)*** 6.7-32µm [93]
Primary γ' size	**3.2 µm (Range 1.6-9.4µm)** *~2µm (Loo Morrey [50])*	*3 µm*	None	*2 µm*	1.99 µm (range 0.5-6.9 µm) [23]	2.52µm (range 0.9-7.6 µm) [23]	**5.1µm (Range 1.6-23.5µm)**
Primary γ' volume fraction	**12.6%**						**17.1%**
Average Grain size from EBSD (γ and γ') from number of grains	**2.2 µm (Range 0.4-10.6µm)**				**2.2 µm (Range 0.4-12.4µm)**	**2.6 µm (Range 0.4-31.9µm)**	**3.1 µm (Range 0.4-21.8µm)**
Average Grain size from EBSD (γ and γ') from area fraction	**5.3 µm**				**4.8 µm**	**12.3 µm**	**10.1 µm**
Secondary γ' size	**119nm (Range 64-207nm)** *100nm (Loo-Morrey [50])*	*80±14nm*	*410±94nm*	*100±23nm*	102 nm (range 51-150nm) [23]	190nm (range 81-300nm) [23]	**146nm (Range 45-625nm)**
Secondary γ' volume fraction	**9.1%**						**15.8%**
Tertiary γ' size	*20nm (Loo Morrey)*	*20±7nm*	*140±35nm*	*10±4nm*	16nm (range 1-45nm) [23]	17nm (range 6-30nm) [23]	Not measured

Table 6: Grain and γ′ size of the materials (measurements done in this work printed in bold, values determined with linear intercept in italics)

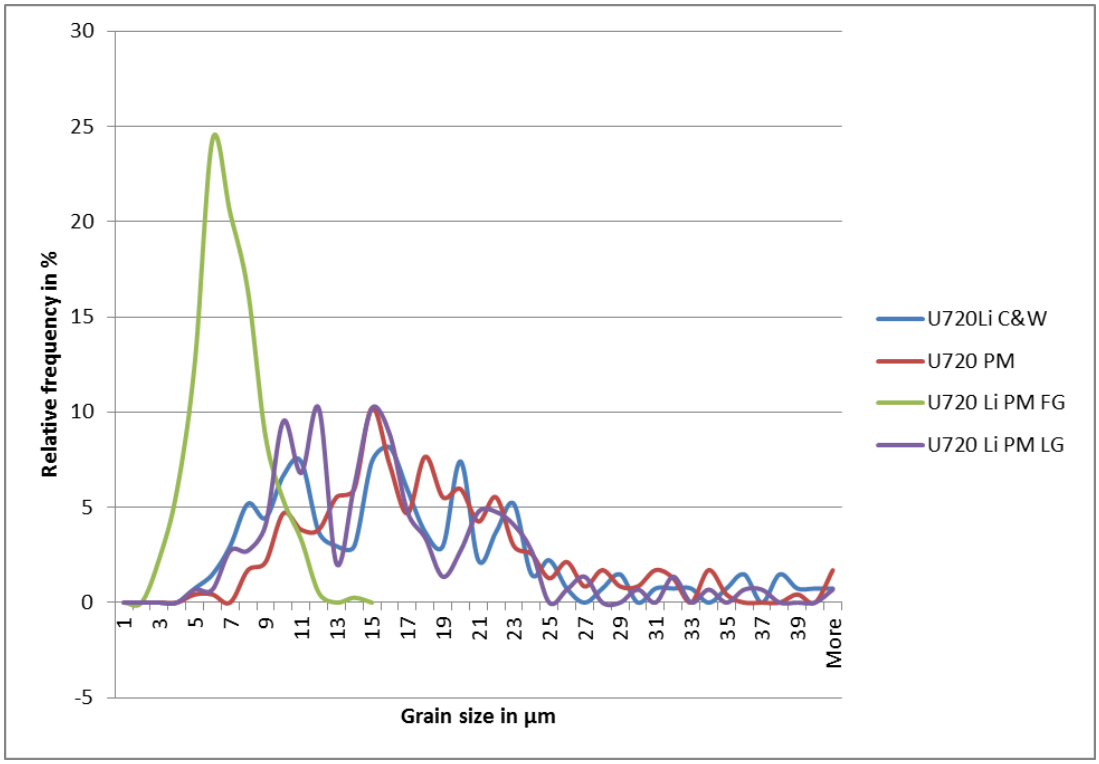

Figure 3-19: Relative frequency of grain size for U720Li C&W, U720 PM, U720Li PM FG and LG [23]

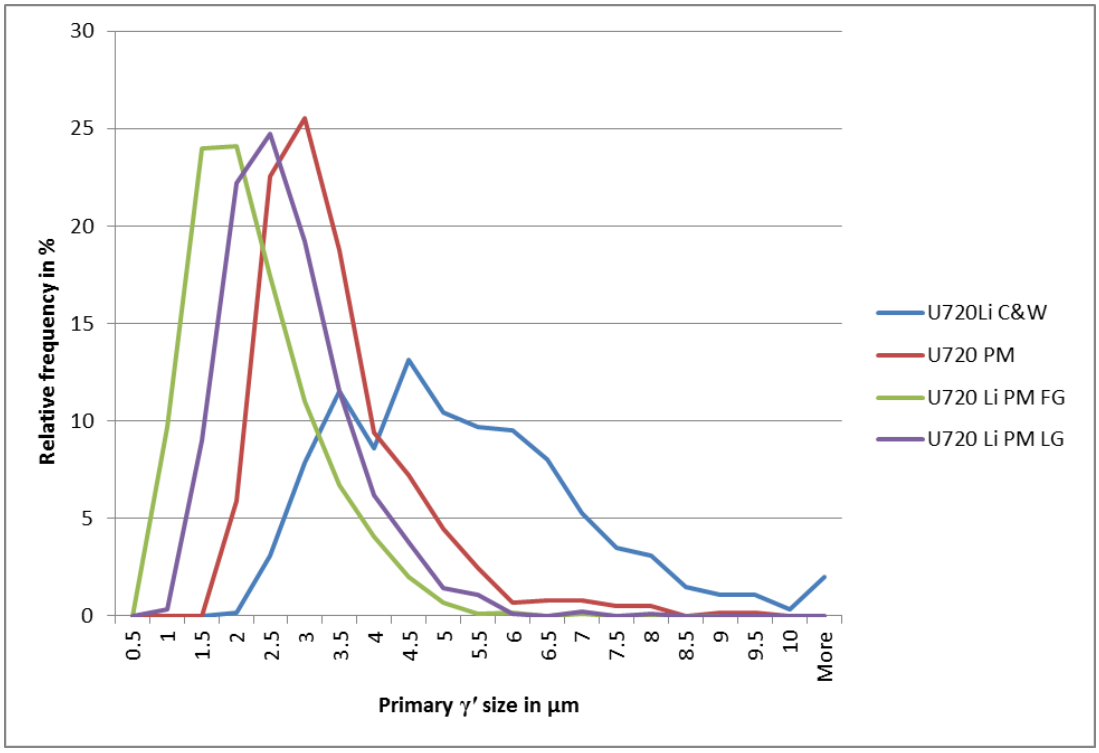

Figure 3-20: Relative frequency of primary γ' size for U720Li C&W, U720 PM, U720Li PM FG and LG [23]

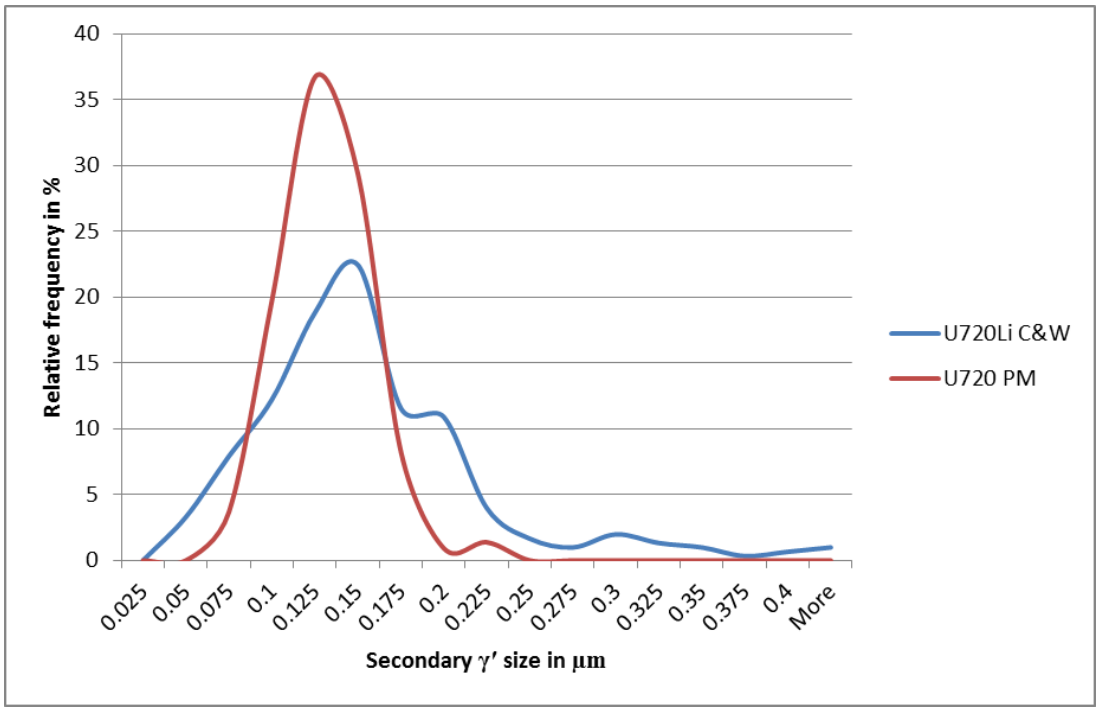

Figure 3-21: Relative frequency of secondary γ′ size for U720Li C&W and U720 PM

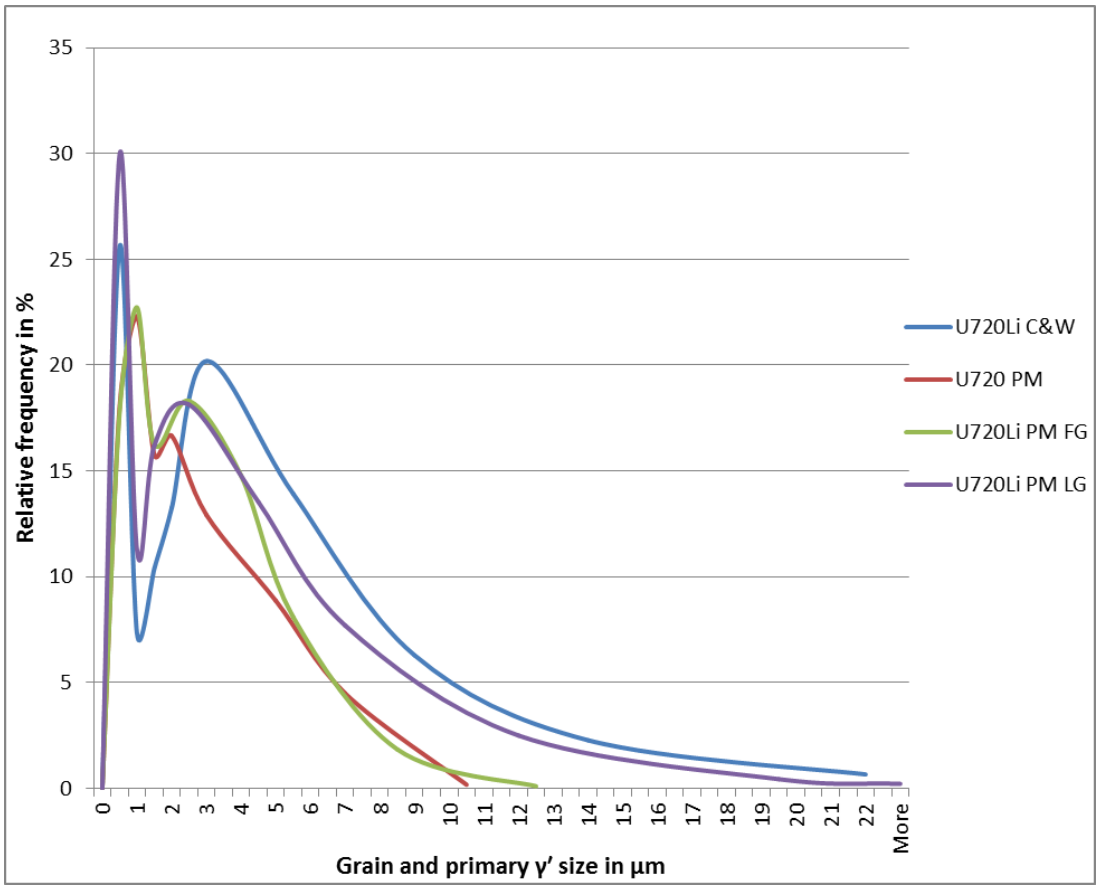

Figure 3-22: Relative frequency of grain and primary γ′ size for U720Li C&W, U720 PM, U720Li PM FG and LG from EBSD

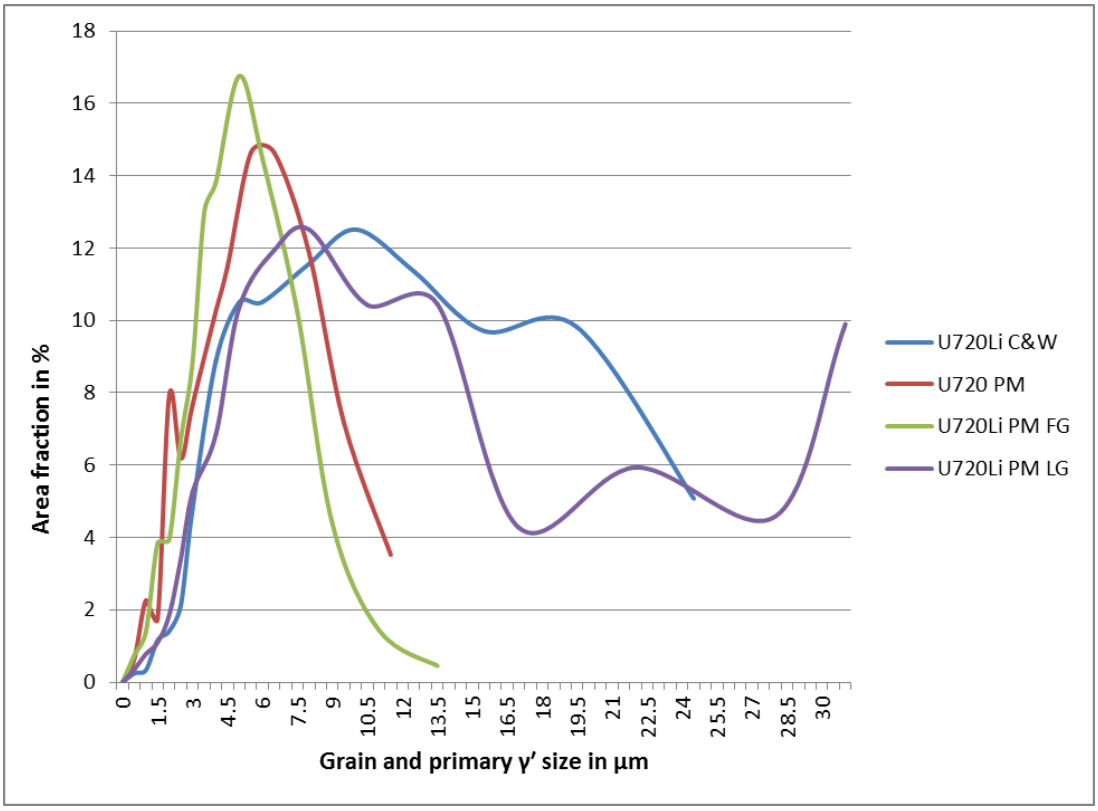

Figure 3-23: Area fraction of grain and primary γ′ size for U720Li C&W, U720 PM, U720Li PM FG and LG from EBSD

3.4 Discussion

3.4.1 Grain size

The average grain sizes measured from the Image J image analysis are similar for the U720Li C&W and the PM LG material at ~16 μm, and Loo-Morrey's U720 PM alloy also has a similar average grain size of ~18 μm. The U720Li FG PM has an appreciably smaller average grain size of 6.4 μm.

When analysing the grain sizes from the EBSD, much smaller grain sizes can be observed. However it is hard to remove the primary gamma prime distributions from the measurement. The average grain size is significantly below the grain size measure from the image analysis, and this number does not fully represent the actual γ grain size, as the number of primary γ' is expected to be greater than the gamma grains. The major peak in the histogram (Figure 3-22) below 2 μm (and probably everything below 3.5 μm) for all 4 materials clearly represents the primary γ', hence the second peak of each material gives a better representation of the average grain size distribution.

The *area fraction* of the γ and γ' histogram (Figure 3-23) gives a more detailed insight into the relatively more significant contribution of the large grains to any crack plane or crack front sampling and here the area fraction of the large grains is similar to that of the small grains (or primary γ'). It should be noted that this average value is however still below the values from the ImageJ analysis, in particular for U720 PM. However EBSD measurements also consider twin boundaries in assessing grain size. Figure 3-15 - Figure 3-18 show that all materials exhibit twins, thus the grain size from EBSD measurements will be smaller.

When comparing the EBSD results in Figure 3-11 and Figure 3-12, U720PM seems to have a much smaller grain size than U720Li C&W. U720 PM could have a larger γ' volume fraction compared to the other alloys, hence partly explaining the large difference between the ImageJ and EBSD results. It is also expected that there is some variation, as measurements have been taken from different regions of the material. U720PM shows a wider range of grain sizes up to 62.6μm in the ImageJ data.

Assuming a similar γ' solvus temperature for all the U720 variants, it is noteworthy that the U720Li C&W received a solution heat treatment of typically between 1080 to 1105°C which spans the solution heat treatments of the U720Li PM FG, which was solution heat treated at 1105°C and the U720PM, which was solution heat treated at 1080°C. The U720Li PM LG has a higher solution treatment temperature of 1135°C, yet the grain size is very similar to the C&W material, whereas the lowest solution heat treatment (the U720) does not have the finest grain size. Within a carefully controlled alloy batch, (as for the U720Li PM variants, where solution heat treatments were specifically varied), it seems that varying heat treatment solution temperature can alter grain size, but no consistent trend is seen across the three compositional/processing U720 variants studied here. It should be noted that grain size is also controlled by other factors (e.g. carbides and borides also pin grain boundaries) as well as the amount of primary γ' pinning grain boundaries. The amount of primary γ' is expected to be controlled both by how close the solution heat treatment is to the γ' solvus, and how long the

material is held at this temperature. Other factors which will control grain size include, for PM alloys: prior powder size, and for C& W materials the degree of recrystallisation occurring after the various forging treatments. It may also be the case that the γ' solvus is appreciably different for the compositions studied here. The role of carbides and borides in grain boundary pinning processes [11] may also be important.

Grain size measurements with the line intercept method have been carried out on U720Li C&W and by Loo-Morrey [50] on the U720 PM and they show smaller values than the measurements produced with ImageJ. It should however be noted that the maximum diameter is measured with ImageJ, whereas with the line intercept method – although effort is made to apply the lines randomly, this will not always systematically pick up the largest diameter of each grain. It may be that the line-intercept method of grain size estimation however provides a more representative sampling of grain boundary intervals, such as a crack front or crack tip process zone might sample.

For the cast and wrought material, distinct bands of fine grains and bands of larger grains have been observed, which is likely to be caused by the casting process and the complex varying recrystallization effects during the forging process. A more consistent grain size distribution (such as that observed in the PM material) is difficult to achieve through this manufacturing route. The range of grain sizes of the C&W material overall varies between 4.5 and 45.3 µm. However the range in the less obviously banded grain structure in U720Li PM LG is found to be similar (between 4.8 and 41.3 µm).

Moreover many more twin boundaries can be observed in the C&W material, possibly due to recrystallisation twinning, which may have an effect on crack initiation and propagation processes, as well as adding potential texture effects.

Small grain sizes have been shown to improve the fatigue crack growth resistance and yield strength of the Nickel based superalloys [13], due to slip being blocked at grain boundaries, where dislocations have to reinitiate. Twin boundaries are also expected to block slip to some extent and have a beneficial effect on yield strength and fatigue resistance.

It is expected that in particular for the material with smaller grain sizes (U720Li PM FG and possibly U720PM, based on EBSD results) should show better fatigue life and yield strength than the other materials.

These materials show a variation in grain size, in particular U720Li C&W shows bands of smaller and larger grains, however EBSD has shown that there are no texture effects, so it seems unlikely that grain orientation (or texture) could be influencing any deflection of the crack.

3.4.2 γ′ sizes and volume fractions

As discussed above, primary γ′ sizes and volume fractions may have a direct effect on final grain size, and also indirectly determine the amount of coherent γ′. Thus they have been measured in ImageJ from etched SEM micrographs. The volume fraction of primary γ′ can also be estimated from the Thermocalc calculation shown in Figure 3-24 by considering the different solution heat treatments (for U720Li PM). The Thermocalc diagram was calculated for the PM U720Li composition in an earlier programme by Hunt [23] and is based on equilibrium predictions of phase amounts. These thermodynamically predicted values (assuming equilibrium phase amounts are produced in the solution treatments in question) are compared in Table 1 with our image analysis derived volume fraction measurements. Primary γ′ size appears to lie between 2-3 μm on average for all alloy variants, but with the C&W showing the larger sizes (both in terms of mean values and the extreme of the range). This is in agreement with the first peaks observed in the histograms from the EBSD, even though they might be even smaller for these measurements.

U720PM shows some variation between the volume fraction measure by Loo-Morrey [50] and calculated from the Thermocalc, possibly due to the different alloy composition.

Generally a volume fraction of 40-55% has been quoted for good strength and fatigue resistance in turbine disc alloys [13], all alloys studied have a volume fraction in this region for combined coherent and incoherent γ′.

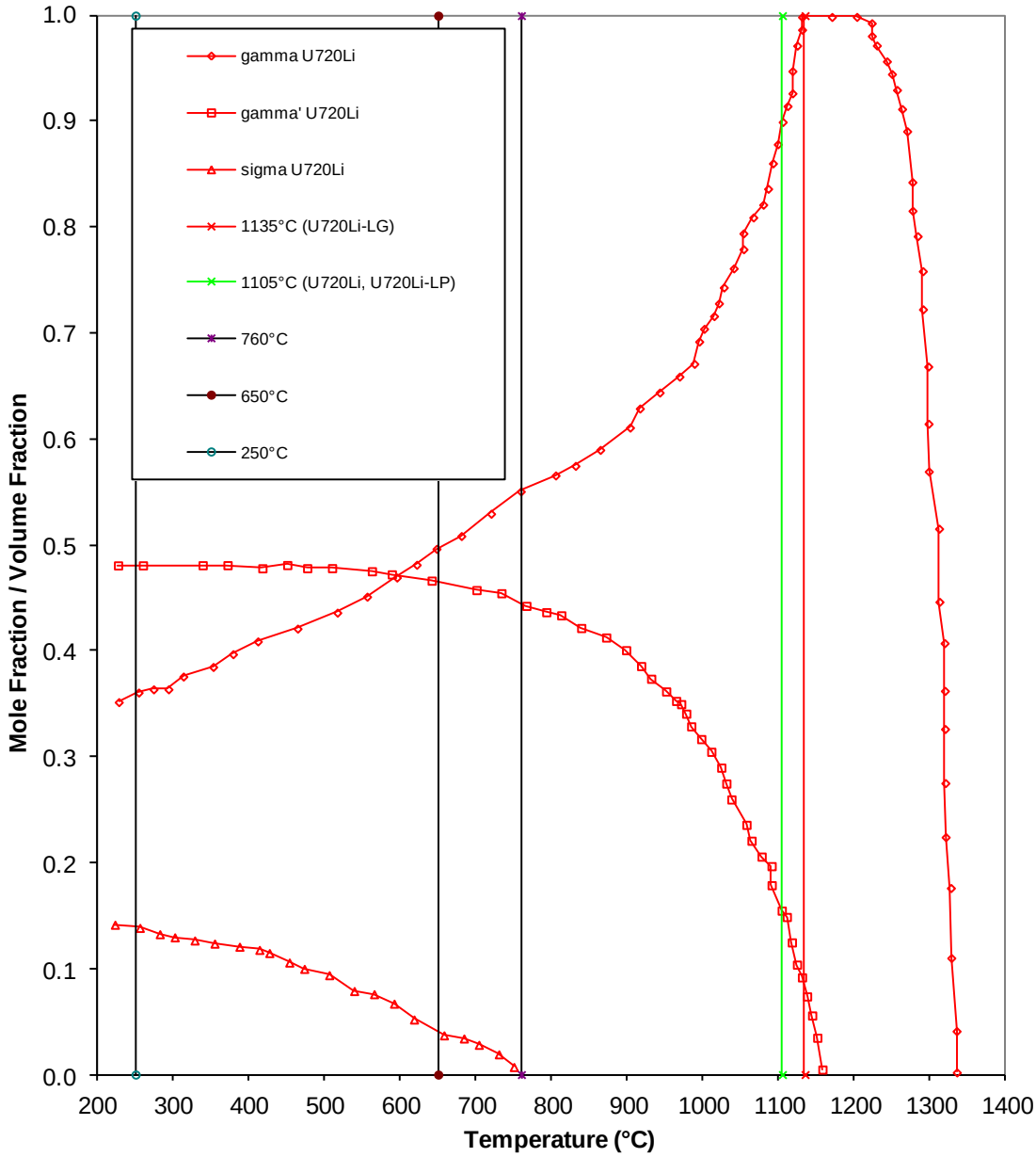

Figure 3-24: Thermo-calc prediction of phase distribution for U720Li [23]

Alloy	**U720 PM**	**U720Li FG PM**	**U720Li LG PM**	**U720Li C&W**
Solution heat treatment	4h 1080°C, oil quench	4h 1105°C, oil quench	4h 1135°C, air cool	4h 1080 to 1100°C, oil quench
Ageing heat treatment	24h 650°C, air cool, followed by 16h 760°C, air cool			16h 760°C, air cool
HV10	**461**	**477.5**	**433.5**	**434**
Grain size (image analysis derived)	**18.1µm**	6.4µm [23]	15.4µm [23]	**16.7 µm**
Primary γ' size (image analysis derived)	**3.18 µm (Range 1.56-9.39µm)**	1.99 µm (range 0.5-6.9 µm) [23]	2.52µm (range 0.9-7.6 µm) [23]	**5.09µm (Range 1.58-23.5µm)**
Primary γ' size (linear intercept method)	~2µm [50]			**10.7 µm**
Primary γ' volume fraction (image analysis derived)	**12.6%**	18.9% [23]	8.6% [23]	**17.1%**
Primary γ' volume fraction (calculated from Thermocalc [23])	~21%	~16%	~8%	16-21%
Secondary γ' size	**119nm (Range 64-207nm)**	102 nm (range 51-150nm) [23]	190nm (range 81-300nm) [23]	**146nm (Range 45-625nm)**
Secondary γ' volume fraction (image analysis derived)	**9.1%**			**15.8%**
Tertiary γ' size	20nm [50] (linear intercept)	16nm (range 1-45nm) [23]	17nm (range 6-30nm) [23]	Not measured
Coherent γ' volume fraction	38.9%	29.1%	39.4%	**30.9%**

Table 7: Size and volume fraction of γ′ for alloy variants studies with heat treatment details (values measured in this work in bold)

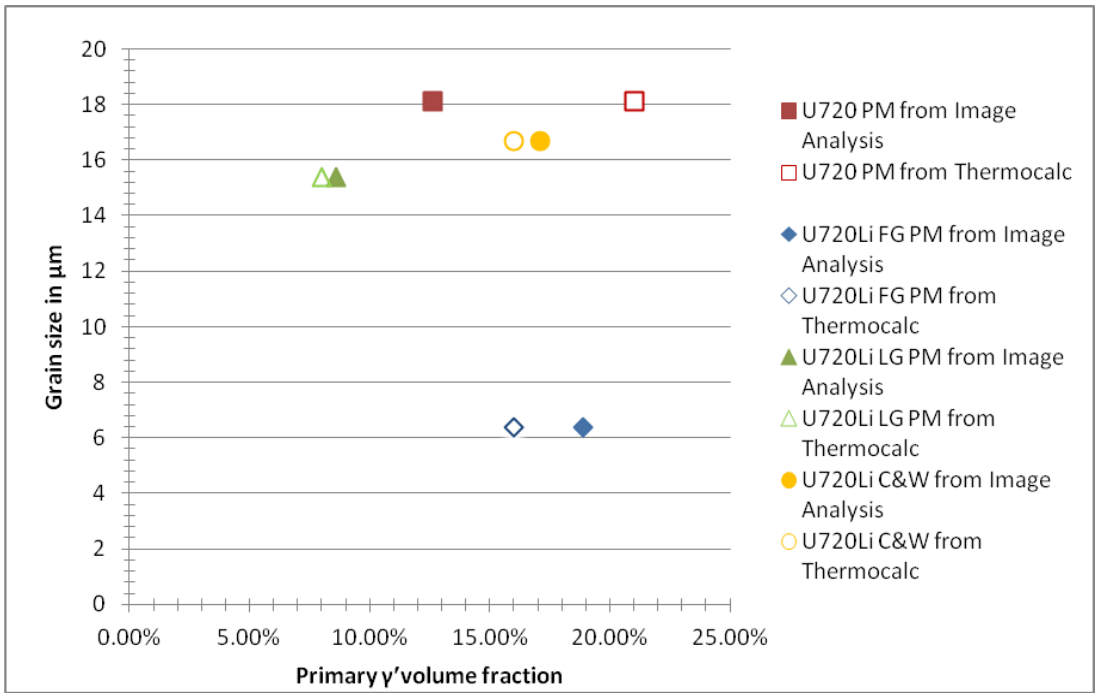

Figure 3-25: Primary γ' volume fraction from Image Analysis and Thermocalc predictions compared to grain size

From Table 7 and Figure 3-25 it can be seen that for the U720 PM the primary γ' volume fraction values vary quite significantly, with the estimated value being considerably larger than the measured one, whilst the comparison between experimentally measured and predicted values (for the Li variants) are much more consistent, as are the ones for the U720Li C&W. It should be noted that the U720 composition varies significantly from the U720Li PM and C&W in B and in C just in the U720Li C&W. It is unclear whether these elements have an effect on the γ' solvus. [13]

It is noteworthy that grain size does inversely scale (to a reasonable extent) with measured (via image analysis) primary γ' volume fraction (note that relatively similar primary γ' sizes mean that volume fraction equates to a similar number of pinning centres to stop grain growth).

Based on the Thermocalc diagram, the total equilibrium volume fraction of γ' can be estimated to be 48% at 300°C (assumed to represent a low temperature state of the alloy). The amount estimated for the remaining coherent γ' can be estimated by subtracting the measured primary γ' volume fraction from the total estimated equilibrium value.

Using this approach, U720Li C&W and U720Li PM FG have similar predicted amounts of coherent γ' (~29-31%), as have U720PM and U720Li PM LG (~39%), so each of these alloy pairs might be expected to show relatively similar slip behaviour, with perhaps more planar slip expected for the higher predicted volume fraction of coherent γ'. In terms of expected secondary γ' size, U720 PM, U720Li C&W and U720Li PM FG are all oil quenched, so should have similar sizes of secondary γ' due to the similar cooling rate, while the U720Li PM LG was

air cooled, i.e. a slower cooling rate, therefore coarser secondary γ' is expected [75]. This seems consistent with the observed measurements.

All materials had the same double ageing heat treatment, except the C&W material which only experienced a single ageing treatment. This is due to a change in ageing practice at Rolls Royce plc. [93].

3.4.3 Yield strength behaviour

The yield stresses σ_y for the PM U720Li variants (FG and LG) have been estimated based on room temperature Vickers Hardness comparisons for the U720Li C&W and U720 PM materials where monotonic yield stress values are available. Based on these room temperature values, extrapolations of the higher temperature monotonic yield stress values have been made, based on known U720 Li C&W data at higher temperature. Values for U720PM have been calculated in the same manner and are in reasonable agreement with the measured data.

The two materials with the smaller grain size, U720Li PM FG and U720PM (based on the EBSD results), show slightly larger yield strength than the ones with larger grain size (U720Li C&W and U720Li PM LG), as one would expect, the larger number of grain boundaries (and twin boundaries) reduce the dislocation motion, making yielding more difficult.

For U720Li PM FG and LG cyclically stabilised yield stress values at 650°C are available from Pang [23]. These were obtained from cyclically stabilised stress strain curves obtained at 650°C from 1.2% strain controlled high temperature LCF tests. These values might be more appropriate in considering yield behaviour in a fatigue test.

With values of 980MPa for the FG and 850MPa for the LG at 650°C the cyclically stabilised σ_y is lower than the estimated one (1161MPa for FG and 1054MPa for LG) which indicates cyclic softening occurs in these systems (as was observed in the LCF testing). It would be of interest to establish cyclically stabilised yield behaviour for U720Li C&W for the current test temperatures.

3.5 Summary

Four variants of Udimet 720 have been studied; the alloys used in this work, mainly U720Li C&W, but also U720Li PM FG and LG, have been compared to U720 PM, which has shown deflected cracking in past work [50].

Slight variations of composition might be expected to have some effect on the high temperature strength and oxidation resistance of the materials.

A variation of γ grain and primary γ' sizes, caused by the different heat treatment routes will also have some effect on the properties. The materials with larger grain sizes (U720Li C&W and PM LG) show slightly lower estimated yield strengths compared to the ones with smaller grain sizes (U720 PM and U720Li PM FG), and are also expected to have better fatigue resistance.

While the U720Li PM FG shows consistent grain sizes, the other alloys show variation in grain size, this microstructure potentially has implications on a the microstructure sampled by a fatigue crack tip.

Some variation between the EBSD and Image analysis measurements for grain size has been observed. Studies with EBSD have shown none of the materials studies show any texture in any of the materials.

Variation was also encountered for the U720 PM and U720Li FG when comparing the primary γ' volume fraction measured from the image analysis with values estimated from a thermocalc prediction for U720Li PM used in previous work.

4 Experimental Methods

4.1 Fatigue Testing

Two types of samples were used in the fatigue tests; Corner Notch in bend (CNB) (Figure 4-1) and Single Edge Notch in bend (SENB) (Figure 4-3) samples.

4.1.1 Corner Notch Fatigue testing

Samples with a corner notch were loaded in four point bend as shown in Figure 4-1. The sample measurements were 12.5x12.5x80mm and the roller span *S* was 15mm.

Samples with a corner notch are typically used by Rolls-Royce plc. to simulate a small defect in turbine components. [22]

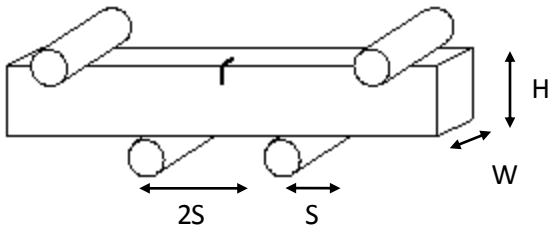

Figure 4-1: Corner Notch Bend (CNB) Sample in four point bend (using Pickard's annotation[94])

Preliminary studies were done on the powder metallurgical Udimet 720 Li, which was used in the fine grained variant (FG) for two tests and the large grained variant (LG) for one test. These three tests were performed at 300°C in air (where sustained deflected crack growth is expected). Problems were encountered in determining the loads necessary to start crack growth; this was attributed to the initial choice of notch manufacturing route which was Electrical Discharge Machining (EDM) in house, leading to a relatively blunt geometry. A larger notch size of a/W=0.08 was therefore chosen and the ΔK_i levels were increased until crack growth started to initiate.

A sample of U720Li C&W was electropolished before testing which reduced the size of the notch to a/W=0.012. Due to the reduced notch size an initial ΔK_i=15MPa√m was necessary to initiate crack growth.

Further testing was done on U720Li C&W CNB samples which were supplied by Rolls Royce plc. with a standard notch of a/W = 0.025. The samples were tested at 300, 600 and 650°C in both air and vacuum all with an initial ΔK_i=12MPa.

4.1.1.1 *ΔK* Calibration

For each test the notch size and specimen cross section was measured and these values were used to calculate the stress intensity factor *K* using an equation of Pickard for corner cracks [94]:

$$K = M_G M_B M_S F(\sigma)\Phi\sqrt{\pi c} \qquad \text{Equation 4-1}$$

where M_G, M_B, M_S and Φ are correction factors, c is the crack length and $F(\sigma)$ is the complex stress function in bend, which can be determined from Pickard [94] for the top and side surface from the crack length and the stress on the top surface, which can be calculated for this specimen geometry in bend with:

$$\sigma = \frac{3PS}{WH^2} \qquad \text{Equation 4-2}$$

where P is the applied compressive load on the rollers, S is the span between the rollers (as shown in Figure 4-1), W is the breadth and H is the height of the specimen (see Figure 4-2). The crack length on the side surface was assumed to be 0.7 of the crack length on the top surface due to the effect of bending, based on experimental observations on semi-elliptical cracks in bend. [80]

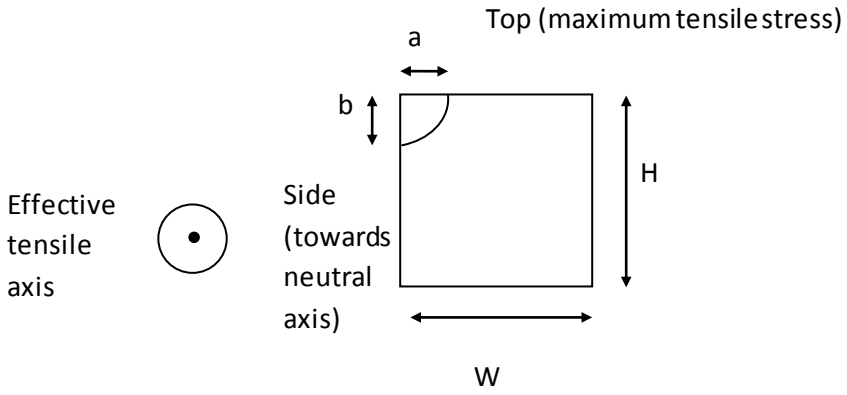

Figure 4-2: Notation in Corner Notch Bend (CNB) sample after Pickard [94]

The correction factors for the surface positions are calculated as followed:

M_G=1.143 (0≤x≤0.2) Equation 4-3

M_G=0.1x^2+0.29x+1.081 (0.2<x≤0.75) Equation 4-4

where x is the larger of (a/W) and (a/H) for the top surface, and the larger of (b/W) and (b/H) for the front surface. a is the crack length on the top surface, b the crack length on the side surface.

M_B=1+0.06x (0≤x≤0.2) Equation 4-5

M_B=0.75x^2-0.185x+1.019 (0.2<x≤0.75) Equation 4-6

where x is (a/W) for the top surface and (b/H) for the side surface.

M_S=1+0.07x (0≤x≤0.2) Equation 4-7

M_S=0.9x^2-0.21x+1.020 (0.2<x≤0.75) Equation 4-8

where x is (b/H) for the top surface and (a/W) for the side surface.

The elliptical correction factor Φ is assumed to be 2/π for a part circular crack. It should however be noted that the crack in bend is not quarter circular.

4.1.2 Single Edge Notch Fatigue Testing

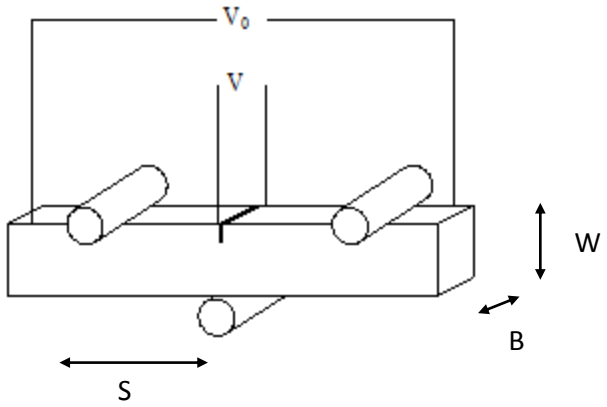

Figure 4-3: Single Edge Notch Bend (SENB) Sample in three point bend

Single Edge Notch Bend (SENB) tests (see Figure 4-3) have been performed in three point bend on U720Li C&W samples with an electrical discharge machined (EDM) notch. a/W=0.25 and the roller span S=2W have been chosen according to the relevant standard BS ISO 12108 [95]. The samples measure breadth B=12.5mm, width W=12.5mm and length L=80mm.

For this standard test K calibration has been carried out after BS ISO 12108, where K is given as

$$K = \frac{P}{BW^{\frac{1}{2}}} g\left(\frac{a}{W}\right) \times 10^{1.5} \quad \text{Equation 4-9}$$

with the applied load P and the stress intensity factor function

$$g\left(\frac{a}{W}\right) = \frac{6\left(\frac{a}{W}\right)^{\frac{1}{2}}}{\left[\left(1+2\frac{a}{W}\right)\left(1-\frac{a}{w}\right)^{\frac{3}{2}}\right]}\left[1.99 - \frac{a}{W}\left(1-\frac{a}{W}\right)\left(2.15 - 3.93\frac{a}{W} + 2.7\left(\frac{a}{W}\right)^2\right)\right] \quad \text{Equation 4-10}$$

for SENB in three point bend.

Samples have been precracked at room temperature in air to ensure that crack growth would occur from a microscopically sharp crack away from any residual effects induced in the machining of the notch.

Initially a sample was precracked at room temperature in air starting at an initial ΔK=20MPa√m, which was stepped down in 10% increments after the crack has grown through at least 4 monotonic plastic zone sizes until ΔK=15MPa√m was achieved. A monotonic plastic zone size r_p was calculated as

$$r_p = \alpha\left(\frac{K_{\max}}{\sigma_y}\right)^2 \qquad \text{Equation 4-11}$$

For the plane stress region:

$$\alpha = \frac{1}{2\pi} \qquad \text{Equation 4-12}$$

after the Rice approximation. [50]

Then the specimen was heated to 300°C and the crack was allowed to propagate under a constant load thus experiencing increasing ΔK conditions from an initial ΔK_i=15MPa√m.

As the deflection only appeared at higher ΔK levels, for all further testing, the samples were precracked at a constant ΔK=20MPa√m at room temperature in air, and growth out started from an initial ΔK_i=20MPa√m after the sample was heated to the required temperature. Tests were carried out at 300, 600 and 650°C in air and vacuum.

Two thin SENB samples (thickness B= 2mm) were tested precracked at a constant ΔK=20MPa√m and then grown out from a ΔK=20MPa√m.

Testing and precracking were carried out with an R-ratio of 0.1 and a sinusoidal waveform with a frequency of 20Hz.

4.1.2.1 Crack Growth Monitoring

In the SENB tests the crack length was monitored using a 4 point probe direct current (DC) electrical potential difference (p.d.). The p.d. wires were spotwelded to the sample on opposite ends of the notch to obtain voltage V and at 30mm distance from the notch to obtain V_0 as shown in Figure 4-3. Insulating ceramic rollers were used to apply the loads.

The calibration function for a/W to V/V_0 was used from another project [96], which was determined using a foil analogue.

$$\frac{a}{W} = 0.00041067\left(\frac{V}{V_0}\right)^3 - 0.02780565\left(\frac{V}{V_0}\right)^2 + 0.3023438\left(\frac{V}{V_0}\right) - 0.02466094 \qquad \text{Equation 4-13}$$

Crack growth information was recorded using Windaq software with a DATAQ DI-700 USB data acquisition instrument connected to a computer with measurements taken every second.

The P.D. and time readings was subsequently converted to corresponding crack length and cycle information. Crack length readings were corrected after the test using a linear correction factor obtained from optical measurements on the fracture surface, corresponding to the notch, precrack and final fracture.

This information was used in a spreadsheet to calculate ΔK, using the K calibration, and the crack growth rates da/dN.

Crack growth rates da/dN were calculated from the measured crack length a and cycles N. a, N data pairs were selected every 400 cycles to minimize noise effects and secant method was used to determine da/dN , where

$$\frac{da_n}{dN_n} = \frac{a_{n+1} - a_{n-1}}{N_{n+1} - N_{n-1}} \qquad \text{Equation 4-14}$$

4.1.3 Test conditions and Test Matrix

Fatigue tests have been carried out on a 50 kN Instron 8501 servohydraulic testing machine fitted with a ESH Ltd. high temperature vacuum chamber. Samples were heated using 4 high intensity quartz lamps, and temperatures were controlled using a Eurotherm 815 thermo-controller and an R-type (platinum + 13% rhodium/platinum) thermocouple spot welded directly to the sample. Temperature control was maintained within ±1°C via thermocouples.

For the vacuum tests the chamber was augmented with an Edwards rotary vacuum pump, Balzers TPU240 turbomolecular vacuum pump and TCP380 electronic drive unit linked to Balzers Pirani and cold cathode pressure gauge heads and TCP300 pressure gauge and controller, allowing the chamber to be evacuated to pressures of 2-4 x10^{-5} mbar.

Initial testing was carried out on U720Li PM in two grain size variations with CNB Samples at 300°C in air. The material U720Li C&W was tested in CNB and SENB samples in air and vacuum and at 300°C, 600°C and 650°C. The test matrix for the U720Li C&W and PM LG and FG material is shown in Table 8. All testing was carried out with an R-ratio of 0.1 and a sinusoidal waveform with 20Hz.

	R=0.1, Freq=20Hz						
	U720Li C&W					U720Li PM FG	U720Li PM LG
Temperature (˚C)	Thick bend bars		Thin SENB			Thick bend bars	
	CNB	SENB	Mode I	high shear	low shear	CNB	CNB
300	air (2x)+vac	air+vac	air (2x)	Air	air	air (2x)	air
600	air+vac	air+vac					
650	air+vac	air+vac					

Table 8: Test Matrix

4.2 Fractography technique

4.2.1 Light Macroscopy

A Wild Macroscope M420 was used to create overview images of the fracture surfaces.

4.2.2 Scanning Electron Microscopy (SEM)

The fracture surface post-failure was observed under the Field Emission Gun Scanning Electron Microscope (FEG-SEM). Secondary electron images were produced on a Jeol JSM6500F FEG-SEM at an acceleration voltage of 10kV and at magnifications of 100, 500 and 2000 with a typical working distance of ca. 10mm.

4.2.3 Profilometry

4.2.3.1 TaiCaan

The fracture surface has also been mapped using the Taicaan Xyris 2000 TL optical profilometer with a triangulation laser. The image is created by sending a point source or line laser to the sample, the light is scattered due to the height difference of the sample surface and can be detected by the detector. This is schematically presented in Figure 4-4. The vertical measuring range (MR) of this profilometer is 2.5–20mm, the spatial resolution (x-y_r) is 0.1 µm, the vertical resolutions (z_r) is 0.25–2µm and angular tolerance is 90 °.

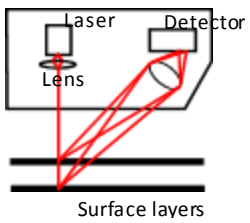

Figure 4-4: Laser triangulation for TaiCaan Optical Profilometer

4.2.3.2 Alicona MeX

Alicona MeX is a software package that takes SEM images and converts them into a 3D surface dataset. By combining 3 images of the same area taken from 3 different angles in the SEM a 3D map of the surface is created.

To create a map of one of the terraces on the fracture surface SEM pictures have been taken from -2, 0 and 2° angles around the surface and at magnifications of 100 and 2000.

4.2.3.3 Alicona Infinite Focus

Alicona InfiniteFocus is an optical 3D measurement device. Its operating principle combines the small depth of focus of an optical system with vertical scanning to provide topographical and colour information from the variation of focus. The software uses algorithms to reconstruct this into a 3D data set with accurate topographical information. Vertical resolutions of up to 10nm can be achieved; however for this work the resolution used was 5µm.

Infinite focus has proven to be the best of the three methods in terms of the balance between resolution and the ability to map the entire surface to allow measurement of macroscopic crack path angles.

4.3 Methodology of detailed analysis of secondary cracks

The side surface of fractured sample had been polished to reveal more detail of these large secondary cracks, the secondary crack tip has been further analysed.

A number of cracks have been observed in the FEG-SEM, some plain polished, some etched 15 sec with nimonic etch. The fracture surface of one sample was nickel plated to provide edge retention using a 99.9% pure Nickel anode in Watt's solution (500ml H_2O, 150g $NiSO_4$, 20g $NiCl_2\,6H_2O$) at 65°C and at a current of 0.4A at 4 V for 90 minutes under constant stirring. Nickel plating did not improve the edge retention when cutting the sample, and was hence not applied to other samples afterwards.

For one such secondary crack, detailed work done in collaboration with Loughborough University using focussed ion beam (FIB) serial sectioning and electron back scattered diffraction (EBSD) data collection has enabled a 3D reconstruction of the crack-tip region. EBSD data were collected (by Dr Geoff West at Loughborough University) using a Hikari EBSD camera attached to an FEI Nova 600 Nanolab Dual-Beam FEG SEM/FIB system. The sample liftout procedure involves plating the area of interest with platinum and cutting a trench around it, as shown in Figure 4-5. Then a probe is attached and the volume is removed (Figure 4-6) and attached to a grid (Figure 4-7) and the probe is removed (Figure 4-8). To be able to orientate the sample, fiducal markers are placed on the grid (Figure 4-9) then the sample is cleaned up and orientated for slice removal and data acquisition, as shown in Figure 4-10.

Data collection at a rate of 30 points per second was performed over a scan area of approximately 40 x 40 x 30 µm (151 slices are removed). A relatively slow collection speed was used as EDS data were collected simultaneously, using an EDAX Silicon Drift Detector Apollo XL (SDD) at an input count rate of 325k counts per second and a processing time of 0.5ms. The

EDX-derived distribution map of chromium was found to be the best indicator of γ and γ' because it highlights γ' phase as being depleted in chromium, owing to the $Ni_3(Al, Ti)$ chemistry of γ' [97]. The EBSD data were processed using TSL OIM Analysis 5.31 and reconstructed using Avizo 6.0.0 software as described in greater detail in [98].

A number of TEM foils at the crack tips were also prepared at Loughborough University using focused ion beam (FIB) lift out method. Perpendicular sections ahead of the crack tip were taken – which contained varying amount of the crack (indicating the crack is sometimes more extensive just below the surface). Samples were mounted onto half Cu grids (Omniprobe) and milled using Ga+ to electron transparency (until they were 100-200nm thick). A Jeol 2000FX TEM was used at Loughborough University (by Dr Zhaoxia Zhou) to record images and diffraction patterns in conjunction with chemical analysis by Oxford Instrument Inca energy dispersive X-ray (EDX) spectroscopy.

TEM foils were taken from locations just ahead of secondary crack tips, such as the one shown in Figure 4-11.

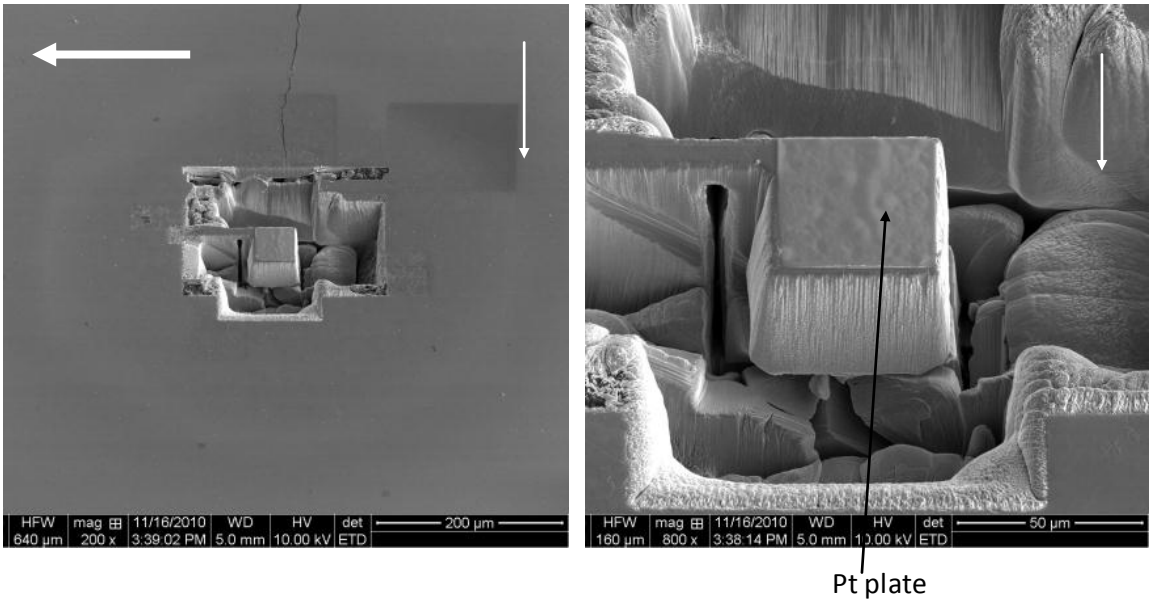

Figure 4-5: Platinum plating and trench cutting around crack tip (the large arrow indicates the overall crack direction, the small arrow indicates the direction of the secondary crack) a:overview b: at higher magnification

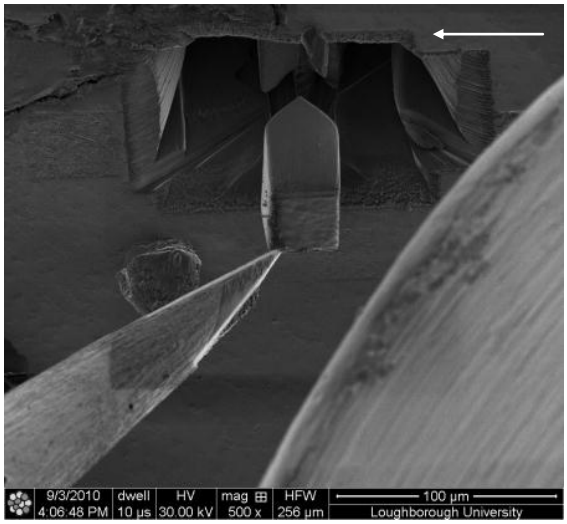

Figure 4-6: Probe attachment and Volume removal (arrow indicates the direction of the secondary crack)

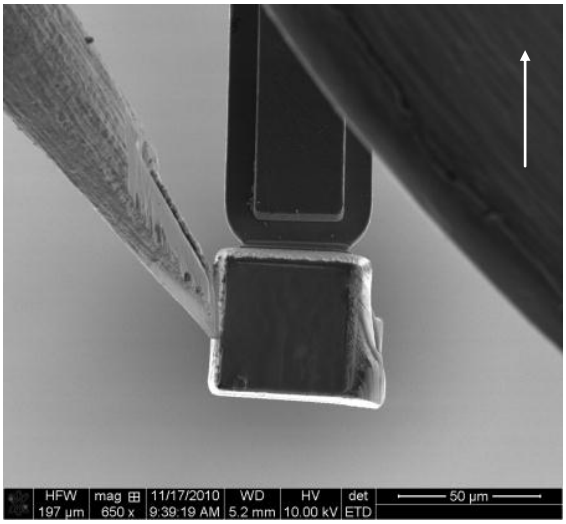

Figure 4-7: Grid attachment (arrow indicates the direction of the secondary crack)

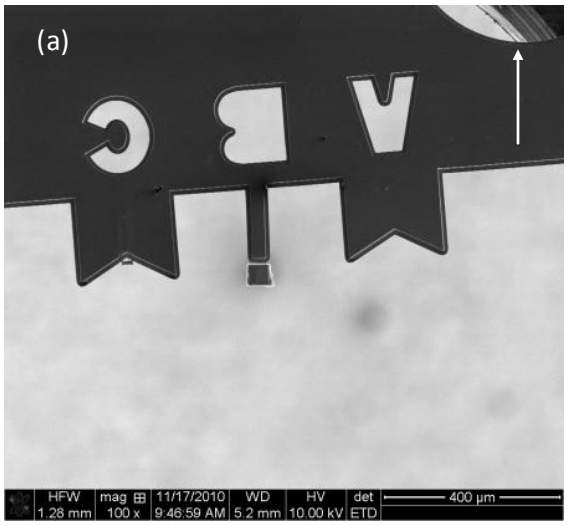

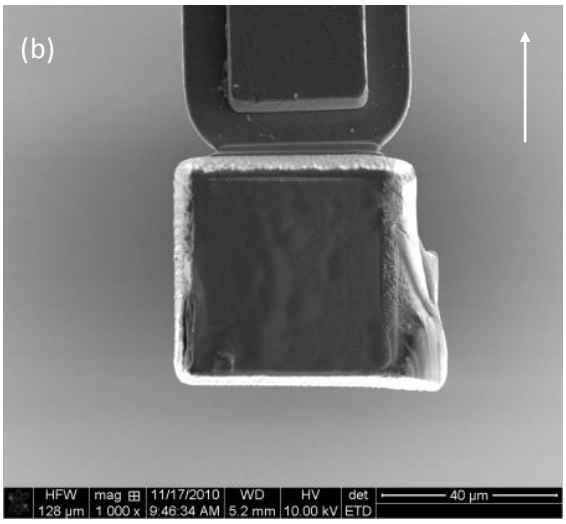

Figure 4-8: Grid attachment and probe detachment (arrow indicates the direction of the secondary crack) (a) overview (b) detail view

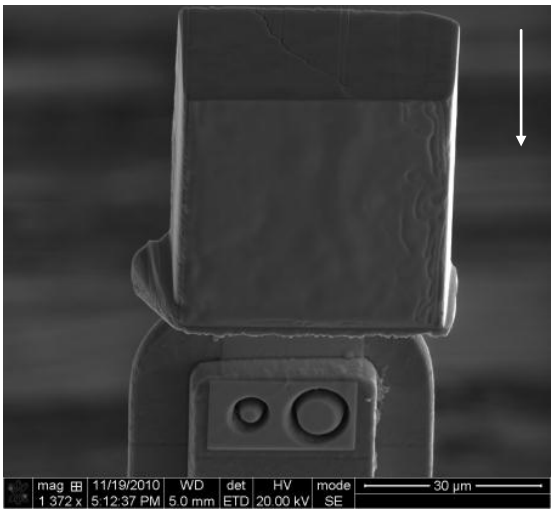

Figure 4-9: Fiducial marker placement for orientation (arrow indicates the direction of the secondary crack)

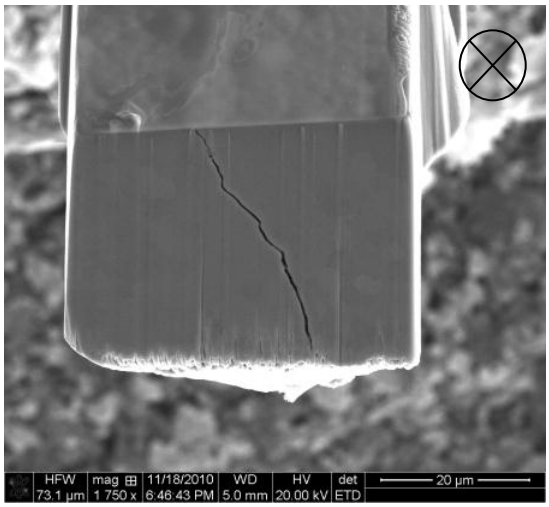

Figure 4-10: Orientation and Volume clean-up and Ready for first data acquisition and subsequent slice removal (crack growth direction into the paper)

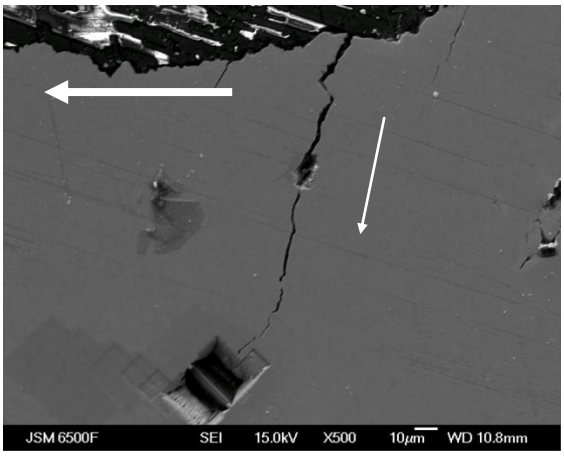

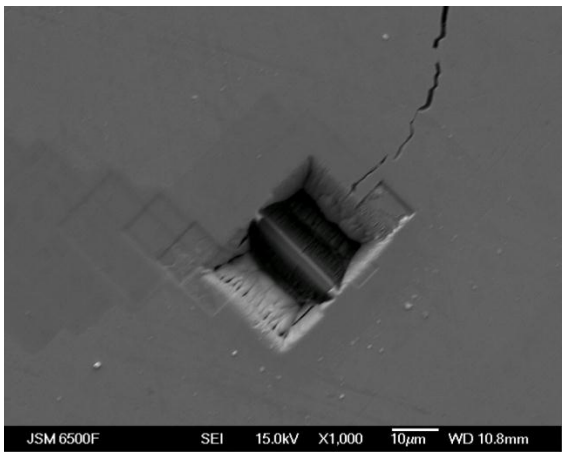

Figure 4-11: TEM foil location in CNB sample tested at 300 C in air with a ΔK_i=12MPa$\sqrt{m}$ at a crack tip at overall crack length a=5.8mm and nominal ΔK=50.5MPa$\sqrt{m}$ at different magnifications (the large arrow indicates the overall crack direction, the small arrow indicates the direction of the secondary crack)

5 Experimental Results

5.1 CNB Testing

Figure 5-1 shows the fracture surfaces of tests carried out in CNB on U720Li PM FG and LG and C&W at 300°C in air.

Due to the bluntness of the notches in the initial testing with the PM materials caused by EDM manufacturing, the initiation of crack growth was difficult, therefore the load levels had to be increased until crack initiation was achieved.

The first test in U720Li PM FG (as tested by H.T. Pang [23]) was started with an initial crack size of 1mm and an initial ΔK_i of 13.3 MPa√m (for the crack on the top surface), based on the Pickard calibration, see Chapter 4.1.1.1. After 1898000 cycles no crack growth was visible, hence the load was increased by 10% to achieve a ΔK_i of 14.6 MPa√m. After 4625100 total cycles the load was increased a further 15%, as there was still no visible crack growth, creating a ΔK_i of 16.8MPa√m. After 218700 further cycles (4842700 total cycles) the load was increased another 5%, causing an initial ΔK of 17.7MPa√m, and the sample failed after 4986700 total cycles. At a conservative estimate the lifetime was 144000 at an initial ΔK of 17.7MPa√m, assuming that initiation only started when the highest load was applied.

A second test was carried on U720Li PM FG under the same conditions as the previous test; only a higher load was applied to get an initial ΔK_i of 15.4MPa√m. After 3562900 the load was increased 5% as no failure was observed, creating a ΔK_i of 16.2MPa√m at the crack tip. This action was repeated at 1031000 cycles (ΔK_i of 17.04MPa√m), 31140900 cycles (ΔK_i of 17.9MPa√m), 42465000 cycles (ΔK_i of 18.8MPa√m) and 45961600 cycles (ΔK_i of 19.7MPa√m), where the crack seemed to initiate and the sample failed after 46117536 total cycles or 155936 cycles at a ΔK_i of 19.7MPa√m.

A U720Li PM sample in a large grain variant (LG) (as tested by H.T. Pang[23]) was tested at the same conditions as the FG variant, only with an initial ΔK_i of 17.2MPa√m and the sample failed after 367479 cycles.

Assuming the first test, which was run on a slightly higher ΔK, did only initiate cracking when the highest load was applied, it would have run for 144000 cycles, which is significantly less than for this test. It is clear that the lack of control in machining the notches has had a significant effect on behaviour.

U720Li C&W samples were supplied by Rolls Royce with a constant notch size of a/W=0.025. A test at 300°C in air was started at an initial ΔK of 8 MPa√m; as no crack growth could be observed after 3224519 cycles, the load was turned up resulting in a ΔK of 10 MPa√m, at which the test was run for a further 1886942 cycles, but as there was still no crack initiation visible, the load was turned up to a ΔK of 12 MPa√m. The test failed after 172000 cycles at this ΔK level.

Another test was carried out on the same material at 300°C in air; however the sample had been electropolished which decreased the notch size to a/W=0.012, an increased ΔK of 15.1 MPa√m was applied. The frequency had to be turned to 18Hz, as the required high loads could not be achieved at 20Hz. The sample failed after 540077cycles.

All the fracture surfaces show some deflection on the free surface however in some samples the terraced region extends deeper into the sample. Due to the different notch sizes and varying initial ΔK levels, it is difficult to compare the results from the tests. A consistent measure of comparing the onset of sustained macroscopic deflection is necessary and is described in section 5.3.

Following this all subsequent testing was carried with ΔK_i=12MPa√m and an initial notch of a/W=0.025 on U720Li C&W at 300, 600 and 650°C in air and vacuum. Figure 5-2 compares the fracture surfaces of these tests.

It can be observed that in air at higher temperatures (600 and 650°C) there is deflection to some extent, even though the terraces do not reach very deep. In Loo-Morrey's work [4] the phenomenon has not been observed at 600°C. In vacuum the effect can be seen at all temperatures tested and the terraces go significantly deeper into the bulk than in the samples tested in air in the U720Li C&W, which has also been observed in previous work [4].

Table 9 shows the number of cycles to failure of the CNB tests. The vacuum tests show a significantly larger number of cycles to failure.

Material	Temperature	ΔK_i (MPa√m)	Notch size (mm)	N_f in air	N_f in Vacuum
U720Li PM FG	300°C	17.7	1.0	144000	
	300°C	19.7	1.0	155936	
U720Li PM LG	300°C	17.2	1.0	367479	
U720Li C&W	300°C	15.1	0.012	540077	
	300°C	12	0.025	172000	3332531
	600°C	12	0.025	72656	747409
	650°C	12	0.025	46626	256138

Table 9: Numbers of cycles to failure for CNB tests

5.1.1 Fractography

Fractography in the FEG-SEM has been carried out on different samples of U720Li PM LG and FG and C&W tested at 300°C in air and vacuum.

The central planar regions have been observed and the terraced regions in the flat and the sheared area (by tilting the SEM stage). Based on the crack length the ΔK is calculated for the areas observed. However the estimates for ΔK are made for the top surface, so in bending the actual ΔK in the diagonal direction from the notch will be somewhat lower. Moreover Pickard's calculations are only accurate up to the neutral axis of the bend bar, so ΔK for crack lengths above 6.25mm may not be correct. Moreover the ΔK calibration assumes a flat crack growth. The arrows in the graphs indicate the overall crack growth direction.

Different areas of U720Li PM FG tested at 300°C in air observed in the SEM were the undeflected region across the sample diagonal, near the notch, and the terraced region on the edge of the specimen, as shown in the specimen overview in Figure 5-3.

Figure 5-4 shows the planar region at a crack length of 4.34mm and an estimated ΔK of ~36 MPa√m, and Figure 5-5 at a crack length of 9.82mm and an estimated ΔK of ~66 MPa√m. Both micrographs show transgranular Stage II crack growth. Parallel 'striation' like features over grain scale and grain orientation can be observed. In Figure 5-4 the spacing of these was measured as between 0.32µm at the smallest and 0.76µm at the highest, and was seen to run in parallel bands over regions of the order of the average grain size of the alloy (6.4µm). Whilst these features were generally striation-like (i.e. shallow surface markings), occasional deep, secondary-crack like traces were seen, along with areas of faceted crack growth, implying local, but limited, susceptibility to a secondary deflected or shear crack growth mode in this region.

Crack growth rate can be estimated using crack growth data (da/dN vs ΔK curves) for U720Li FG and U720Li LG at 20°C in a sinusoidal waveform (20 Hz) from Pang [23] and for U720 Loo Morrey.
As there is no data in the literature for U720Li PM FG and U720Li PM LG at 300°C, the assumption is made that the crack growth rates are the same as for the test performed at 20°C, as the data for U720 is similar for both temperatures (Figure 5-8). The crack growth rate at this ΔK level can be estimated from Pang's data [23] for da/dN vs. ΔK (for 20°C), suggesting a value of ~0.06µm/cycle, which is an order of magnitude smaller than the measured fracture surface feature spacing. The features also change orientation at approximately the average grain size. This suggests that these features are slip traces. It should be noted that planar slip characteristics near threshold are still observed in U720 at 300 °C and so at these temperatures planar slip can still be seen. [4]

At the higher ΔK level, i.e. longer crack length, (Figure 5-5) these features can still be observed, but there are more secondary cracks and some of them seem to merge over the grain size. This is clearly a material with a propensity for secondary cracking which increases at higher ΔK.

In the terraced region the flat regions of the terraces were observed (Figure 5-6). The fracture surface in the flat regions look similar to the surface in the teardrop region (Stage II) and shows the same striation like features and secondary cracks.

Figure 5-7 shows the terraced region at a higher ΔK level. Between the flat stage II and shear or deflected growth mode in the terraced regions, a secondary crack is visible, which indicates that the shear crack growth seems to go beyond the flat, mode I dominated growth. In the first instance some form of competition between two distinct growth modes is suggested to control the overall crack deflection process (shear vs. mode I)

Figure 5-10 to Figure 5-13 show the SEM Fractography in different areas of U720Li PM LG tested in air at 300°C with a ΔK_i=17.2MPa√m. The specimen overview is shown in different areas as shown in Figure 5-9. Striation like features and corresponding secondary cracks can be seen in both the central Stage II and planar terraced regions, indicating that the same mechanisms are operating in this material. Thus it is not necessarily a competition between two different mechanisms, but between two different crack growth directions.

Figure 5-15 to Figure 5-18 show the SEM Fractography in different areas of U720Li C&W tested in air at 300°C with a ΔK_i=12MPa√m, in different areas as shown in Figure 5-14. Similiar mechanisms can be observed as in the previous samples, striation like features and corresponding secondary cracks can be seen in both in planar and deflected regions.

The striation like features have been measured and at ΔK=27 MPa√m they have a distance between ca. 0.29 to 0.45 µm, the crack growth rates from Rolls Royce plc. (R-R), as shown in Figure 5-19 [93]. Based on this ΔK the crack growth rate is ca. 0.143 µm/cycle. At ΔK=42 the features have a distance between ca. 0.31 to 0.55 µm, the crack growth rates from R-R for this ΔK is ca. 0.57 µm/cycle, so at higher ΔKs, these are likely to be striation like features.

Figure 5-21 to Figure 5-24 show the SEM Fractography in different areas of U720Li C&W tested in air at 300°C with a ΔK_i=15MPa√m (and a small initial defect), in different areas as shown in Figure 5-20. Again striation like features and secondary cracks can be observed in planar and deflected regions.

U720Li C&W tested at 300°C in vacuum has been observed. The fracture surface is shown in Figure 5-25, where the position of the different areas on the fracture surface observed in the SEM are described. Near the notch a fretted area can be observed as shown in Figure 5-26.

The onset of the first terrace is a higher crack length, i.e. higher ΔK. The first flat terrace is shown in Figure 5-27 at a nominal ΔK value of 36 MPa√m. Figure 5-28 shows a flat terrace at a higher ΔK value of 36 MPa√m. The 'teardrop' region is shown at similar ΔK levels in Figure 5-29 to Figure 5-31. In these regions slip traces and secondary cracks can be observed, as seen in the previous samples.

At ΔK=36 MPa√m the features have a distance between ca. 0.36 to 0.5 µm, and the crack growth rates from R-R for this ΔK is ca. 0.353 µm/cycle.

The fracture surface is more faceted as compared to the air test under the same conditions, which is expected in a vacuum test due to more reversible slip processes operating.

The deflected areas of the terraced regions have been observed at different crack lengths in U720Li C&W tested at 300°C in air (Figure 5-32 and Figure 5-33) and in vacuum (Figure 5-34 and Figure 5-35). The behaviour in these regions is similar to the behaviour in the flat regions, however the secondary cracks represent mode I crack growth. The vacuum sample exhibits more faceted crack growth, which was also seen in the flat regions.

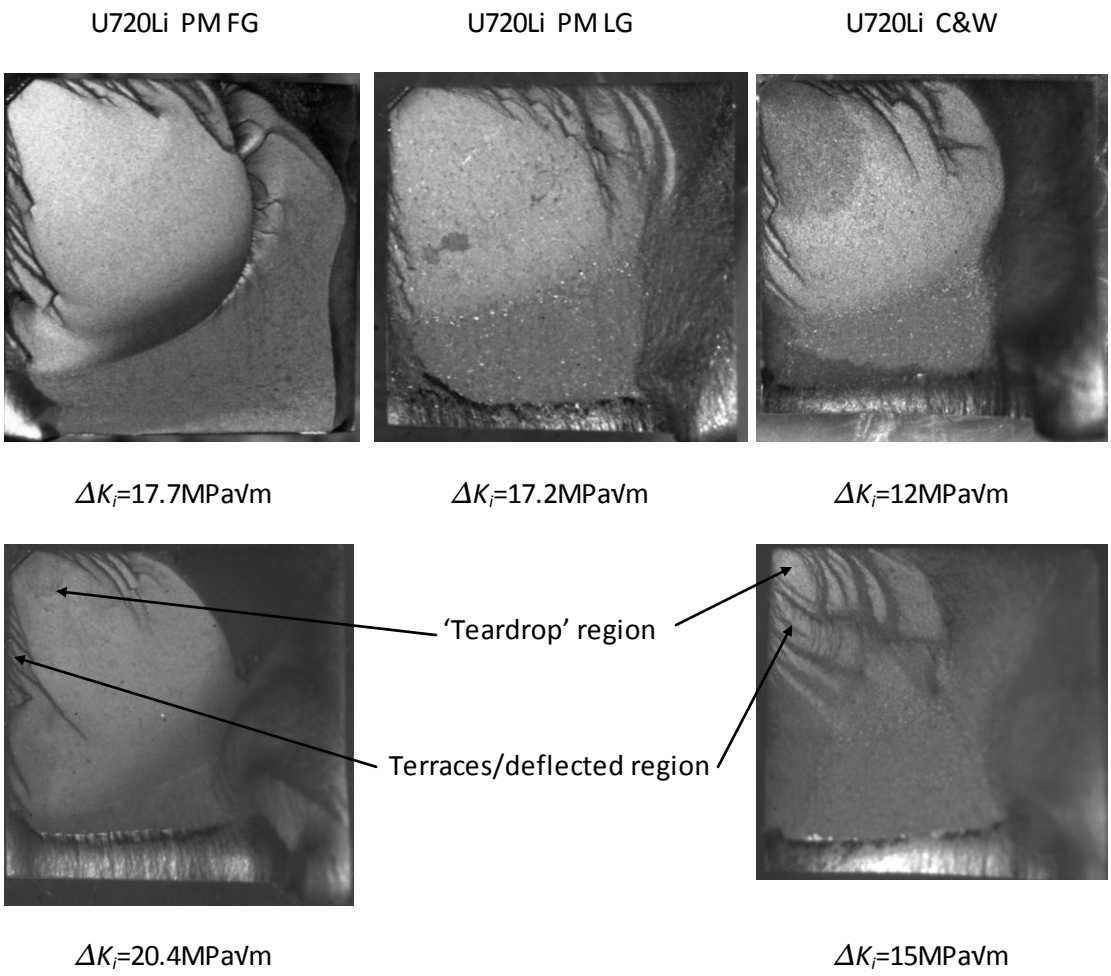

Figure 5-1: CNB Fracture Surfaces for U720Li PM FG, PM LG and C&W at 300°C in air with different ΔK_i

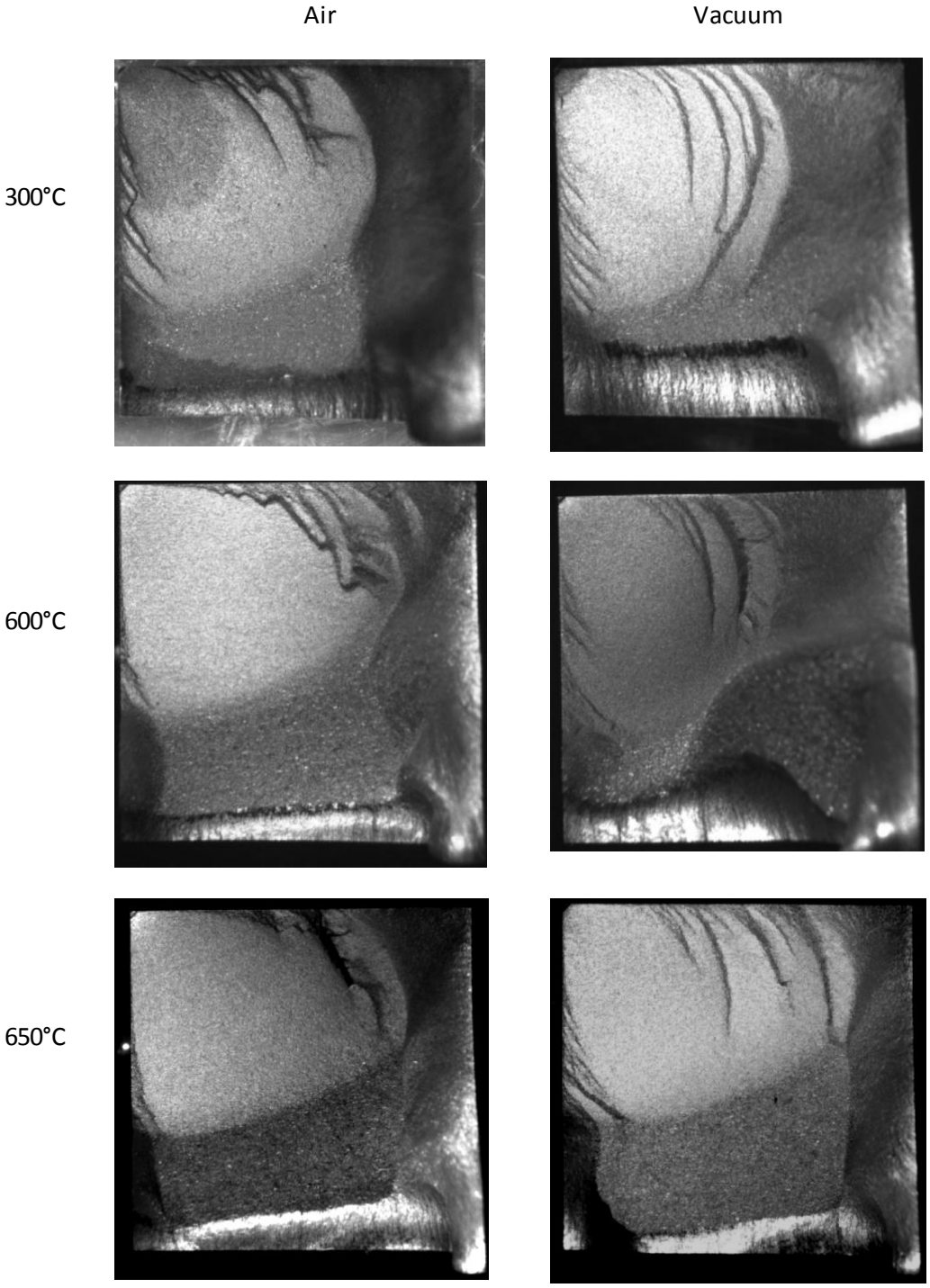

Figure 5-2: CNB Fracture Surfaces for U720Li C&W at 300, 600 and 650°C in air and vacuum with ΔK_i=12MPa$\sqrt{m}$

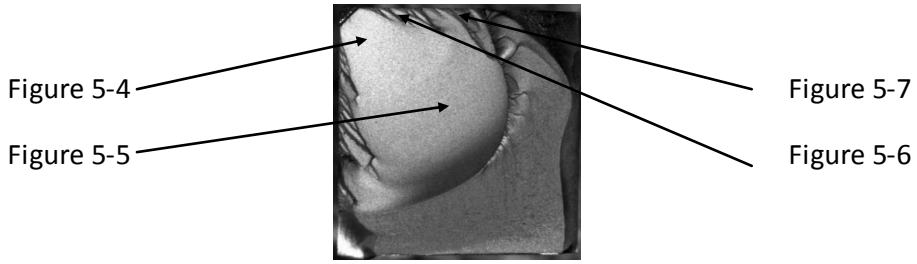

Figure 5-3: CNB Fracture Surface U720Li PM FG at 300°C, 20Hz, ΔK_i=17.7MPa√m

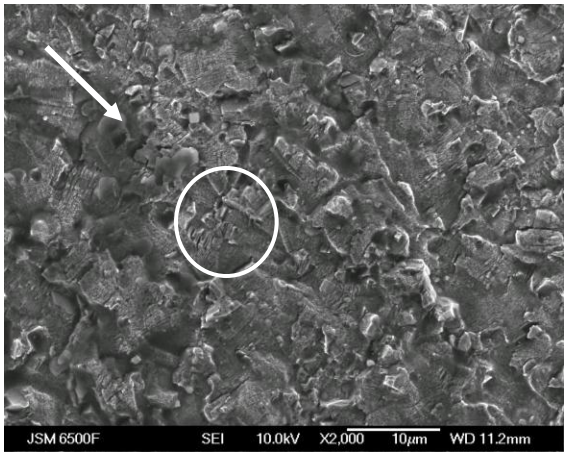

Figure 5-4: Fracture surface of U720Li FG PM at 300°C in air ΔK_i=17.7MPa√m in the planar region at c=4.34 mm and an estimated ΔK≈39MPa √m showing stage II crack growth with slip traces and secondary cracks (Arrow indicates crack growth direction, circle shows secondary cracks)

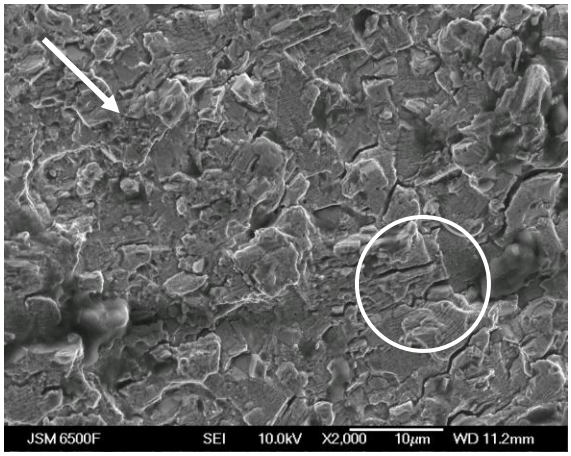

Figure 5-5: Fracture surface of U720Li FG PM at 300°C in air ΔK_i=17.7MPa√m in the planar region at c=9.82 mm and an estimated ΔK≈68.5MPa √m showing larger secondary cracks merging over several grain sizes (Arrow indicates crack growth direction, circle shows secondary cracks)

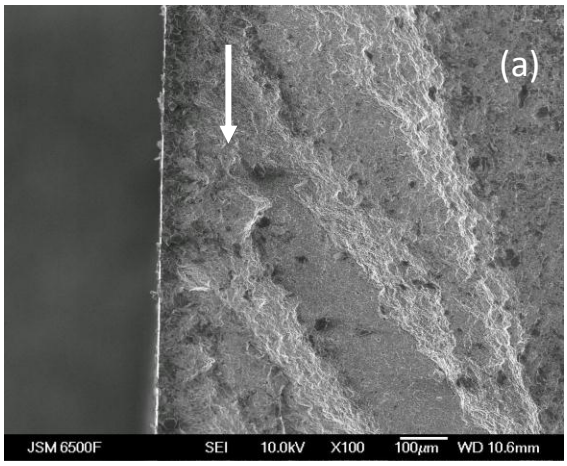

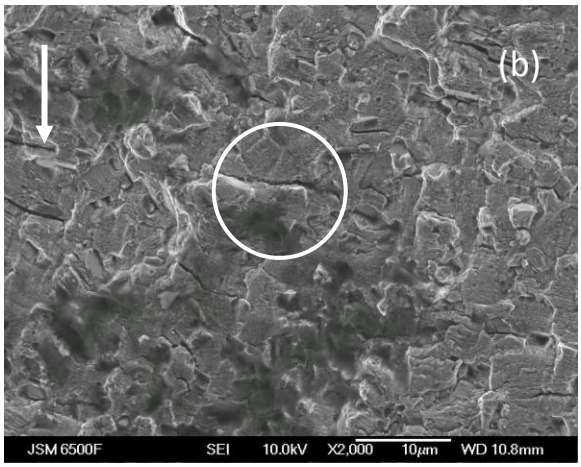

Figure 5-6: Fracture surface of U720Li FG PM at 300°C in air ΔK_i=17.7MPa√m in in the Terraced region at c=5.2mm and an estimated ΔK≈42MPa √m (Arrow indicates crack growth direction, circle shows secondary cracks) (a) at low magnification showing the flat and deflected terraces (b) At higher magnification showing stage II growth in the flat region with slip traces and secondary cracks merging over several grain sizes

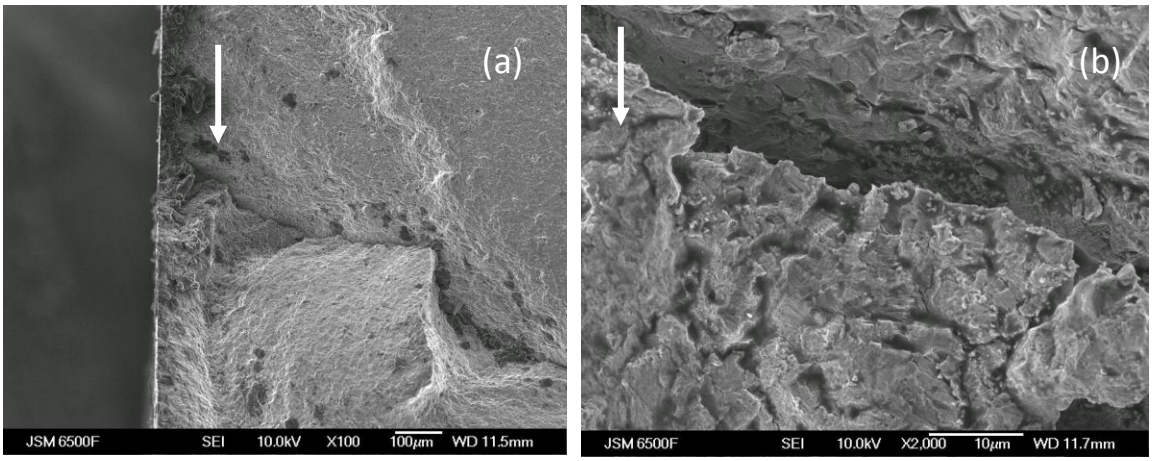

Figure 5-7: Fracture surface of U720Li FG PM at 300°C in air ΔK_i=17.7MPa√m at the end of the Terraced region at c=7.4mm and an estimated ΔK≈50MPa √m showing a large secondary crack between opening and shear terraces (Arrow indicates crack growth direction) (a) At low magnification (b) At higher magnification

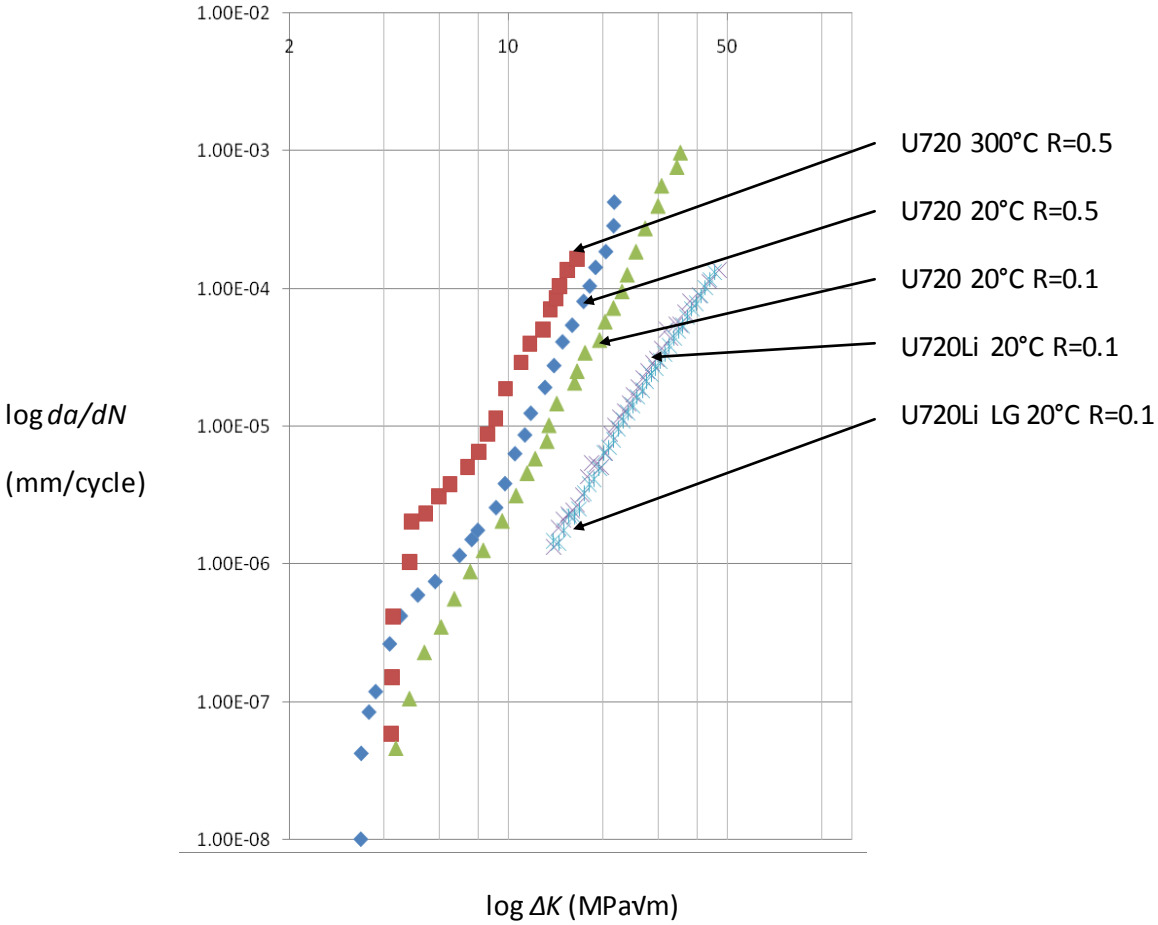

Figure 5-8: Crack growth rate da/dN vs ΔK for U720, U720Li and U720LiLG at 20Hz in air

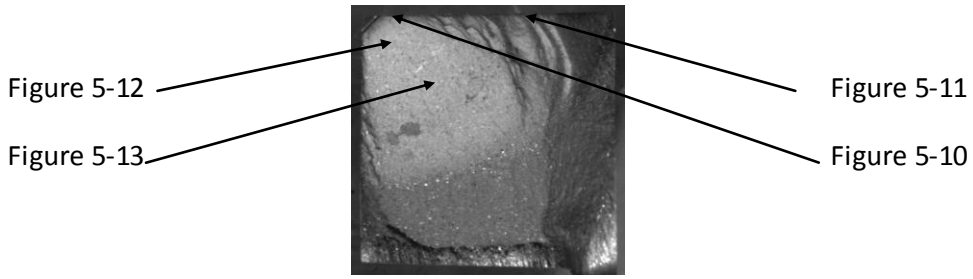

Figure 5-9: CNB Fracture Surface U720Li PM LG at 300°C, 20Hz, ΔK_i=17.2MPa√m

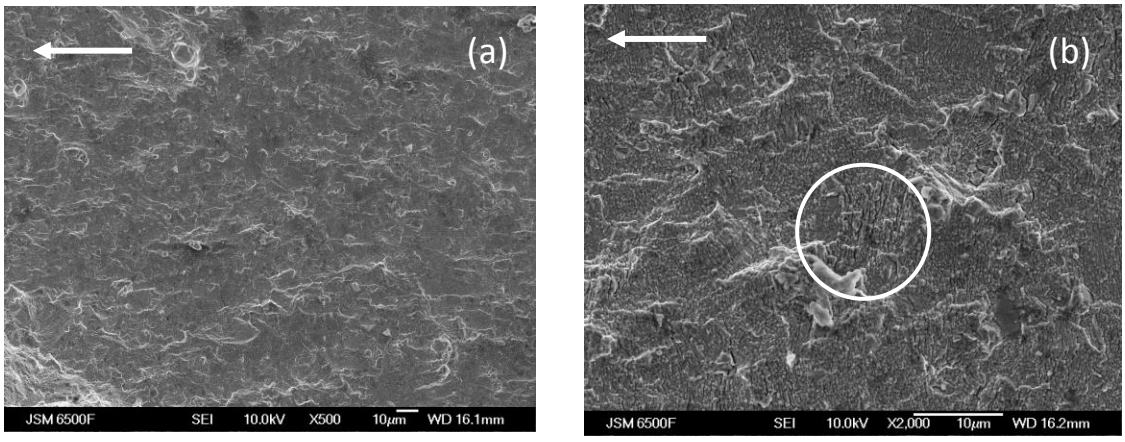

Figure 5-10: Fracture surface of U720Li LG PM at 300°C in air ΔK_i=17.2MPa√m in the Terraced region at c=1.8mm and an estimated ΔK≈22MPa √m (Arrow indicates crack growth direction, circle shows secondary cracks) (a) at low magnification (b) at higher magnification showing slip traces with varying direction at grain size

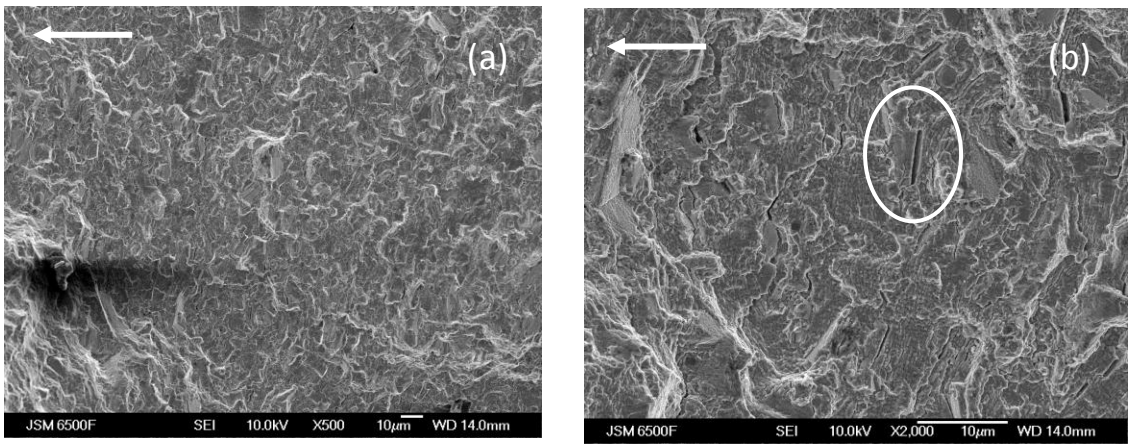

Figure 5-11: Fracture surface of U720Li LG PM at 300°C in air ΔK_i=17.2MPa√m at the end of the Terraced region at c=9.3mm and an estimated ΔK≈62MPa √m (Arrow indicates crack growth direction, circle shows secondary cracks) (a) at low magnification showing stage II growth (b) at high magnification showing secondary cracks

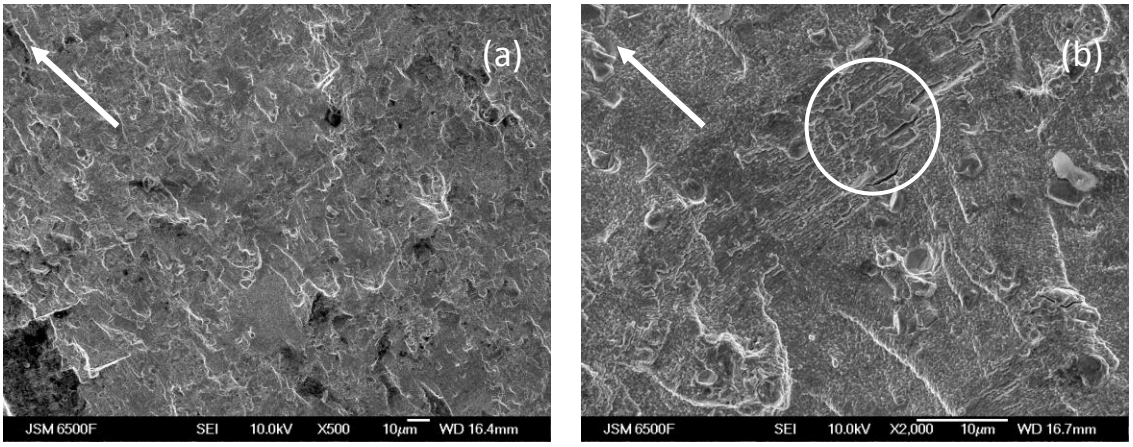

Figure 5-12: Fracture surface of U720Li LG PM at 300°C in air ΔK_i=17.2MPa√m in the planar region at c=2.87mm and an estimated ΔK≈28MPa √m (Arrow indicates crack growth direction, circle shows secondary cracks) a) at low magnification showing stage II growth (b) at high magnification showing secondary cracks

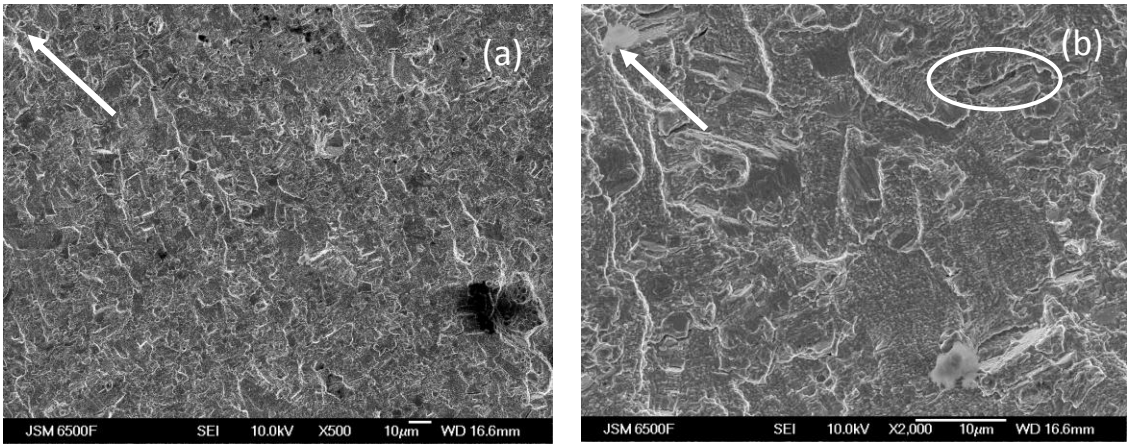

Figure 5-13: Fracture surface of U720Li LG PM at 300°C in air ΔK_i=17.2MPa√m in the planar region at c=4.9mm and an estimated ΔK≈49MPa √m (Arrow indicates crack growth direction, circle shows secondary cracks) (a) at low magnification showing stage II growth (b) at high magnification showing secondary cracks

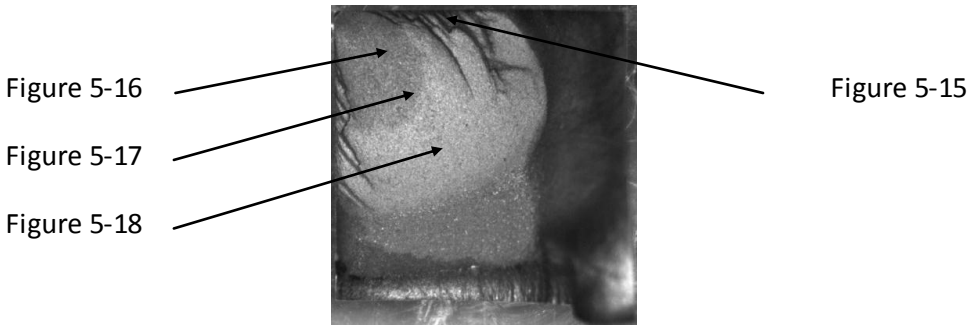

Figure 5-14: CNB Fracture Surface U720Li C&W at 300°C in air, 20Hz, ΔK_i=12MPa√m

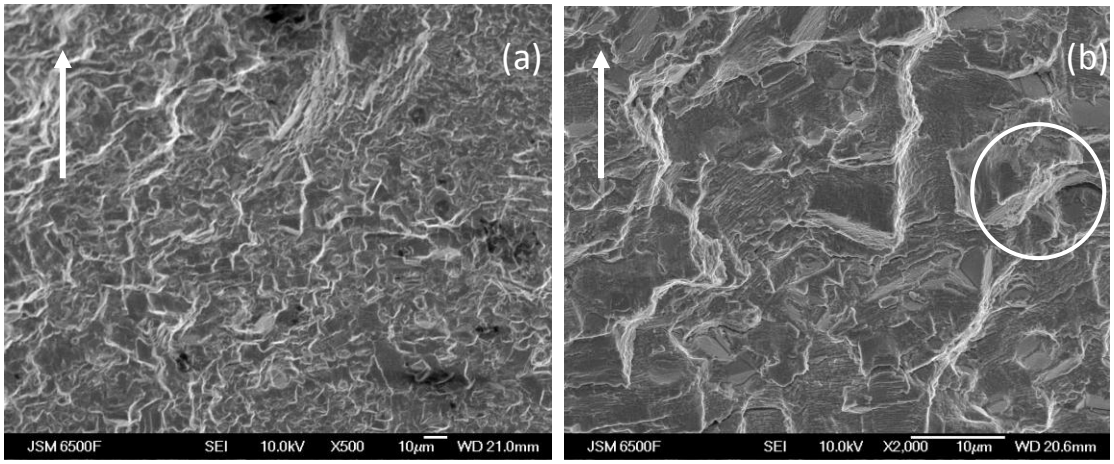

Figure 5-15: Fracture surface of U720Li C&W at 300°C in air ΔK_i=12MPa√m in the Terraced region at *c*=7.09mm and an estimated ΔK≈56MPa √m (Arrow indicates crack growth direction, circle shows secondary cracks) a) at low magnification showing stage II growth (b) at high magnification showing slip traces and some secondary cracks

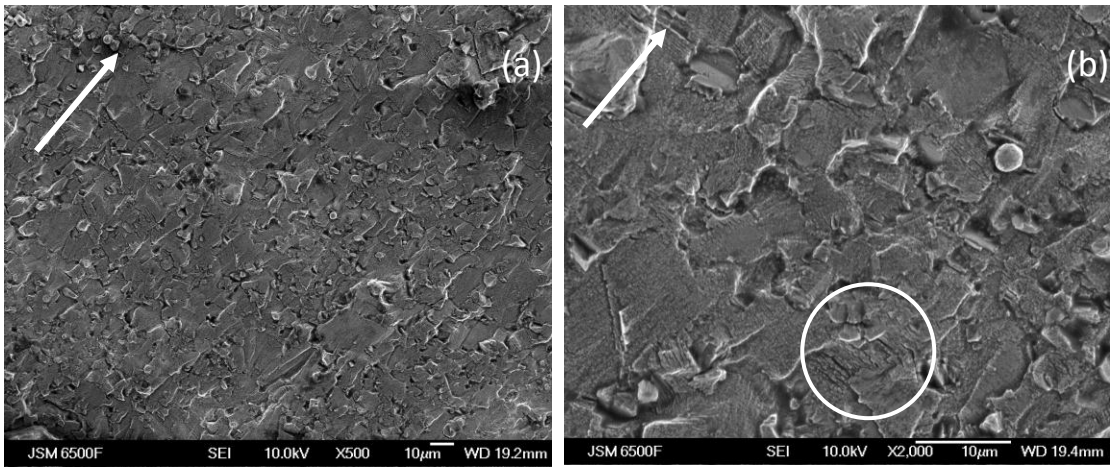

Figure 5-16: Fracture surface of U720Li C&W at 300°C in air ΔK_i=12MPa√m in the planar region at *c*=2mm and an estimated ΔK≈27MPa √m (Arrow indicates crack growth direction, circle shows secondary cracks) (a) at low magnification showing stage II growth (b) at high magnification showing slip traces and secondary cracks

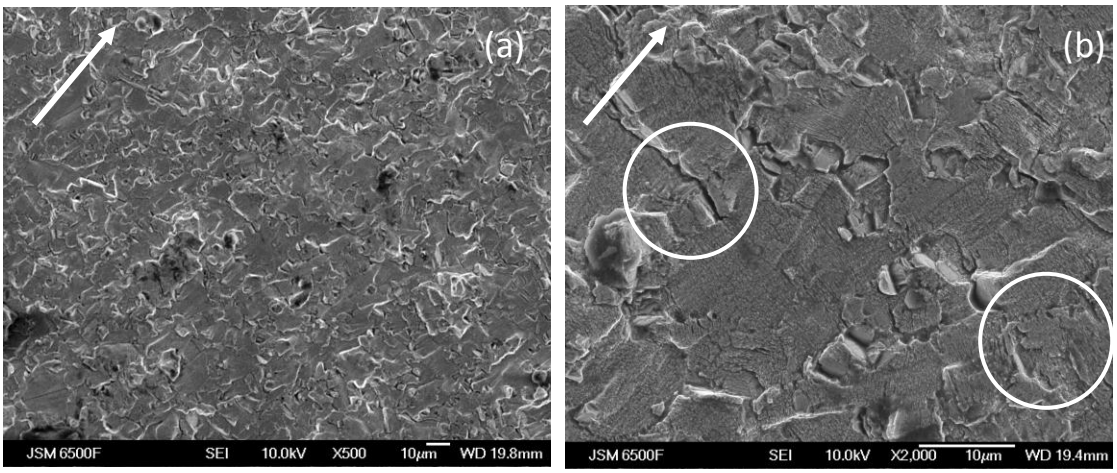

Figure 5-17: Fracture surface of U720Li C&W at 300°C in air ΔK_i=12MPa√m in the planar region at c=4.7mm and an estimated ΔK≈42MPa √m (Arrow indicates crack growth direction, circle shows secondary cracks) (a) at low magnification (b) at high magnification showing slip traces and secondary cracks over several grain sizes

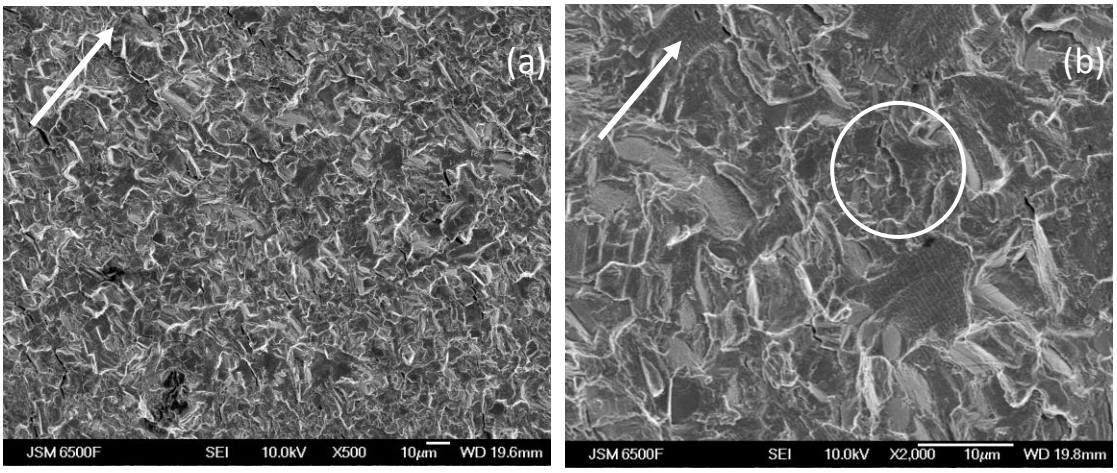

Figure 5-18: Fracture surface of U720Li C&W at 300°C in air ΔK_i=12MPa√m in the planar region at c=6.2 mm and an estimated ΔK≈68MPa √m (Arrow indicates crack growth direction, circle shows secondary cracks) (a) at low magnification showing stage II growth (b) at high magnification showing secondary cracks

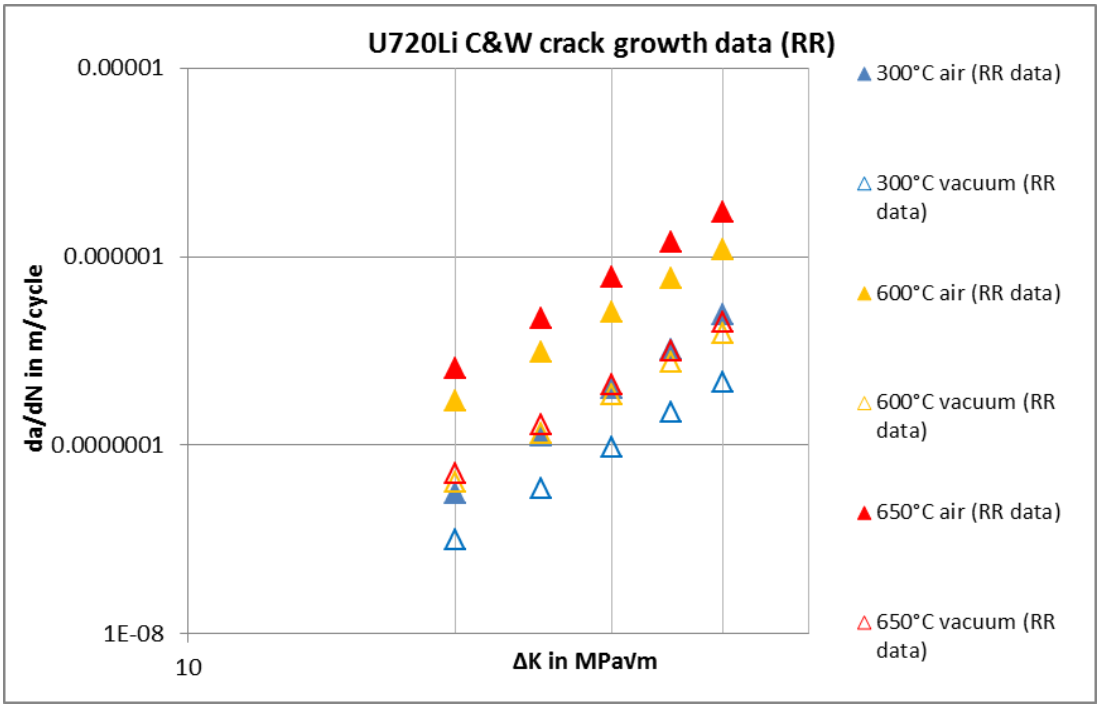

Figure 5-19: Crack growth rate *da/dN* vs ΔK for U720Li C&W from Rolls Royce plc. [93]

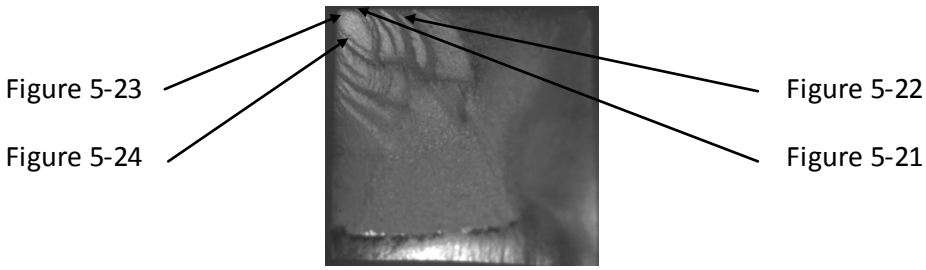

Figure 5-20: CNB Fracture Surface U720Li C&W at 300°C in air, 20Hz, ΔK_i=15MPa√m

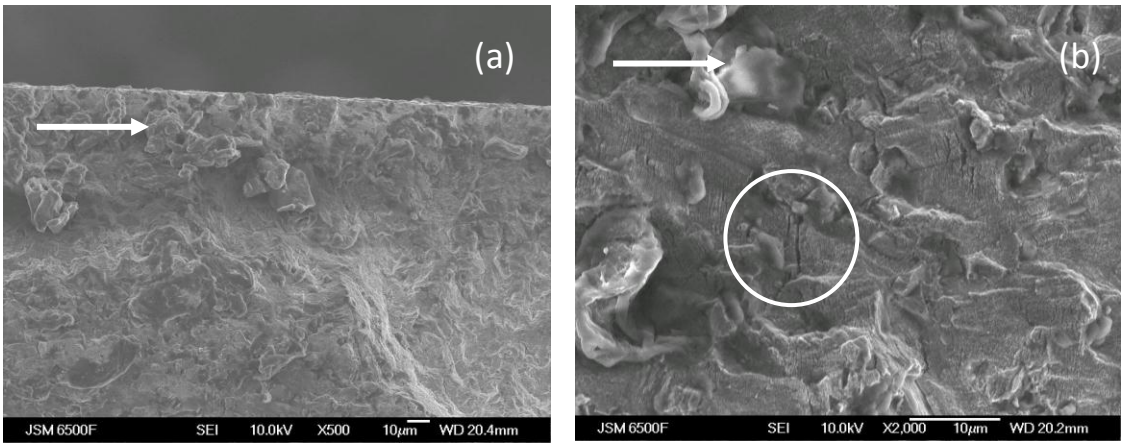

Figure 5-21: Fracture surface of U720Li C&W at 300°C in air ΔK=15MPa√m in the terraced region at c=0.69mm and an estimated ΔK≈32MPa √m (Arrow indicates crack growth direction, circle shows secondary cracks) (a) at low magnification (b) at high magnification showing some secondary cracks

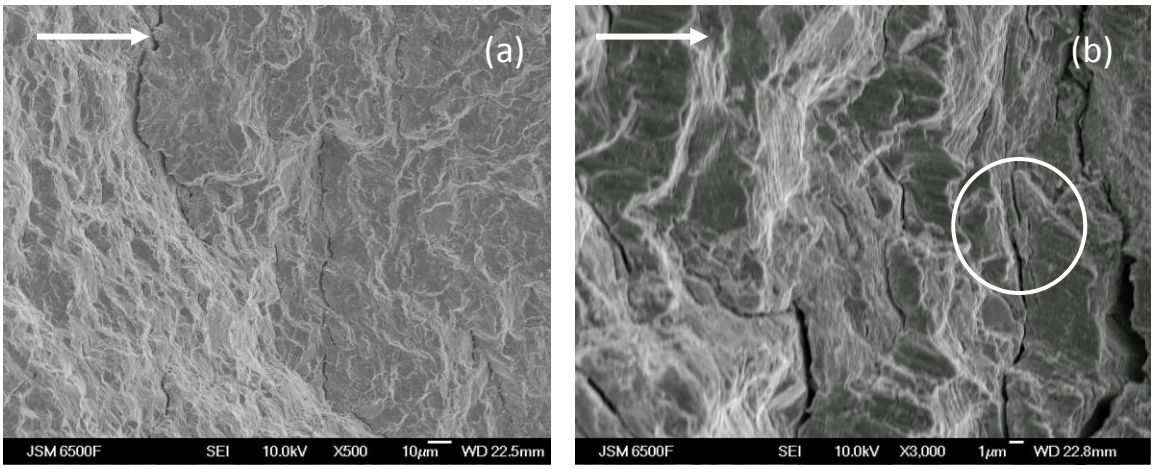

Figure 5-22: Fracture surface of U720Li C&W at 300°C in air ΔK=15MPa√m in the terraced region at c=4mm and an estimated ΔK≈75MPa √m (Arrow indicates crack growth direction, circle shows secondary cracks) (a) at low magnification showing deflected crack growth on the left and flat stage II growth on the right and a large secondary crack between the two growth modes (b) at high magnification showing large secondary cracks

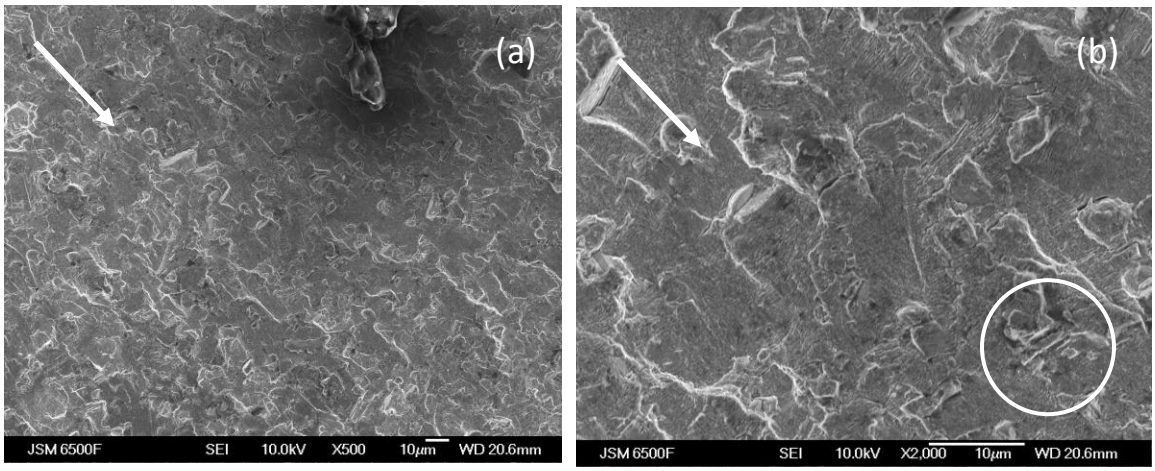

Figure 5-23: Fracture surface of U720Li C&W at 300°C in air ΔK=15MPa√m in the planar region at c=0.6 mm and an estimated ΔK≈30MPa√m (Arrow indicates crack growth direction, circle shows secondary cracks) (a) at low magnification showing stage II growth (b) at high magnification showing slip traces and secondary cracks

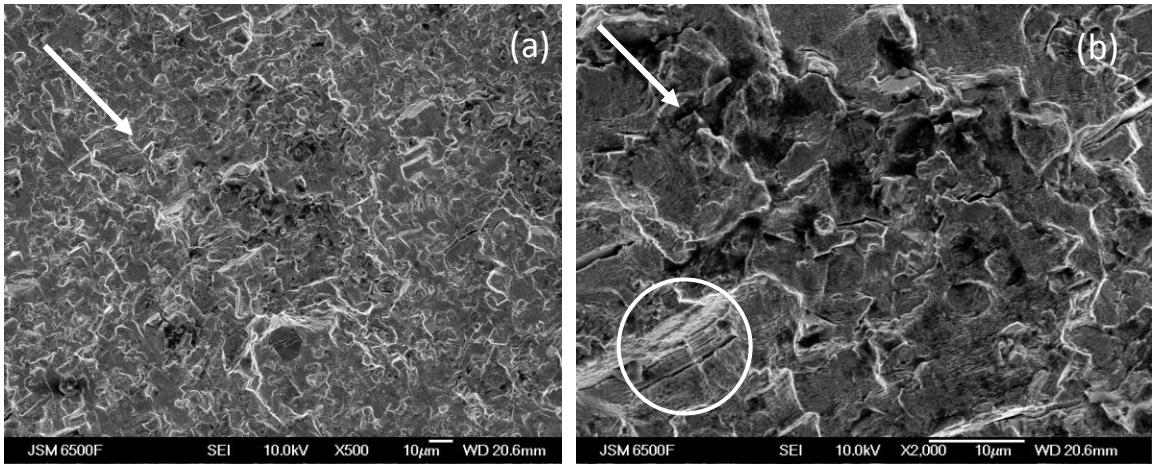

Figure 5-24: Fracture surface of U720Li C&W at 300°C in air ΔK_i=15MPa√m at the end of the planar region at c=1.8mm and an estimated ΔK≈51MPa√m (Arrow indicates crack growth direction, circle shows secondary cracks) (a) at low magnification showing stage II growth (b) at high magnification showing slip traces and secondary cracks

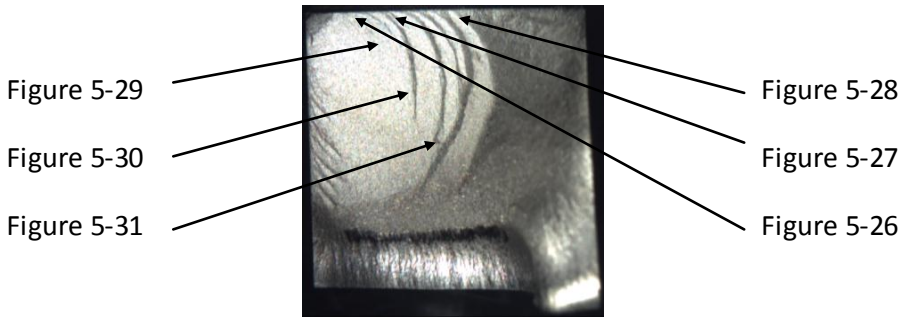

Figure 5-25: CNB fracture surface U720Li C&W at 300°C in vacuum, 20Hz, ΔK_i=12MPa√m

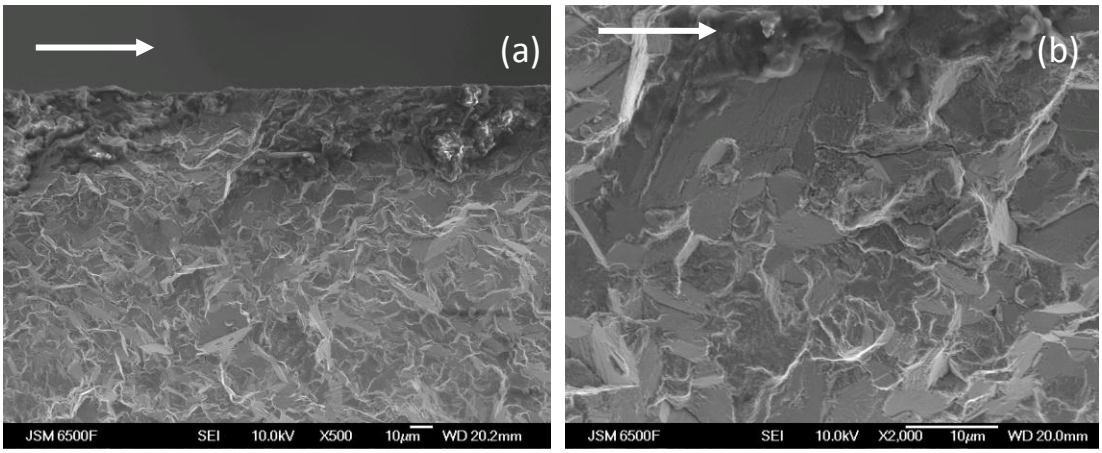

Figure 5-26: Fracture surface of U720Li C&W at 300°C in vacuum ΔK_i=12MPa√m in terraced region at c=1.08mm and an estimated ΔK≈21MPa√m (fretted region) (Arrow indicates crack growth direction) showing a fretted area near the notch (a) at low magnification (b) at higher magnification

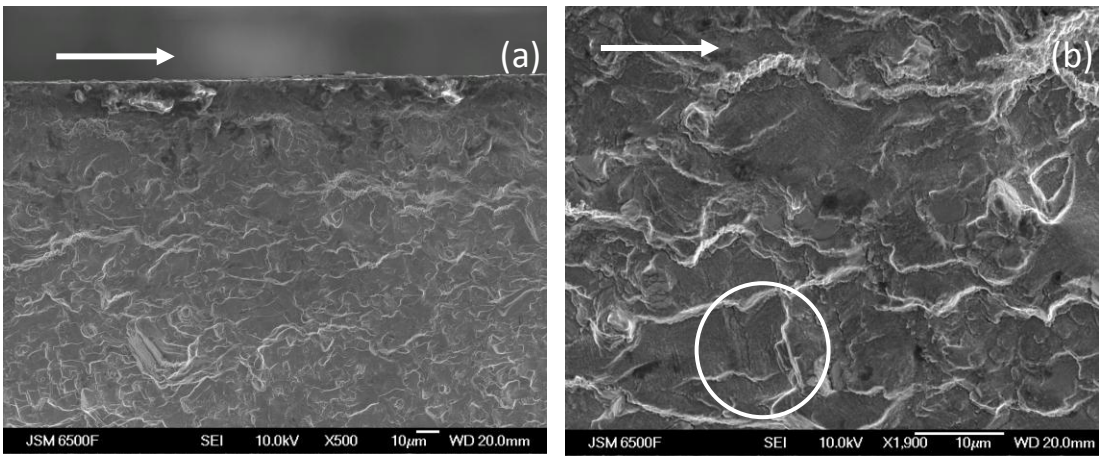

Figure 5-27: Fracture surface of U720Li C&W at 300°C in vacuum ΔK_i=12MPa√m in terraced region at c=3.4mm and an estimated ΔK≈36MPa√m (Arrow indicates crack growth direction, circle shows secondary cracks) showing more faceted crack growth (a) at low magnification (b) at higher magnification showing slip traces

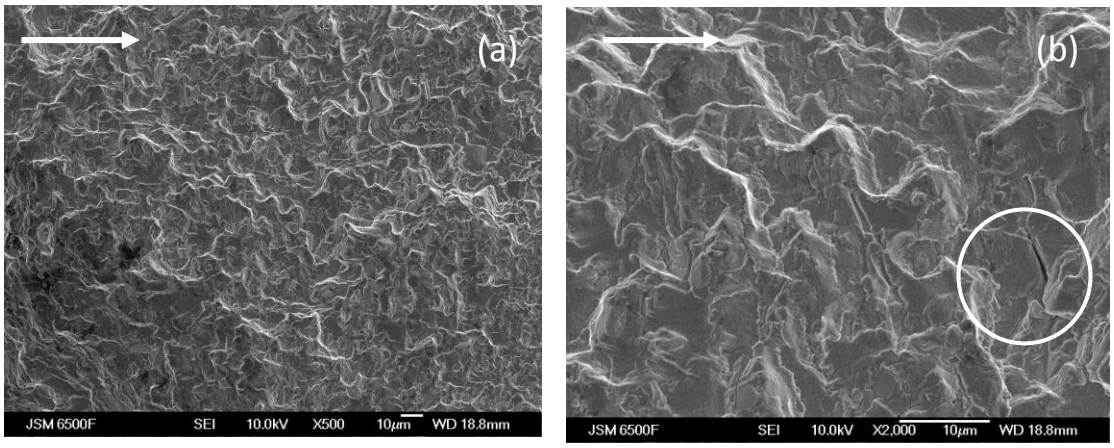

Figure 5-28: Fracture surface of U720Li C&W at 300°C in vacuum ΔK_i=12MPa√m in terraced region at c=6.9mm and an estimated ΔK≈56MPa√m (Arrow indicates crack growth direction, circle shows secondary cracks) (a) at low magnification showing stage II growth (b) at high magnification showing secondary cracks

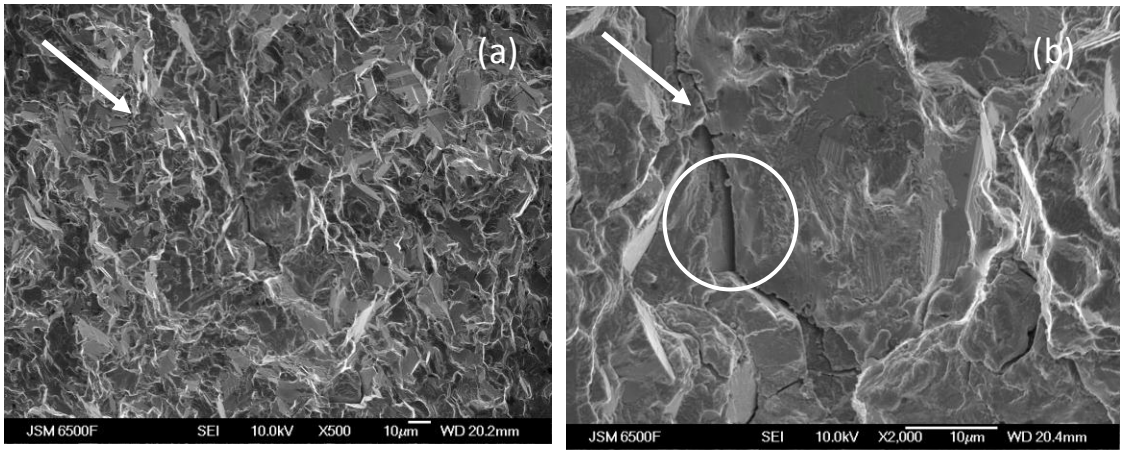

Figure 5-29: Fracture surface of U720Li C&W at 300°C in vacuum ΔK_i=12MPa√m in planar region at c=0.97mm and an estimated ΔK≈20MPa√m showing the fretted area near the initial notch (Arrow indicates crack growth direction, circle shows secondary cracks) (a) at low magnification (b) at high magnification showing large secondary cracks

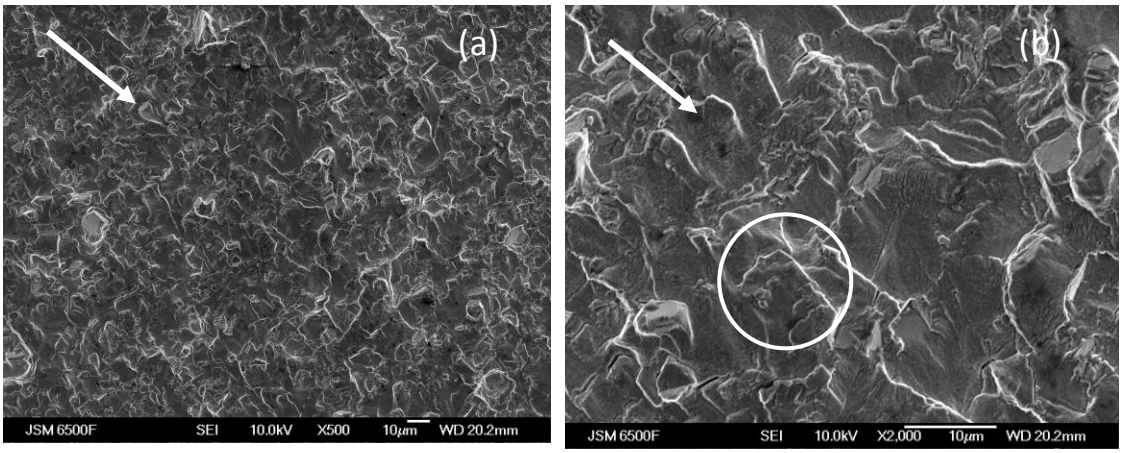

Figure 5-30: Fracture surface of U720Li C&W at 300°C in vacuum ΔK_i=12MPa√m in the teardrop region at c=3.401mm and an estimated ΔK≈36MPa√m (Arrow indicates crack growth direction, circle shows secondary cracks) (a) at low magnification showing faceted surface (b) at high magnification showing secondary cracks and a faceted surface

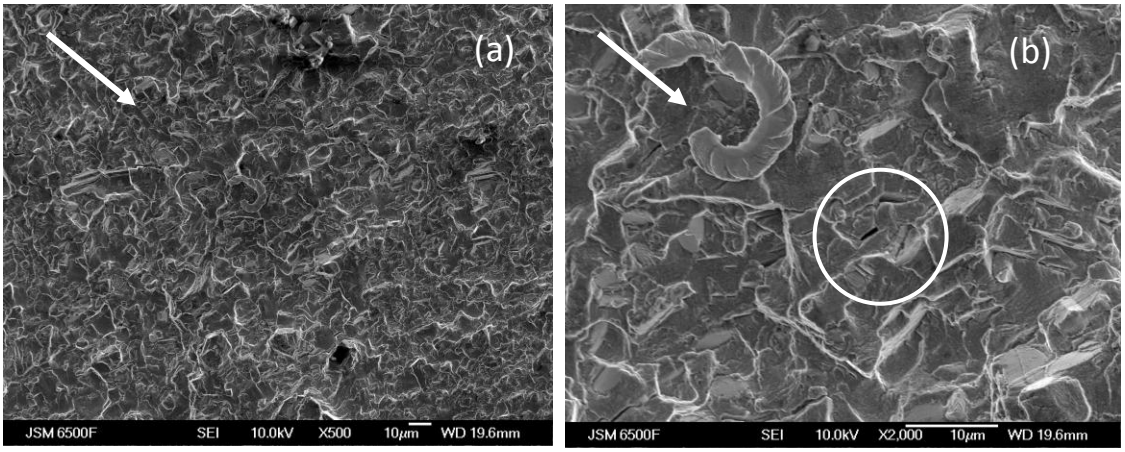

Figure 5-31: Fracture surface of U720Li C&W at 300°C in vacuum ΔK_i=12MPa√m in planar region at c=7.2mm and an estimated ΔK≈58MPa√m (Arrow indicates crack growth direction, circle shows secondary cracks) (a) at low magnification showing faceted surface (b) at high magnification showing secondary cracks and a faceted surface

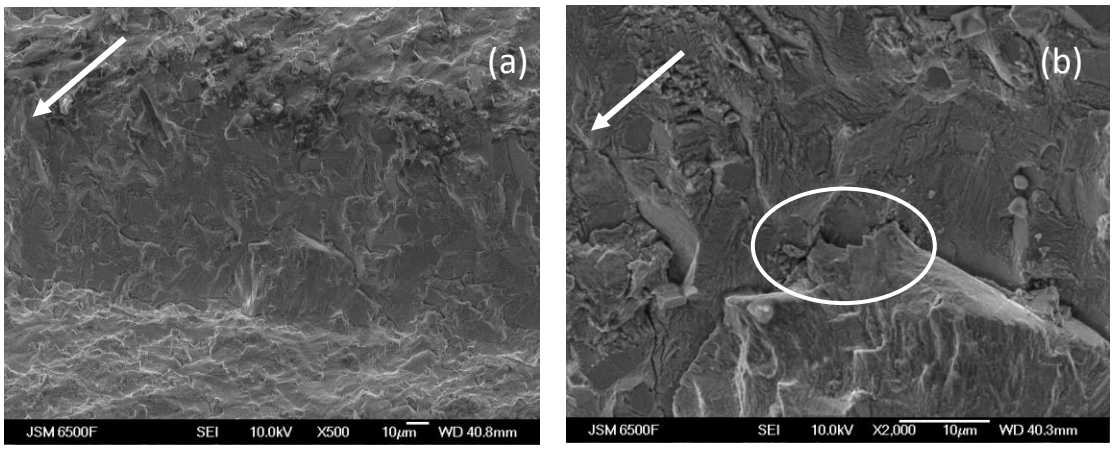

Figure 5-32: Fracture surface of U720Li C&W at 300°C in air ΔK_i=12MPa√m in terraced region at a tilt angle of 30° for the second terrace c≈1.8mm and an estimated ΔK≈26MPa√m (Arrow indicates crack growth direction, circle shows secondary cracks) (a) at low magnification showing shear and opening terraces (b) at higher magnification showing large secondary cracks in the shear terrace

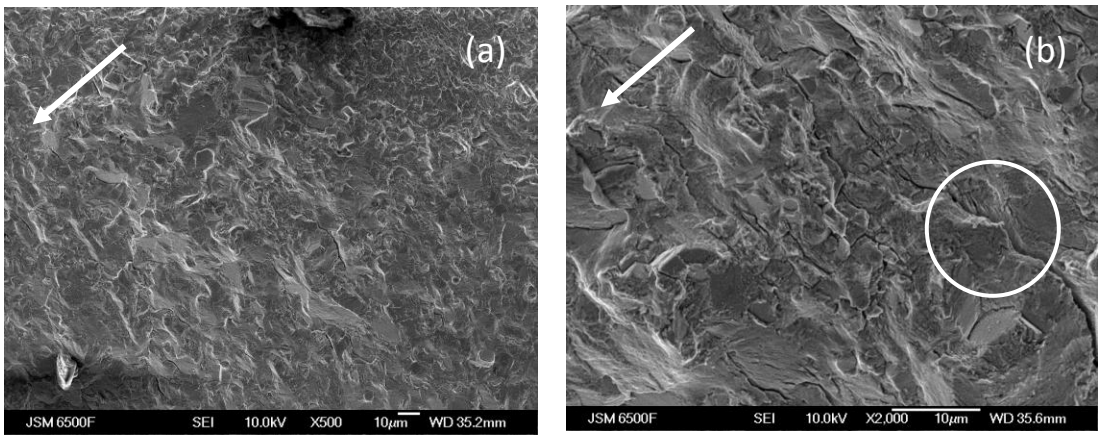

Figure 5-33: Fracture surface of U720Li C&W at 300°C in air ΔK_i=12MPa√m in terraced region at a tilt angle of 25° for the last terrace c≈6.1mm and an estimated ΔK≈50MPa√m (Arrow indicates crack growth direction, circle shows secondary cracks) (a) at low magnification (b) at high magnification showing large secondary cracks over several grain sizes

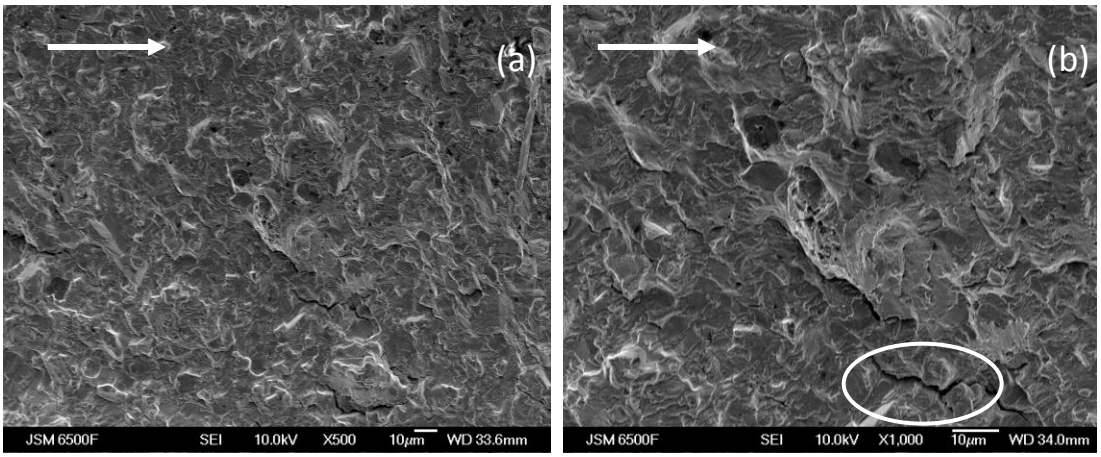

Figure 5-34: Fracture surface of U720Li C&W at 300°C in vacuum ΔK_i=12MPa√m in terraced region at a tilt angle of 30° for the second terrace c≈3.5mm and an estimated ΔK≈36MPa√m (Arrow indicates crack growth direction, circle shows secondary cracks) (a) at low magnification (b) at higher magnification showing secondary cracks

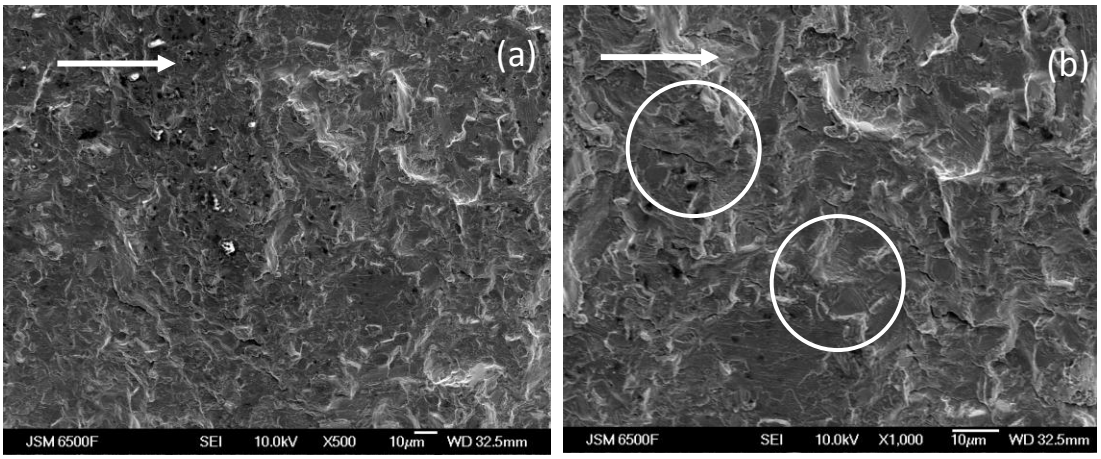

Figure 5-35: Fracture surface of U720Li C&W at 300°C in vacuum ΔK_i=12MPa√m in terraced region at a tilt angle of 30° for the last terrace c≈7mm and an estimated ΔK≈56MPa√m (Arrow indicates crack growth direction, circle shows secondary cracks) (a) at low magnification showing stage II crack growth (b) at higher magnification showing slip traces and secondary cracks

5.2 SENB Testing

SENB testing has been carried out on U720Li C&W. The first sample was precracked from 20MPa√m down to 15 MPa√m, and then grown out at constant load at 300°C in air. Figure 5-36 shows the fracture surface with initial notch precrack and growth out. Deflected terraces can only be observed late in the growth out near the final fracture on both free surfaces of the sample.

It is assumed the ΔK levels were too low to clearly trigger deflection, therefore further testing was carried out with precracking at a constant ΔK_i=20 MPa√m and growth out from that level, to achieve an earlier onset of deflection. Tests were precracked at room temperature in air and the grown out at 300, 600 and 650°C in air and vacuum.

The fracture surfaces of these tests are shown in Figure 5-37. The deflected terraces can now be seen on both sides of the sample at 300°C in air and vacuum, and at 600 and 650°C in vacuum. Lifetimes of the tests are shown in Table 10.

Temperature	ΔK_i (MPa√m)	N_f in air	N_f in Vacuum
300°C	20	29318	37662
600°C	20	12082	20868
650°C	20	15500	18520

Table 10: Lifetime of SENB samples tested at 300, 600 and 650°C in air and vacuum

Two thin SENB tests have been carried out to assess crack growth behaviour under more plane stress conditions. The samples were precracked at room temperature in air at a constant ΔK of 20MPa√m. The load was turned up to achieve a ΔK of 25MPa√m for the growth out and the tests were run at a temperature of 300°C in air. Crack growth has been monitored using PD. The fracture surfaces are shown in Figure 5-38 and Figure 5-39. After the precrack a stage II region can be observed in the centre, and the deflected crack growth can be seen to dominate over the larger proportion of the sample as ΔK (crack length) increases. The estimated ΔK level at the point where the deflected terraces from both side meet, i.e. the end of the stage II region is at approx. 45MPa√m in the second sample.

5.2.1 Fractography

Figure 5-41 to Figure 5-43 show the SEM fractography of thick SENB U720Li C&W sample tested in vacuum at 300°C with a ΔK_i=20MPa√m, looking at the deflected region in different areas as shown in Figure 5-40. Fractography has also been carried out on the second thin SENB sample tested in air as shown in Figure 5-45 to Figure 5-48, in the areas described in Figure 5-44.

In both the thick and the thin SENB sample similar mechanisms as in the CNB samples can be observed, i.e. slip traces and secondary cracks both in the planar and the deflected region.

5.2.2 Crack growth data

From the PD readings of the SENB crack growth data has been produced and compared for the two sample thicknesses and all test conditions. The results are shown in Figure 5-49. As expected higher temperatures show faster crack growth rates and vacuum conditions lead to lower crack growth rates.

A lower crack growth rate can be observed for the thin sample as compared to the thick sample at the same conditions, which may be due to the plane stress conditions or to the larger proportion of deflected area in this sample. This crack growth data is averaged across Stage II and deflected crack growth and the PD and *K* calibrations both assume normal stage II through thickness growth (which is valid up to 25MPa√m). Local crack growth rates for Stage II crack growth are most closely defined by data from the thick SENB, but local *da/dN* under the characteristic driving force for sustained deflected crack growth are still needed, and not obtainable from the test conditions thus far.

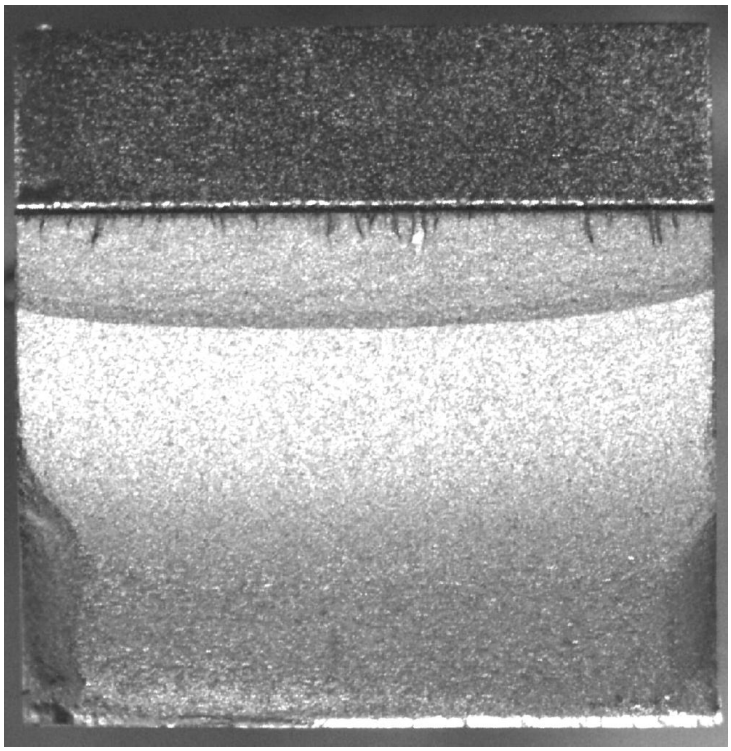

Figure 5-36: SENB Fracture Surface of U720Li C&W at 300°C in air with ΔK_i=15MPa√m

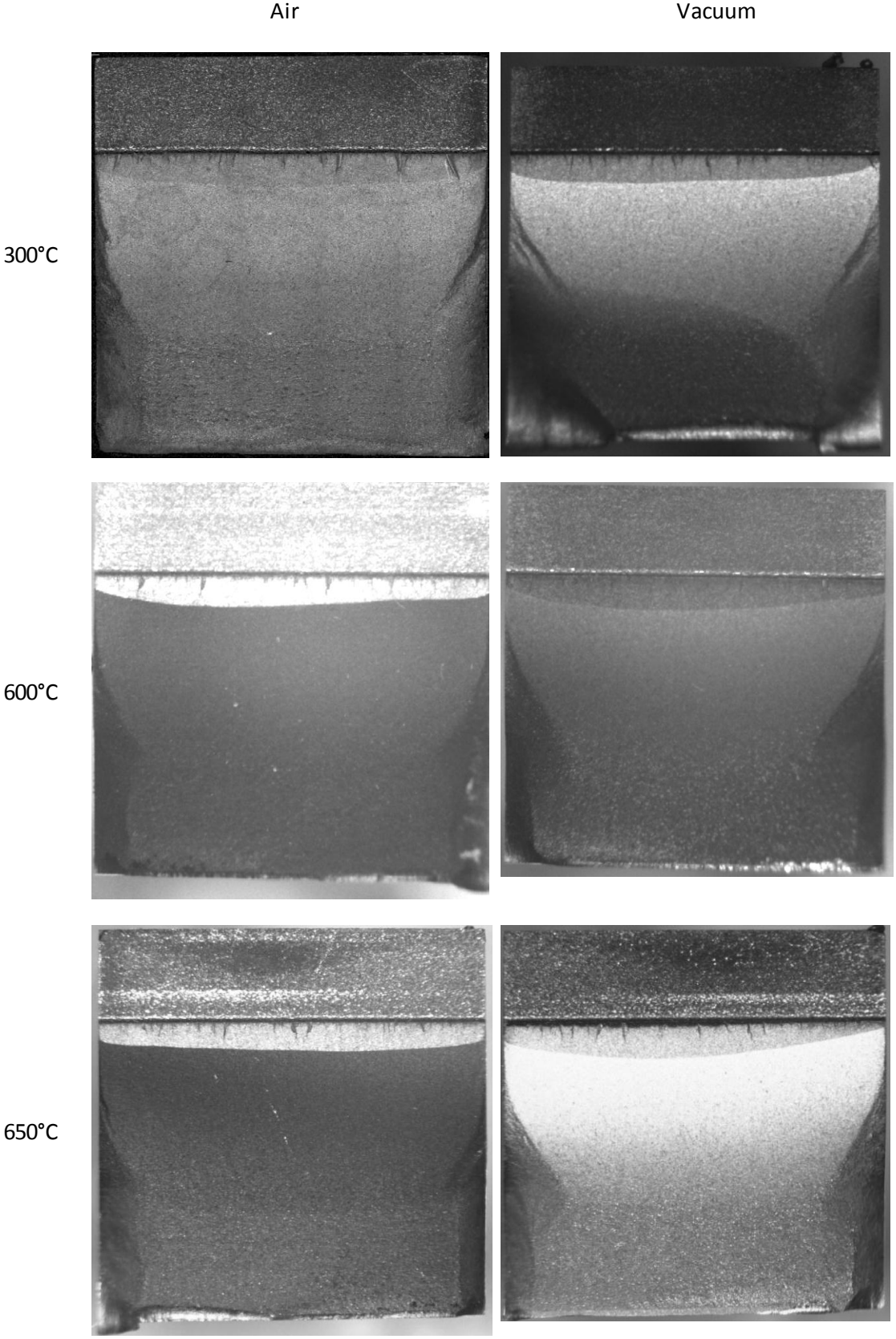

Figure 5-37: SENB Fracture Surface of SENB U720Li C&W at 300, 600 and 650°C in air and vacuum with ΔK_i=20MPa√m

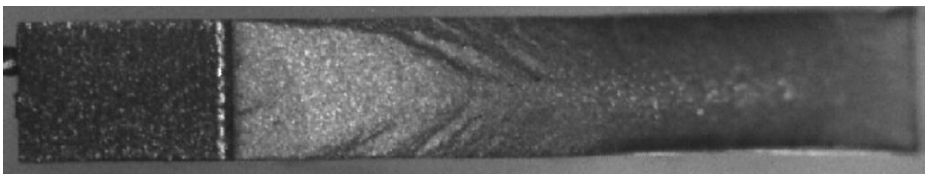

Figure 5-38: Fracture surface of thin SENB, U720Li C&W tested at 300°C in vacuum, 20Hz, ΔK_i=20MPa√m

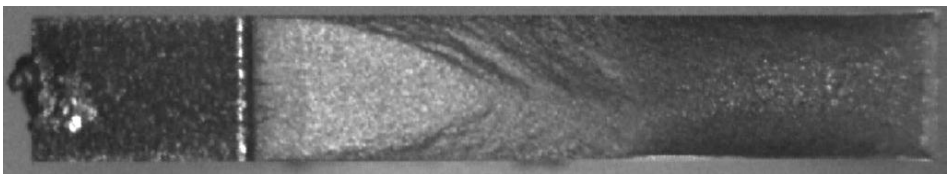

Figure 5-39: Fracture surface of thin SENB U720Li C&W tested at 300°C in vacuum, 20Hz, ΔK_i=20MPa√m

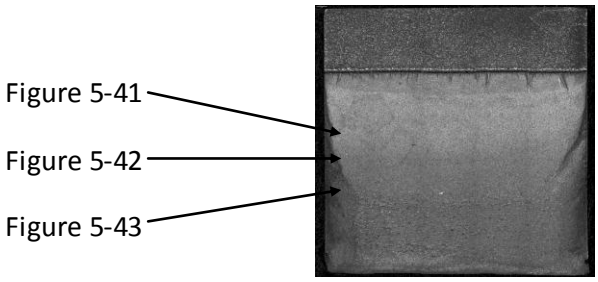

Figure 5-40: Fracture Surface of U720Li C&W SENB tested at 300°C in vacuum, 20Hz, ΔK_i=20MPa√m

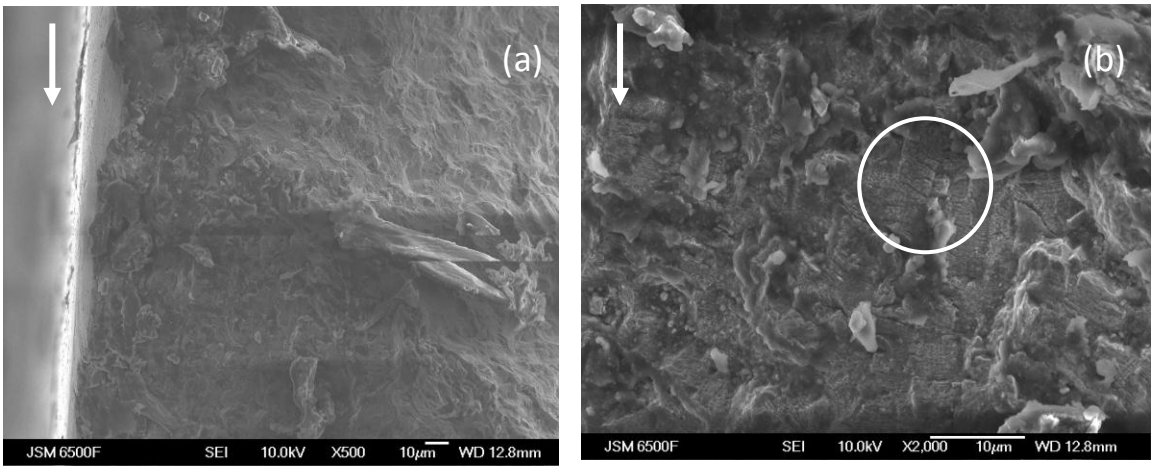

Figure 5-41: Fracture surface of U720Li C&W SENB tested at 300°C in vacuum, in terraced region at c=5.29mm and an estimated ΔK≈25MPa √m (Arrow indicates crack growth direction, circle shows secondary cracks) (a) at low magnification (b) at high magnification showing slip traces/secondary cracks

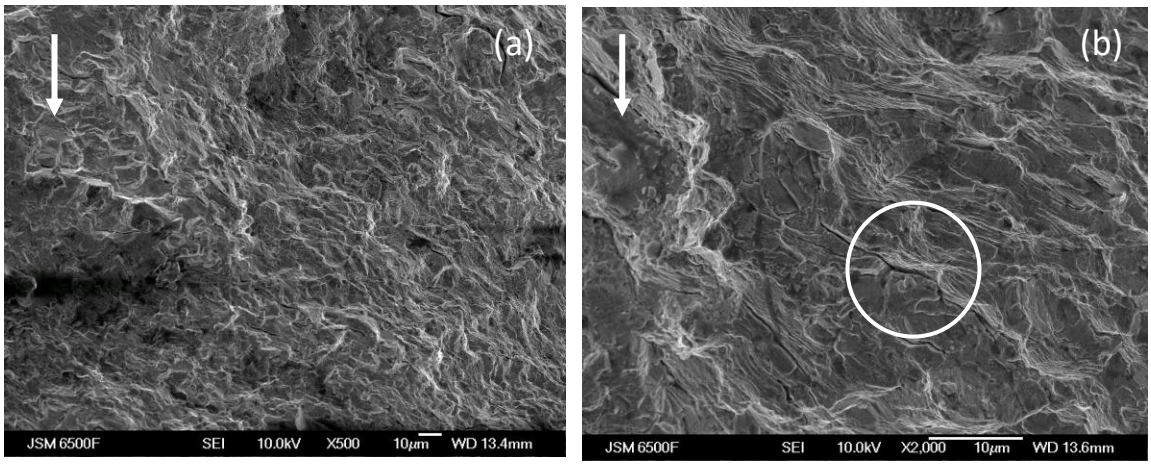

Figure 5-42: Fracture surface of U720Li C&W SENB tested at 300°C in vacuum, in terraced region at c=7.16mm and an estimated ΔK≈40MPa √m (Arrow indicates crack growth direction, circle shows secondary cracks) (a) at low magnification showing stage II growth (b) at high magnification showing secondary cracks

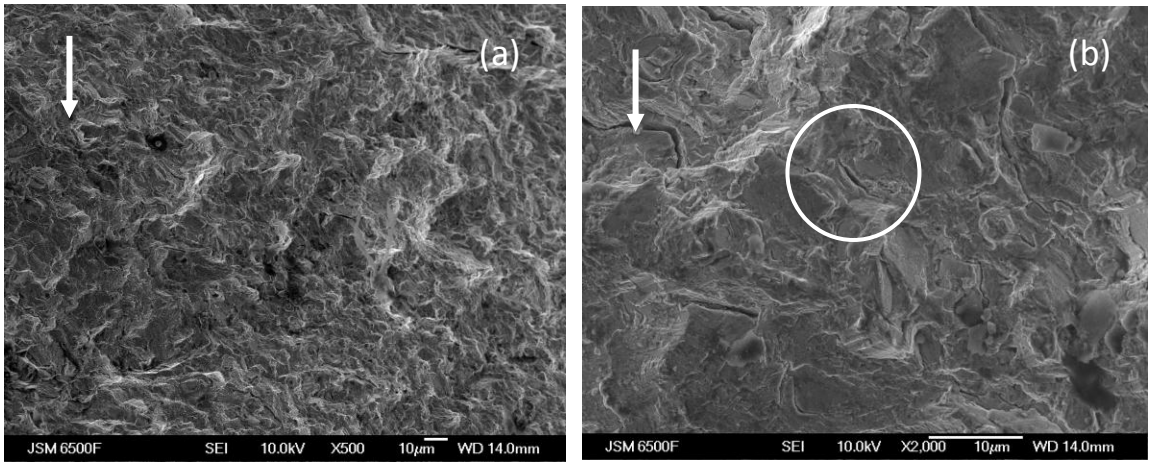

Figure 5-43: Fracture surface of U720Li C&W SENB tested at 300°C in vacuum, in terraced region at c=7.78mm and an estimated ΔK≈50MPa √m (Arrow indicates crack growth direction, circle shows secondary cracks) (a) at low magnification showing stage II growth (b) at high magnification showing large secondary cracks

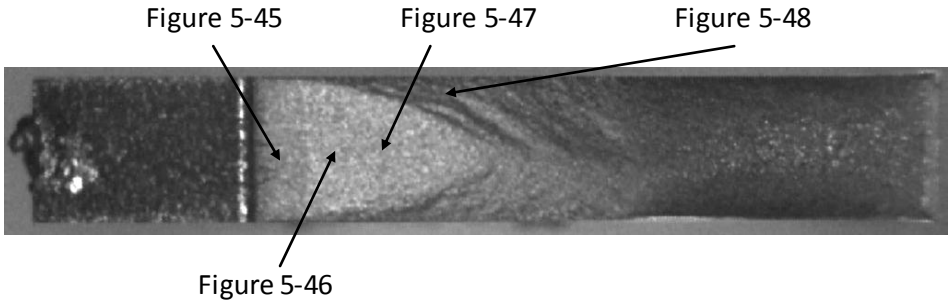

Figure 5-44: Fracture surface of thin SENB (U720Li C&W) tested at 300°C in air, showing locations of SEM fractography

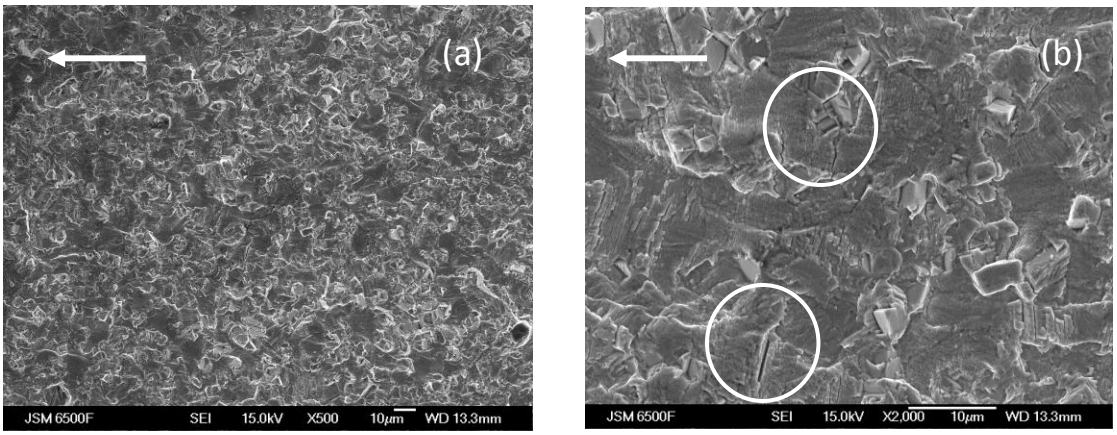

Figure 5-45: Fracture surface of thin SENB (U720Li C&W) tested at 300°C in air, in the centre of the sample in the precrack region at *c*=3.5mm and an estimated $\Delta K \approx 20$MPa $\sqrt{m}$ (Arrow indicates crack growth direction, circle shows secondary cracks) (a) at low magnification showing stage II growth (b) at high magnification showing slip traces and secondary cracks

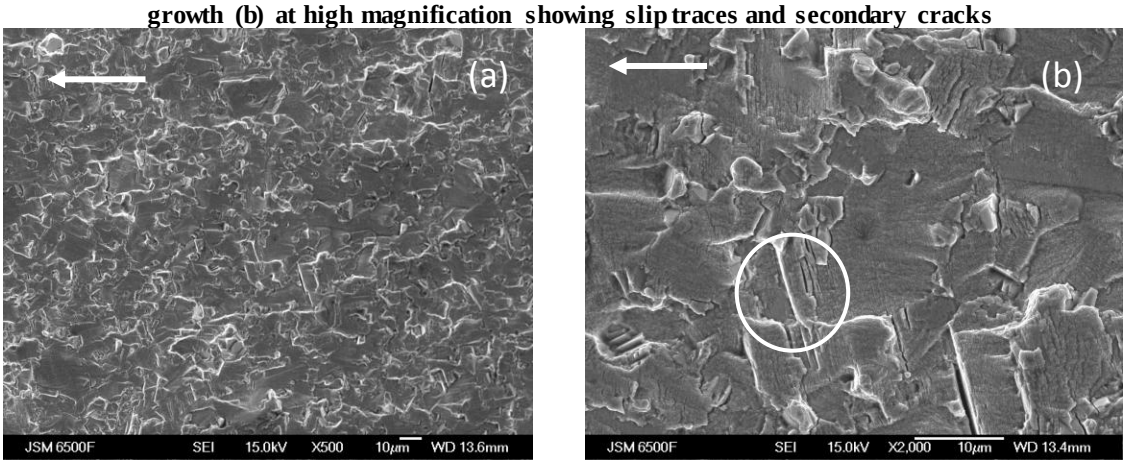

Figure 5-46: Fracture surface of thin SENB (U720Li C&W) tested at 300°C in air, in the centre of the sample at *c*=4.55mm and an estimated $\Delta K \approx 20$MPa $\sqrt{m}$ (Arrow indicates crack growth direction, circle shows secondary cracks) (a) at low magnification showing stage II growth (b) at high magnification showing slip traces and large secondary cracks

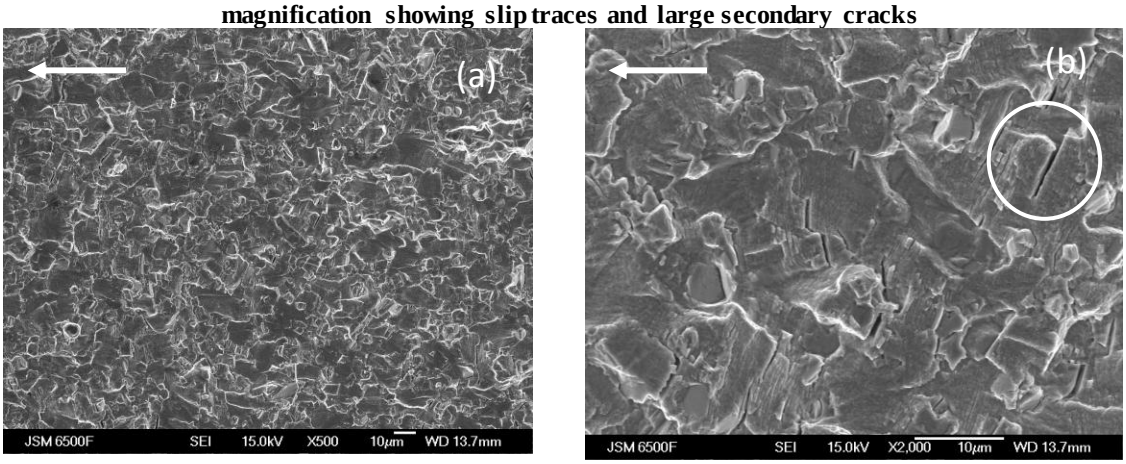

Figure 5-47: Fracture surface of thin SENB (U720Li C&W) tested at 300°C in air, in the centre of the sample at *c*=5.561mm and an estimated $\Delta K \approx 25$MPa $\sqrt{m}$ (Arrow indicates crack growth direction, circle shows secondary cracks) (a) at low magnification showing stage II growth (b) at high magnification showing slip traces and secondary cracks

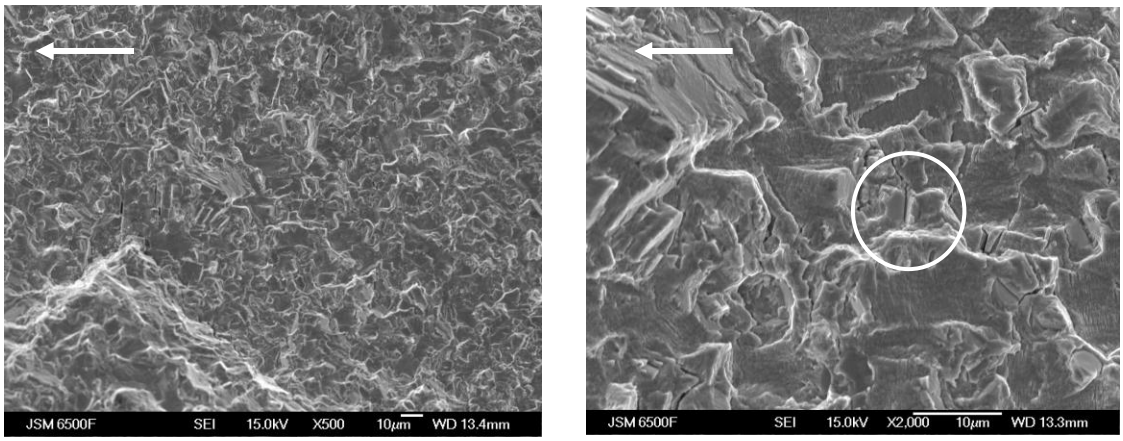

Figure 5-48: Fracture surface of thin SENB (U720Li C&W) tested at 300°C in air, in terraced region at c=6.282mm and an estimated ΔK≈30MPa √m (Arrow indicates crack growth direction, circle shows secondary cracks) (a) at low magnification showing stage II growth (b) at high magnification showing secondary cracks

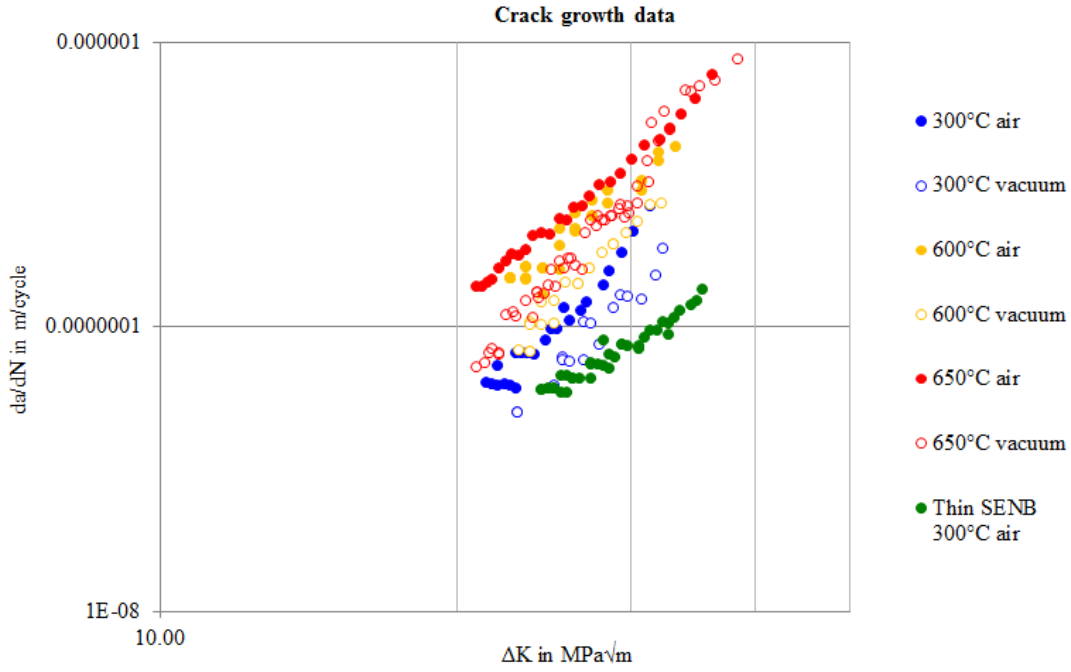

Figure 5-49: da/dN vs. ΔK curve for U720Li C&W at 300, 600 and 650°C in air and vacuum from SENB thick samples and 300°C in air from thin SENB sample

5.3 Measurements of onset of deflection for comparison

An important factor in comparing different tests is to determine when the deflection firstly appears and also how large the deflected terraces are. For different sample sizes and types, different notch sizes and initial ΔK_i levels, a consistent measure is proposed to be the onset ΔK level of the first terrace.

At first instance the depth of the terraces can be measured using the Wild Macroscope M420 and plotted against the nominal ΔK level (for the corresponding crack length). The exact onset of terracing is somewhat subjective and it should also be noted that the plane stress region is expected to produce shear lips in conventional fatigue cracking [45], hence it is important to establish to what extent the shear crack growth is sustained beyond the expected plane stress plastic zone size. The onset of *sustained* deflected crack growth is thus proposed to be deflection beyond the expected plane stress plastic zone size (PZS).

The monotonic plastic zone size during fatigue can be calculated using a number of approximations: Rice, Irwin and Dugdale, as described in Chapter 2.2.4.

They all take the same general form:

$$r_p = \alpha \left(\frac{K_{\max}}{\sigma_y} \right)^2 \qquad \text{Equation 5-1}$$

where the value of α varies between $1/2\pi$ for Rice, $1/\pi$ for Irwin and $\pi/8$ for Dugdale for the plane stress region.

Thus it can be seen that the Rice approximation is the lower bound and the Dugdale approximation is the upper bound beyond which no plane stress effect is expected. Hence the onset of terracing can be identified as being between where the terrace extends beyond the monotonic plane stress PZS after the Rice approximation and monotonic plane stress PZS after the Dugdale approximation. Yield stress values for U720Li C&W for the relevant test temperatures have been supplied by Rolls Royce plc. [93]

The fracture surfaces were measured for the CNB samples (for the U720Li C&W) and the depth of deflection has been mapped against the nominal ΔK value. The measurements for the CNB sample are shown in Figure 5-50 to Figure 5-55.

Beyond the Rice approximation, which is the most conservative plane stress PZS estimate, some deflection may still be expected as we may not be entirely out of the plane stress affected region, while beyond the Dugdale plane stress plastic zone size, which is the largest, the crack is expected to grow under plane strain conditions. Any deflection here is certainly anomalous and indicative of the onset of the macroscopic sustained deflected crack growth, which is a key component of the 'teardrop cracking' phenomenon. In this work a working definition of the onset of anomalous macroscopic deflection is proposed: if a deflection extends further than both measures of plane stress plastic zone size, it is clearly an anomalous crack deflection. Below the Dugdale PZS, it could still be defined as expected deflection (or shear lip formation) due to plane stress conditions.

To allow a more systematic assessment of which samples are exhibiting sustained macroscopic deflection, a template was created based on this definition of the onset of terracing which allows the user to input test conditions and specimen geometry to delineate the plastic zones on a fracture surface, thus allowing the analysis of fracture surfaces to determine whether they exhibit sustained deflected crack growth. An Excel spreadsheet was created that calculates the monotonic plane stress plastic zone size (PZS) for the lower bound (Rice PZS) and upper bound (Dugdale PZS), it also maps out the specimen fracture surface outline. The following inputs are used: the width and breadth of the sample, the size of the notch, the initial ΔK_i, R-ratio and the yield strength of the material at the test temperature of interest. An image of the fracture surface is added at the appropriate size to compare the observed deflection to the estimated PZS. This provides a quick reference as to how much of the deflection is as expected (occurring within a plane stress dominated region) and whether it can be identified as sustained macroscopic deflection.

All deflected crack terraces can be compared in this way with the expected plane stress plastic zone size mapped onto each fracture surface. The variation of ΔK-onset for CNB fracture surface for U720Li C&W are shown in Figure 5-56 and for the thick SENB in Figure 5-57, for both at 300, 600 and 650°C in air and vacuum, where the expected plane stress plastic zone sizes have been overlaid across the fracture surfaces. From those the range of onset ΔK of this deflected crack growth have been read and are shown in Table 11 for all the U720Li C&W tested for each test condition and for both specimen types SENB and CNB.

For the tests carried out in air, the results for the two specimen types are consistent. When comparing the behaviour of U720Li C&W tested at different temperatures in air, an increase in temperature results in both an increase in onset ΔK and the range over which it occurs. At 600 and 650°C it should be noted that the upper value (derived from the Dugdale comparison) is close to expected K-levels near failure and/or plastic collapse in this sample/material combination, where significant shear lips would be expected anyway. Hence we do not consider this case as showing evidence of anomalous deflection, as there is a large variation between the Rice and the Dugdale values of onset. This is also in agreement with the observations in previous work, where the effect was not seen above 600°C in air. [4]

When tested in vacuum the onset of terracing occurs at significantly higher ΔK in the CNB (compared to the equivalent air case) however there is little variation with temperature. So it appears that the sustained deflected crack growth is retained by vacuum conditions even at higher temperatures such as 650°C, in vacuum the deflection also goes significantly deeper into the bulk. It is notable that ΔK onsets change with temperature and environment in the SENB in a different way to that observed for the CNB. In the SENB case the vacuum condition (for all temperatures) did not cause the onset to occur later, but at a similar ΔK as in the air tests at 300°C.

Temperature and environment	ΔK (MPa√m) at				Temperature and environment	ΔK (MPa√m) at			
	Lower bound (Rice PZS)		Upper bound (Dugdale PZS)			Lower bound (Rice PZS)		Upper bound (Dugdale PZS)	
300°C air	CNB	SENB	CNB	SENB	300°C vacuum	CNB	SENB	CNB	SENB
	25	22.5	28	26		33.5	21.5	35.5	24.5
600°C air	CNB	SENB	CNB	SENB	600°C vacuum	CNB	SENB	CNB	SENB
	26	27.5	53	-		31	22	38	25
650°C air	CNB	SENB	CNB	SENB	650°C vacuum	CNB	SENB	CNB	SENB
	34	31.5	57	-		33	22.5	35.5	24.5

Table 11: ΔK onset of terracing in U720Li C&W at 300, 600 and 650°C in air and vacuum

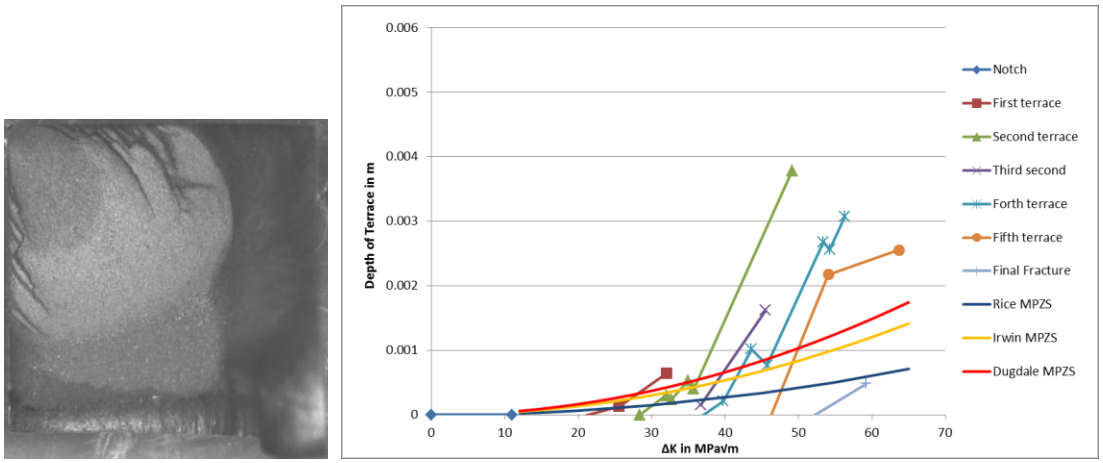

Figure 5-50: ΔK vs Depth of terrace map for U720Li C&W at 300°C in air 20Hz

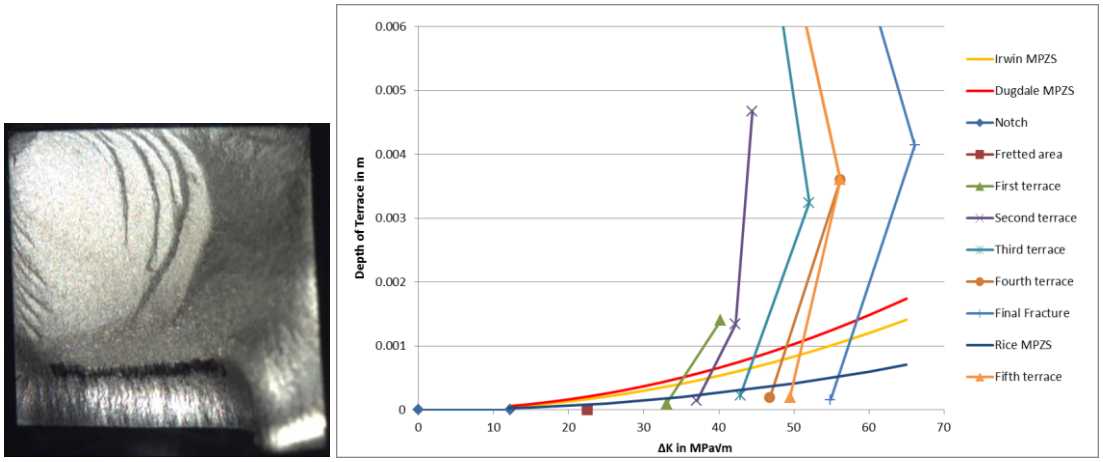

Figure 5-51: ΔK vs Depth of terrace map for U720Li C&W at 300°C in vac 20Hz

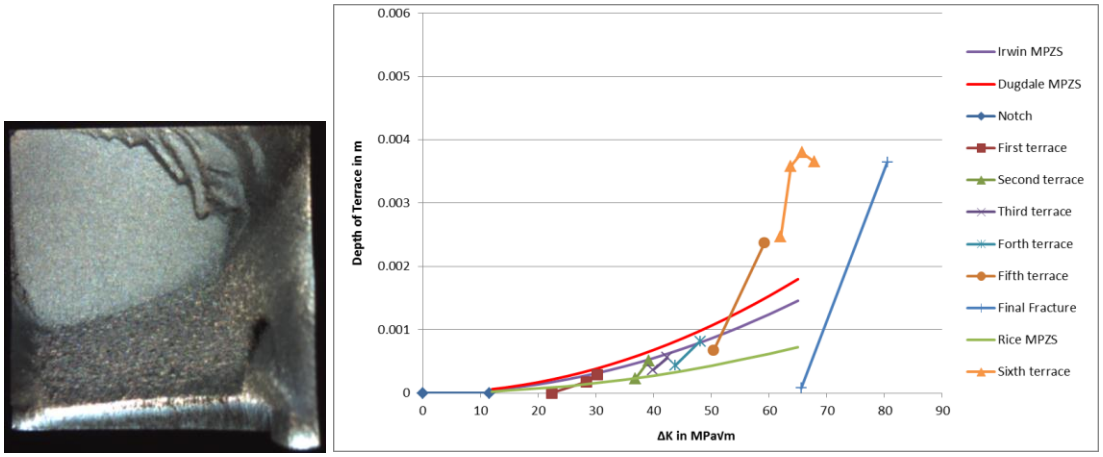

Figure 5-52: ΔK vs Depth of terrace map for U720Li C&W at 600°C in air 20Hz

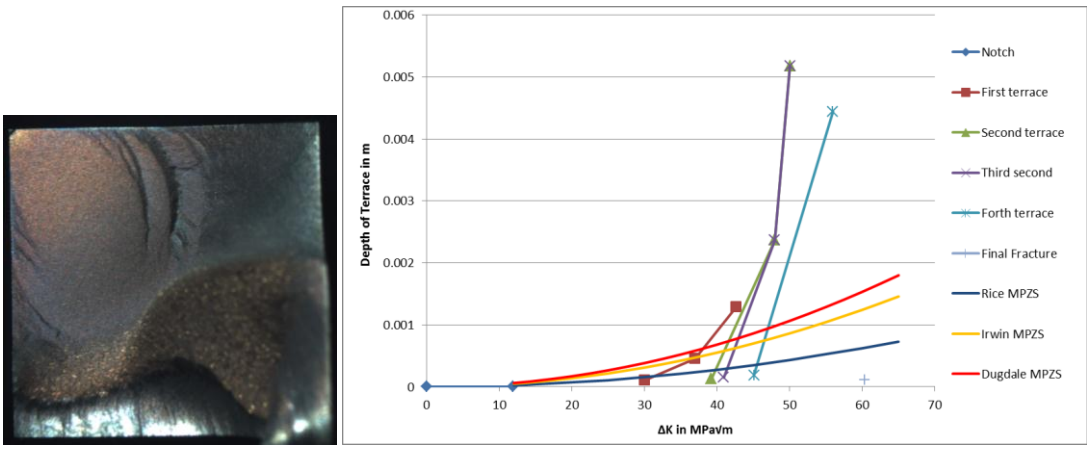

Figure 5-53: ΔK vs Depth of terrace map for U720Li C&W at 600°C in vac 20Hz

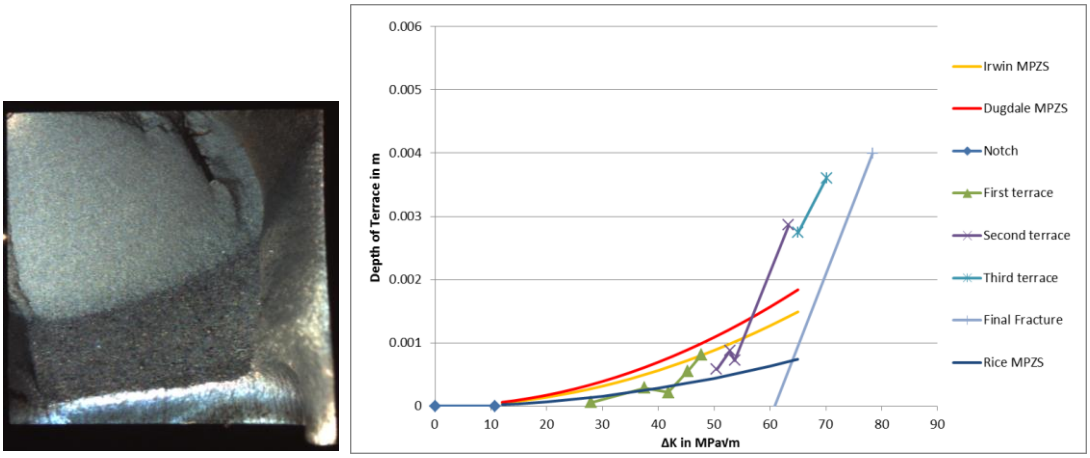

Figure 5-54: ΔK vs Depth of terrace map for U720Li C&W at 650°C in air 20Hz

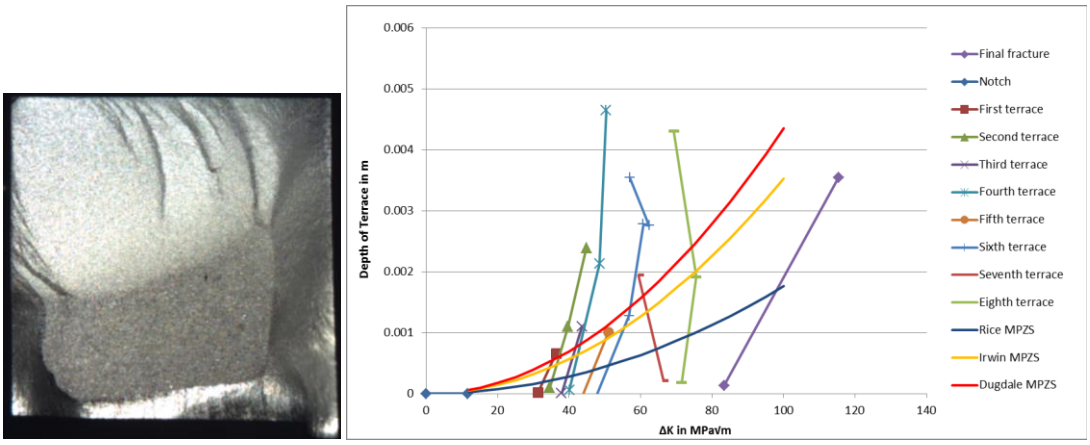

Figure 5-55: ΔK vs Depth of terrace map for U720Li C&W at 650°C in vac 20Hz

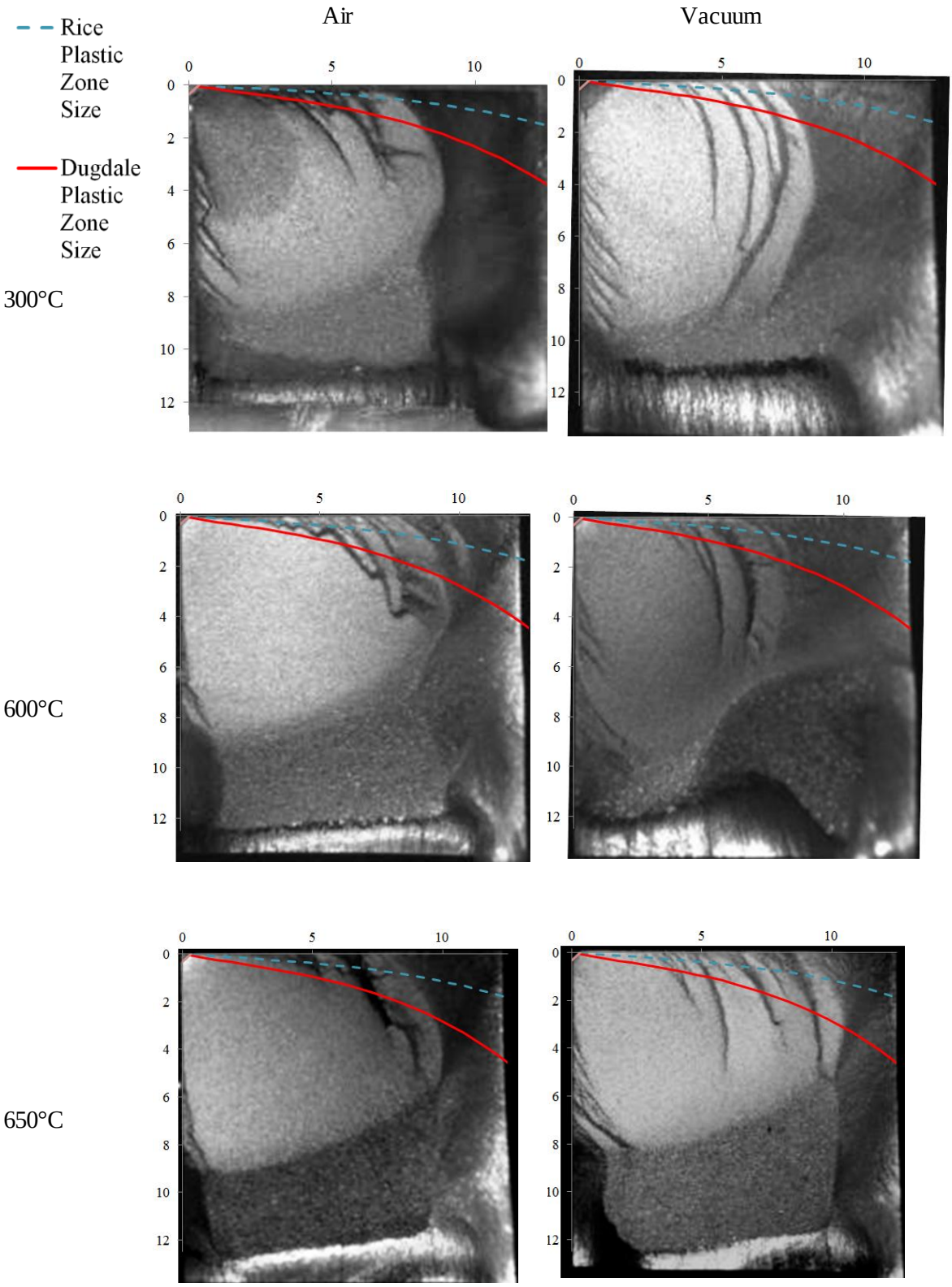

Figure 5-56: CNB samples showing Rice and Dugdale plastic zone (Scale in mm)

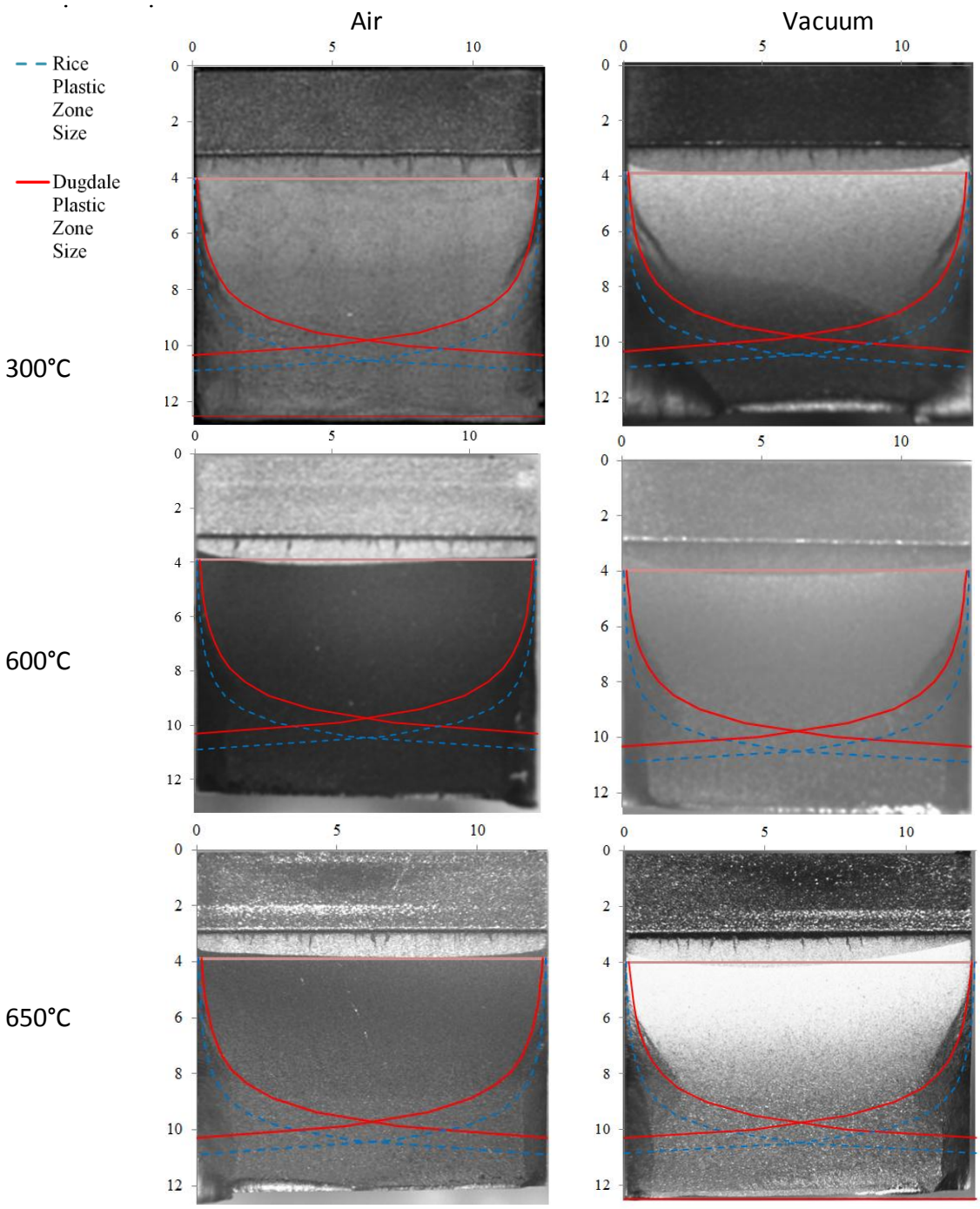

Figure 5-57: SENB samples showing Rice and Dugdale Plastic zone sizes (Scale in mm)

5.4 Profilometry

Measures of the macroscopic crack deflections were also needed, to further analyse the crack path. Three different methods to create a 3D profile of a fracture surface have been compared.

5.4.1 TaiCaan

A 3D map of the fracture surface of the CNB sample of U720Li PM FG with ΔK_i=17.7MPa√m was created with 601x601 surface points. Figure 5-58 shows the 3D map from different perspectives.

Particular areas of interest have been looked at in detail. Figure 5-59 shows the profile of the top surface and indicates from where on the fracture surface it was taken. The terracing can be clearly observed. Figure 5-60 shows the profile of the front surface and indicates from where on the fracture surface it was taken. Figure 5-61 shows the profile through the diagonal and indicates from where on the fracture surface it was taken.

5.4.2 Alicona MeX

A 3D map of the fracture surface of U720Li PM FG CNB sample with ΔK_i=17.7MPa√m tested at 300°C in air has been created from SEM pictures (taken from -2, 0 and 2° angles) using Alicona MeX, which is shown in Figure 5-63. Another map is created using higher magnification SEM pictures from the same location, shown in Figure 5-64. The position of the maps is shown in Figure 5-62. A 2D profile can be measured along any line on the map, one example is shown in Figure 5-65.

5.4.3 Alicona Infinite Focus

The fracture surface of U720Li PM FG CNB sample tested with ΔK_i=17.7MPa√m at 300°C in air has also been scanned with Alicona Infinite Focus. A 3D view of the fracture surface is shown in Figure 5-66. A more detailed view of the terraces is shown in Figure 5-67. A 2D profile can be measured in any line in the map, one example is shown in Figure 5-68. Overall the Infinite Focus system shows a better balance between resolution as compared to the TaiCaan system and scanning sufficient area to describe the macroscopic crack deflection that needs to be characterised, cf. MeX software applied to SEM images.

Therefore further profilometry has been carried out with this method on the U720Li C&W CNB samples tested at 300°C air, as shown in Figure 5-69, and 300°C vacuum, as shown in Figure 5-71 (with ΔK_i=12MPa√m). 2D measurements on the edge of the fracture surface of the 300°C air test have been carried out and are shown in Figure 5-70.

The surface of the thick U720Li C&W SENB sample (300°C air with ΔK_i=20MPa√m) has been mapped as well. The 3D map of the fracture surface is shown in Figure 5-72. Figure 5-73 shows one example of a 2D profile of the terraced region from which angles could be measured. Measurements have been carried out for a number of 2D profiles in the terraced regions on both sides of the sample; the range of tilt angles is approximately between 30 and 50°.

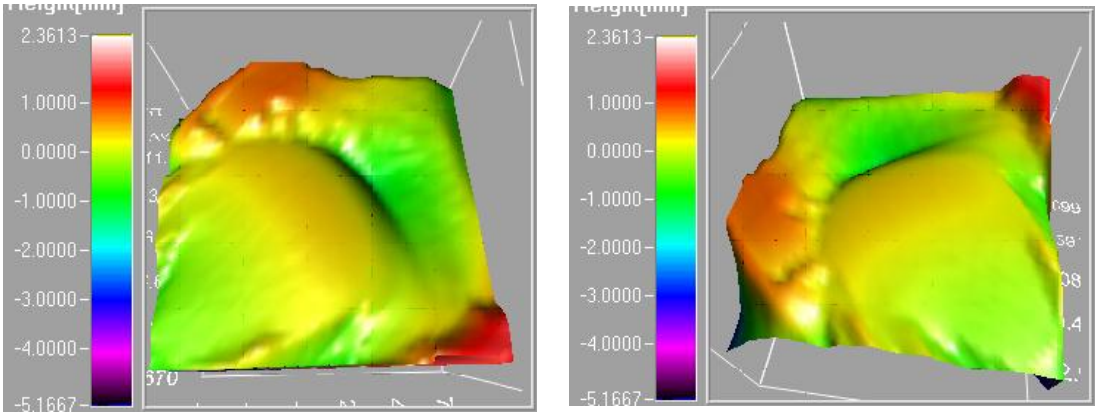

Figure 5-58: Profile of Fracture Surface of U720Li PM FG with ΔK_i=17.7MPa√m from different perspectives

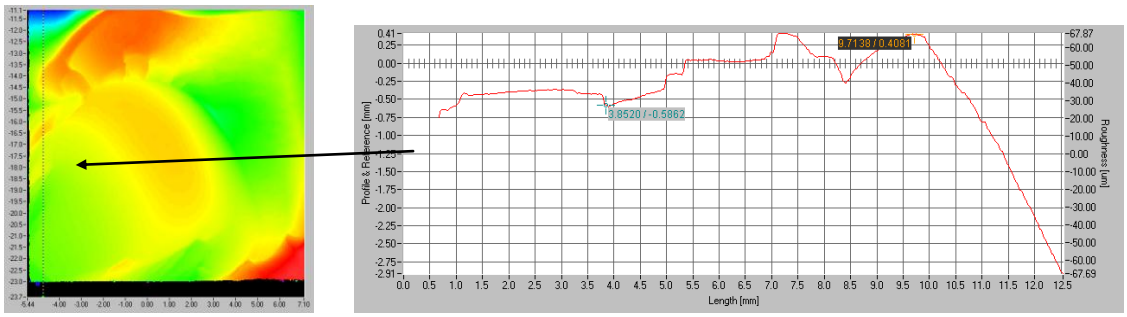

Figure 5-59: 2D Profile of Fracture Surface of U720Li PM FG with ΔK_i=17.7MPa√m near the top surface of sample

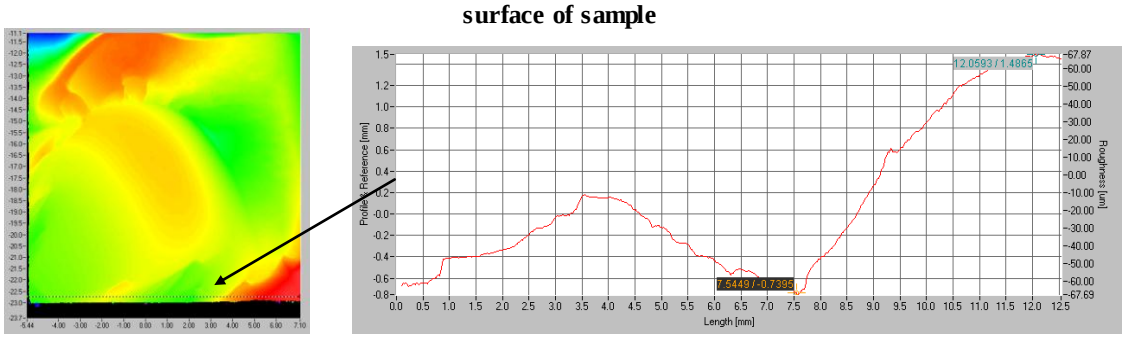

Figure 5-60: 2D Profile of Fracture Surface of U720Li PM FG with ΔK_i=17.7MPa√m near the side surface of sample

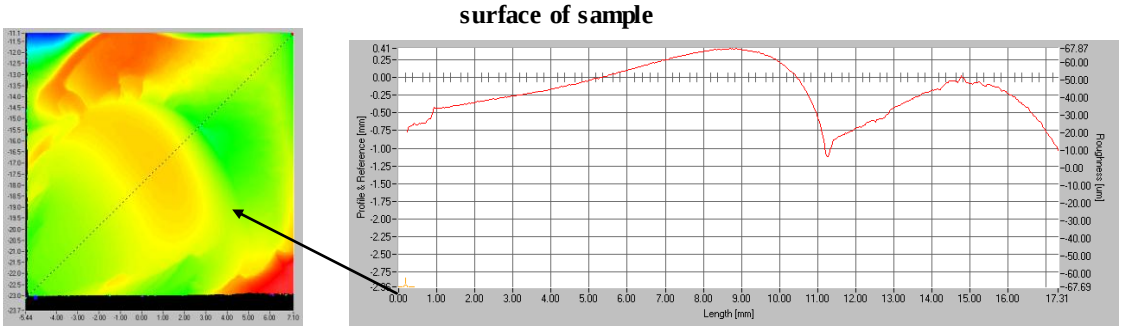

Figure 5-61: 2D Profile of Fracture Surface of U720Li PM FG with ΔK_i=17.7MPa√m diagonally through sample in crack growth direction

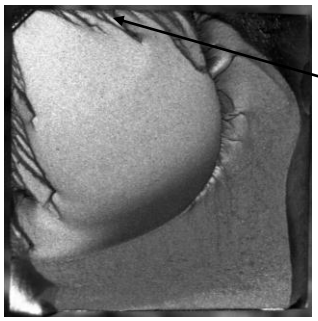

Figure 5-62: Fracture surface of U720Li PM FG with ΔK_i=17.7MPa$\sqrt{m}$ at 300°C in air

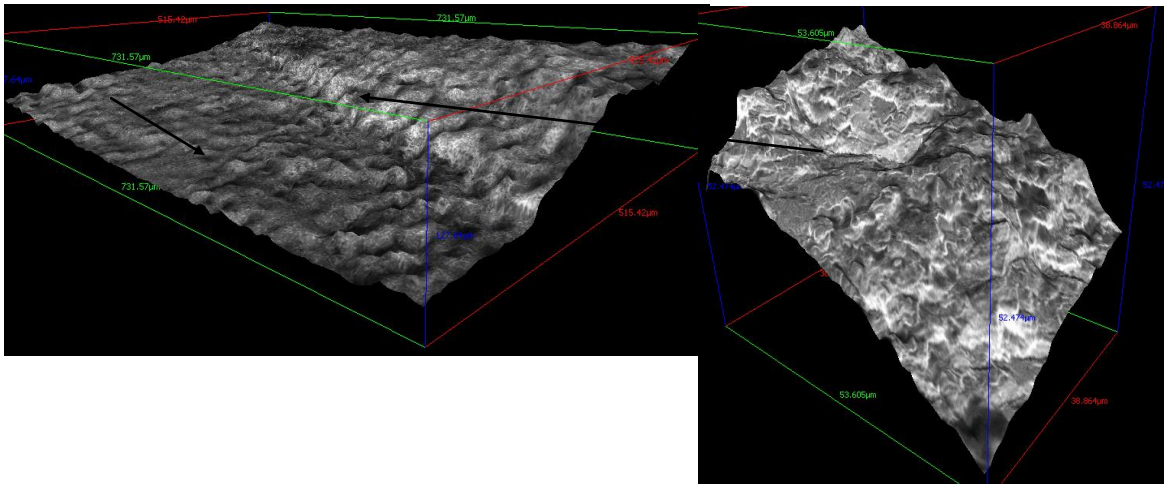

Figure 5-63: Fracture Surface of U720Li PM FG with ΔK_i=17.7MPa$\sqrt{m}$ at 300°C in air with Alicona MeX

Figure 5-64: Fracture Surface of U720Li PM FG with ΔK_i=17.7MPa$\sqrt{m}$ at 300°C in air with Alicona MeX (higher magnification)

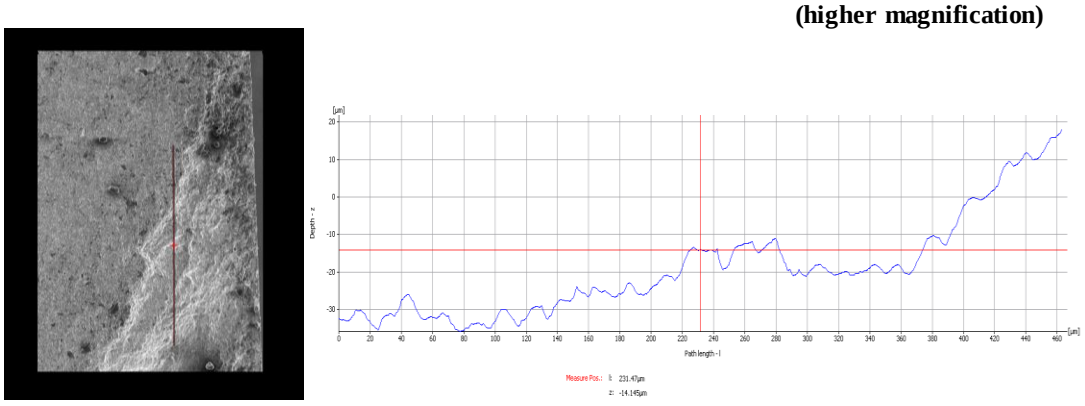

Figure 5-65: 2D Profile of Fracture Surface U720Li PM FG with ΔK_i=17.7MPa$\sqrt{m}$ near the side surface of sample with Alicona MeX

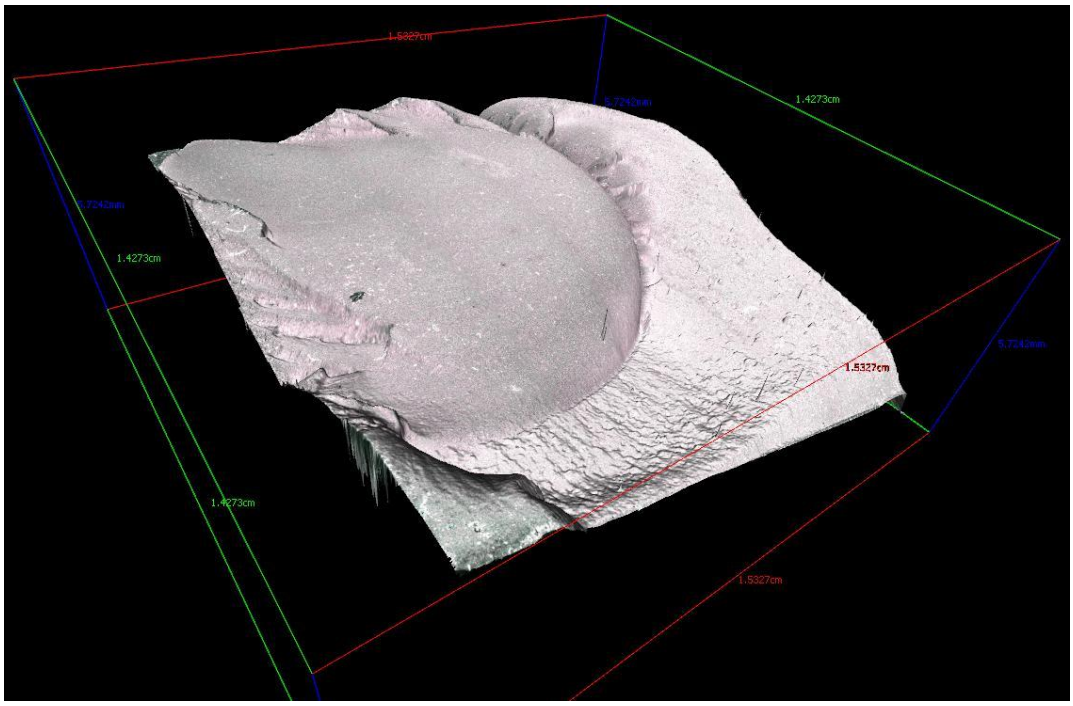

Figure 5-66: Fracture Surface of U720Li PM FG with ΔK_i=17.7MPa√m at 300°C in air with Alicona Infinite Focus

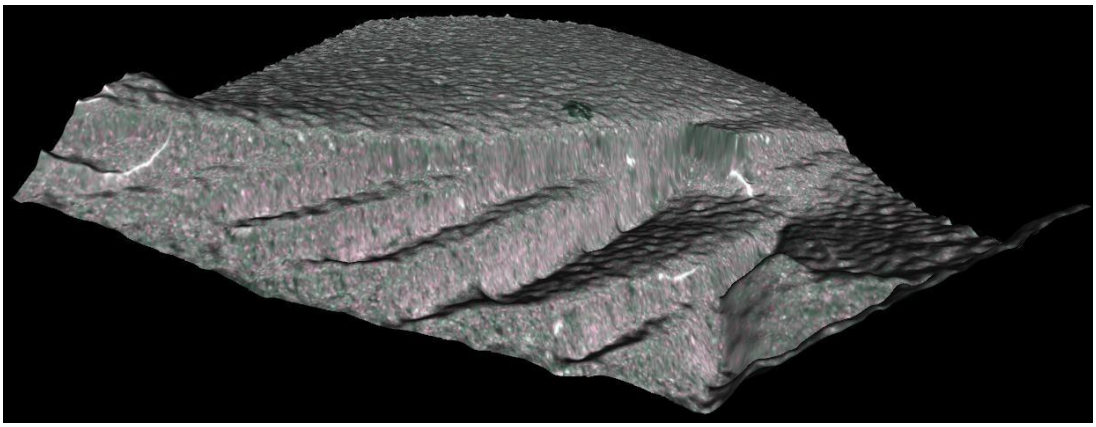

Figure 5-67: Fracture Surface of U720Li PM FG with ΔK_i=17.7MPa√m at 300°C in air with Alicona Infinite Focus in detailed view

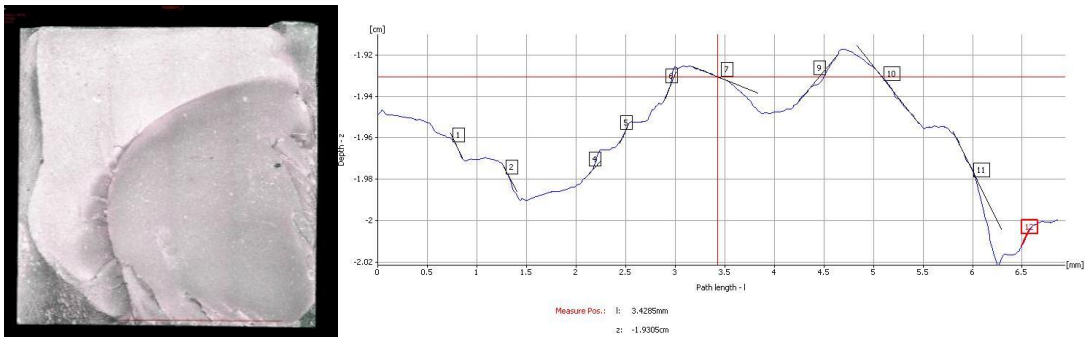

Figure 5-68: 2D Profile of Fracture Surface of U720Li PM FG with ΔK_i=17.7MPa√m at 300°C in air near the side surface of sample with Alicona Infinite Focus

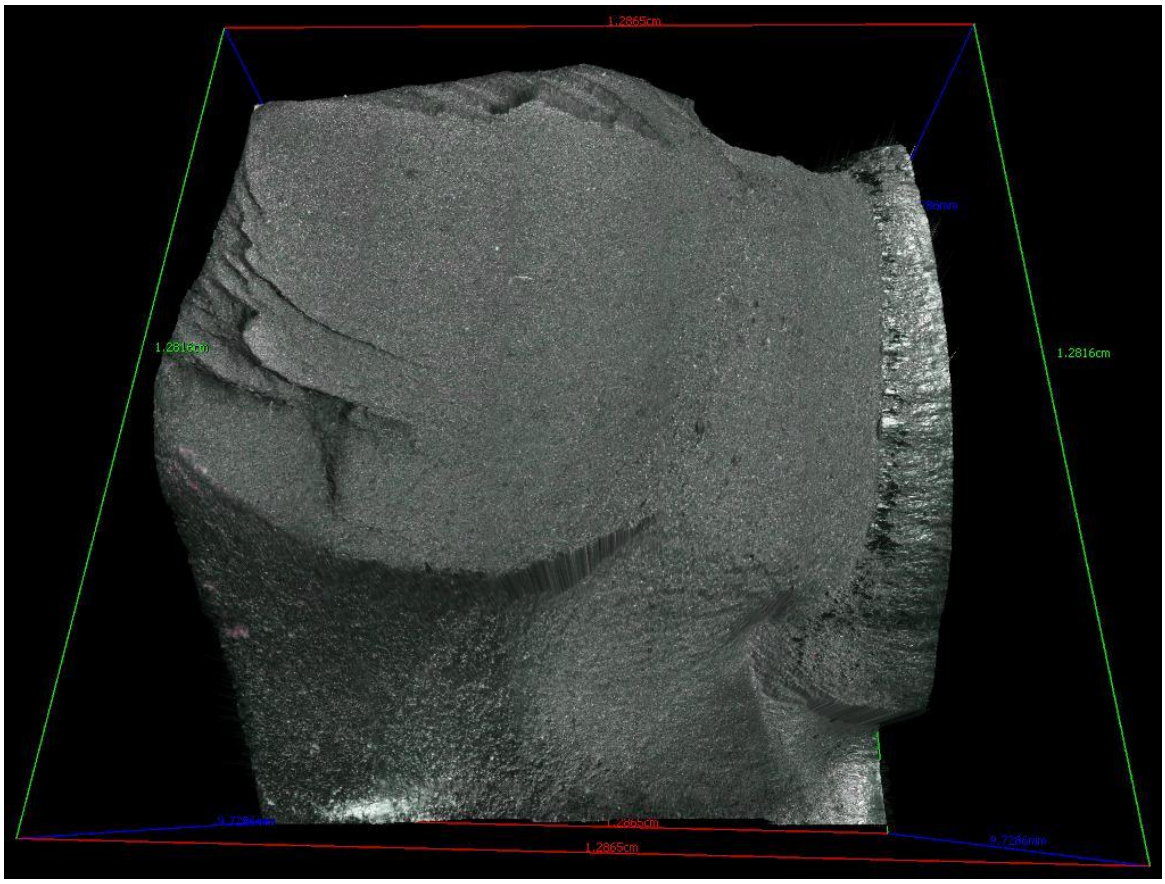

Figure 5-69: Fracture Surface of U720Li C&W with ΔK_i=12 MPa√m at 300°C in air with Alicona Infinite Focus

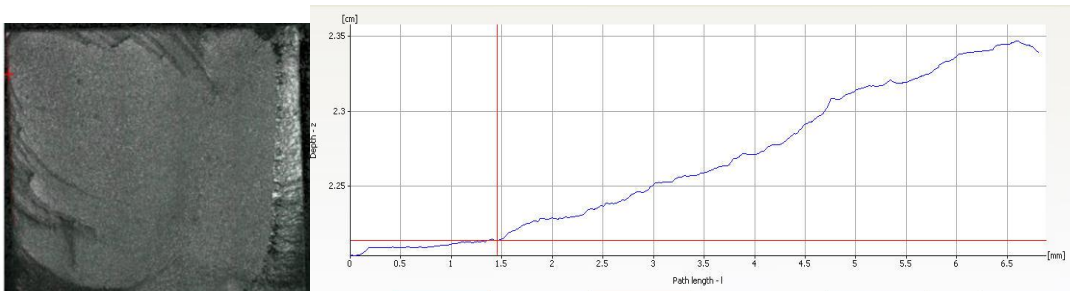

Figure 5-70: 2D Profile of Fracture Surface of U720Li C&W with ΔK_i=12MPa√m at 300°C in air near the top surface of sample with Alicona Infinite Focus

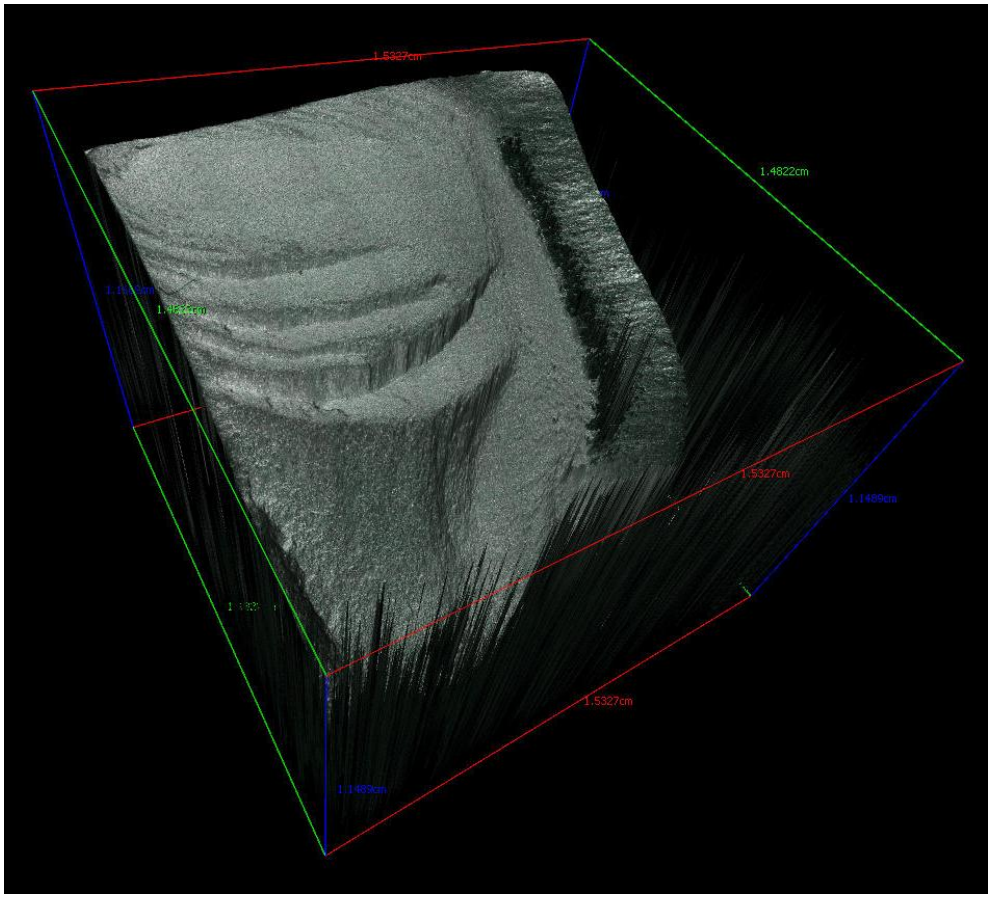

Figure 5-71: Fracture Surface of U720Li C&W with ΔK_i=12 MPa√m at 300°C in vacuum with Alicona Infinite Focus

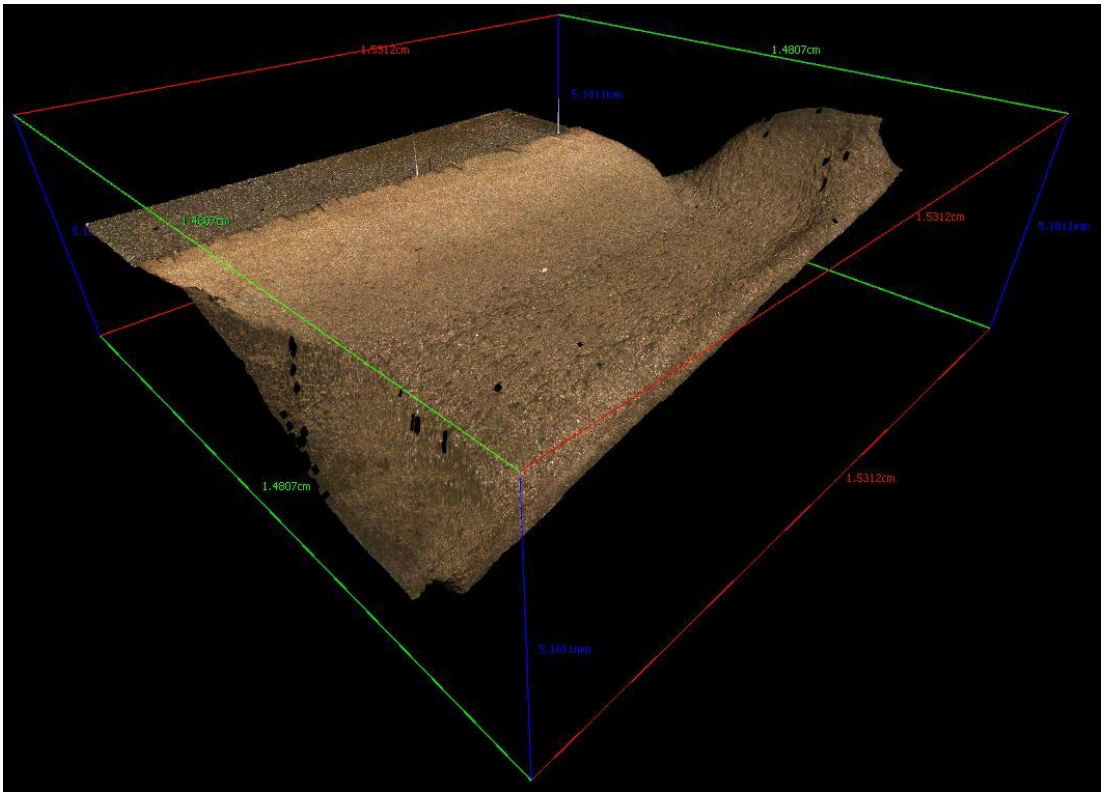

Figure 5-72: Fracture Surface of thick SENB U720Li PM FG at 300°C in air ΔK_i=20MPa√m with Alicona Infinite Focus

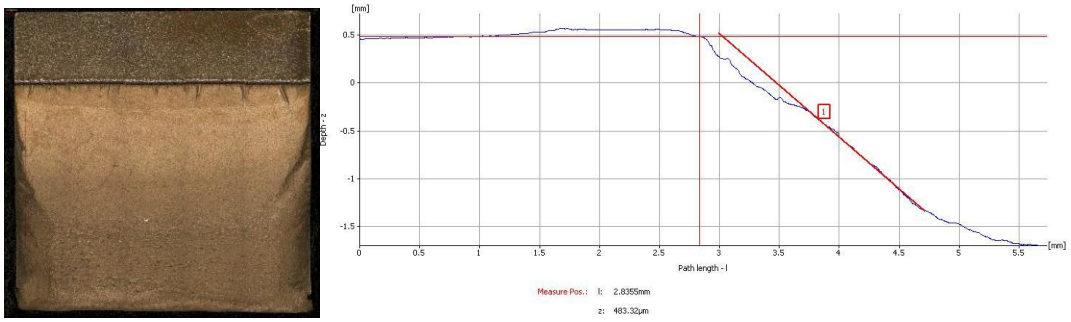

Figure 5-73: 2D Profile of Fracture Surface of U720Li C&W SENB with ΔK_i=20MPa√m at 300°C in air near the surface of sample with Alicona Infinite Focus

5.5 Further analysis of secondary cracks

The surfaces of a number of fractured samples have been polished, as described in the metallography section 3.2, to reveal more detail of the large secondary cracks. These have been observed in the SEM.

Figure 5-74 shows the largest secondary crack seen in the SENB sample tested at 300°C in air, which had been nickelplated before mounting for edge retention. The large secondary crack continuing from the shear terrace bifurcates and one crack tip continues in the shear direction, while the other continues approximately in the opening direction. Etching with nimonic etch for 15 seconds has been carried out on this SENB sample as shown in Figure 5-75 . This reveals the secondary crack can be observed to grow between some primary γ', but then continues to grow through a larger γ grain. It bifurcates in this grain and then stops. This surface observation does not indicate that the crack path follows any specific microstructural features, and there is no clear evidence of a preference for either intergranular failure, γ' decohesion or transgranular or slip-band dominated crack growth. It should be noted this is only a surface observation.

Some smaller cracks in this sample have also been observed. Figure 5-76 shows a very small crack that arrests at some primary γ'. Figure 5-77 shows a secondary crack growing along what appears to be a slip band. Figure 5-78 shows a crack that grows between a number of primary γ'.

Some smaller secondary cracks could be observed in the CNB 300°C in vacuum, Figure 5-79 shows the largest of the secondary cracks, which turns back in the mode I direction, and then bifurcates in both mode I and II direction.

A large secondary crack has been observed in CNB U720Li C&W 300°C in air as shown in Figure 5-80. This sample has been studied in further detail by FIB tomography.

It would be useful to be able to assess more completely the crack tip growth mechanisms of such deflected cracks over a more representative area than revealed by a simple surface observation, and to this end the focussed ion beam (FIB) serial sectioning and electron back scatter diffraction (EBSD) data collection have been used on one of these secondary crack tips (from the U720Li C&W CNB sample tested at 300°C in air) to build up a 3D reconstruction of the crack-tip region.

Moreover some TEM has been carried out just ahead of other secondary cracks in this sample.

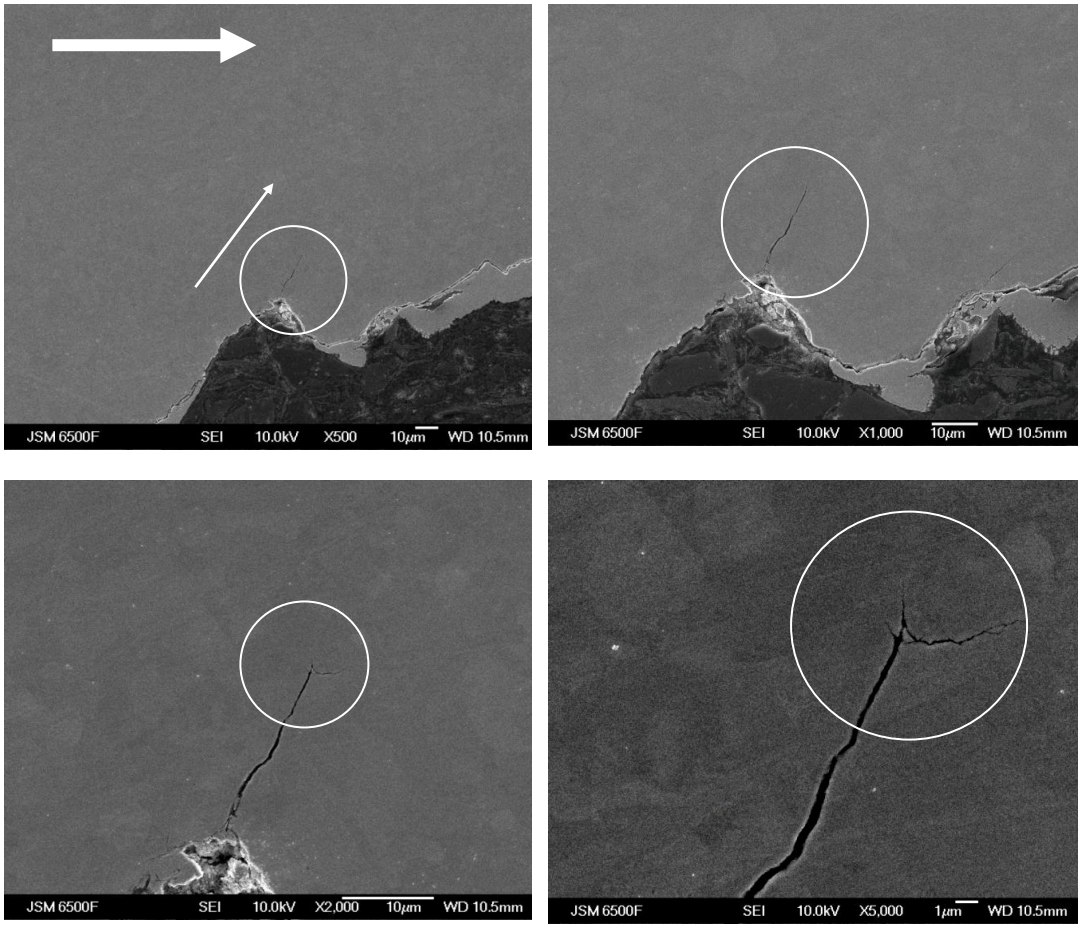

Figure 5-74: Secondary crack in SENB 300°C air sample at crack length a=5.7mm and a ΔK≈29.3MPa√m at different magnifications, bifurcates before arresting (Circle shows the crack tip, large arrow indicates overall crack growth direction, small arrow indicates (shear) direction of secondary crack)

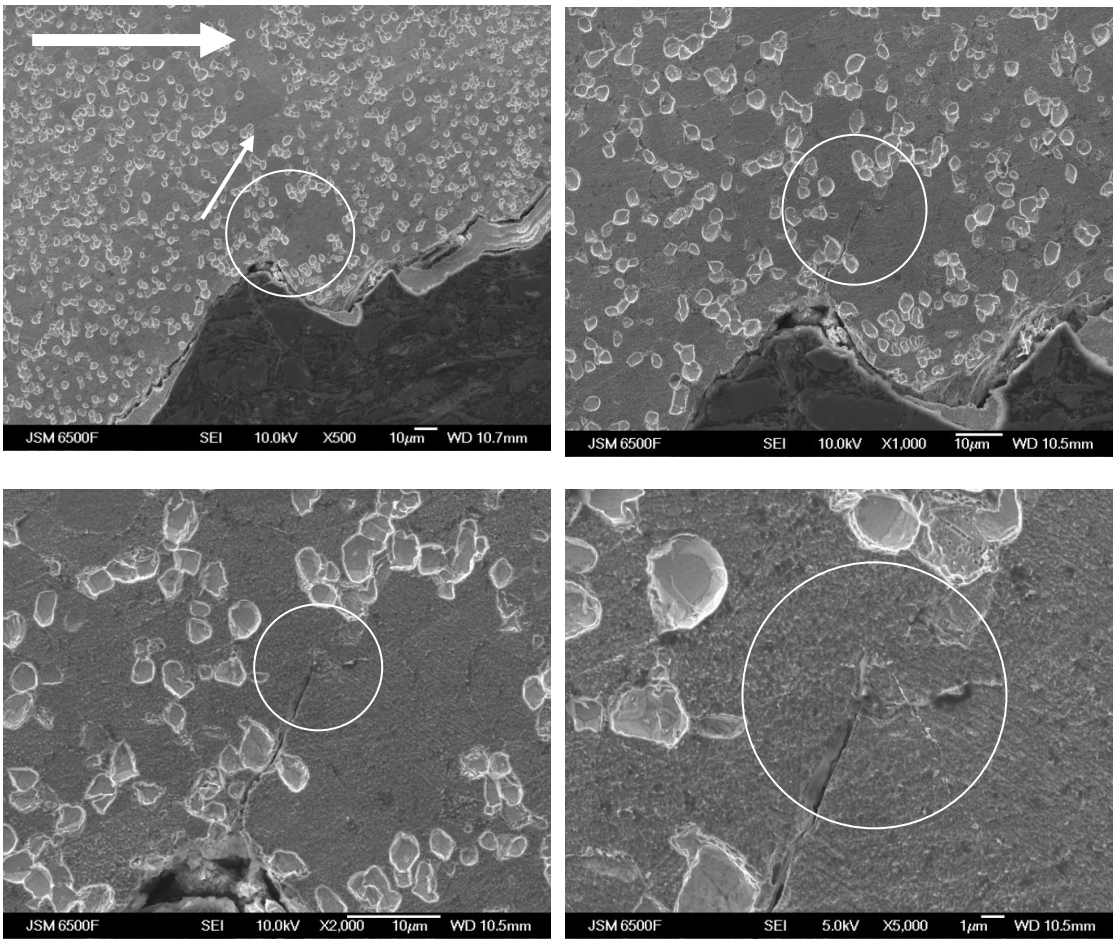

Figure 5-75: Secondary crack in SENB 300°C air sample etched 15 seconds with nimonic etch showing primary γ′ at crack length a=5.7mm and a ΔK≈29.3MPa$\sqrt{m}$ at different magnifications. The crack is growing along several primary γ′ and inside a γ grain, where it bifurcates and arrests (Circle shows the crack tip, large arrow indicates overall crack growth direction, small arrow indicates (shear) direction of secondary crack)

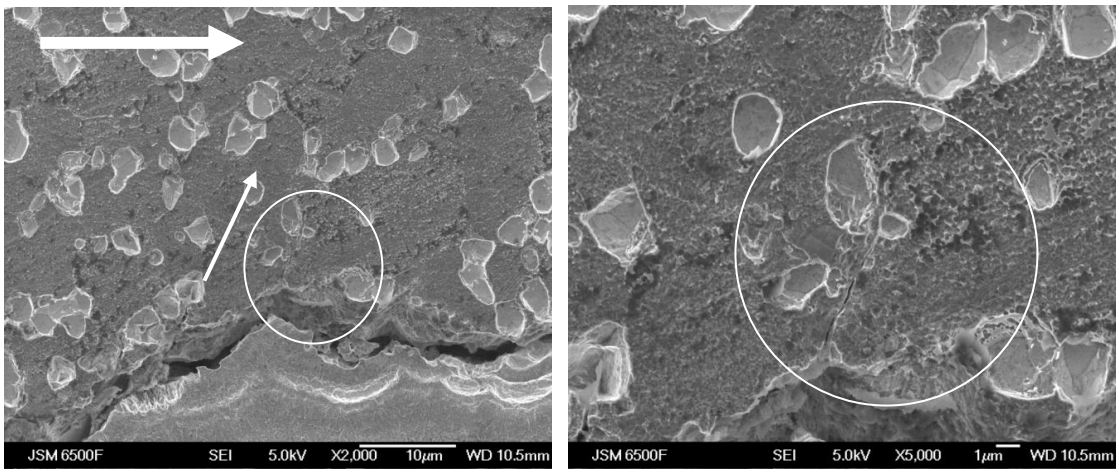

Figure 5-76: Secondary crack in SENB 300°C air sample etched 15 seconds with nimonic etch showing primary γ′ at crack length a=5.6mm and a ΔK≈28.1MPa√m at different magnifications. The crack is growing along several primary γ′ (possibly on a grain boundary) (Circle shows the crack tip, large arrow indicates overall crack growth direction, small arrow indicates (shear) direction of secondary crack)

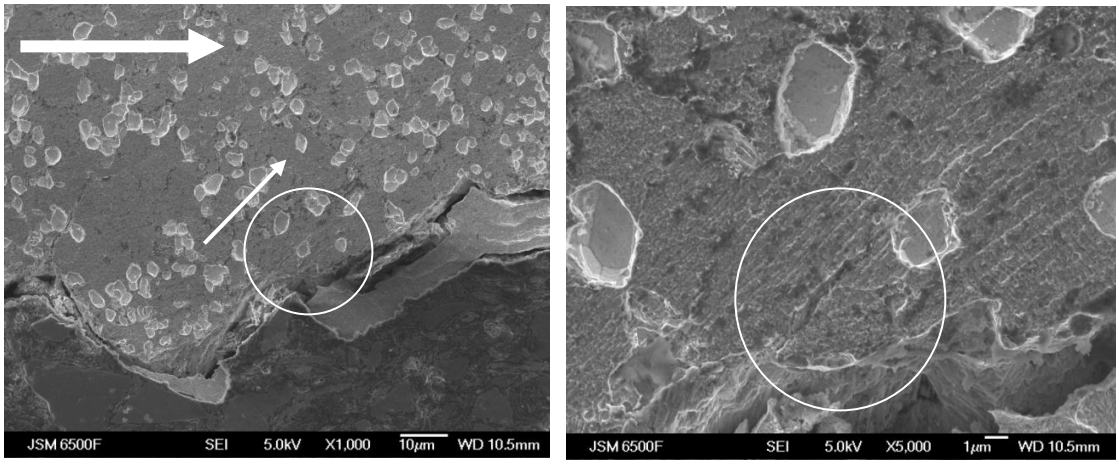

Figure 5-77: Secondary crack in SENB 300°C air sample etched 15 seconds with nimonic etch showing primary γ′ at crack length a=5.8mm and a ΔK≈29.6MPa√m at different magnifications. The crack seems to be growing along a slip band in a γ grain (Circle shows the crack tip, large arrow indicates overall crack growth direction, small arrow indicates (shear) direction of secondary crack)

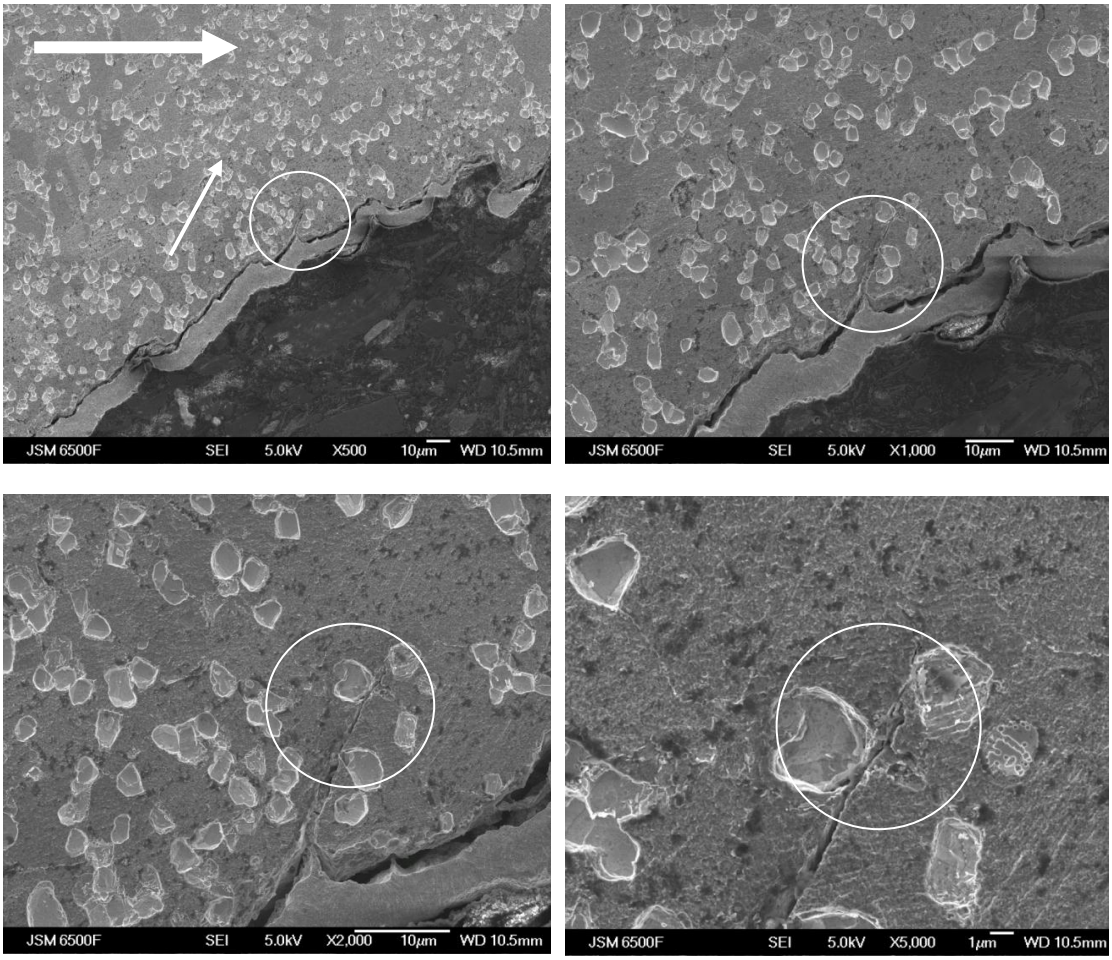

Figure 5-78: Secondary crack in SENB 300°C air sample etched 15 seconds with nimonic etch showing primary γ′ at crack length a=6mm and a $\Delta K \approx 31.8 MPa\sqrt{m}$ at different magnifications. The crack grows through a γ′ grain and arrests between 2 primary γ′ precipitates. (Circle shows the crack tip, large arrow indicates overall crack growth direction, small arrow indicates (shear) direction of secondary crack)

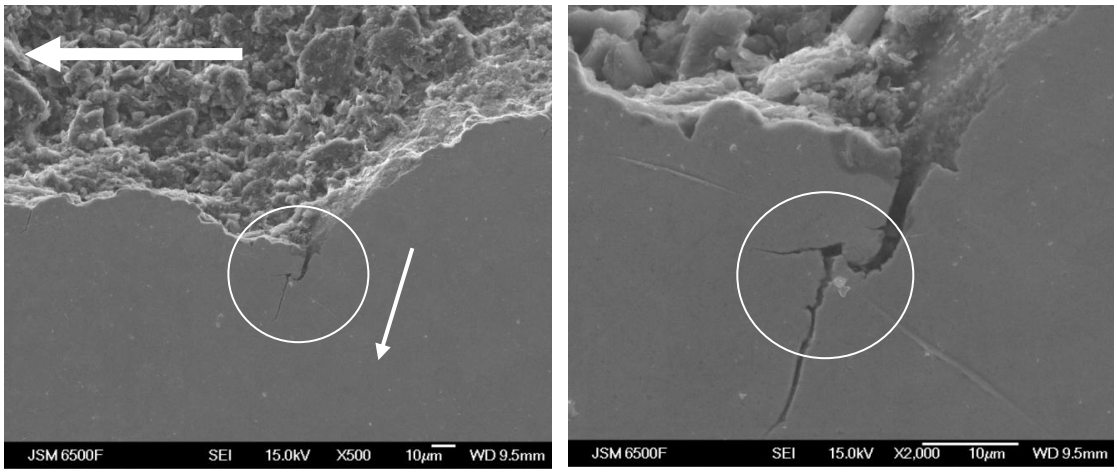

Figure 5-79: Secondary crack in SENB 300°C in vacuum sample at crack length a=5.7mm and a ΔK≈29.4MPa√m at different magnifications, growing in a shear direction, then turns in opening direction, before bifurcating. It continues growing in the shear direction for another 10µm before arresting. (Circle shows the bifurcation, large arrow indicates overall crack growth direction, small arrow indicates (shear) direction of secondary crack)

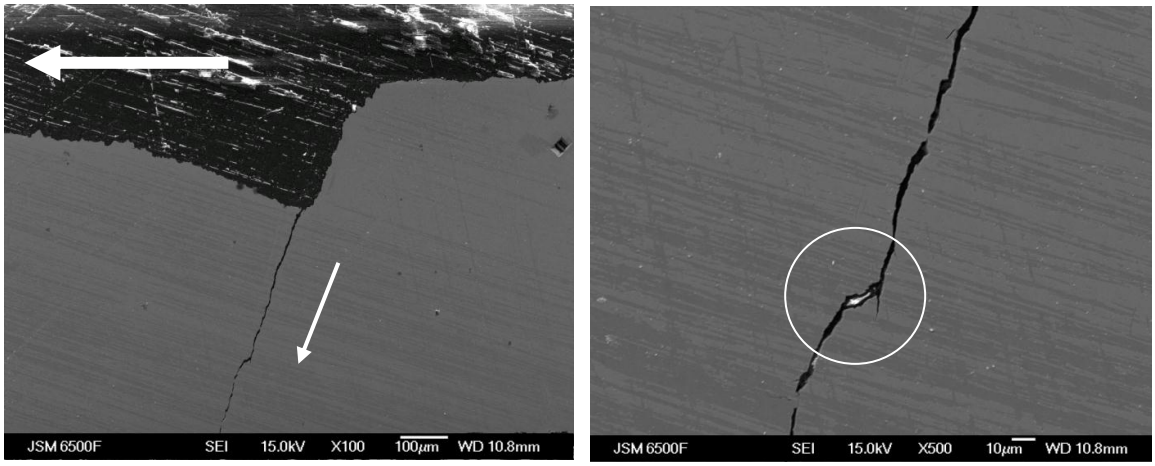

Figure 5-80: Secondary crack in CNB 300°C air sample at crack length a=6.4mm and a ΔK≈54.5MPa√m at different magnifications, growing in shear direction, including some small bifuration (Circle shows the birfuration, large arrow indicates overall crack growth direction, small arrow indicates (shear) direction of secondary crack)

5.6 More detailed micromechanistic Processes – 3D EBSD Assessment

To further assess the interaction of the microstructure with the deflected crack, the crack-tip region of an arrested secondary crack that has been examined further using the FIB/ EBSD and EDX serial sectioning and reconstruction approach, as described in some detail in section 4.3. This crack started from an approximate overall (mode I) crack length of ca. 5.1 mm, at which the nominal ΔK level is 45.6 MPa√m. The final assessed volume that has been removed for analysis is small – 40 x 40 x 30 μm. The secondary crack with the crack tip region removed for analysis is shown the SEM pictures in Figure 5-81.

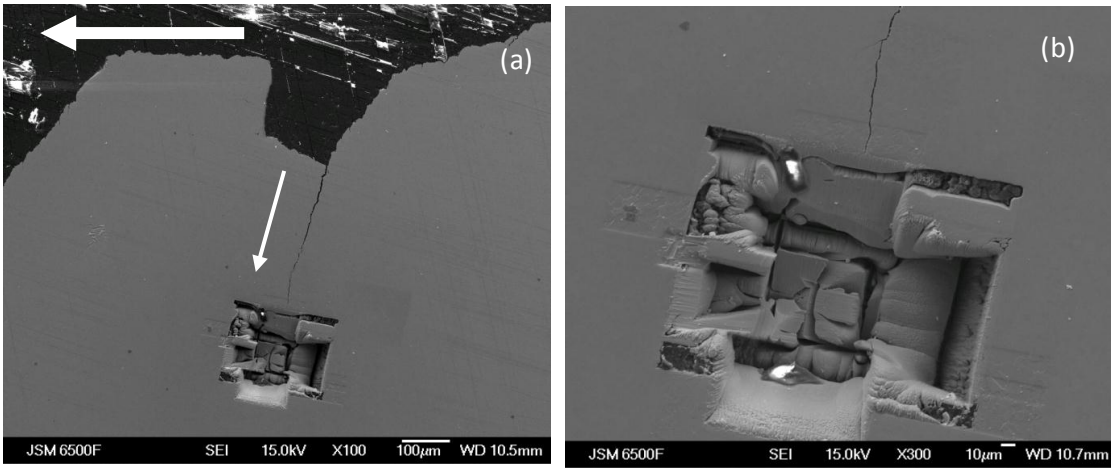

Figure 5-81: Location of secondary crack tip for 3D analysis in a CNB sample tested at 300°C air and ΔK_i=12 MPa√m at a overall crack length a=5.1 mm and nominal ΔK=45.6 MPa√m (a) overview (b) detailed view (Large arrow indicates overall crack growth direction, small arrow indicates (shear) direction of secondary crack)

A series of 2D slices were produced which can be viewed in a number of different modes: Image quality (IQ) (see Figure 5-82 for slice 1) can be used as a proxy for the crack itself, allowing the crack plane to be segmented out (Figure 5-83). Image quality is derived from the average intensity of the Hough peaks; good patterns tend to have intense strong peaks and hence high IQ.

The 3D reconstruction of the crack shows areas where it seems to deflect around grains, and other quite planar areas indicating failure along slip bands. The crack tip itself appears discontinuous, further evaluation of the microstructure ahead of the crack tip could identify what arrests the crack or what aids its propagation.

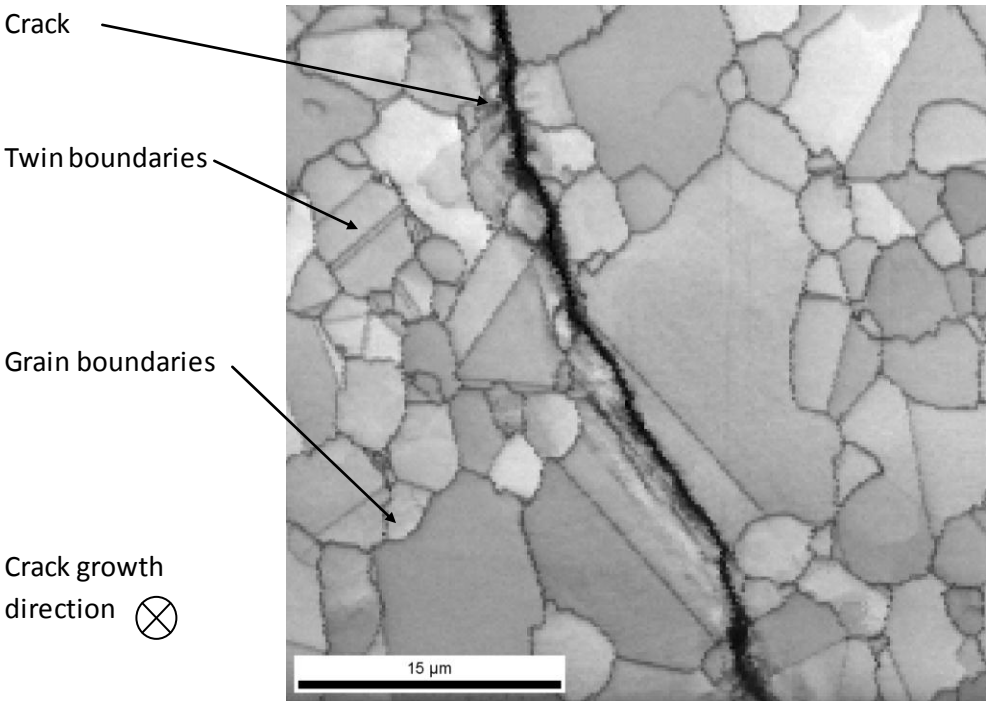

Figure 5-82: Image Quality (IQ) map of FIB Slice1showing the crack and twin and grain boundaries

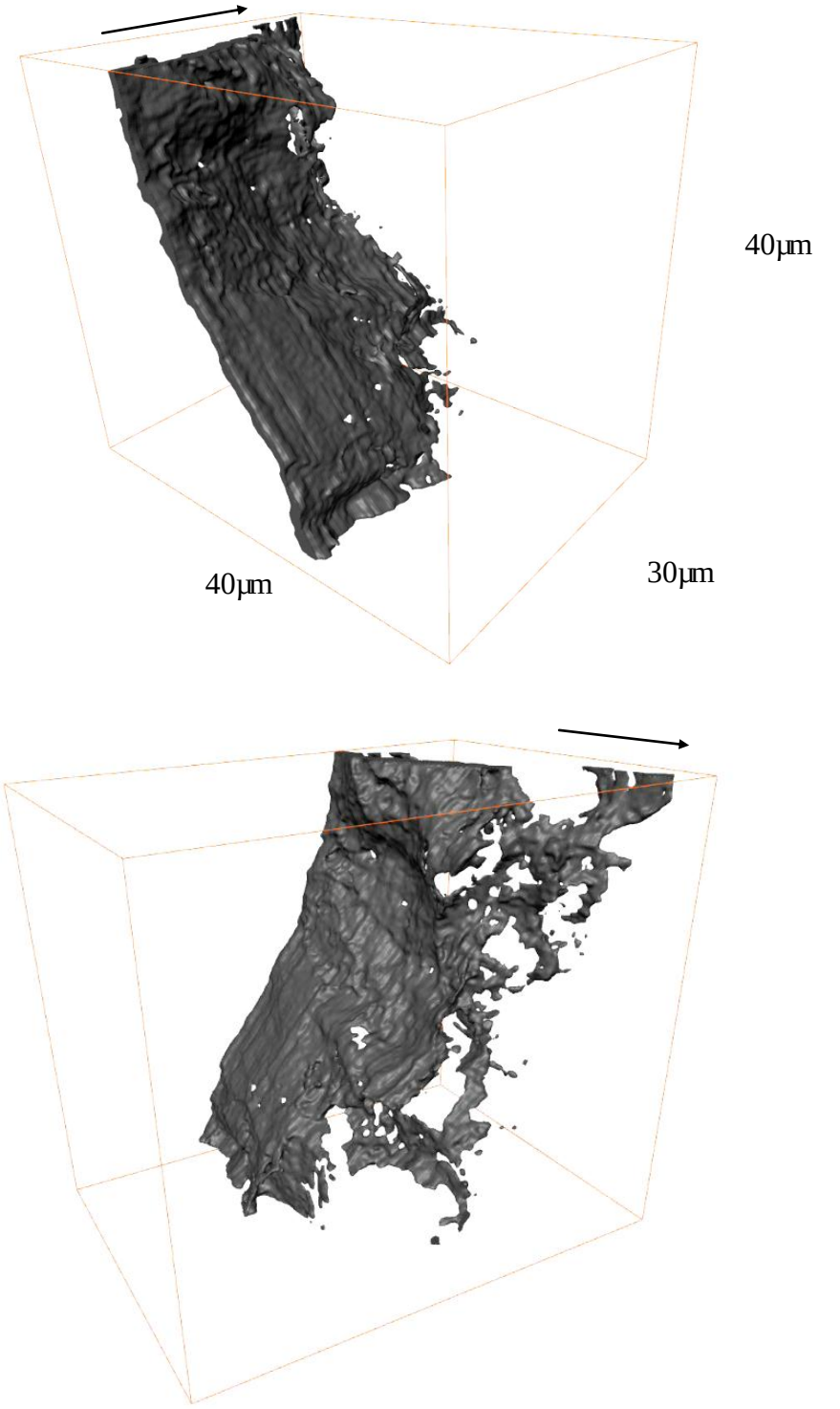

Figure 5-83: 3D reconstruction of the crack from EBSD IQ data from different orientations showing a discontinous crack tip (arrow indicating crack growth direction)

EBSD data can be gathered to identify the location (and orientation) of grains and precipitates. The grains and precipitates adjacent to the crack have been individually selected in each of the slices, using slices showing Image Quality from the EBSD. The slices of the EBSD results have then been reconstructed, and the grains adjacent to the crack have been individually selected to show their interaction with the crack, as shown in Figure 5-85. The colours of the inverse pole figure (IPF) represent a relative average grain orientation in 2D space. Grain orientation (inverse pole figure - IPF) colours are added from the 2D EBSD slices manually (as shown for example in Figure 5-84), which therefore means small variations inside each grain are not considered. The crack has been reconstructed in the same manner from the Image Quality maps.

By its very nature though, this detailed sectioning, analysis and subsequent assessment is restricted to small volumes of material.

Figure 5-85 shows the crack tip and adjacent grains with the IPF colours representing relative grain orientation. From the particular sample volume reconstructed the following observations can be made: It can be seen that the crack is sometimes growing along the grain boundaries (and possibly avoiding primary γ'), but also through large grains, where it is showing quite planar (perhaps slip-band) crack growth. Twin boundaries do not seem to affect growth. These 3D data suggest that crack growth is more transgranular towards the crack tip. The crack tip itself is discontinuous and this technique shows how further detailed evaluation of the microstructure ahead of the crack tip can be obtained, giving greater insight into what promotes, arrests or deflects local crack growth. This detailed investigation has also shown that there is no simple or obvious relationship between this deflected crack growth and grain orientation thus confirming that this phenomenon is not affected by local texture effects.

Visualisation and representation of such data-rich images is challenging – the additional compositional (phase identification), orientation and deformation/strain mapping features of this approach together with the spatial information in 3D require new approaches to data presentation. A video of this reconstruction can be found on:

http://archive.ses.soton.ac.uk/public/ebsd/cs1o07/3D_EBSD.hx.mpg

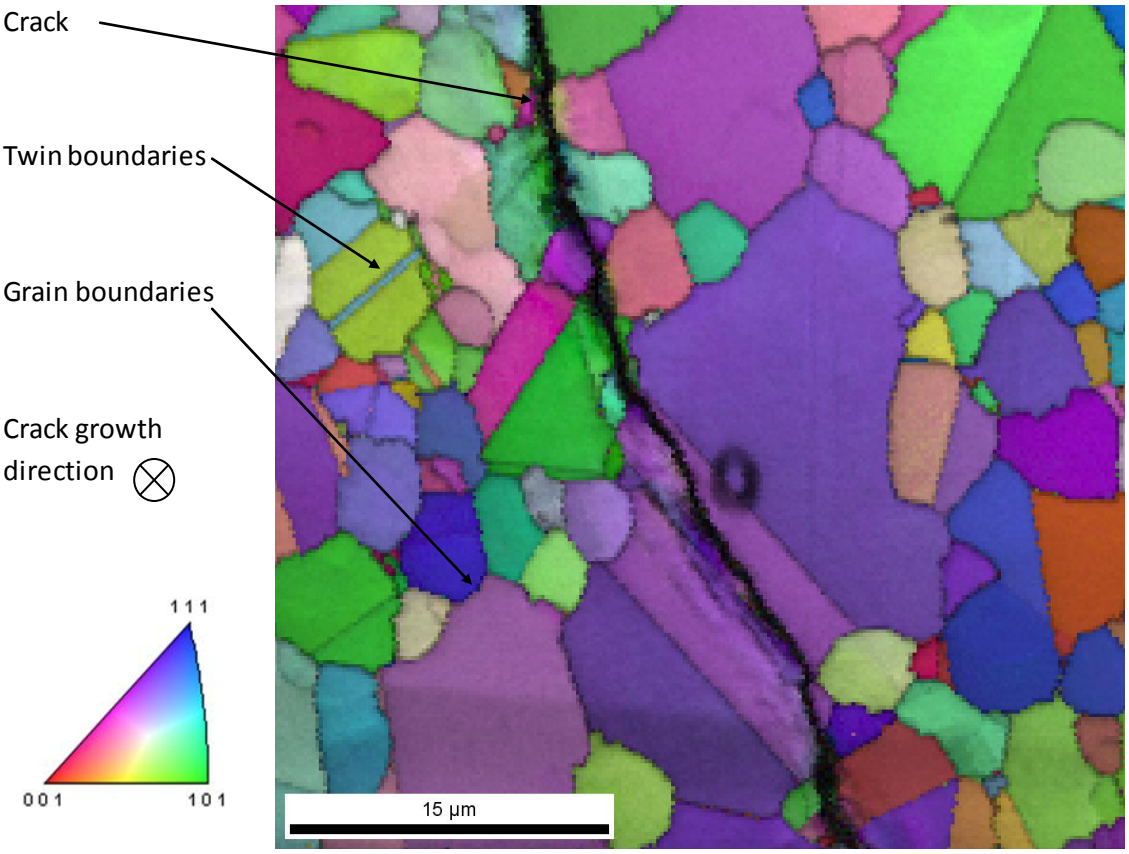

Figure 5-84: FIB Slice 1 with IPF showing grain orientation (see legend) and IQ showing crack and grain boundaries

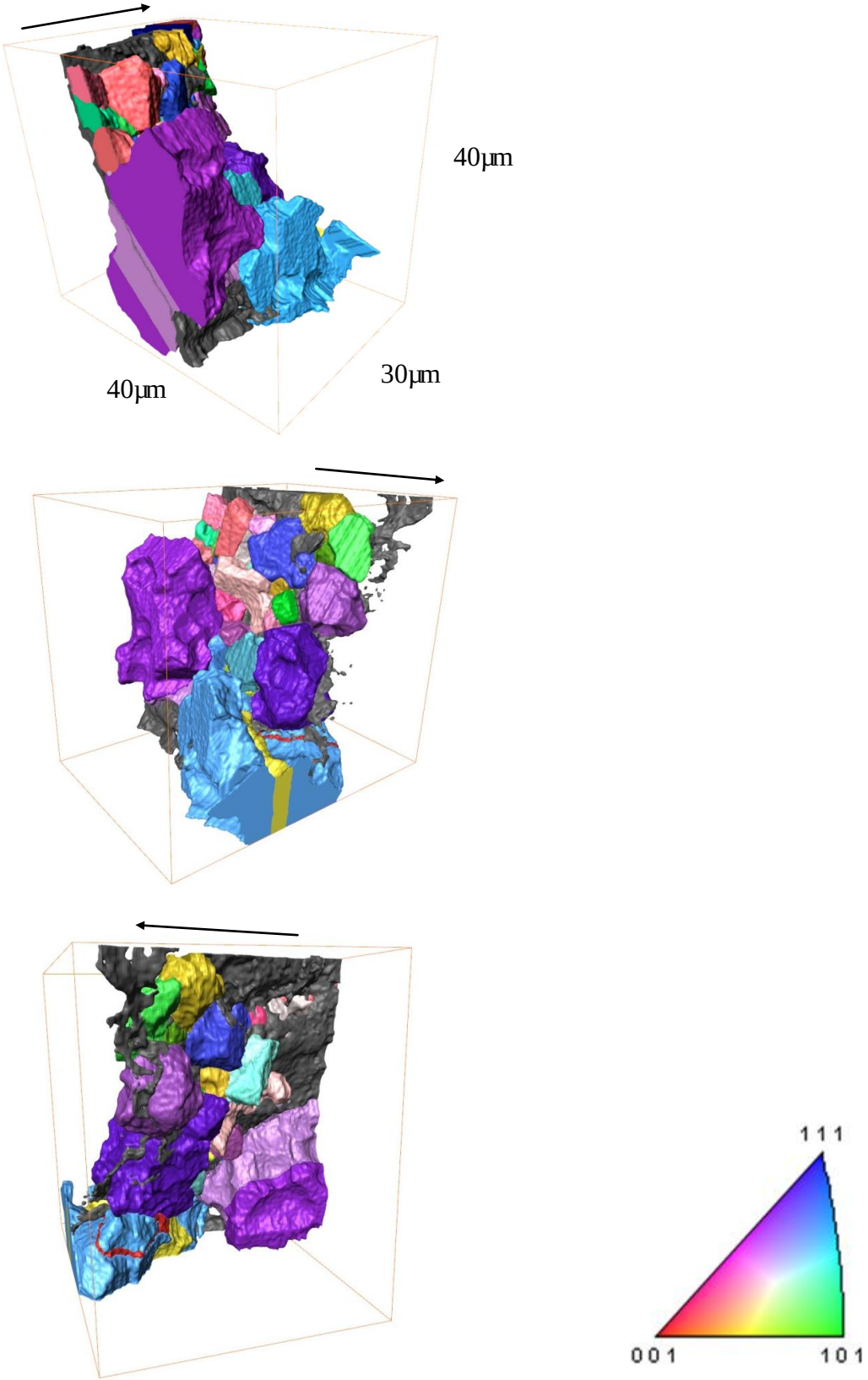

Figure 5-85: Crack and adjacent grains in IPF colours from different perspectives, showing intergranualar and transgranular crack growth

From the EDX data collected the primary γ′ were reconstructed by consideration of the chromium maps (shown for slice 1 in Figure 5-86), which have shown the best results for identifying γ′ in previous work [97]. A 3D map has therefore been created from the results of the EDS Chromium map showing the primary γ′ in the volume scanned, giving some indication about grain size and distribution around and beyond the crack, and the crack has again been reconstructed from the EBSD IQ maps. This representation allows the microstructure to be visualized beyond the immediate grains around the crack tip by effectively making the γ matrix 'transparent'. Viewing this in conjunction with the previous two figures for example, allows one to identify the large 'void' that indicates the position of the large γ grain containing a twin. The crack exhibits mostly transgranular crack growth in this large grain which (Figure 5-87) is apparently unaffected by the twin boundary. We can also see that the 3D distribution of primary γ′ gives a quite different indication of how a crack tip will interact with the grain and precipitates *cf.* conventional 2D representations.

A video of this reconstruction can be found on:

http://archive.ses.soton.ac.uk/public/ebsd/cs1o07/3D_gamma_prime.mpg

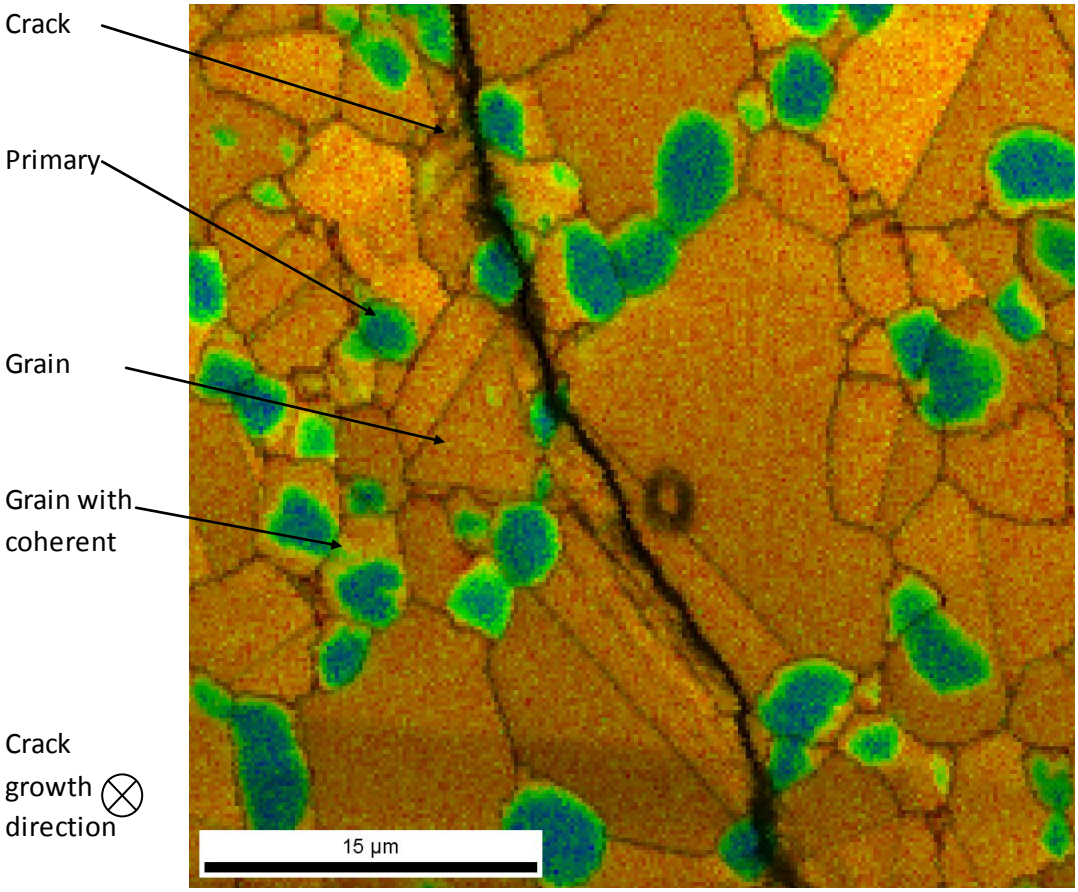

Figure 5-86: Slice 1 in EDS Chromium map and IQ, showing γ′ in green. The primary γ′ are where the green areas coincide with grain boundaries (from the IQ), but sometimes the green area is part of a γ grain, a large coherent γ′

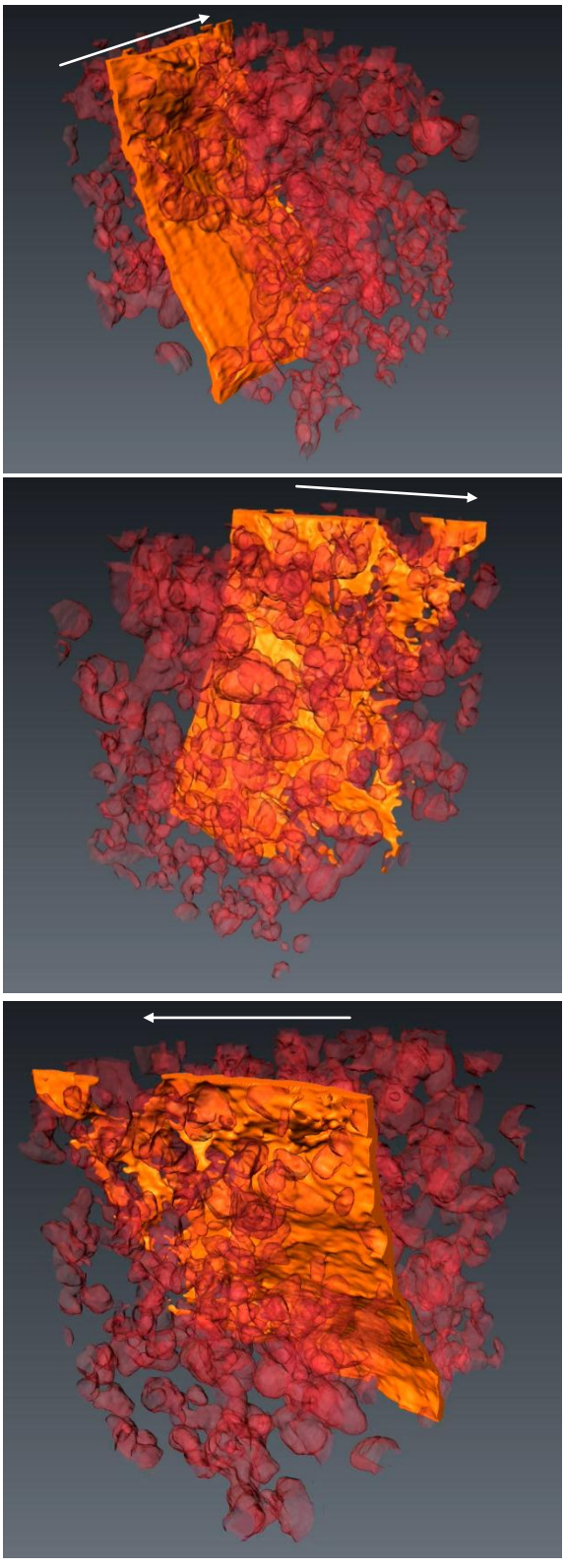

Figure 5-87: Crack (in orange) and primary γ′ (in red) showing the interaction of crack and microstructure, location of grains can be estimated between the primary γ′ (arrow indicating crack growth direction)

In the next approach it was considered in more detail, whether γ grains or primary γ′ precipitates have different effects on the crack path. For the reconstruction of the grains adjacent to the crack the previous reconstruction of the EBSD results has be en recoloured to show γ and γ′. Comparison of EDS (chromium maps) and EBSD (Image Quality maps) show that some primary γ′ (blue areas in the EDS map) have coherent boundaries with the surrounding γ grain (as shown by the IQ map) (Figure 5-86 shows slice 1). They are usually of the size of a primary γ′ and represent a large part of the γ grain.

In the reconstructions the primary γ′ have been marked in red, as shown in Figure 5-88, the 'grains' including large coherent γ′ in orange as shown in Figure 5-89, and the γ grains in blue as shown in Figure 5-90.

However this in depth evaluation does not appear to show any influence on the crack path, the crack shows both transgranular and intergranular behaviour, both for the γ′, the γ grains, and the γ grains containing coherent γ′.

A video of this reconstruction can be found on:
http://archive.ses.soton.ac.uk/public/ebsd/cs1o07/3D_gamma_gamma_prime.hx.mpg

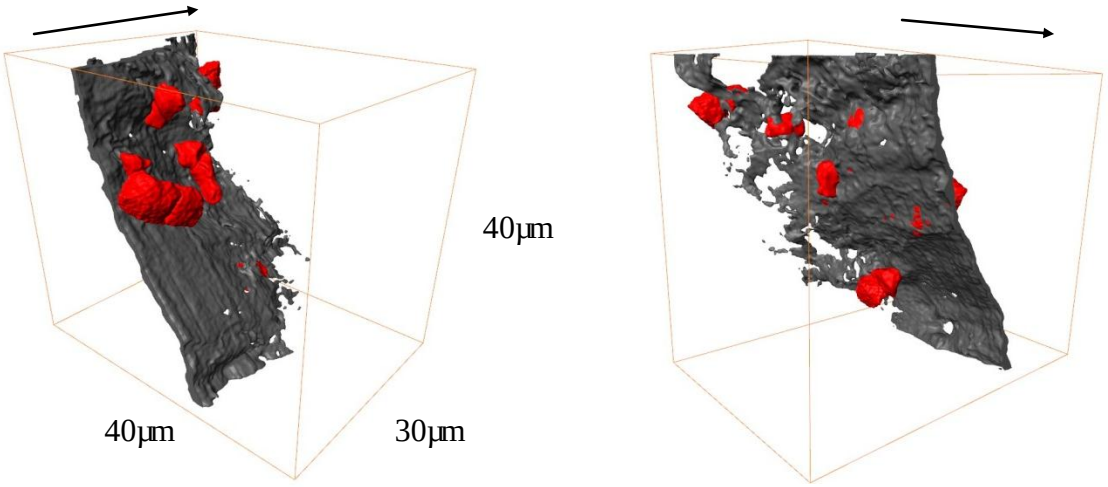

Figure 5-88: Crack with adjacent primary γ′ (in red)

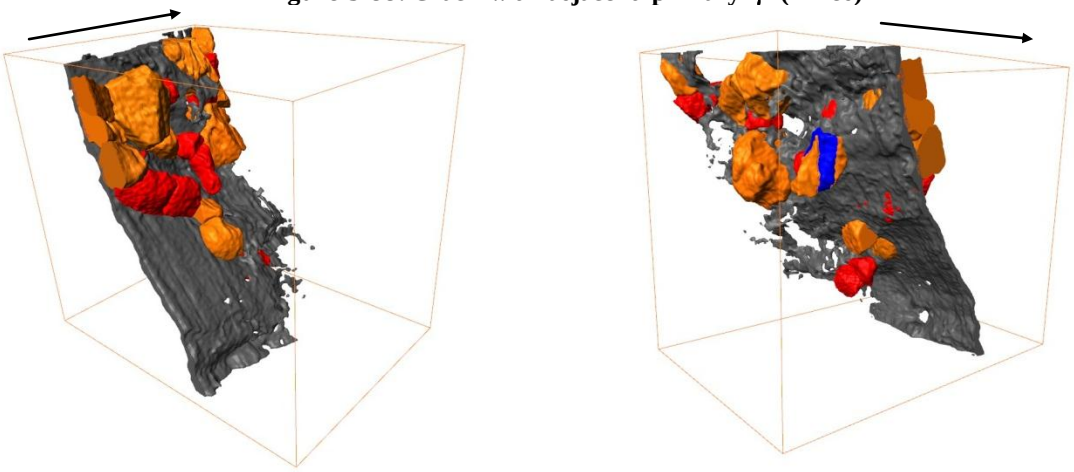

Figure 5-89: Crack with adjacent primary γ′ (in red), grains/γ′with coherent boundaries (in orange)

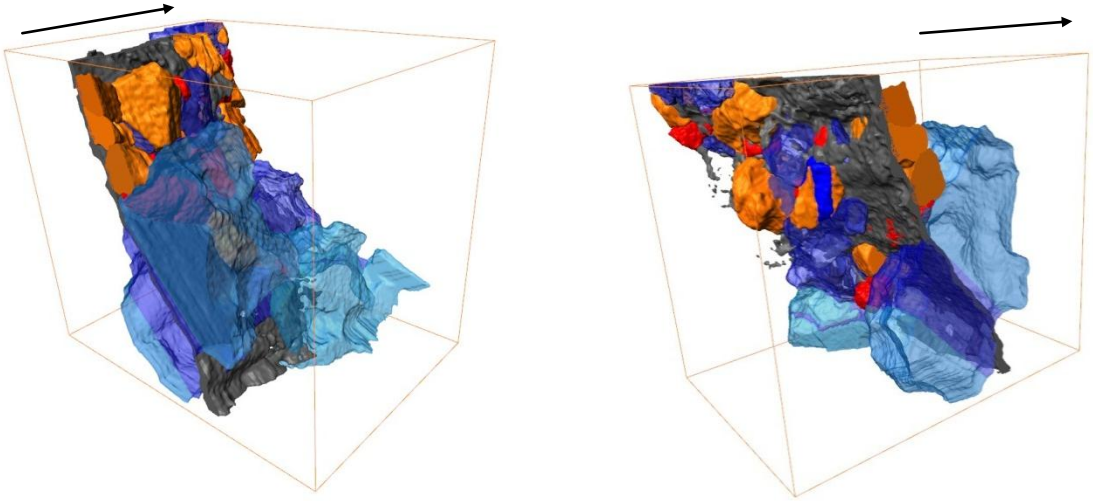

Figure 5-90: Crack with adjacent primary γ′ (in red), grains/γ′ with coherent boundaries (in orange), and grains (in blue)

Within the grains in the results of the EBSD, a variation of IPF colours can be observed, showing the variations of grain orientation within the grain (Misorientation). A 3D reconstruction of the crack and these areas of misoriention has been made using 'GROD' (Grain Reference Orientation Deviation) showing the deviation of each point in the grain with respect to the average orientation of the grain. These regions are located mainly along the crack, and increase closer to the crack tip. This can be considered a measure of crack-tip deformation or strain, and hence a method to visualise plastic wakes and plastic zones ahead of the crack tip.

Greater indications of deformation zones at the crack tip indicate the process zone (crack tip plastic zone) and there is no clear evidence of strain localisation or shear band formation ahead of the crack tip in this volume.

A video of this reconstruction can be found on:

http://archive.ses.soton.ac.uk/public/ebsd/cs1o07/3D_GROD.mpg

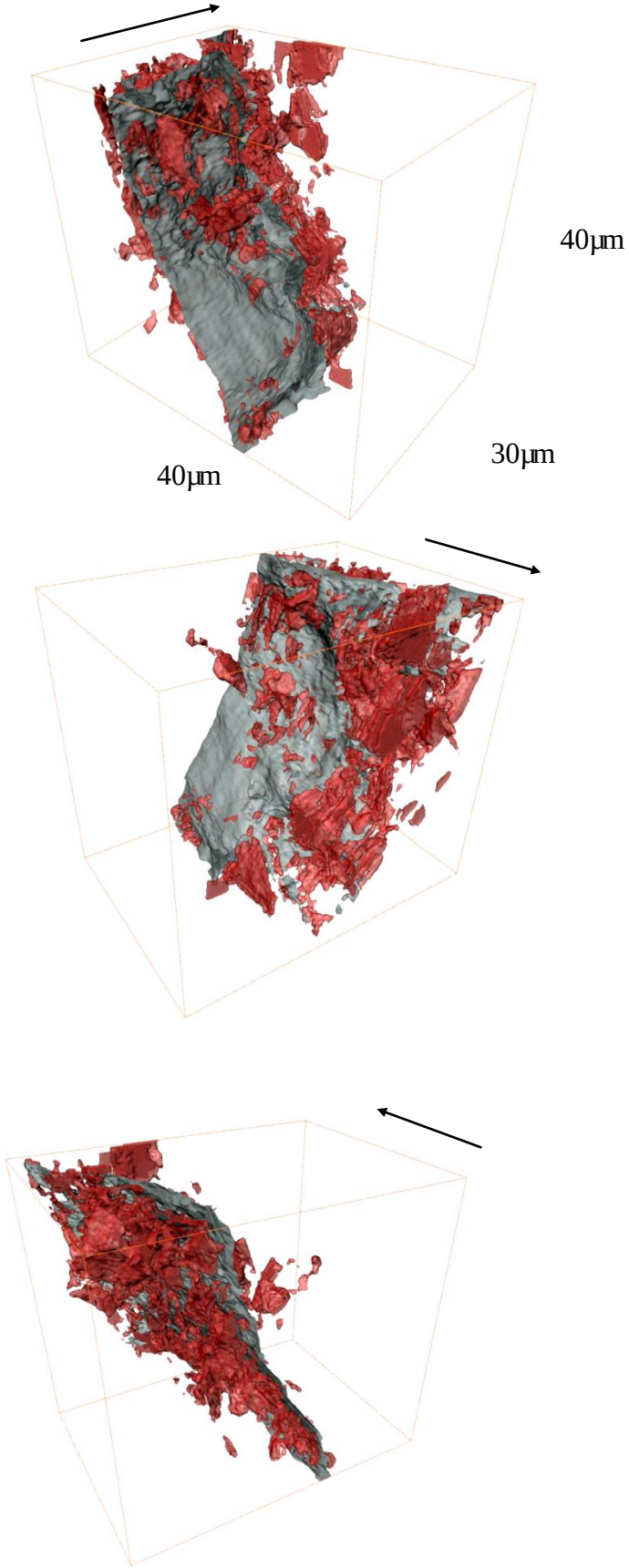

Figure 5-91: Crack and 'GROD' showing the areas of misorientation within grains, these are located mainly along the crack, and increase closer to the crack tip

As shown in the results of the SEM fractography slip traces and secondary cracks indicate a competition between Mode I and II controlled crack growth modes in both the shear and the stage II regions. In the region near the free surface this leads to macroscopic deflection under mode II loading and then back to mode I, while in the central region, there is no macroscopic deflection.

The more detailed evaluations afforded by the 3D reconstruction of the crack tip confirm that the crack growth mode in sustained deflected cracks is not noticeably different from that in 'Stage II' regions – with evidence of both transgranular (possibly slip-band) cracking and growth between and around γ grains and primary γ' particles occurring. There is no evidence that any particular texture or grain orientation is responsible for the deflected crack growth.

As shown here in more detail this material has a propensity to secondary cracking, so this is clearly important in the initiation of this deflection, however the results indicate that it is not the microstructure that causes the deflection to be sustained.

It should be noted that this 3D scan is only taken from a very small section of the entire volume (40x40x30µm), which may not representative for the material. Maybe the crack has arrested in this area because the microstructure is distributed like this, so further deflected crack growth is not promoted in this area. However this result is in agreement with what was seen in the FEG SEM, that this alloy did not show different crack growth behaviour in the planar and the deflected area.

5.7 TEM results

TEM foils were taken from locations just ahead of secondary crack tips using FIB. The foil might show more or less crack tip, as it is difficult to predict how much crack tip there is just from the surface observation. In the following a sample containing a crack tip has been further analysed using TEM.

Figure 5-92 a shows the bright field TEM image showing diffraction patterns (Figure 5-92 b and c) obtained above and below the secondary crack in the top grain, indicating the crack is growing through a γ grain as both patterns show identical orientation [112] of γ phase.

Figure 5-93 a shows the bright field image of the same crack, but now showing respective diffraction patterns (Figure 5-93 b and c) obtained above and below the same secondary crack in the lower grain (viewed at a slightly different tilt angle), indicating the crack is now growing through a γ' precipitate. The same orientation [112] of γ' is observed, the superlattice spots confirm it is the ordered γ' phase.

An EDX chemical analysis was carried out, the results are shown in Table 12. It suggests the grains on top of the crack and below the crack are of similar composition (Sites 1 *vs.* 2 and 3 *vs.* 4), indicating that they are more likely to be the same grain before the cracking occurred, confirming that the crack grew transgranularly through both γ and γ'. In addition, note the high

Cr concentration in the top grain, i.e. the γ grain, which is consistent with the 3D-FIB EDS work, where Cr maps have been used to distinguish between γ and γ′.

This limited TEM work supports the previous observation from the 3D EBSD and the FEG-SEM that the sustained macroscopic crack deflection does not seem to be caused purely by microstructure.

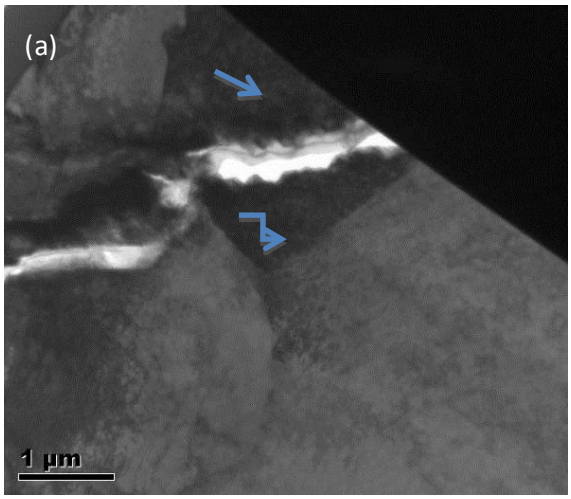

Figure 5-92: (a) TEM bright field image showing diffraction patterns obtained (b) above and (c) below the secondary crack in the top grain, indicating crack is growing through a γ grain

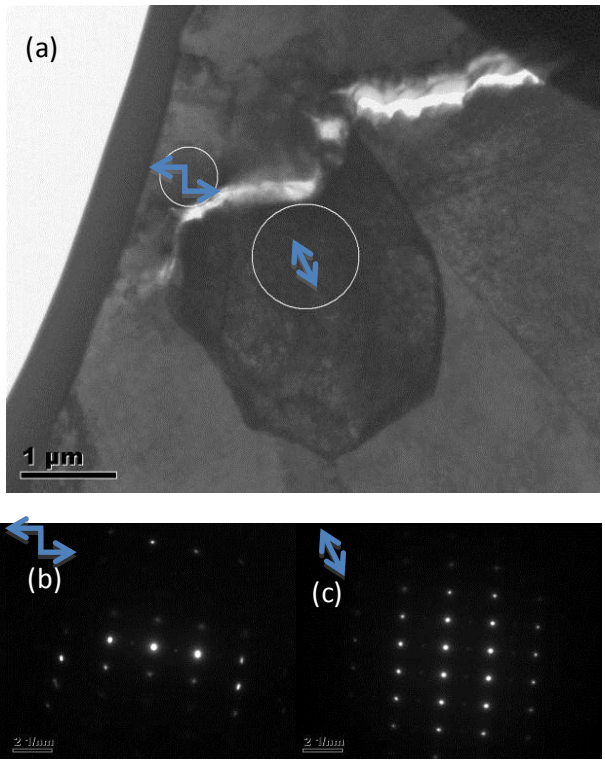

Figure 5-93: (a) TEM bright field image of secondary crack showing respective diffraction patterns obtained (b) above and (c) below the same secondary crack in the lower grain (viewed at a slightly different tilt angle), indicating the crack is now growing through a γ′ precipitate.

Site	Al	Ti	Cr	Co	Ni
1. Figure 5-92 a above crack	4.14	2.67	21.92	16.95	54.32
2. Figure 5-92 a below crack	5.80	6.22	18.60	16.39	52.99
3. Figure 5-93 a above crack	13.64	14.82	2.49	7.26	61.79
4. Figure 5-93 a below crack	12.92	13.32	3.10	8.55	62.11

Table 12: EDX chemical analysis of a fine spot in the areas above selected for diffraction, at %

5.8 Discussion

5.8.1 Definition of terms

The term teardrop cracking (TDC) as used in previous work [4, 5] does not describe the phenomenon very well as it only refers to the crack morphology produced in one specimen geometry (CNB or CN in tension), while the same crack growth mechanism has been seen in SENB and CDB [50].

The 'tear drop' region of the fracture surface is the area where the crack grows in stage II, parallel to the opening mode as would be expected. In previous work distinctions have been drawn between open and closed TDC. This however depends simply on the initial notch size, the overall specimen size and the initial ΔK level.

The unusual crack growth mode of interest is the deflected, terraced region near the free surface, as such it is proposed that this crack growth mode should be defined as sustained macroscopic deflected crack growth (SMDCG). Even though the SMDCG extends well beyond the plane stress region, it seems to be triggered by plane stress. The suggested consistent way to define the phenomenon is to describe the ΔK at the onset of terracing/SMDCG as has been shown in the results section.

The ΔK onset of deflection/SMDCG for U720Li C&W occurs at around 25MPa√m for 300°C in air for CNB and SENB, but the onset values increase at high temperature (600 and 650°C) to levels near the plastic collapse for the Dugdale PZS (if exceeding this at all). At these levels significant crack deflection may be expected anyway.

In the SENB in vacuum the values are similar to the values at 300°C and do not vary with temperature. For the CNB in vacuum however the deflection occurs at a higher ΔK_{Onset} (above 30MPa√m), but the deflection goes significantly deeper into the bulk. Vacuum conditions might be expected to promote more reversible slip processes than in air (all other factors being equivalent). However it is unclear why onset values are different for the two specimen types in vacuum.

The grain sizes studied here (up to ~18µm on average) are larger than in previous reports [4, 5] of when SMDGC has previously been observed, however it is below the very coarse grain size (~ 50µm) where Brooks' tests [91] on coarse grained U720 did not show SMDCG. This suggests that there might be a specific grain size below which it occurs. It is possible that the grain size could also influence the onset or extent of deflected cracking. In a larger sample (allowing higher ΔK levels to be reached) deflection could take place once a specific crack tip process zone encompassing a sufficient number of grains has been set up. To analyse whether the SMDCG could be occurring once the crack tip process zone is comparable to some measure of the grain size. Table 13 shows the reversed and monotonic plane stress plastic zone sizes (PZS) (using Irwin, Rice and Dugdale approximations) for U720Li PM LG and FG and C&W for the ΔK onset at 300, 600 and 650°C measured for CNB in U720Li C&W in air and an average value of 25MPa√m was used for all (This does not take into account that the value seen for vacuum was higher). The reversed PZS for the Rice approximation is the smallest estimate, and is in the same range as the grain size. For the LG variant the PZS is 21µm compared to the grain

size of 16µm, and it is the same for the C&W material. For the FG variant however the PZS is 17 µm, with is nearly three times the size of the grain size of 6.4µm. The monotonic PZS are significantly larger (as would be expected) as are the estimations based on Irwin and Dugdale. The effect of temperature is quite modest on the predicted PZS (no matter whether reversed, monotonic or which approach is taken). In terms of monotonic behaviour, the temperature dependence of the ΔK onset is not explained by some simplistic comparison of grain size to crack tip plastic zone, nor does this correlate with the observed differences in the ΔK onset for the different alloys (where any difference is too slight to be linked to the number of grains being encompassed by a process zone). However it should be noted that onset values were higher in vacuum for CNB (but not SENB), this would cause a larger PZS at the onset in vacuum.

Yield strength values for these calculations have been estimates based on Vickers Hardness measurements for the PM U720Li as shown in Table 4 (based on comparison with U720Li C&W) . For U720Li PM FG and LG cyclically stabilised yield strength are also available from Pang [23], which are also shown in Table 13. Cyclically stabilised stress strain curves were obtained at 650°C from 1.2% strain controlled high temperature LCF tests. As an effect of this, the PZS (independent of the approximation used) increases 40% for the FG and 54% for the LG, due to the significant cyclic softening exhibited. Data for cyclically stabilized σ_y should be obtained in the same way as for the C&W material and for temperatures 300, 600 and 650°C for comparison, in case this does provide a more appropriate correlation to the ΔK onset.

Plane stress PZS in µm				Rice		Irwin		Dugdale	
	Grain Size	Temperature in °C	σ_y (MPa)	Monotonic	Reversed	Monotonic	Reversed	Monotonic	Reversed
U720Li C&W	16.7 µm	300	1084	105	21	209	42	258	52
		600	1067	108	22	216	44	266	54
		650	1055	110	22	221	45	272	55
U720Li PM FG	6.4µm	300	1193	86	17	173	35	213	43
		600 (test not done)	1174	89	18	178	36	220	45
		650 (test not done)	1161	91	18	182	37	225	46
U720Li PM FG	cyclically stabilised	650 (test not done)	980	128	26	256	52	316	64
Change				0.40	0.40	0.40	0.40	0.40	0.40
U720Li PM LG	15.4 µm	300	1083	105	21	210	42	258	52
		600 (test not done)	1066	108	22	216	44	267	54
		650 (test not done)	1054	111	22	221	45	273	55
U720Li PM LG	cyclically stabilised	650 (test not done)	850	170	34	340	69	419	85
Change				0.54	0.54	0.54	0.54	0.54	0.54

Table 13: Plane stress plastic zone sizes in µm at the ΔK onset (assuming 25MPa$\sqrt{m}$ in air for all) for U720Li PM FG and LG and C&W at different temperature

5.8.2 Mechanism of SMDCG

A competition between two crack propagation processes appears to be occurring (one dominated by shear loading and one by tensile loading) This seems to explain the alternating of the deflected and 'normal' Stage II type crack growth. Based on the results of the SEM fractography in all samples, in both the deflected and the stage II crack growth areas a similar crack growth mechanism is seen. 'Striation' like features have been observed. Measurements of the spacing between the features compared to *da/dN* data for tests at 300°C in air and vacuum, shows values are of the same order of magnitude, i.e. the features could be striations, however spacing measurements for the U720Li PM FG are different, but the *da/dN* values are estimations, as there is no *da/dN* data for this alloy available at 300°C.

The features also are seen to run in parallel bands over regions of the order of the average grain size, and then change direction. It is therefore concluded that the features are most likely to be slip traces. Moreover secondary cracks also occur in the same direction/orientation. Visually (or qualitatively) they can be observed to increase in size and number with higher ΔK and large secondary cracks can be observed at the point where mode I switches to mode II in the terraced region.

Both the slip traces and secondary cracks indicate a competition between Mode I and II controlled crack growth modes. In the region near the free surface this leads to macroscopic deflection under mode II loading and then back to mode I, while in the central stage II (teardrop) region, there is no macroscopic deflection. Therefore the plane stress region seems to have an effect in triggering this phenomenon, however it should be noted that the terraces extend much further than the plane stress region.

In the U720Li C&W sample tested in vacuum at 300°C, a more faceted surface can be observed which is believed to be due to more reversible slip processes in vacuum, thus more planar slip processes and more pronounced Stage I type crack growth is observed. In the near notch region, a fretted area can be observed, that could be caused by rewelding of fracture surfaces at low ΔK in vacuum. This and previous work seem to indicate that SMDCG occurs under conditions which are also linked to more planar slip processes. SMDCG is more pronounced (deflected crack extends further into the sample) in vacuum, where slip is more reversible and hence more planar, but seems to occur at a higher ΔK onset.

Wavy slip processes are usually considered to be well established at 600°C, above this temperature the SMDCG effect has not been seen in air.

It is significant that vacuum conditions promote, while higher temperatures seem to suppress the deflected crack growth. Slip processes are expected to be more heterogeneous at lower temperatures and in vacuum, due to the slip reversibility in vacuum. There seems to be a link between the sustained deflected crack growth and the slip character. The slip traces and secondary cracks observed in the fractography support this. However the phenomenon is suppressed at low temperature in vacuum, where slip is heterogeneous, so this cannot be the sole cause of deflection.

As shown by the SEM fractography this material has a propensity to secondary cracking, so this is clearly important in the initiation of this deflection.

The more detailed evaluations afforded by the 3D reconstruction of the secondary crack tip have confirmed that the crack growth mode in sustained deflected cracks is not noticeably different from that in 'Stage II' regions – with evidence of both transgranular (possibly slip-band) cracking and growth between and around γ grains and primary γ' particles occurring. This has also been seen in the crack tip TEM. There is no evidence that any particular texture or grain orientation is responsible for the deflected crack growth. It should be noted that only a small area has been used for these measurements.

Clearly the secondary cracking is critical in triggering this deflection; however it is not the microstructure that sustains the deflection, hence the stress field at the surface seems to give rise to this unusual deflection. The plane stress region seems to have an effect in triggering this phenomenon, however it should be noted that the terraces extend much further than the plane stress region. The evolving crack-tip stress state as the complex 3D crack path develops must be further evaluated. Clearly a detailed assessment of when and how much the crack deflects is needed to understand the possible lifetime effects in any component situation.

5.8.3 Crack growth rates

The *da/dN* vs. ΔK curves have been measured from the U720Li C&W SENB samples at 300, 600 and 650°C in air and vacuum and for 300°C in air for a thin SENB sample. As expected at higher temperatures crack growth rates are higher, while vacuum conditions reduce crack growth rates compared to the same temperature tests in air.

However for the thin sample at 300°C in air crack growth rates are much lower than for the equivalent thick SENB, this might be due to the dominating plane stress conditions, but it is also possible that, as this sample showed a much larger proportion of deflected crack growth, the deflection caused crack tip shielding, which reduced the effective crack driving force.

The C&W material performs better than U720 PM, according to comparison with Loo-Morrey's data, however it should be noted that her measurements are for R=0.5, as they are the only available data for 300°C, and as previously shown in Figure 5-8 the R=0.5 data shows worse performance than R=0.1 at room temperature, this has been attributed to reduced closure effects at the higher R-ratio.

da/dN data for the largely Stage II crack growth regions has now been identified, however it is necessary to acquire *da/dN* data as a function of appropriate *K*-parameters for the more complex deflected crack growth in the deflected regions, to be able to describe the *da/dN* of the SMDCG.

The end goal of this would to be to predict crack growth rates for this phenomenon, and to also be able to assess the crack driving force (i.e. the required combination of appropriate *K*-parameters) that will also define the direction of crack growth in order to develop lifing procedures that can allow for this phenomenon.

5.9 Summary

Initial fatigue testing has been carried out on Corner Notch samples in bend (CNB) on U720Li PM FG and LG at 300°C in air.

Further CNB and Single Etch Notched Bend (SENB) testing have been performed on U720Li C&W at 300, 600 and 650°C in air and vacuum. All testing in this project was performed at 20Hz with a sinusoidal waveform and at an R-ratio of 0.1. Two thin (plane stress dominated) SENB samples were also tested for comparison. In the SENB tests PD measurements were used to gain crack growth data. The crack growth rates from tests compare very well to each other as well as to the crack growth data from Rolls Royce plc. from Corner Notch tests in tension (CNT).

All tests showed some deflected crack growth at the free surface. The fracture surfaces showed a central flat 'teardrop' region and terraced regions starting from the top and side surface, where flat and shear crack growth mode were alternating. As teardrop cracking really only describes the effect in a CNB or CNT sample and also refers to the planar region, which is behaving as expected, the phenomenon is better described as sustained macroscopic deflected crack growth (SMDCG).

To characterise the onset of the deflection in a systematic manner, independent of sample size, notch size and initial ΔK levels, the onset of deflection has been consistently measured, and given as a range of nominal ΔK values where the deflection exceeds the monotonic plane stress plastic zone size (defined as the range between Rice and Dugdale approximation), in which some deflection might be expected. In the C&W material an increase in onset ΔK values can be seen with increasing temperature in air testing for both CNB and SENB tests, indicating the effect being reduced at higher temperature. However in vacuum testing values are relatively independent of temperatures. The ΔK ranges in vacuum are however higher than in air in the CNB, but at a similar range for the SENB.

3D maps of the fracture surfaces have been created using different techniques of which Alicona Infinite Focus has been chosen to be the most appropriate, as it has the best balance between resolution and area that could be scanned. The system is a microscope that scans over the fracture surface and automatically focuses on the height of the sample, and works out a 3D height profile. These 3D maps can be used to measure deflection angles and to create finite element models to predict crack growth.

The fracture surfaces of samples from the different test geometries and test conditions have been observed via FEG-SEM. In both the central planar region, and the near-surface terraces in flat and deflected regions, slip traces and secondary cracks were seen, which could be evident of local competition between opening and shear growth, which may then be expected to control the macroscopic deflection. The effect could be linked to planar slip, as it is more pronounced in vacuum, where slip is more reversible, while they are suppressed at 600°C in air, where usually wavy slip would be expected. However in previous work the effect has not been seen at room temperature, where planar slip would usually be expected.

Further work with EBSD serial sectioning and 3D reconstruction of the secondary crack tip and crack tip TEM confirmed that the deflected (secondary) crack behaves like a planar crack

growing transgranularly and occasionally intergranulary through γ and γ'. There is also no underlying texture/grain orientation that influences the deflection.

To understand whether a component is exhibiting SMDCG it is necessary to establish what the crack driving force is, that causes the crack to deflect, and how this could be applied to the complex stress state in a component.

6 Study of existing deflected fractures

6.1 Introduction

Deflected fatigue crack growth may occur for a number of reasons, it could be caused by shear lip formation, mixed mode loading or tunnelling due to creep, as described by Antunes et al. [92]. Not every deflection in fatigue is necessarily SMDCG, as discussed in section 5.3, SMDCG has now been defined to occur at intermediate temperatures in air and to be sustained to higher temperatures in vacuum.

The key issue is to establish when SMDCG is occurring to enable better prediction of crack paths in components. A number of rigtests that showed unusual deflection have therefore also been analysed to confirm whether the SMDCG phenomenon has occurred, i.e. is it low/intermediate temperature sustained crack deflection.

The following chapter therefore considers a re-analysis of the extent of deflected crack crack growth occurring in other researchers' test samples and a number of tested components observed at Rolls Royce plc. to extend the test matrix to a wider range of testing conditions and to link the observations from various test configurations to what is seen in a component to more fully understand the influence on lifetimes and what effect this should have on R-R lifing methodology.

6.2 Comparison to other tested samples (from other research programmes)

A number of samples from previous work on 'teardrop' cracking have been re-examined. This consists of a number of CNB and SENB samples of U720 tested by Loo-Morrey [50] and some U720Li C&W corner notched tensile (CNT) samples tested at the University of Birmingham, some of which have experienced large dwells and some bithermal tests, with alternating high and low temperature cycles. The approach taken here has involved mapping any sustained deflected crack growth (e.g. giving rise to terracing) on the fracture surfaces and comparing the extent of such regions to expected plane stress plastic zone sizes.

The template tools created in this work, the spreadsheet (using test data) described in section 5.3, have been applied to these fractures where possible to map the expected plane stress plastic zones for the specimen cross-section which could then be overlaid on a fracture surface to see if any terracing had fallen outside the expected plane stress plastic zones.

6.2.1 Corner notched Bend (CNB) samples tested prior to this work

The CNB samples analysed were from fatigue tests carried out by Loo-Morrey in [50]. The specimens were 12.5x12.5x80mm, contained an initial corner cut of 350μm and were loaded in four point bend. Tests were carried out at temperatures of 300 and 600°C in both air and vacuum conditions with an alternating R-ratio between 0.1 and 0.5 (where K_{max} was held constant whilst changing R-ratio) and an initial ΔK_i level of 12 MPa√m, see Figure 6-1. This allowed the crack front to be clearly identified (and showed that the shear crack regions formed during fatigue crack growth and were not a final failure mode due to the crack tunnelling). In addition there are further samples tested with constant R-ratios of 0.1 and 0.5

at 300°C in a vacuum and an initial ΔK_i level of 12 MPa√m and these are compared to the alternating R-ratio test at the same conditions, to investigate the effect of R-ratio, as shown in Figure 6-2. A further set of tests, again at 300°C under vacuum conditions at an R-ratio of 0.1 looked at the effect of varying initial ΔK_i values: of 8 and 18 MPa √m, and are compared to the test with ΔK_i of 12 MPa √m, as shown in Figure 6-3. Pickard's analysis was used to determine ΔK levels [94] along the crack tip. The template has been applied to all fracture surfaces to show the PZS compared to the terraces. For the purposes of this analysis an R-ratio of 0.1 was used in calculating ΔK levels for the alternating R-ratio, the smaller PZS for R=0.1 being more conservative.

Figure 6-4 to Figure 6-11 also show the fracture surfaces and the crack deflection regions of the samples plotted against the plastic zone sizes as a function of ΔK for each test from which onset measurements can be taken. Table 14 summarises the measured onset of terracing in the CNB samples and compares with data obtained in this thesis as described in Chapter 5.

Loo-Morrey's data in the PM U720 alloy agrees with the current work (in U720Li C&W), when a consistent definition of K onset is applied, confirming deflection occurs at 300°C in air and vacuum and is sustained to 600°C in vacuum, and also showing similar values for ΔK_{onset}. However the test carried out by Loo-Morrey at 300°C in vacuum with an R=0.1 and ΔK_i=12 MPa √m shows significant variation, with the apparent ΔK_{onset} being significantly lower than found for the other CNB tests in vacuum. There is however some uncertainty over the accuracy of the ΔK calculations due to an apparent error in the Pickard calibration when calculating the initial ΔK during the original testing by Loo-Morrey and there was insufficient information in [50] to follow her calculations, so there is the some lack of confidence in the actual applied ΔK for this sample.

There seems to be a limited effect of the variation in R-ratio on the onset ΔK, if this test at R=0.1, 300°C, vacuum is ignored, and we consider the one from chapter 5 instead. The use of a variety of initial ΔK levels by Loo-Morrey in Figure 6-3 clearly shows that this does not play a role in establishing when the deflection occurs, it always occurs at the consistent ΔK_{onset} level established.

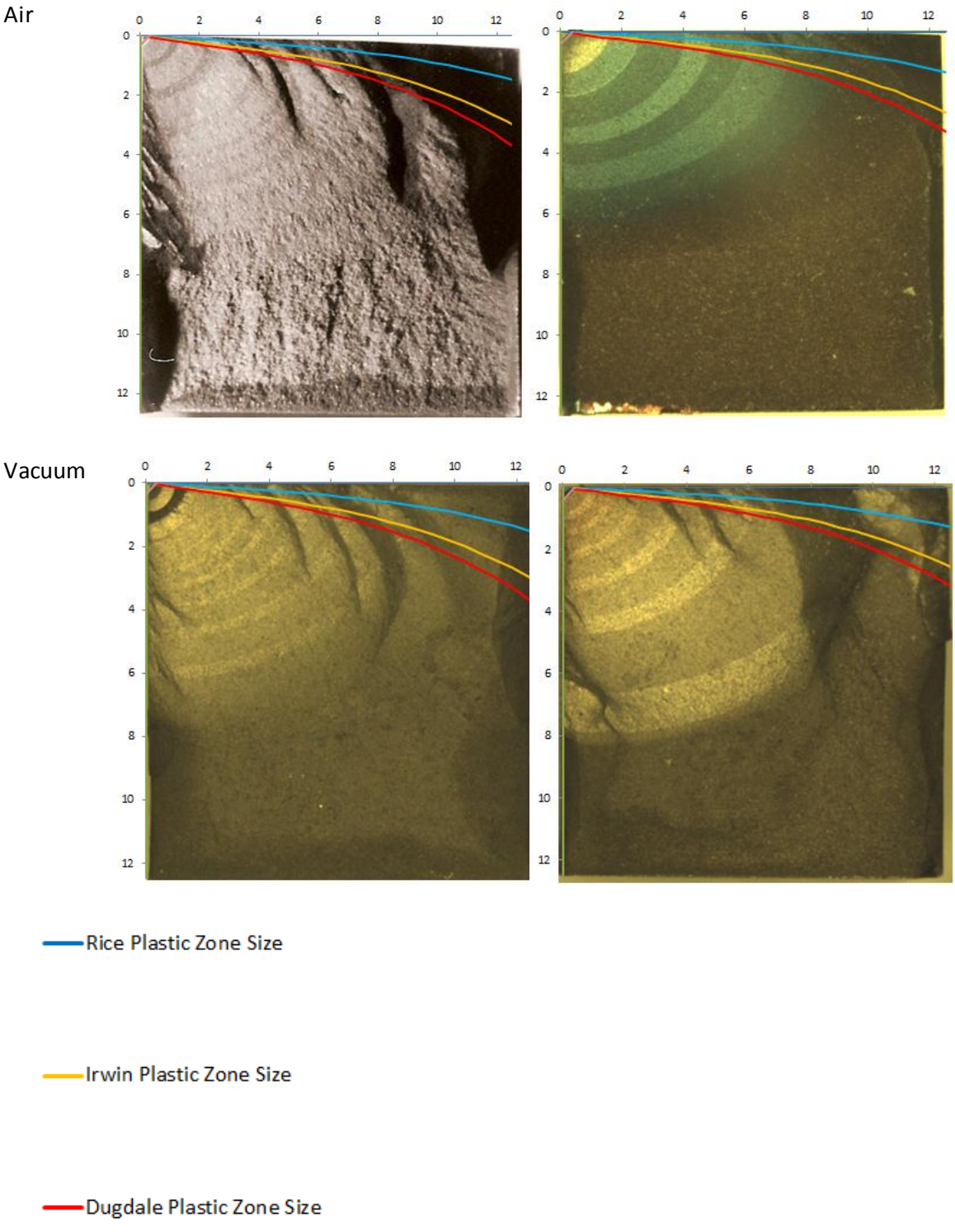

Figure 6-1: CNB samples tested at 300 and 600^{0}C, in air and vacuum, all at ΔK_i=12 MPa $\sqrt{m}$ and alternating R-ratio, template has been applied to show plane stress plastic zone sizes

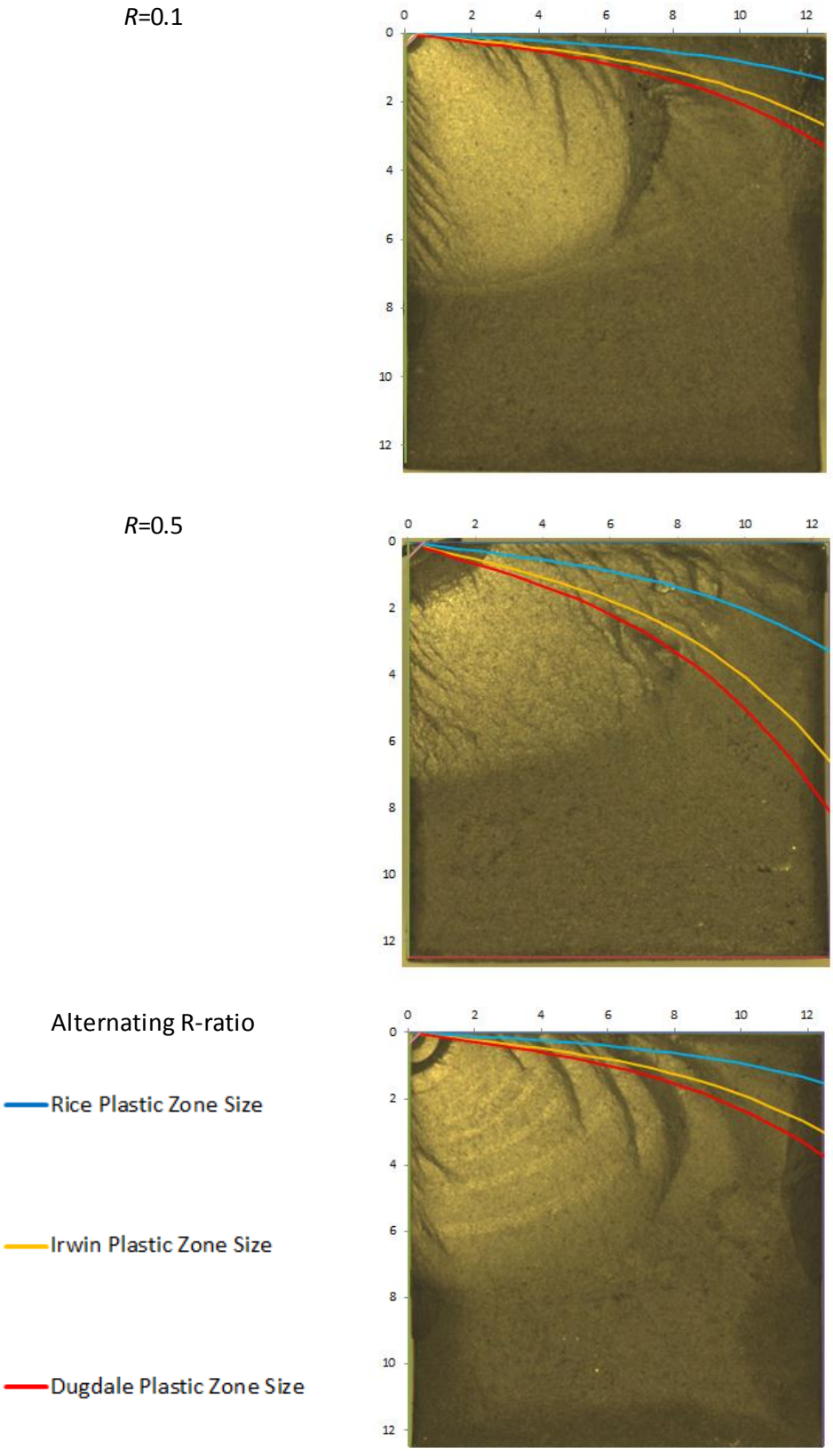

Figure 6-2: CNB samples tested at 300^{0}C, in vacuum at ΔK_i=12 MPa $\sqrt{m}$ at R=0.1, R=0.5 and alternating R-ratio, template has been applied to show plane stress plastic zone sizes

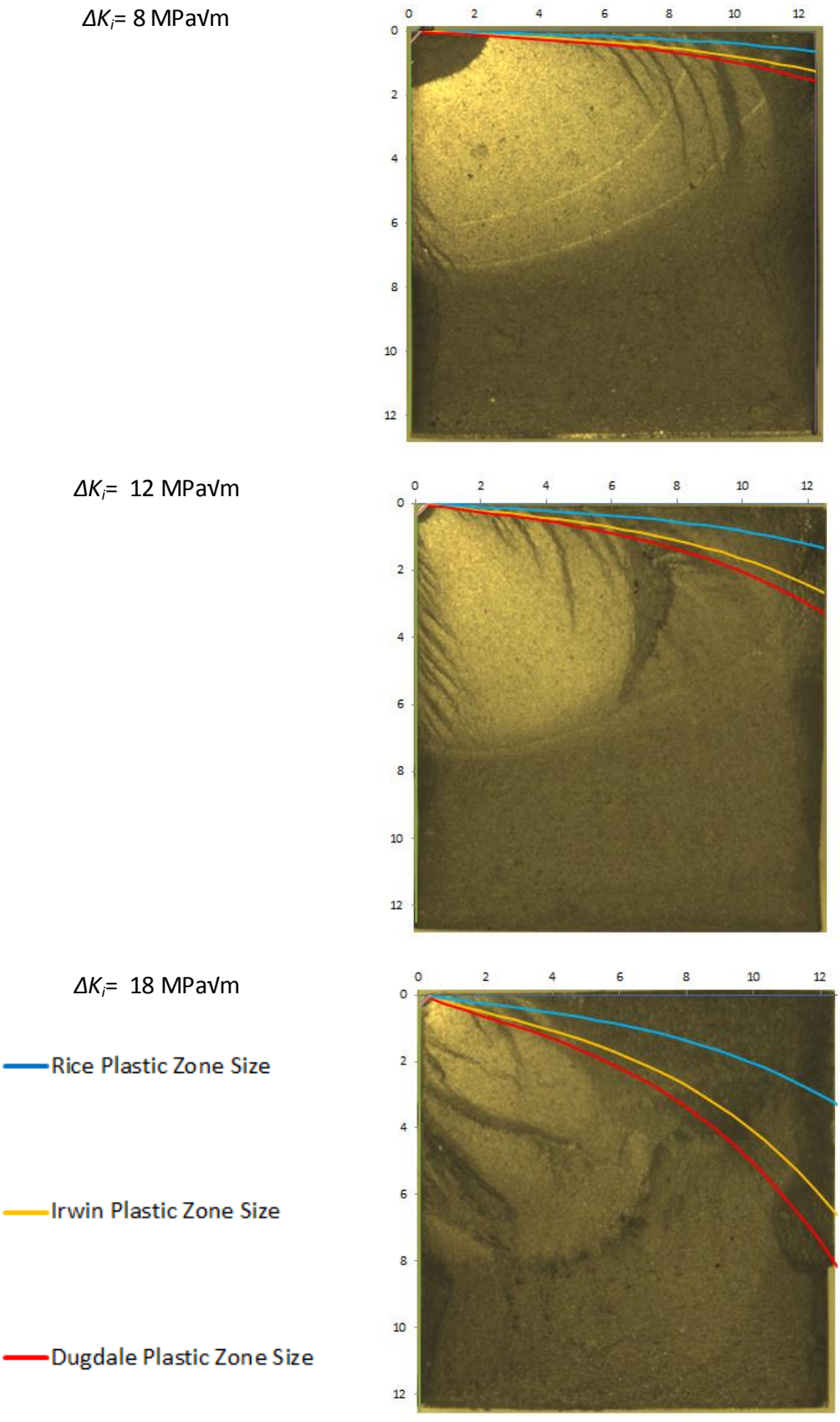

Figure 6-3: CNB samples tested at 300 ^{0}C in vacuum, R = 0.1, at ΔK_i=8, 12 and 18 MPa $\sqrt{m}$, template has been applied to show plane stress plastic zone sizes

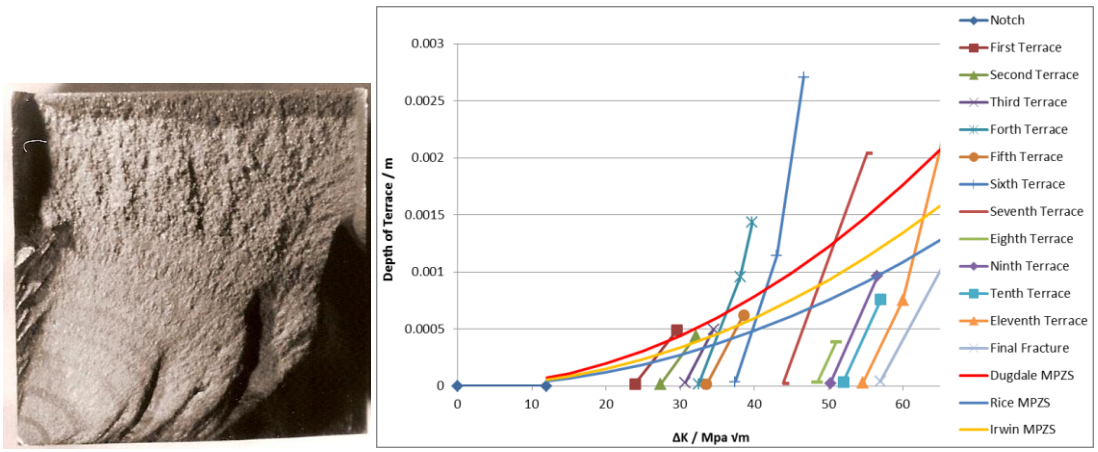

Figure 6-4: Fracture surface of CNB tested at 300^{0}C, air, ΔK_i=12 MPa √m, alternating R-ratio – for full test information see [50]

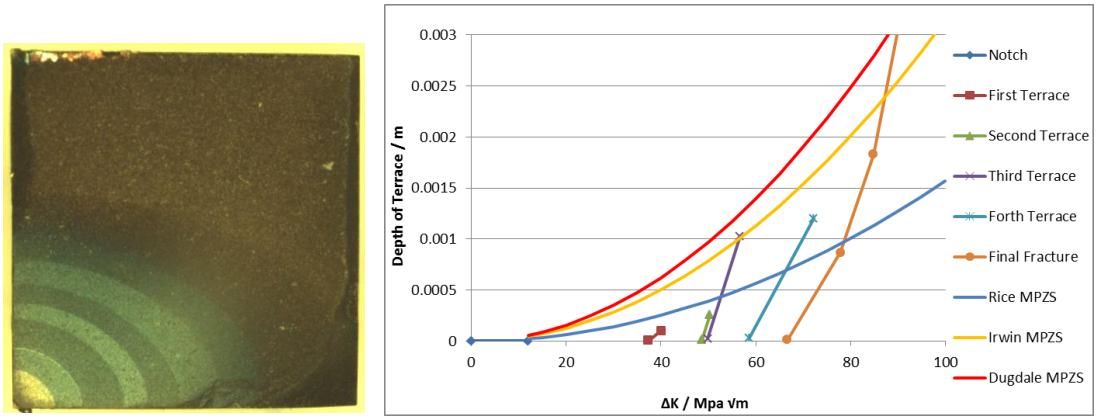

Figure 6-5: Fracture surface of CNB tested at 600^{0}C, air, ΔK_i=12 MPa √m, alternating R-ratio – for full test information see [50]

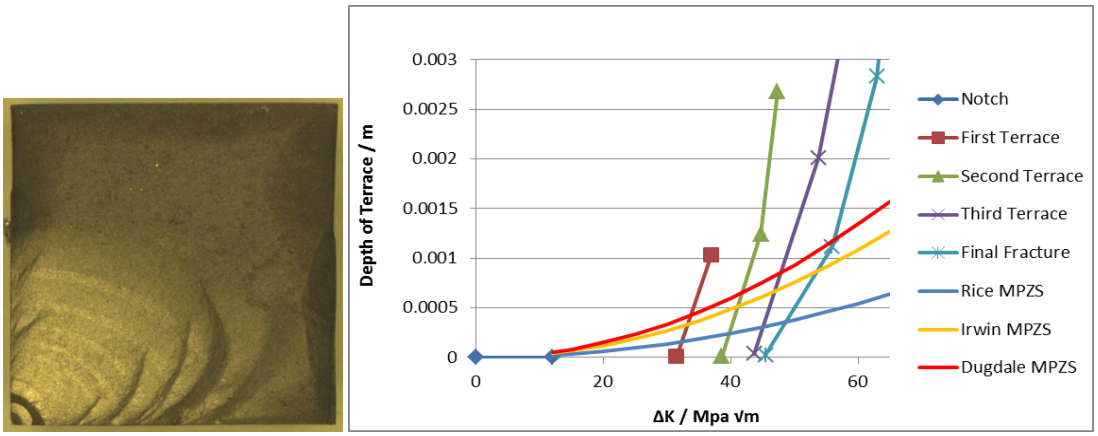

Figure 6-6: Fracture surface of CNB tested at 300^{0}C, vacuum, ΔK_i=12 MPa √m, alternating R-ratio – for full test information see [50]

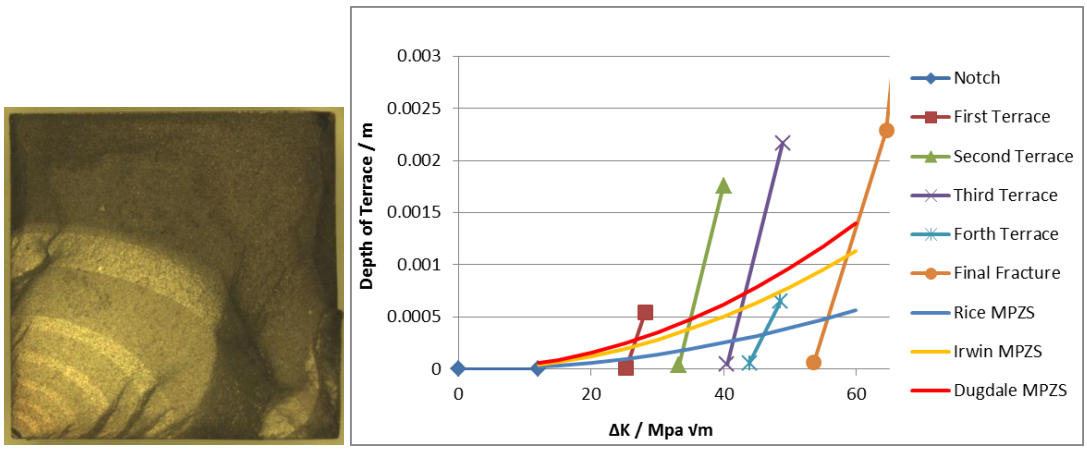

Figure 6-7: Fracture surface of CNB tested at 600^{0}C, vacuum, ΔK_i=12 MPa$\sqrt{m}$, alternating R-ratio – for full test information see [50]

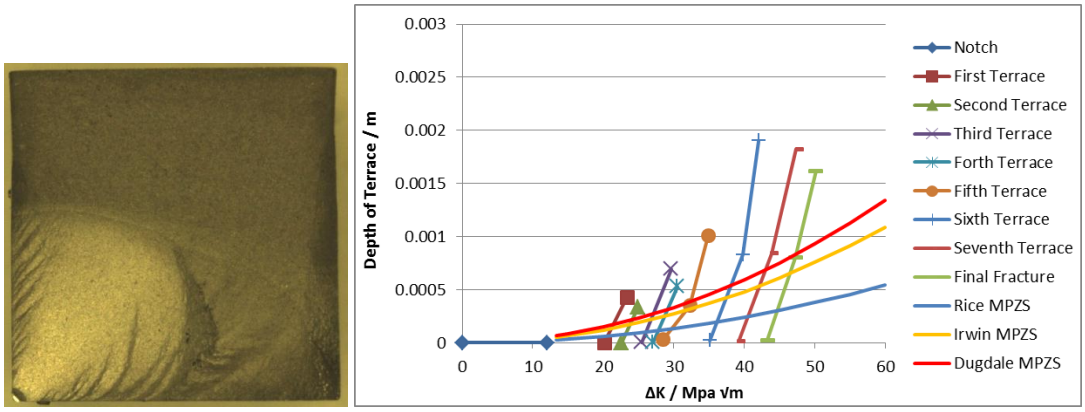

Figure 6-8: Fracture surface of CNB tested at 300^{0}C, vacuum, ΔK_i=12 MPa$\sqrt{m}$, R-ratio= 0.1 - for full test information see [50]

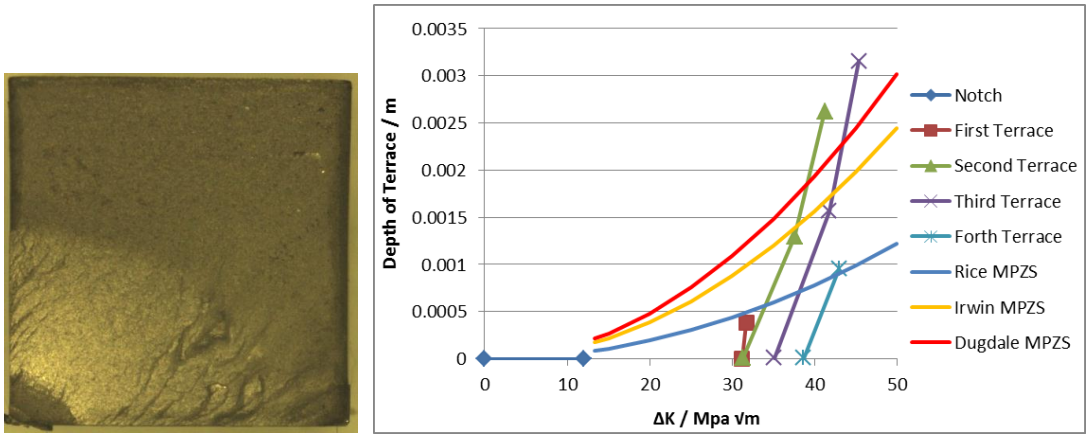

Figure 6-9: Fracture surface of CNB tested at 300^{0}C, vacuum, ΔK_i=12 MPa$\sqrt{m}$, R-ratio= 0.5– for full test information see [50]

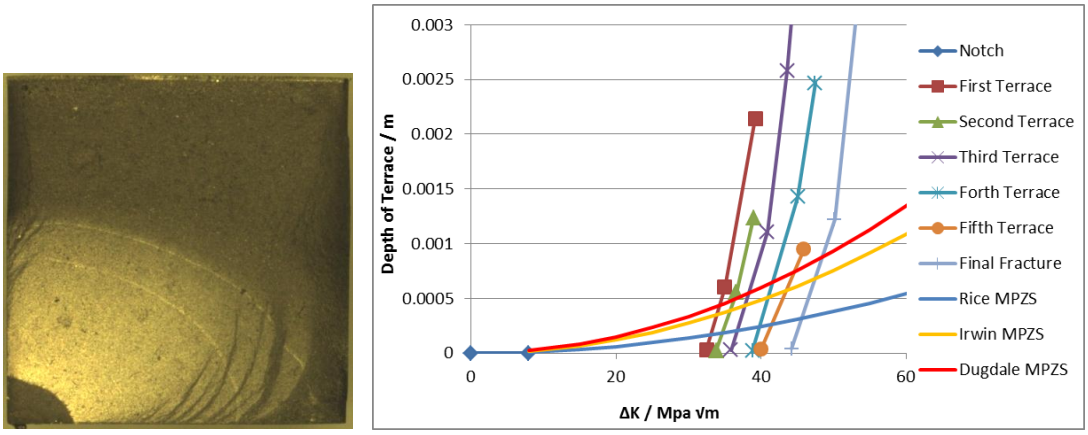

Figure 6-10: Fracture surface of CNB tested at 300^{0}C, vacuum, ΔK_i=8 MPa$\sqrt{m}$, R-ratio = 0.1– for full test information see [50]

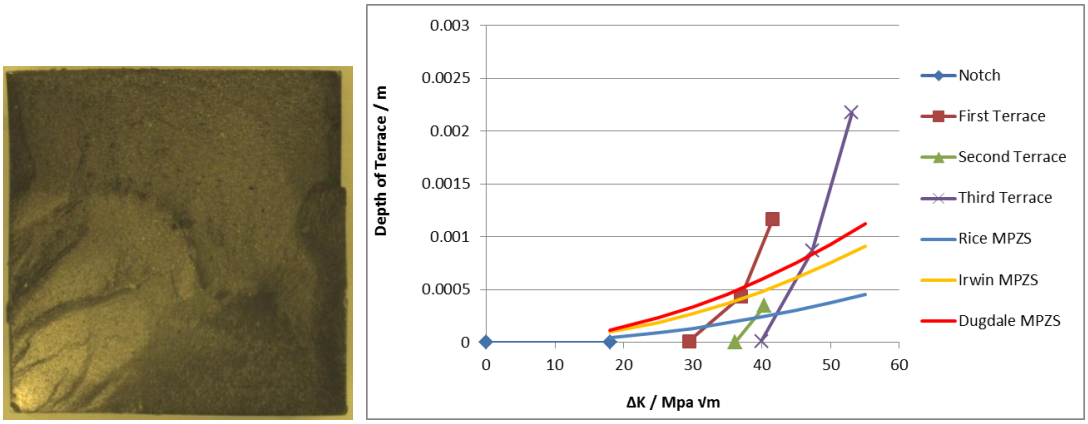

Figure 6-11: Fracture surface of CNB tested at 300^{0}C, vacuum, ΔK_i=18 MPa $\sqrt{m}$, R-ratio = 0.1– for full test information see [50]

T/ °C	Environment	R-ratio	ΔK_i / MPa $\sqrt{m}$	Onset of terracing ΔK / MPa $\sqrt{m}$					Shows sustained deflected cracking
				Loo-Morrey [50]		Current work (Chapter 5)		In agreement	
				Rice mpzs	Dugdale mpzs	Rice mpzs	Dugdale mpzs		
300	Air	Alternating	12	26	28.5	-	-	-	Yes
300	Air	0.1	12	-	-	25	28	-	Yes
300	Vac	Alternating	12	32.5	33.5	-	-	Yes	Yes
300	Vac	0.1	12	20.5	21.5	33.5	35.5	No	Yes
300	Vac	0.5	12	34	39	-	-	-	Yes
300	Vac	0.1	8	33	34	33.5	35.5	Yes	Yes
300	Vac	0.1	18	32	37.5	33.5	35.5	Yes	Yes
600	Air	Alternating	12	53	90	-	-	-	No
600	Air	0.1	12	-	-	26	53	-	No
600	Vac	Alternating	12	25.5	26.5	-	-	No	Yes
600	Vac	0.1	12	-	-	31	38	-	Yes

Table 14: ΔK onset of terracing in U720 corner notched samples tested by Loo-Morrey [50] compared with results from current work

6.2.2 SENB samples tested prior to this work

The SENB samples analysed were from fatigue tests also carried out by Loo-Morrey as described in [50]. The specimens were 12.5x12.5x80mm, contained an initial cut of 3.5mm and were loaded in three point bend. Tests were carried out at temperatures of 20, 300 and 600°C in air and an initial ΔK_i level of 15. An R-ratio of 0.1 was used plus an extra test at 300°C with an R-ratio of 0.5. For this test the K calibration from BS ISO 12108 was used, as described in section 4.1.2.

Figure 6-12 shows the fracture surface with the template for the PZS against the deflection, showing clearly unusual deflection in the tests at 300°C. Figure 6-13 to Figure 6-16 show the fracture surfaces and the deflections from one side of the sample against the theoretical plastic zone sizes. Table 15 shows where the onset of terracing occurs in the SENB samples.

The results for the onset values of the SENB tests at 300°C in the PM U720 tested by Loo-Morrey do seem to be slightly lower than those observed for the SENB tests carried out in this work (U720 Li C&W), and for the R=0.5 they show a quite wide spread, while the deflections in the 600°C air test always stay below the Dugdale PZS, showing it expected deflection due to plane stress, which is in agreement with the results of the current work.

The test at 20°C in Figure 6-13 clearly shows no deflection at all, which is in agreement with reports by previous workers [50, 91].

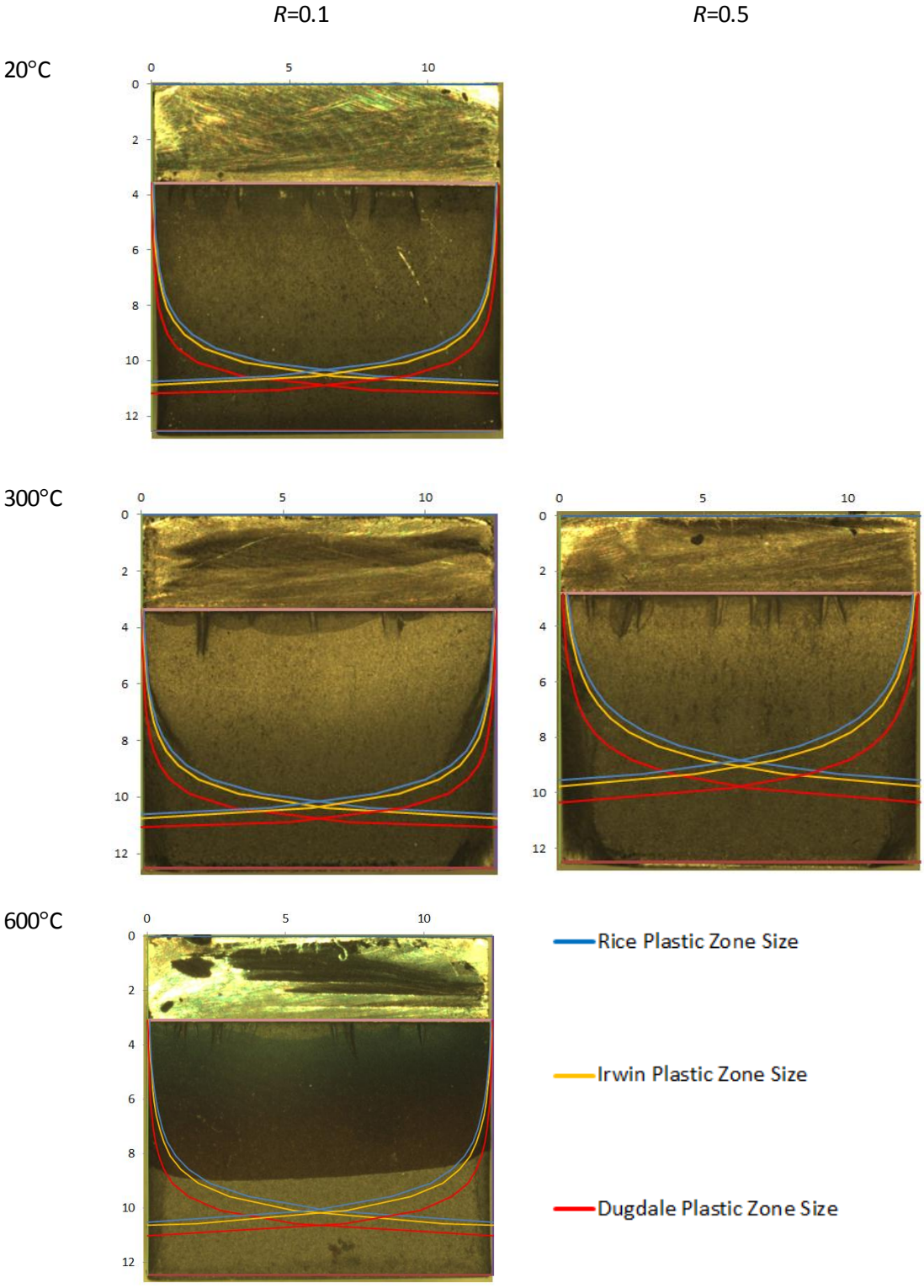

Figure 6-12: SENB samples tested at 20, 300 and 600^{0}C in air and 300^{0}C in vacuum, ΔK_i=15 MPa$\sqrt{m}$, R-ratio = 0.1, template has been applied to show plane stress plastic zone sizes

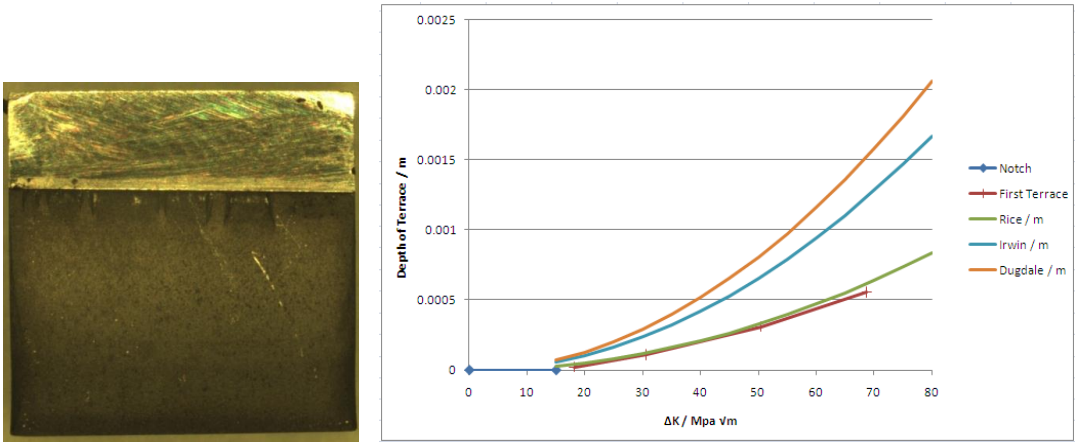

Figure 6-13: Fracture surface of SENB tested at 20^0C, air, ΔK_i=15 MPa $\sqrt{m}$, R-ratio = 0.1- for full test information see [50]

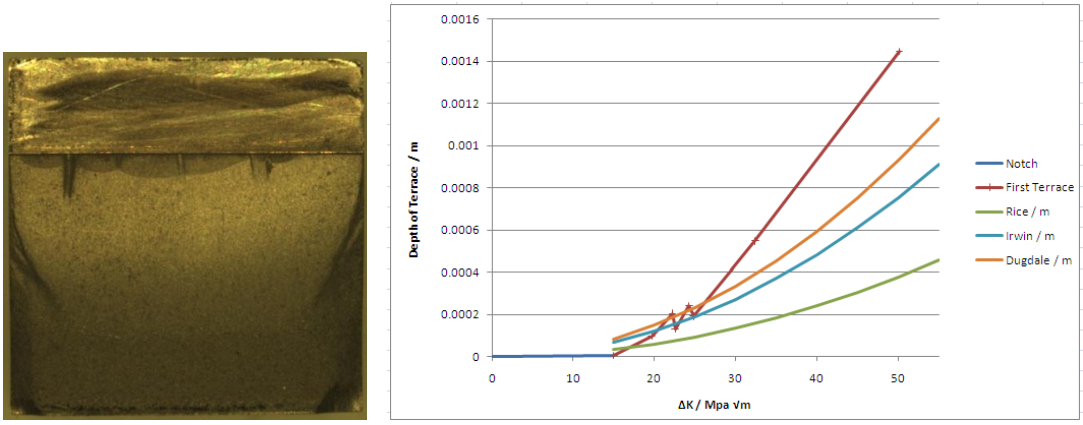

Figure 6-14: Fracture surface of SENB tested at 300^0C, air, ΔK_i=15 MPa $\sqrt{m}$, R-ratio = 0.1- for full test information see [50]

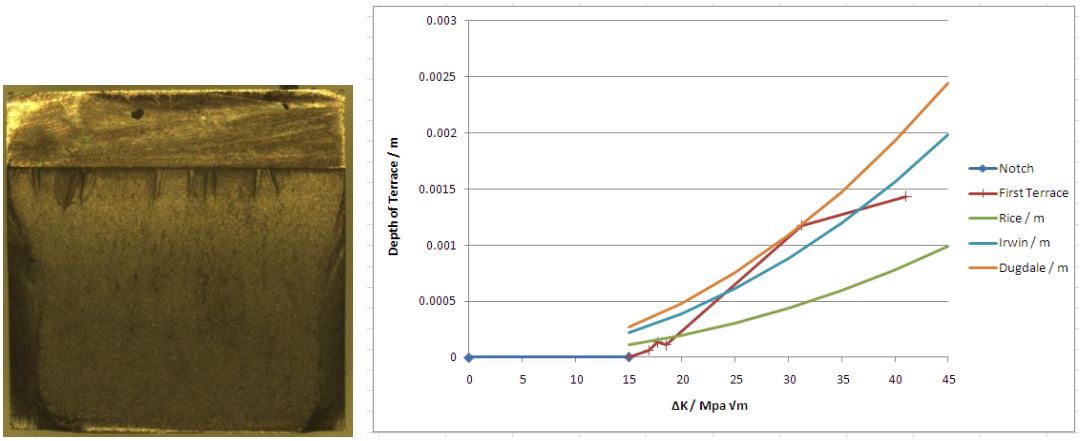

Figure 6-15: Fracture surface of SENB tested at 300^0C, air, ΔK_i=15 MPa $\sqrt{m}$, R-ratio = 0.5- for full test information see [50]

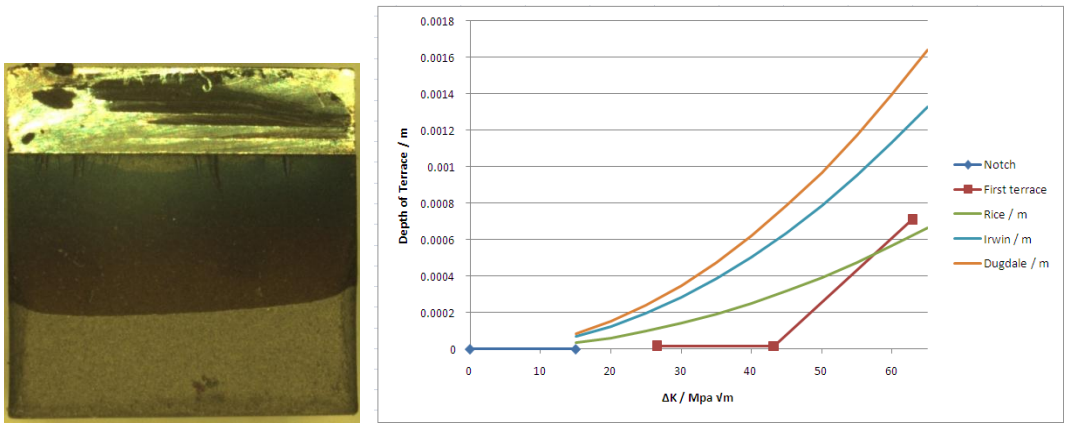

Figure 6-16: Fracture surface of SENB tested at 600^{0}C, air, ΔK_i=15 MPa $\sqrt{m}$, R-ratio = 0.1- for full test information see [50]

Temp ^{o}C	R-ratio	Onset of terracing ΔK / MPa √m in Loo-Morrey's [50] samples		Onset of terracing ΔK / MPa √m in current work (see Chapter 5)	
		Rice MPZS	Dugdale MPZS	Rice MPZS	Dugdale MPZS
20	0.1	-	-	N/A	N/A
300	0.1	17	21.5	22.5	26
300	0.5	19.5	30	N/A	N/A
600	0.1	57.5	-	27.5	-

Table 15: ΔK_{onset} of terracing in U720 SENB samples in air compare to U720Li C&W SENB in current work

6.2.3 Long dwell CNT samples tested at the University of Birmingham

Fatigue tests have been carried out on corner notched in tension (CNT) samples at the University of Birmingham by Dr Hangyue Li. The aim of this work was to consider fatigue propagation under a more typical engine life cycle – with far longer dwells at higher temperatures. The material tested was U720Li C&W in 7 by 7mm bars. The R-ratio of the tests was 0.1 and P_{max} was 26kN. Vacuum tests have been carried out at temperatures of 600 or 650°C using trapezoidal dwell waveforms of either 1-120-1-1 or 1-3600-1-1. Two air tests were also carried out at 525 and 550°C with a 3600 sec dwell. Tests were precracked in air. To speed up testing a 1-1-1-1 waveform was used for a number of cycles between the long dwell cycles. This was carried out through approximately half the sample, which is of interest, and then the crack was grown out under a 1-1-1-1 waveform and at room temperature to final failure. On the fracture surface this is the area that is not heat tinted, and this is not used for the analysis. Pickard's calibration is also mostly not valid in this area. Table 16 is the test matrix for the analysed specimens.

Sample	Temperature (°C)	Environment	Waveform	ΔK_i (MPa√m)
CC047	525	Air	1-3600-1-1	17.2
CX020	550	Air	1-3600-1-1	16.8
CX037	600	Vacuum	1-3600-1-1	17.3
CX034	650	Vacuum	1-3600-1-1	14.3
CX045	600	Vacuum	1-120-1-1	16.2
CX031	650	Vacuum	1-120-1-1	17.3
CX033	650	Vacuum	1-120-1-1	16.5

Table 16: Tensile corner notch test matrix conducted at Birmingham University

The *K* calibration for the tensile corner notch geometry test is as follows, where *B* is the width of the sample and *W* is the depth, using the Pickard calibration [94] for a corner crack in tension:

$$K = \frac{(1-R)Y P_{max}\sqrt{\pi a}}{WB}$$

Equation 6-1

$$Y = 0.6799 + 0.119\frac{a}{W} - 1.2266\frac{a}{W}^2 + 7.8729\frac{a}{W}^3 - 10.396\frac{a}{W}^4 + 4.714\frac{a}{W}^5$$

Equation 6-2

The effect of dwell on the sustained deflected crack growth can be assessed from these fracture surfaces. Based on previous results, at 650°C and below in vacuum, sustained deflected cracking is expected to occur. For the tests below 600°C (525 and 550°C) sustained deflected cracking in air might be possible as well, but could also be suppressed.

The template for CNT was used to analyse whether sustained macroscopic deflection was present, for each of the samples. The results are shown in Figure 6-17 to Figure 6-23.

The two tests in air clearly show no unusual deflection in Figure 6-18 and Figure 6-17, this may indicate the temperatures of 525 and 550°C are too high for sustained deflection to occur in air and the result is as it would be expected if dwell was not present. Therefore dwell does not seem to affect SMDCG in air.

Some very strong deflection exceeding both plastic zone sizes are seen in Figure 6-19. These are not showing terracing, and seem atypical for SMDCG these are also observed in Figure 6-21, in the 600°C vacuum test with the 120 s dwell and the 600°C vacuum test with 3600 s dwell which also shows deflections larger than the Dugdale PZS, although these are not as pronounced.

In the current work, no major difference between 600 and 650°C has been observed.

In contrast, none of the 650 vacuum tests exceed the Dugdale PZS, one of the 120 s dwell tests clearly exceed the Rice PZS (see Figure 6-22), the other 120s (Figure 6-23) and the 3600s (Figure 6-20) dwell tests, show very little deflection. The difference between 600 and 650°C is difficult to explain.

The effect of the dwell on the occurrence of sustained deflected crack growth is unclear, but it might be reducing the tendency for deflection. While sustained deflected crack growth was expected in all tests to some extent, based on the results of the current work in vacuum at 600 and 650°C, only a few have shown clear deflection beyond the defined PZS.

Onset of deflection can be seen at ΔK values of 35MPa√m for the Rice, and 41.5MPa√m for the Dugdale PZS for the test with 120s dwell and 41.5 and 52MPa√m for the test with 3600s dwell respectively. These values are higher than the expected onset values based on the samples tested without dwell in vacuum, in particular for the 3600s dwell, where they are near the expected levels where plastic collapse will occur.

It is not clear what the mechanism of deflection observed in the very long dwell tests might be. The deflection may also be caused by creep tunnelling effects [92]. Vacuum long dwell at high temperature may be expected to show some significant creep effects. This is supported by the fact that the sample with the longer dwell time has also shown the significantly stronger deflection. It is however unclear why it can be only seen at 600°C, and not at 650°C.

Air

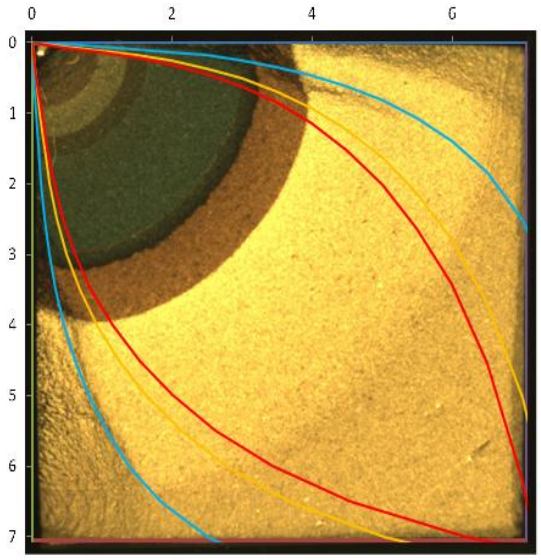

Figure 6-17: CNT sample tested at 525°C, air, waveform 1-3600-1-1 (sample CC047)

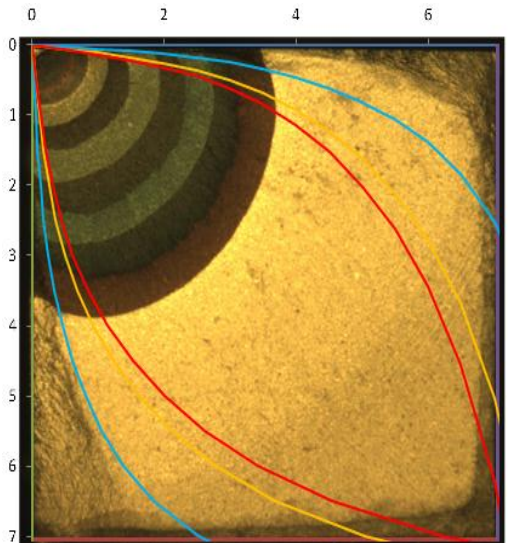

Figure 6-18: CNT sample tested at 550°C, air, waveform 1-3600-1-1 (sample CX020)

Vacuum

600°C

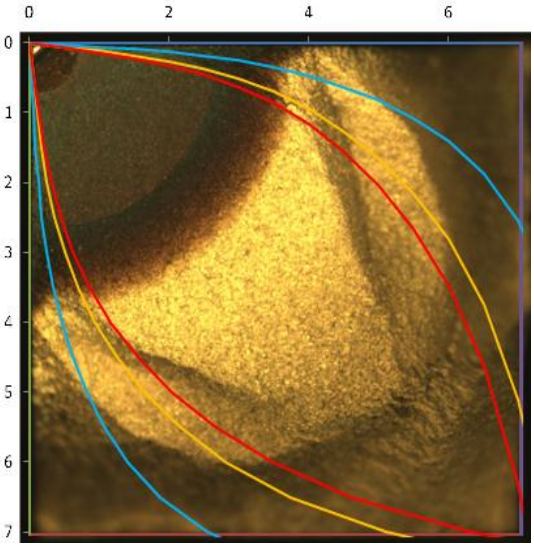

Figure 6-19: CNT sample tested at 600°C, vacuum, waveform 1-3600-1-1 (sample CX037)

650°C

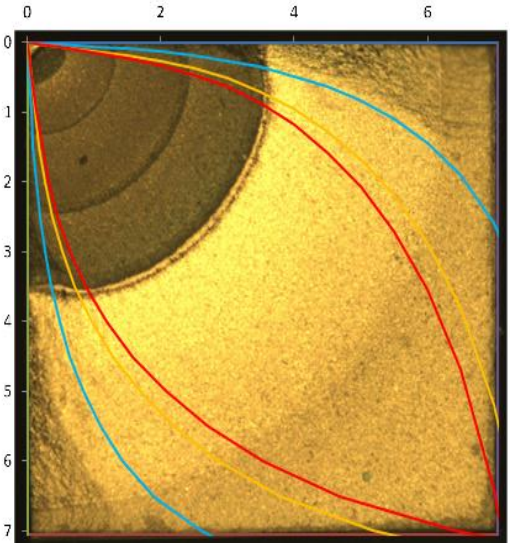

Figure 6-20: CNT sample tested at 650°C, vacuum, waveform 1-3600-1-1 (sample CX034)

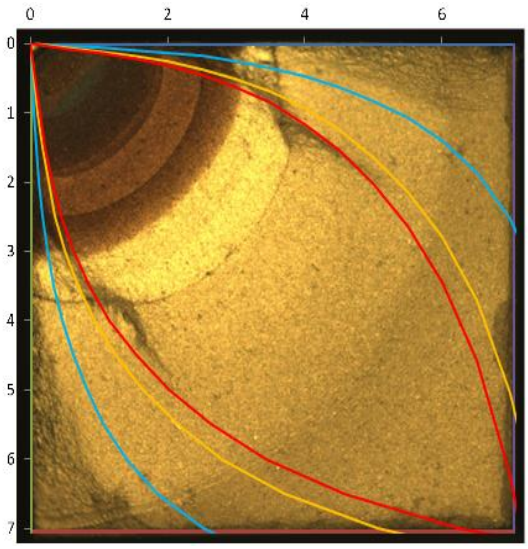

Figure 6-21: CNT sample tested at 600°C, vacuum, waveform 1-120-1-1 (sample CX045)

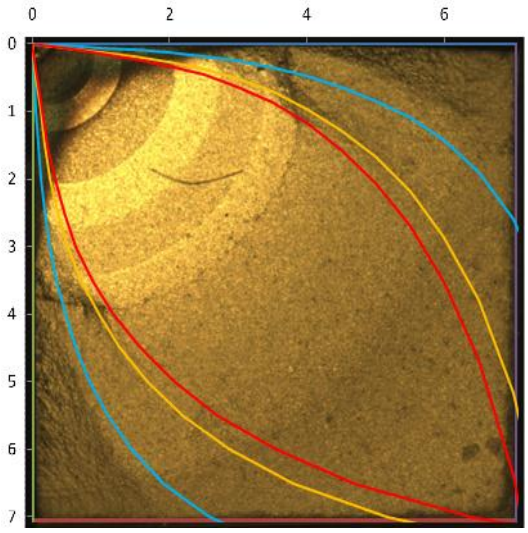

Figure 6-22: CNT sample tested at 650°C, vacuum, waveform 1-120-1-1 (sample CX031)

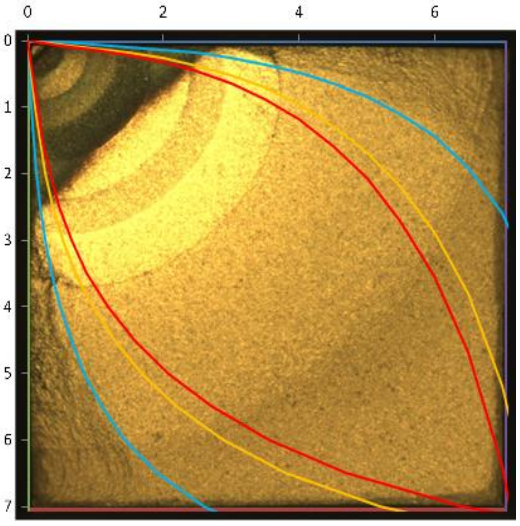

Figure 6-23: CNT sample tested at 650°C, vacuum, waveform 1-120-1-1 (sample CX033)

6.2.4 Bithermal tests at the University of Birmingham

A number of bithermal test have been carried out at the University of Birmingham by Dr Hangyue Li on CNT samples. All tests were carried out in air, precracked at room temperature, and then grown out with a 1-1-1-1 cycle. Test conditions are described in detail in Table 17.

Again any deflection in the final growth out stage at room temperature can be ignored, as it will be related to expected shear lip formation due to plastic collapse/plane stress effects.

400 and 650°C were chosen as they are representative of temperatres that a firtree/rim of a disc would experience during different phases of a flight cycle. While the maximum operating temperature is above the 'threshold' temperature for SDMGC, these areas will also experience lower temperatures (e.g. during cruise). Lower rated engines may have a lower maximum operating temperature that potentially may be in the SMDCG regime. This is represented by samples CC001-C004, with temperatures varying in the region of 240-540°C. [99]

The tests carried out between 400 and 650°C, shown in Figure 6-26 to Figure 6-28 show very limited deflection, which fits with the expected effect of the higher temperature.

Some small deflections appearing and disappearing can be observed in Figure 6-25 (the detailed view of the edge of sample CC011), changing between the beachmarks, which suggests that, the higher temperature cycles do switch back from deflection just after onset, so switching between lower and higher temperature appears to cancel the SMDCG effect out.

Changing the loads, and load ratio between the two temperatures or the initial ΔK_i did not seem to affect the sustained deflected crack growth.

For lower temperature tests, Figure 6-32 (sample CC01) shows large deflections and terracing, Figure 6-30(CC02) and Figure 6-31 (CC04) show some deflection as well. These tests were carried out in the temperature ranges between 240 and 540^{o}C, both temperatures may be showing the sustained deflection. CC001 shows a greater degree of deflection than the other, possibly due to the fact that crack growth was started at a shorter crack length (but also a smaller ΔK), while the CC002 and CC004 have a long precrack and do not grow over as much crack length at temperature.

Figure 6-33 (CC003) does not show any deflection, despite being in a similar temperature regime, however a significant part of the crack growth has been carried out at 500°C, and only a short time at 300°C (only the last segment). This crack is therefore dominated by the higher temperature crack growth.

Specimen ID	Size (mm^2)	Test condition										
		T1 (°C)	P_{max1} (kN)	*T2* (°C)	P_{max2} (kN)	*T3* (°C)	P_{max3} (kN)	a_0 (mm)	Δa (mm)	No. segs	ΔK_i	*R*
CC013	10×10	400	44	650	44			0.89	0.28-0.81	8	14.4	0.1
CC011	10×10	650	50	400	56			2.65	0.15	10	30	0.1
CC016	10×10	650	56	400	50			2.64	0.16	10	33.4	0
CC012	10×10	650	50	400	56			2.57	0.08, 0.04	20	29.3	0
CC014	10×10	650	50	400	56			2.63	0.04, 0.08	20	29.8	0.1
CC002	7×7	240	25	510	26.25	300	25	2.37	0.21	6	30	0.1
CC004	7×7	260	28.25	540	25	300	28.25	2.63	0.21	6	37	0.1
CC001	7×7	260	28.25	540	25			0.97	*	10	19.4	0.1
CC003	7×7	500	25	300	25			3.37	0.31	1	41.7	0.1

Table 17: Testing matrix of bithermal tests carried out in air with 1-1-1-1 cycle, showing sample number and size, test temperatures and loads, initial ΔK_i, R-ratio, number of segments (how often the temperature was switched), inital crack length a_0 and distance Δa at which temperature is changed (* Except the first and last segments each segment in this test has an equal number of cycles of 1700) [99]

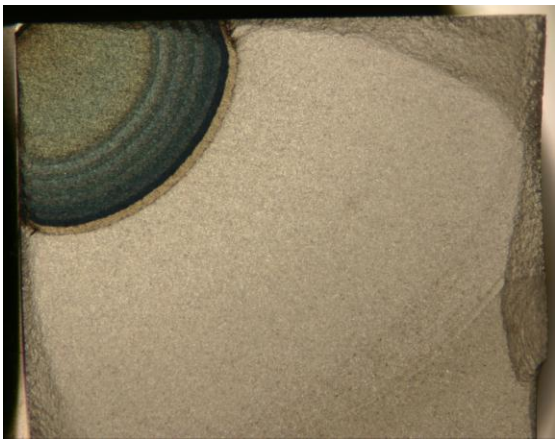

Figure 6-24: Fracture surface of CNT test carried out in air at 650 and 400°C (more details in Table 17) (sample CC011)

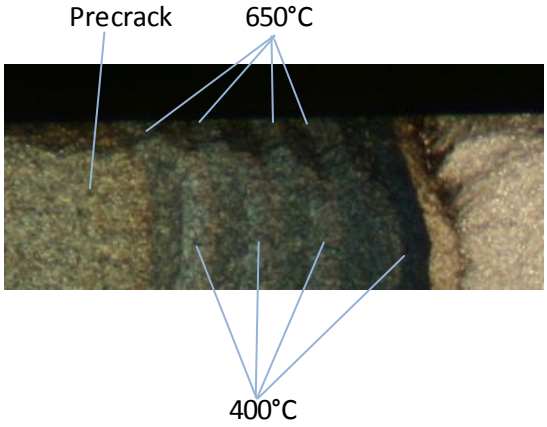

Figure 6-25: Detailed view of deflection of sample CC011

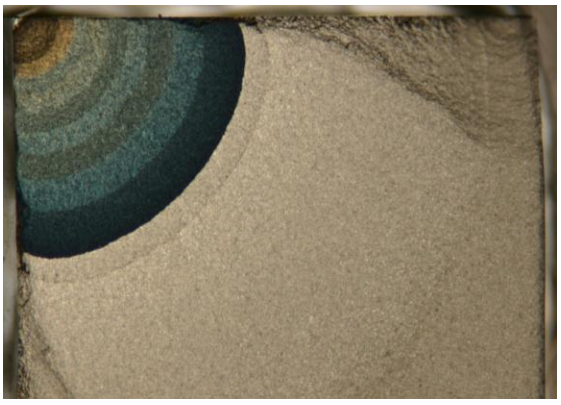

Figure 6-26: Fracture surface of CNT test carried out in air at 400 and 650°C (more details in Table 17) (sample CC013)

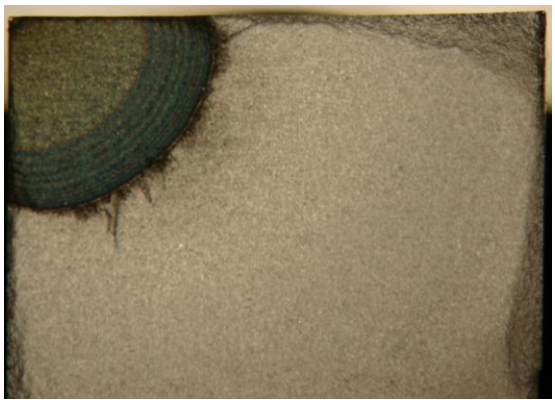

Figure 6-27: Fracture surface of CNT test carried out in air at 650 and 400°C (more details in Table 17) (sample CC012)

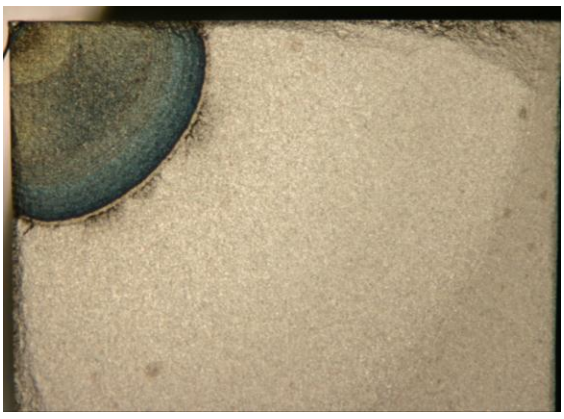

Figure 6-28: Fracture surface of CNT test carried out in air at 650 and 400°C (more details in Table 17) (sample CC014)

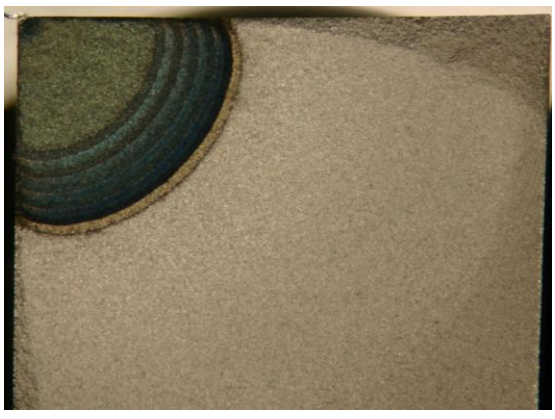

Figure 6-29: Fracture surface of CNT test carried out in air at 650 and 400°C (more details in Table 17) (sample CC016)

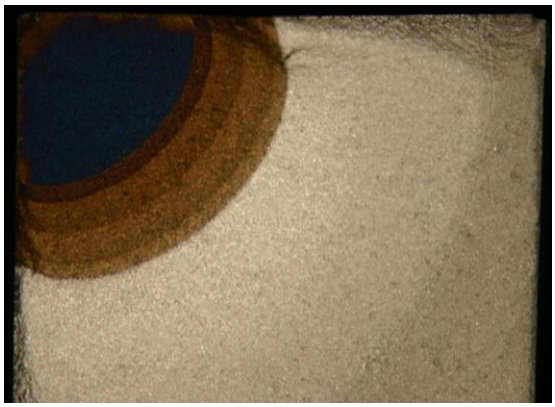

Figure 6-30: Fracture surface of CNT test carried out in air at 240, 510 and 300°C (more details in Table 17) (sample CC002)

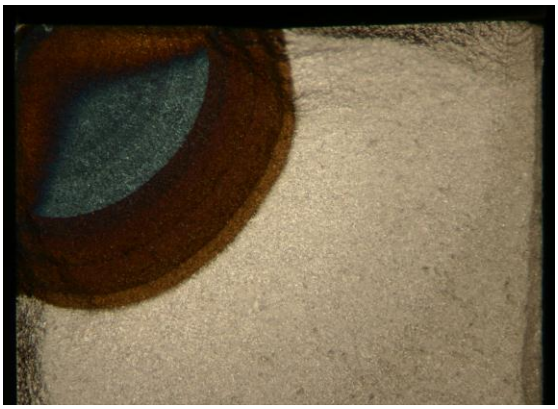

Figure 6-31: Fracture surface of CNT test carried out in air at 260, 540 and 300°C (more details in Table 17) (sample CC004)

Figure 6-32: Fracture surface of CNT test carried out in air at 260 and 540°C (more details in Table 17) (sample CC001)

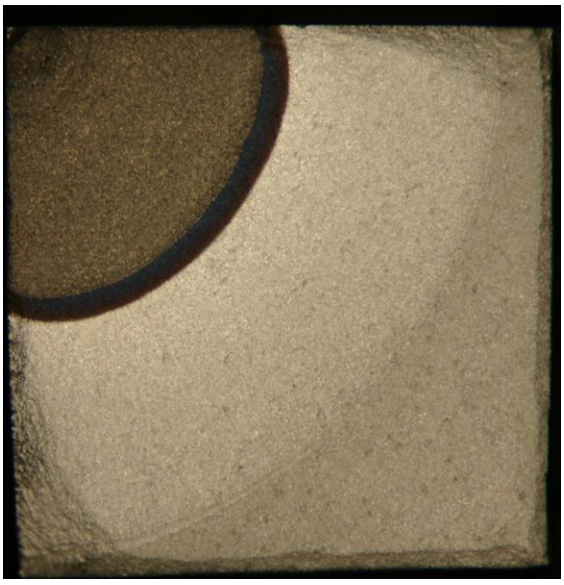

Figure 6-33: Fracture surface of CNT test carried out in air at 500 and 300°C (more details in Table 17) (sample CC003)

6.2.5 Tension-tension sample tested at Rolls Royce

This U720Li C&W sample (same specification as tested in this work) has been fatigue tested in tension under partial vacuum (exact values could not be retrieved) at a test temperature of 675°C. It was a strain controlled test carried out at R-R, at 0.74% strain on a 7x7mm sample in a 1-1-1-1 cycle [93]. The crack naturally initiated from the corner. The fracture surface in Figure 6-34 shows large deflected areas from the free surfaces. The challenge was to identify if this was "normal" deflection in a plane stress dominated region or was showing the sustained macroscopic deflection that is the topic of this thesis.

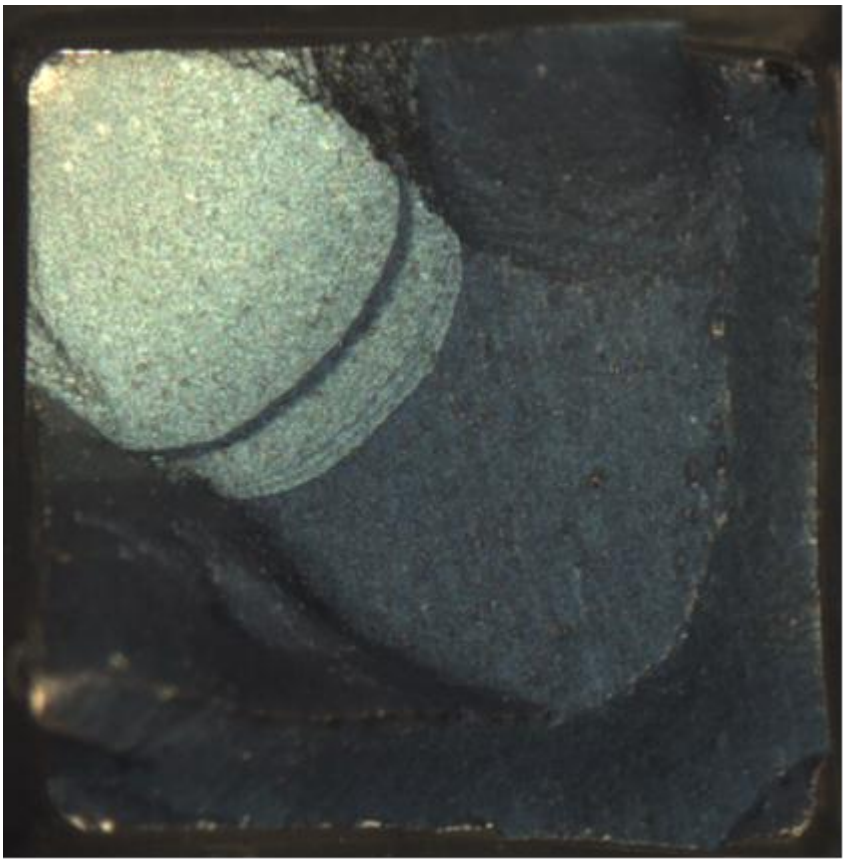

Figure 6-34: Strain controlled sample fracture surface tested at 675°C in partial vacuum

Although strain was controlled for this sample and the applied load was varied continuously, the ΔP was on average around 58kN, only varying within ± 3.5kN. The test data available was load (and stress) as it varied with cycles, and it was not possible to calculate the load as a function of crack length, in the absence of crack growth data for this temperature. So the assumption that ΔP was constant at 58kN seemed reasonable. In the same manner an approximate R-ratio of -0.25 (± 0.05) was used.

This assumption allowed calculation of the K levels and hence PZS for the increasing crack lengths and these were then plotted in the template for a CNT. The crack initiated from a corner hence the Pickard calibration for a corner crack tension has been used, as described in section 6.2.3.

$$K = \frac{(1-R)YP_{max}\sqrt{\pi a}}{WB}$$

Equation 6-3

$$Y = 0.6799 + 0.119\frac{a}{W} - 1.2266\frac{a}{W}^{2} + 7.8729\frac{a}{W}^{3} - 10.396\frac{a}{W}^{4} + 4.714\frac{a}{W}^{5}$$

Equation 6-4

The template in Figure 6-35 clearly shows that the deflection is smaller than all the plane stress plastic zone sizes, hence these deflections seem not to be SMDGC, as defined in this work.

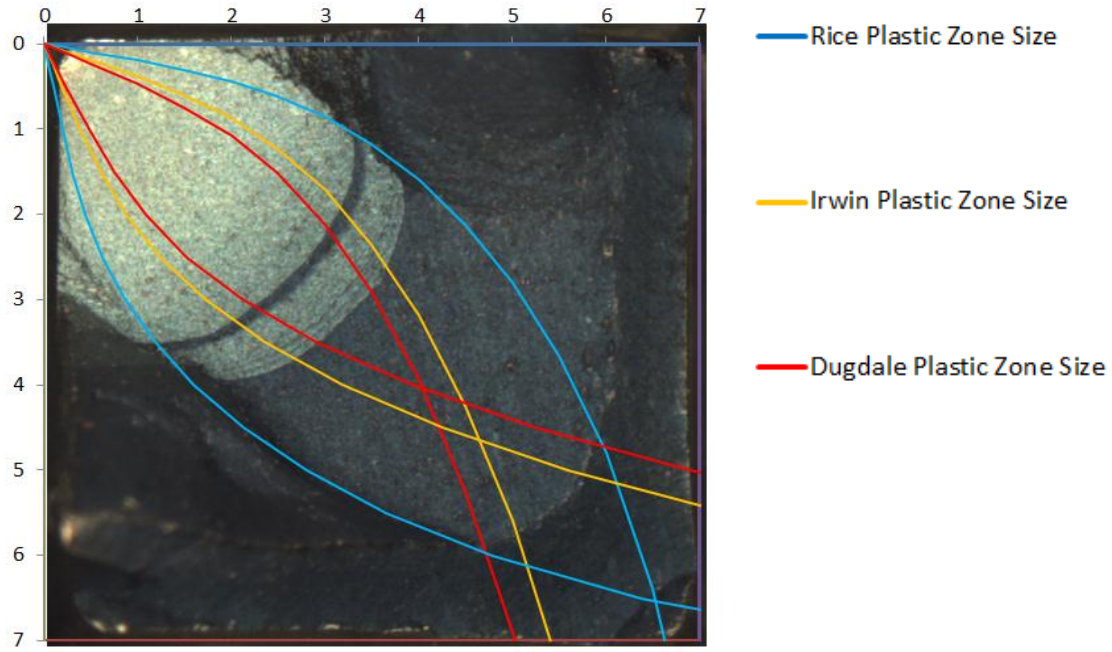

Figure 6-35: Template applied to strain controlled test, assuming a constant ΔP of 58kN and R of -0.25

SEM Fractography has been carried out on this sample in both deflected and the planar regions to observe whether the mechanisms observed are similar to the samples tested in the main test programme reported in this thesis in Chapter 5. Figure 6-36 shows from which area on the sample the relevant micrographs have been taken. The deflection from the top edge is shown in more detail in Figure 6-37 to Figure 6-39, and regions from the side edge deflection are shown in Figure 6-40 to Figure 6-42. These show secondary cracks in the areas between the planar and non-planar crack growth. The planar region viewed in Figure 6-43 and Figure 6-44 shows Stage II crack growth and secondary cracking as well. More detail is given in the figure captions. It seems that the same mechanism is observed here as in the U720Li C&W samples tested in the current work.

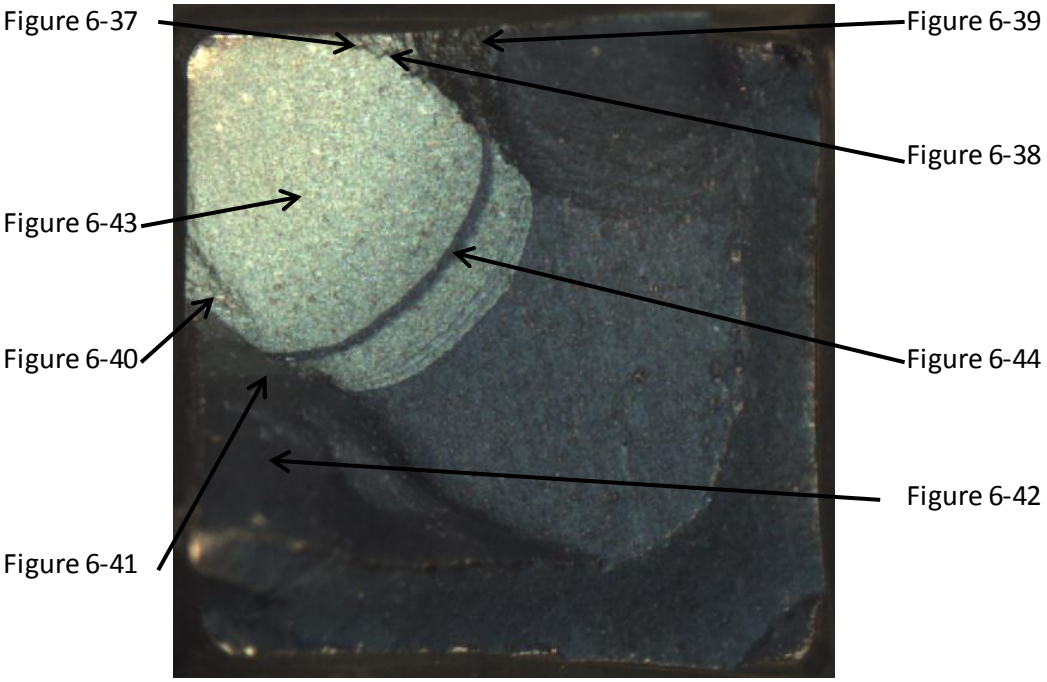

Figure 6-36: Location of SEM pictures

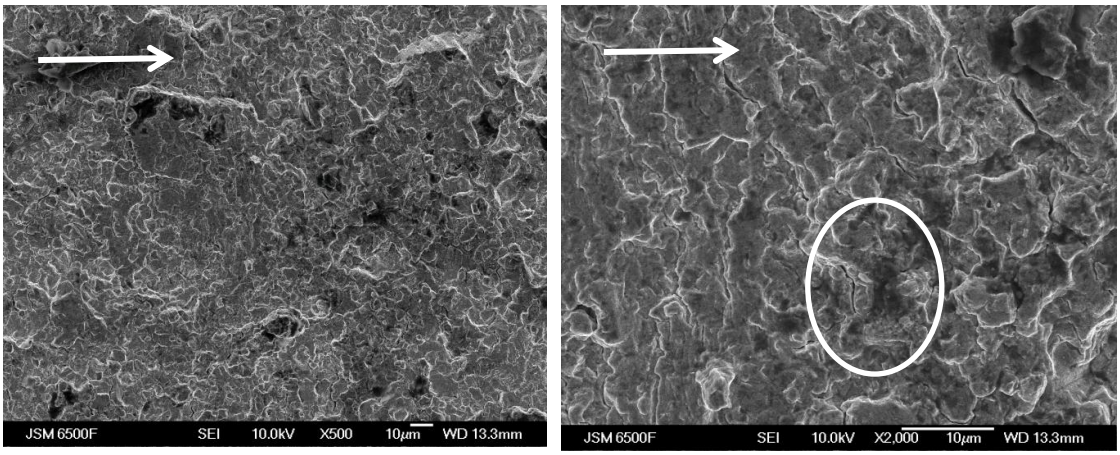

Figure 6-37: Fracture surface of the strain controlled test of U720Li C&W at 675°C in partial vacuum in the deflected region at the top edge at c=1.7mm and an estimated $\Delta K \approx 64 MPa\sqrt{m}$ (Arrow indicates crack growth direction) a) at low magnification showing stage II growth (b) at high magnification showing slip traces and secondary cracks (marked by circle)

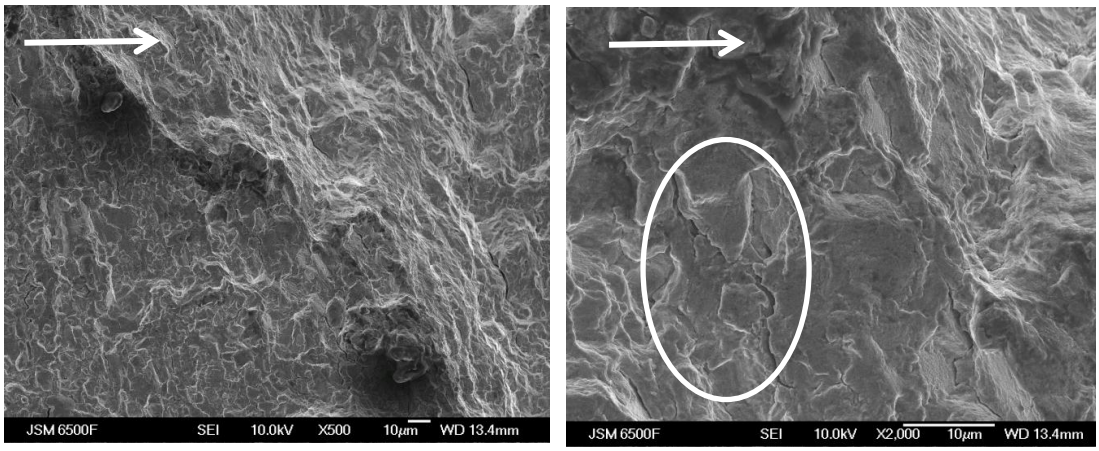

Figure 6-38: Fracture surface of the strain controlled test of U720Li C&W at 675°C in partial vacuum in the deflected region at the top edge at c=2.4mm and an estimated ΔK≈82MPa $\sqrt{m}$ (Arrow indicates crack growth direction) a) at low magnification showing stage II growth (b) at high magnification showing slip traces and secondary cracks (marked by circle)

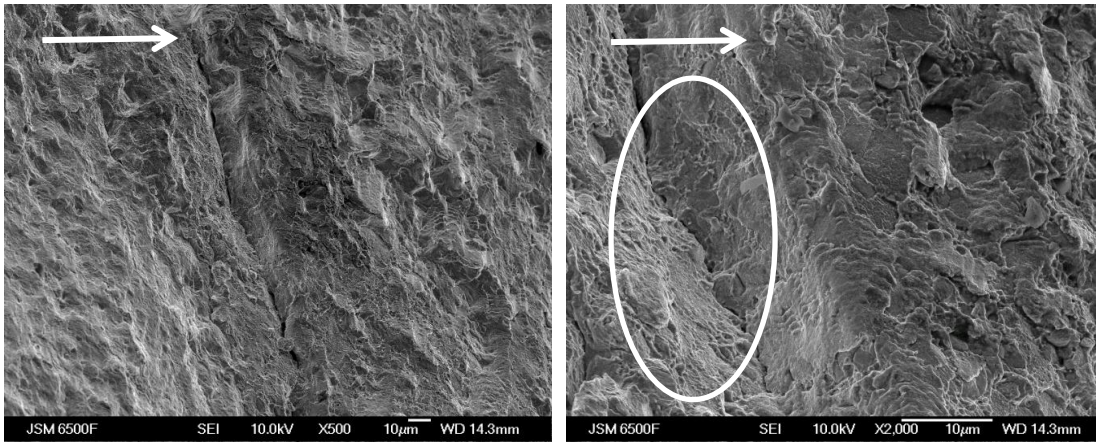

Figure 6-39: Fracture surface of the strain controlled test of U720Li C&W at 675°C in partial vacuum in the deflected region at the top edge at c=3.1mm and an estimated ΔK≈104MPa$\sqrt{m}$(Arrow indicates crack growth direction) a) at low magnification showing deflected and planar terrace and large secondary crack between them (b) at high magnification showing large secondary crack (marked by circle)

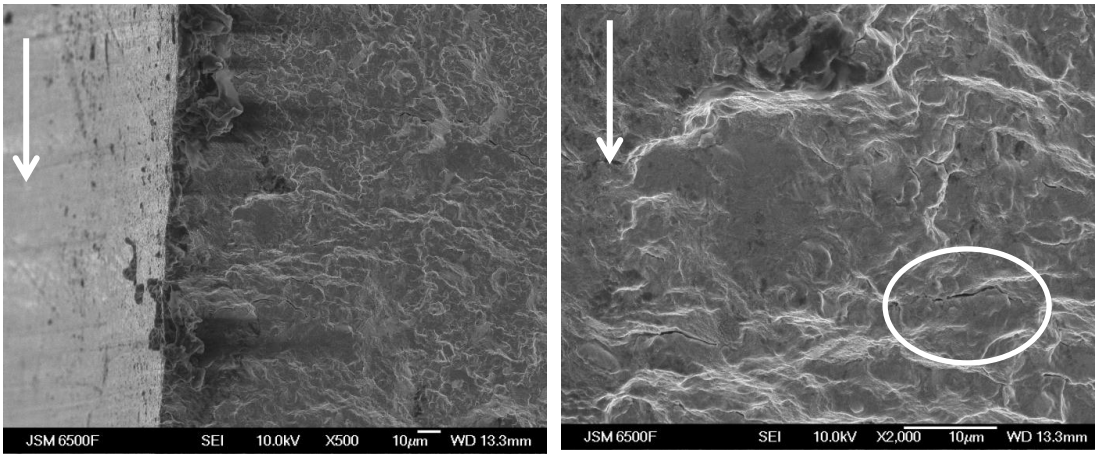

Figure 6-40: Fracture surface of the strain controlled test of U720Li C&W at 675°C in partial vacuum in the deflected region at the side edge at c=2.2mm and an estimated ΔK≈76.8MPa $\sqrt{m}$ (Arrow indicates crack growth direction) a) at low magnification showing stage II growth (b) at high magnification showing slip traces and secondary cracks (marked by circle)

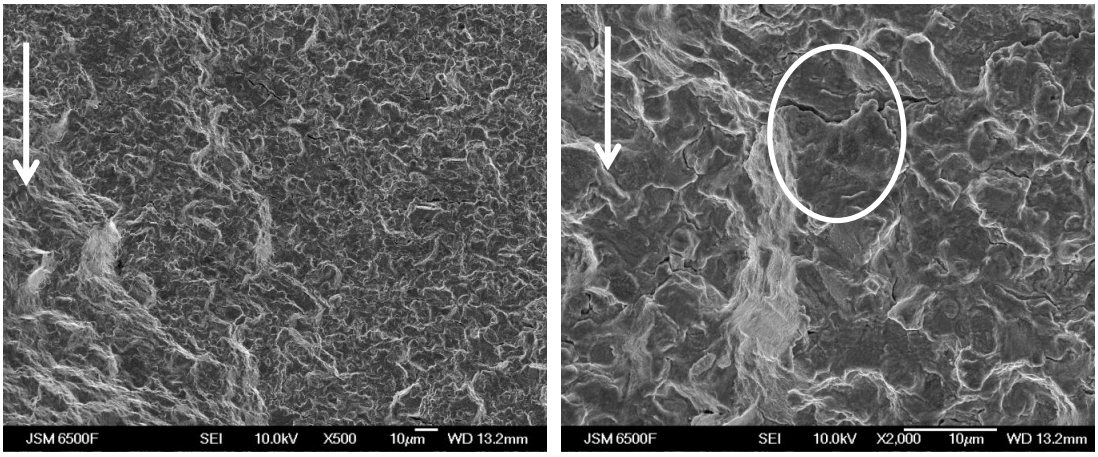

Figure 6-41: Fracture surface of the strain controlled test of U720Li C&W at 675°C in partial vacuum in the deflected region at the side edge at c=2.4mm and an estimated ΔK≈83MPa $\sqrt{m}$ (Arrow indicates crack growth direction) a) at low magnification showing stage II growth (b) at high magnification showing slip traces and secondary cracks (marked by circle)

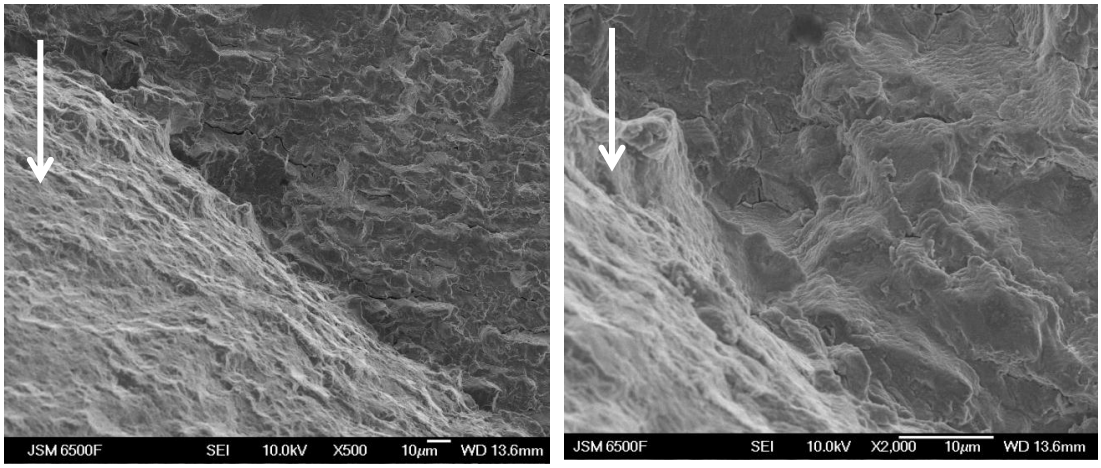

Figure 6-42: Fracture surface of the strain controlled test of U720Li C&W at 675°C in partial vacuum in the deflected region at the side edge at c=3.1mm and an estimated ΔK≈103MPa $\sqrt{m}$ (Arrow indicates crack growth direction) a) at low magnification showing transition between planar and deflected crack growth (b) at high magnification showing slip traces and secondary cracks

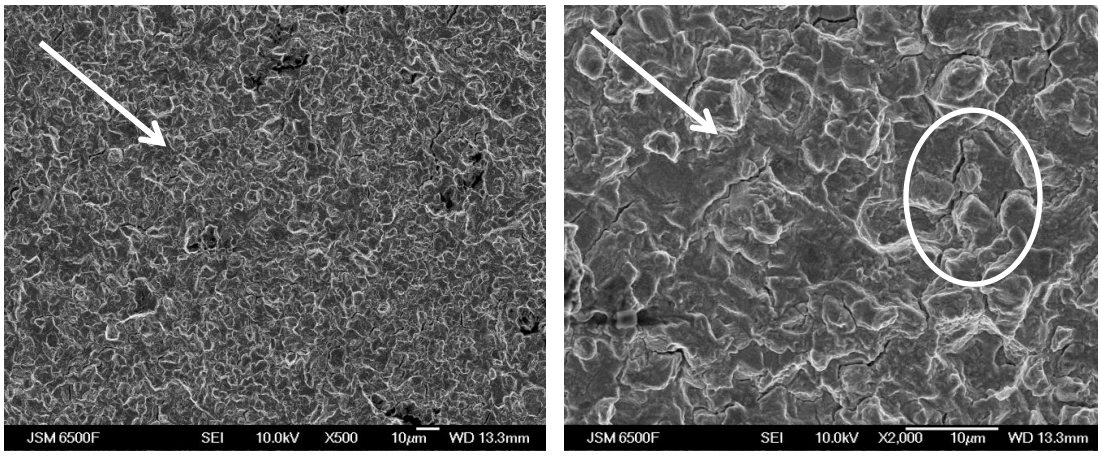

Figure 6-43: Fracture surface of the strain controlled test of U720Li C&W at 675°C in partial vacuum in the planar region in the centre at c=1.4 mm and an estimated ΔK≈58MPa $\sqrt{m}$ (Arrow indicates crack growth direction) a) at low magnification showing stage II growth (b) at high magnification showing slip traces and secondary cracks (marked by circle)

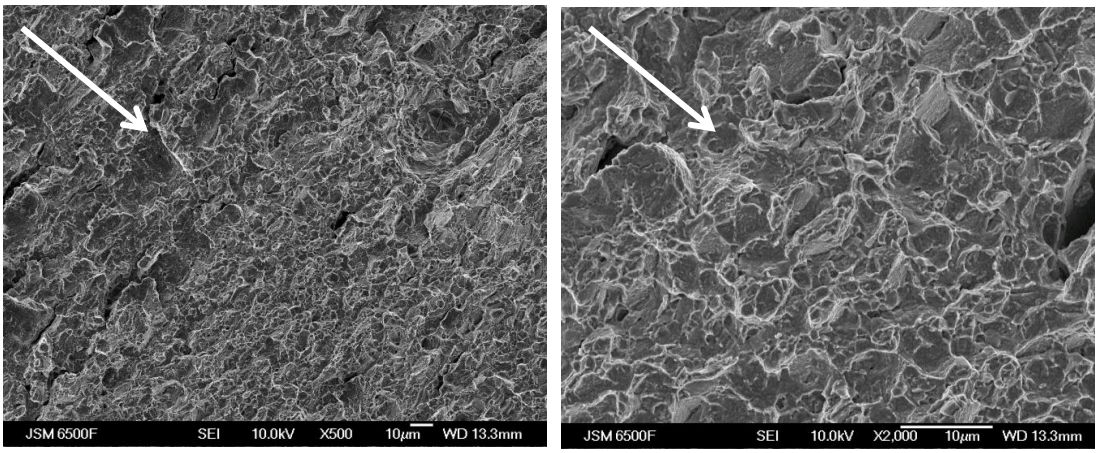

Figure 6-44: Fracture surface of the strain controlled test of U720Li C&W at 675°C in partial vacuum in the planar region in the centre at c=3.8mm and an estimated ΔK≈128MPa $\sqrt{m}$ (Arrow indicates crack growth direction) a) at low magnification showing stage II growth (b) at high magnification showing a quite faceted fracture surface

6.3 Limited Component Analysis

A small number of engine components from spin tests have also been studied in similar detail to compare with the tested samples. These deflected fractures come from spin tests have been carried out on turbine disks at Rolls Royce plc. It is important to establish whether any deflected crack growth observed under these more complex service conditions is the sustained macroscopic deflection process studied in detail in this work.

6.3.1 Firtree

The phenomenon has been reported in the rim region of a disc in a spin test carried out in partial vacuum (no further details are available). A crack was initiated in a corner of a firtree, and started deflecting towards the centre of the disc. In this area a planar crack could cause the loss of two blades, which is not so problematic; however a deflected crack initiated from the firtree could grow into the hoop stress field of the disc and potentially cause a disc failure. The position of the defect in the firtree is schematically described in Figure 6-45. The material of this disk was U720 PM (as also tested by Loo-Morrey [50], and described before). This test was carried out in the early 1990s, so it was difficult to find all the test details.

The temperatures of the test were 295°C (±10°C) at the rim of the disc and increasing towards the bore to 490°C (±10°C) and kept at these levels during the rig test. The area where the crack initiated therefore had a temperature of ~300°C, which is clearly within the temperature range in which sustained deflected crack growth was observed. In the maximum cycle the disc has 21350 rev/min and in minimum cycle 2135 rev/min, hence the R-ratio is 0.1. [100]

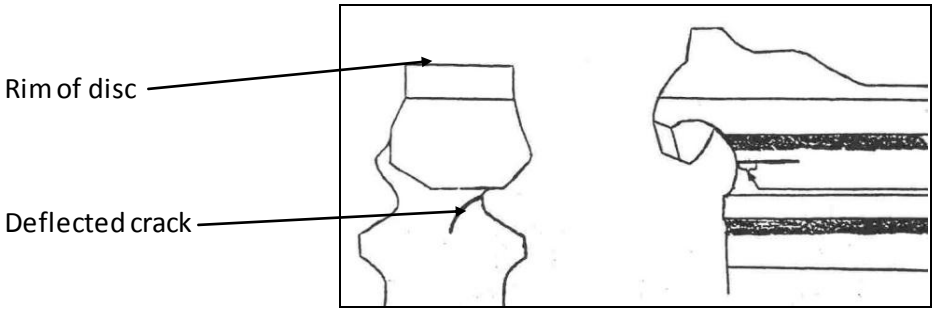

Figure 6-45: Schematic picture of firtree and deflected crack [100]

The fracture surface of the deflected crack is shown in Figure 6-46 and Figure 6-47. The crack initiated from a corner and shows a large deflection on one edge, and a smaller deflection on the other edge.

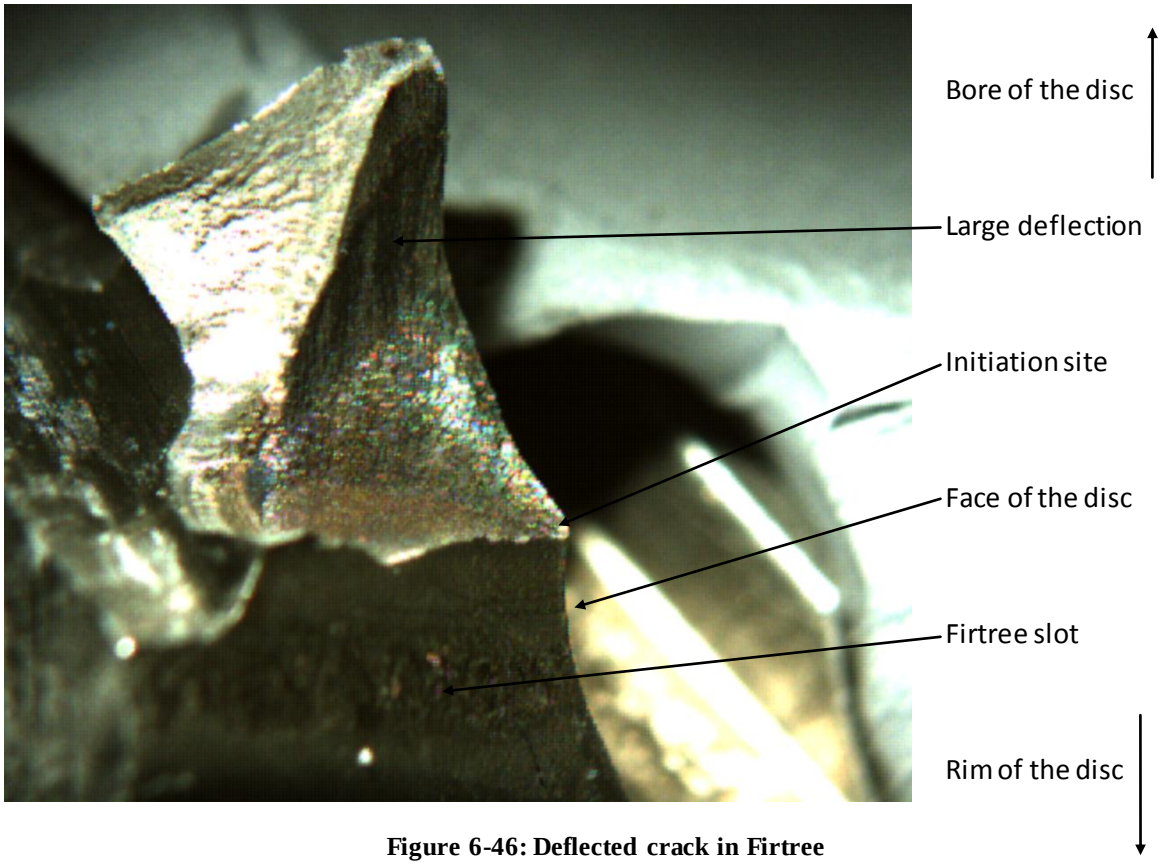

Figure 6-46: Deflected crack in Firtree

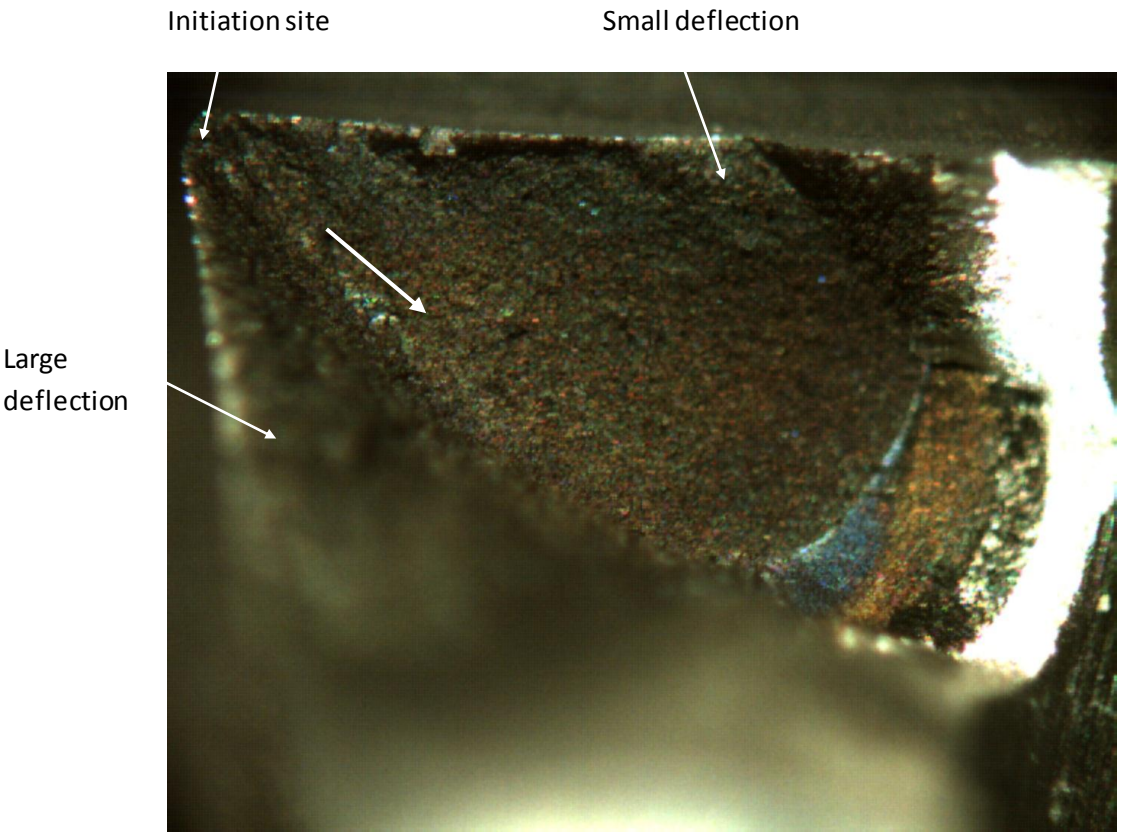

Figure 6-47: Fracture surface of deflected crack in firtree (looking from the centre of the disc, arrow indicates crack growth direction)

A stress analysis has been carried out using an existing model of an EJ200 engine high pressure turbine disc at Rolls Royce plc, using the in-house Finite Element software SC03 and the axisymmetric model of a section of the disc is shown in Figure 6-48 (this is sufficient to calculate the stresses in this disc), these sections can be combined to show the entire disc (Figure 6-49). A dummy blade weight is in the firtree in the position of the blade, with an applied load equivalent to a turbine blade.

The maximum principle stresses in the firtree are indicated in Figure 6-50. The maximum stress levels are very high in this region. Assuming that the area is mostly dominated by tensile stresses, and as the crack is initiated in the corner, the Pickard calibration for tension is used. The stresses on the 2 deflected edges have been measured at a number of points in a crack plane (for an assumed planar crack), and the respective K_{max} have been calculated for these positions, allowing us to estimate the plastic zone sizes at these positions which can be connected for the onset model.

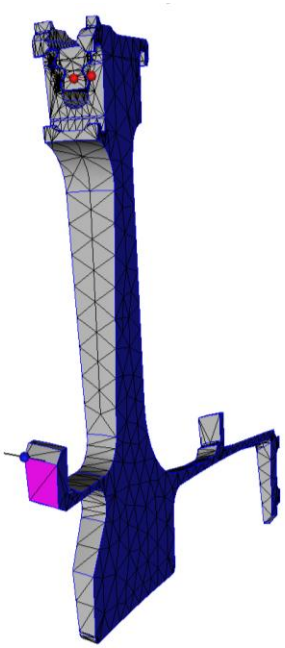

Figure 6-48: Model of turbine disc section (in SC03)

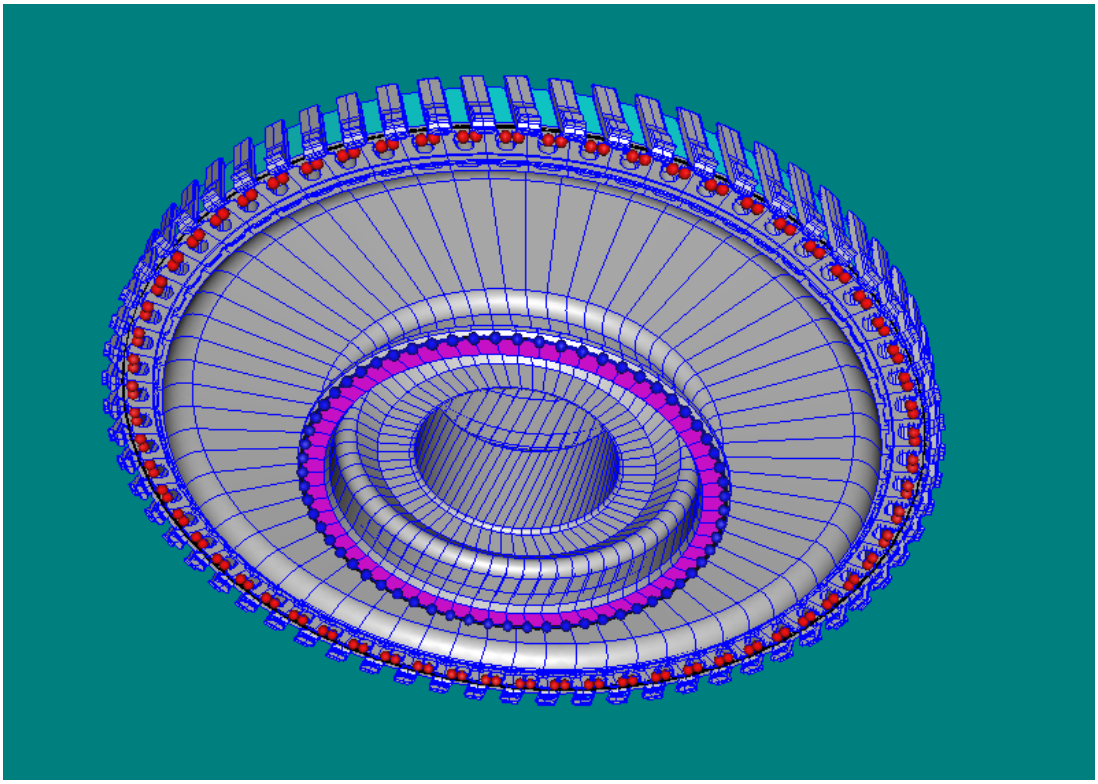

Figure 6-49: Model of turbine disc (in SC03)

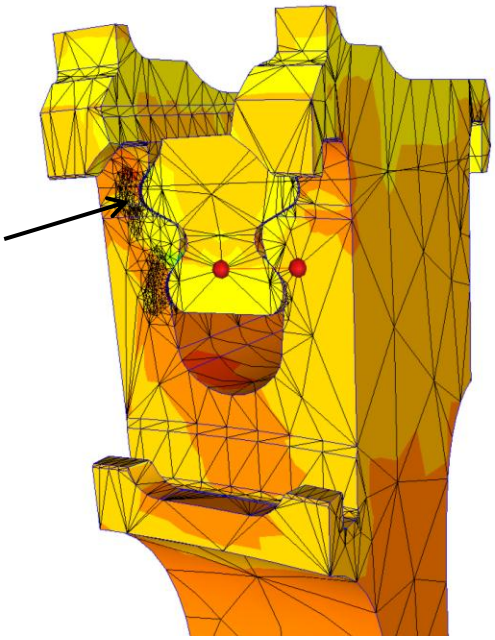

Figure 6-50: FE model of Firtree indicating maximum principle stress level (red indicating the highest levels, arrow indicating the initiation site of crack) (in SC03)

Figure 6-51 shows the fracture surface together with the expected plane stress plastic zone sizes calculated using the derived stress and temperature conditions for the more deflected side. The strongly deflected side is larger than the respective Rice PZS, but smaller than the Irwin and Dugdale PZS. It could therefore be concluded that this deflection is most likely to be the expected deflection due to plane stress rather than sustained macroscopic deflection.

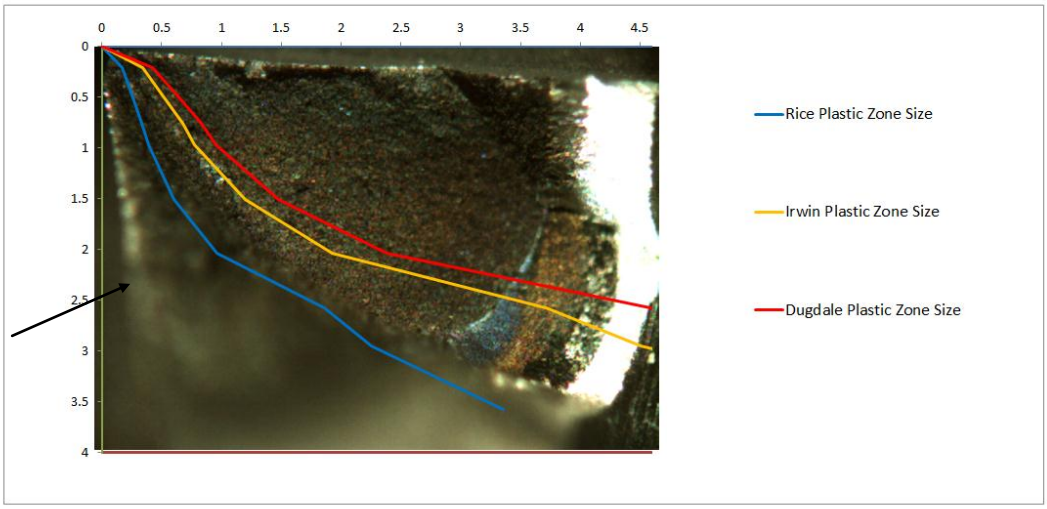

Figure 6-51: Template for large deflection at the side surface as indicated by arrow (looking on the fracture surfaces from the centre of the disc)

On the less deflected top surface in Figure 6-52 very little deflection is seen. When analysing the PZS of this side, it can be seen that all PZS are much larger than the deflection, showing that this deflection is what would be expected in the plane stress region.

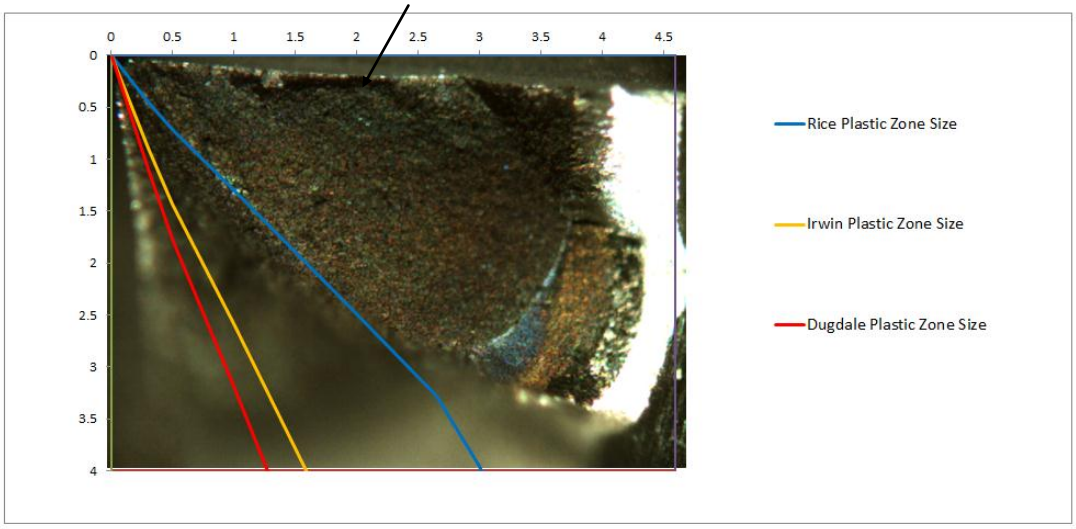

Figure 6-52: Template for (less deflected) top surface as indicated by arrow (looking on the fracture surfaces from the centre of the disc)

Fractography was performed with the FEG SEM on the planar and deflected region; the locations of the SEM pictures are shown in Figure 6-53.

The ΔK values are approximated from the stress measurements taken at the nearest position to the location of the SEM picture. The large deflection from the top edge in Figure 6-58 and Figure 6-59 show large secondary cracks and the slightly deflected region from the side edge in Figure 6-56 and Figure 6-57 show secondary cracks and larger ones in the areas between the planar and non-planar crack growth. The planar region in Figure 6-54 and Figure 6-55 shows Stage II crack growth and secondary cracking as well. More detail is described in the figure captions. It seems that the same secondary cracking mechanism is observed here as in the samples tested in this work, but it has to be noted that pictures have been taken at very high K levels (which have been achieved in the component due to its size, but are rarely found in test coupons). At such high ΔK levels it is likely that the crack growth rates are extremely high and close to final failure.

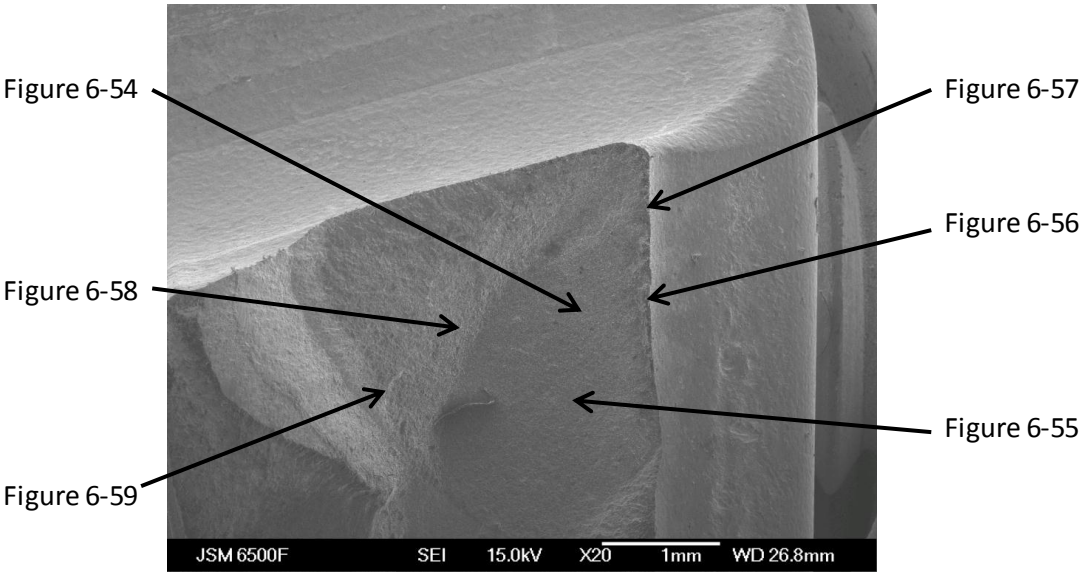

Figure 6-53: Locations of SEM Micrographs or firtree deflections

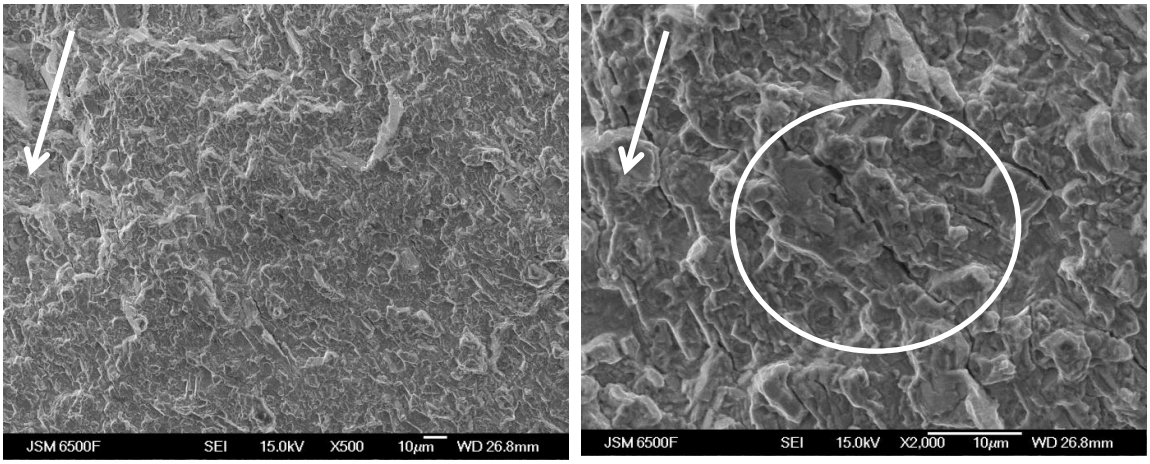

Figure 6-54: Fracture surface of the firtree failure of U720 at ca. 300°C in the planar region in the centre at c=1mm and an estimated $\Delta K \approx 90$MPa $\sqrt{m}$ (Arrow indicates crack growth direction) a) at low magnification showing transition between planar and deflected crack growth (b) at high magnification showing slip traces and secondary cracks (marked by circle)

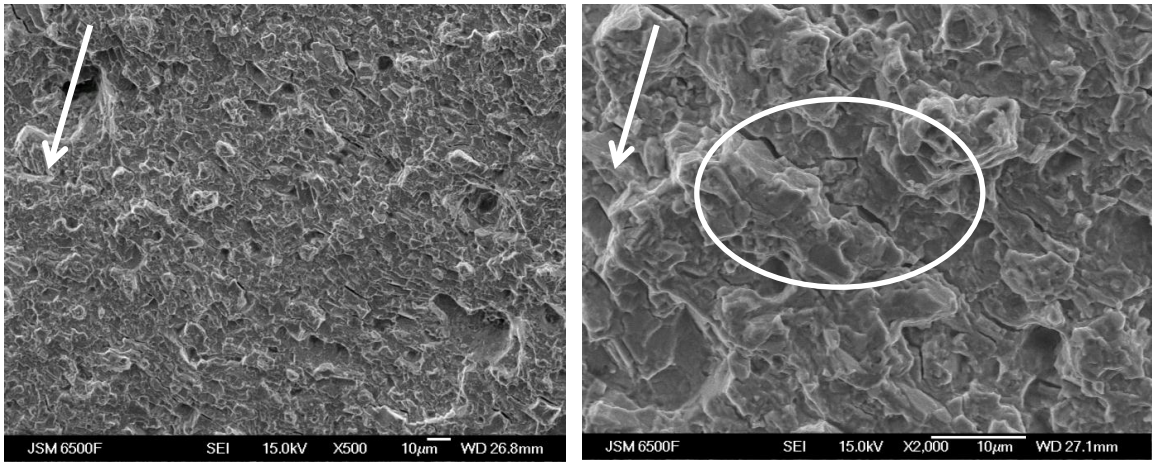

Figure 6-55: Fracture surface of the firtree failure of U720 at ca. 300° in the planar region in the centre at c=1.9mm and an estimated ΔK≈130MPa $\sqrt{m}$ (Arrow indicates crack growth direction) a) at low magnification showing transition between planar and deflected crack growth (b) at high magnification showing slip traces and secondary cracks (marked by circle)

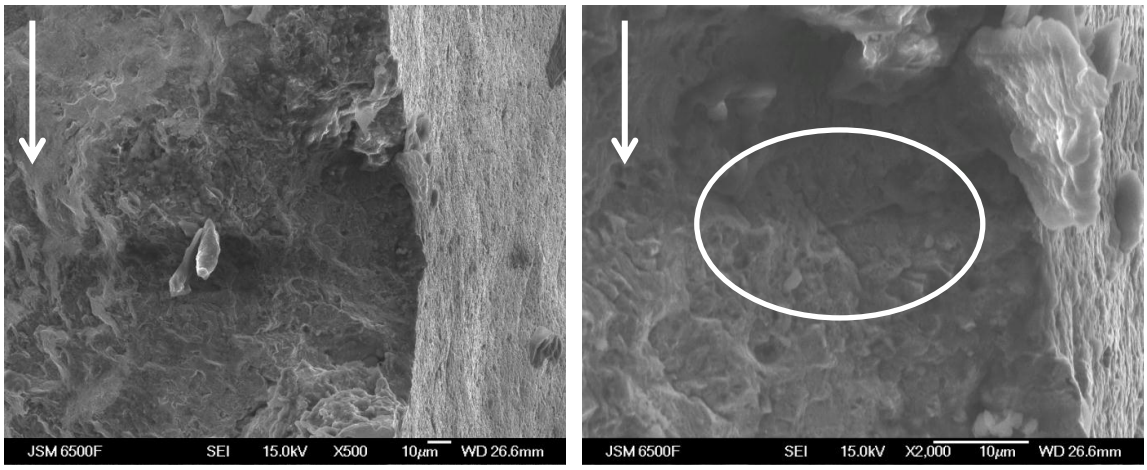

Figure 6-56: Fracture surface of the firtree failure of U720 at ca. 300° in the deflected region at the top edge at c=1.2mm and an estimated ΔK≈90MPa $\sqrt{m}$ (Arrow indicates crack growth direction) a) at low magnification showing transition between planar and deflected crack growth (b) at high magnification showing slip traces and secondary cracks (marked by circle)

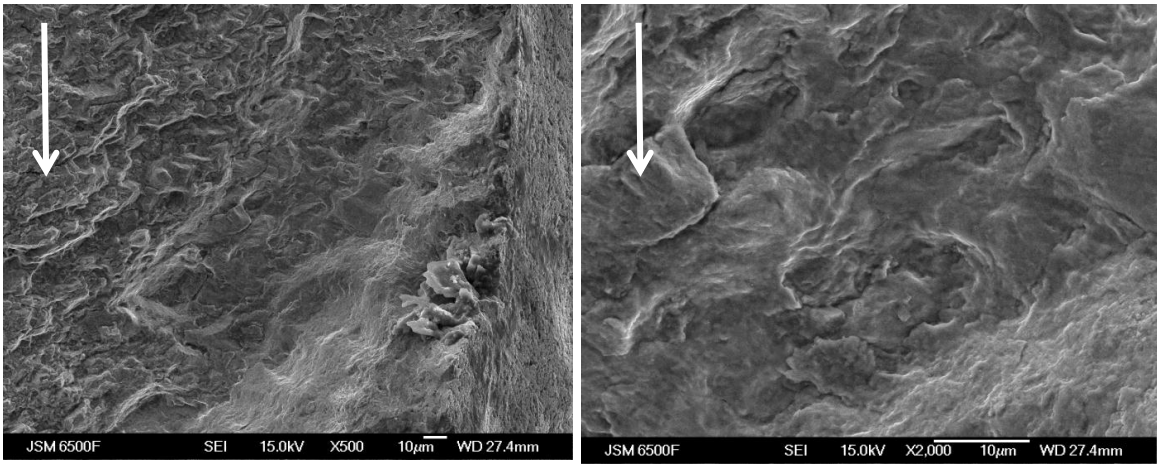

Figure 6-57: Fracture surface of the firtree failure of U720 at ca. 300° in the deflected region at the side edge at c=2.7mm and an estimated ΔK≈140MPa √m (Arrow indicates crack growth direction) a) at low magnification showing transition between planar and deflected crack growth (b) at high magnification showing slip traces and secondary cracks

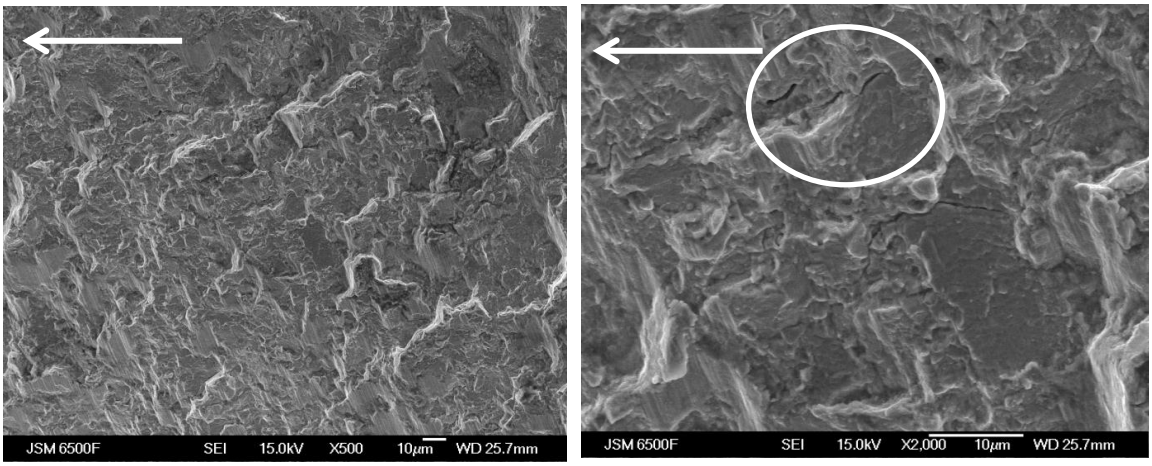

Figure 6-58: Fracture surface of the firtree failure of U720 at ca. 300°C in the strongly deflected region at the side edge at c=1.3mm and an estimated ΔK≈52MPa √m tilted at an angel of 25° (Arrow indicates crack growth direction) a) at low magnification showing transition between planar and deflected crack growth (b) at high magnification showing slip traces and secondary cracks (marked by circle)

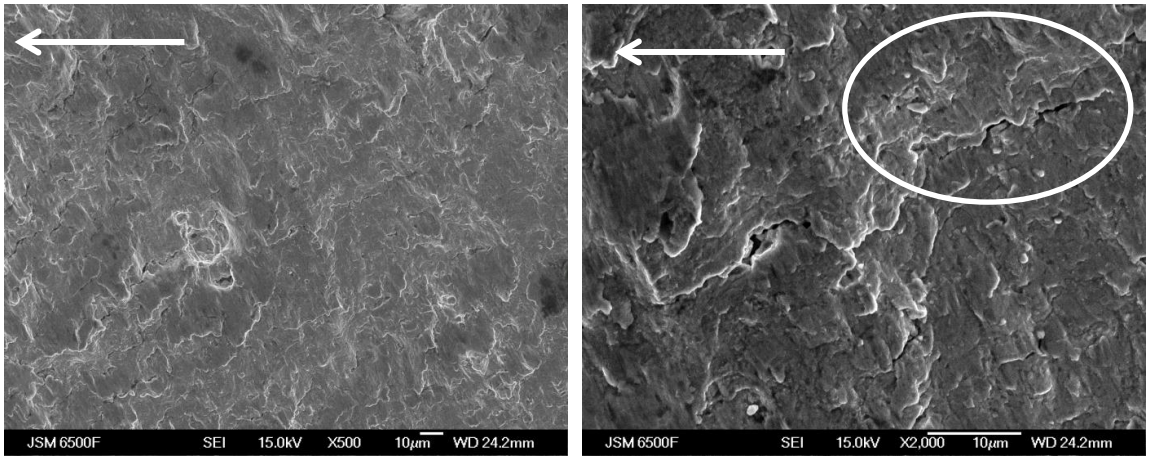

Figure 6-59: Fracture surface of the firtree failure of U720 at ca. 300°C in the strongly deflected region at the side edge at c=3.2mm and an estimated $\Delta K \approx 125 MPa\sqrt{m}$ tilted at an angel of 25° (Arrow indicates crack growth direction) a) at low magnification showing transition between planar and deflected crack growth (b) at high magnification showing slip traces and secondary cracks (marked by circle)

6.3.2 Disc Holes

Three similar deflected cracks have been observed in an U720Li C&W disc spin test which experienced temperatures of 600°C in partial vacuum (no exact information available). The test was carried out at a 30-5-30-1 cycle. They were all initiated at chamfers in air holes, in the bore of the disc. [93, 101]

The positions of the three deflected cracks are shown in Figure 6-60, Figure 6-62 and Figure 6-64, and the fracture surfaces are shown with deflections in Figure 6-61, Figure 6-63 and Figure 6-65 for the respective positions.

Stress Analysis for these components were not available for these fractures, so the ΔK levels are unknown, however deflected regions can be observed after the initiation site in all three cases, which could potentially be sustained deflected crack growth.

In the specimen test considered in Chapter 5, temperatures of 600°C in air did not exhibit sustained macroscopic deflection, but did show this in vacuum. However the level of the partial vacuum here is unknown, so the effect of vacuum on the SMDCG could be limited. As the stress levels are unknown, it cannot be confirmed with certainty whether these deflections are sustained deflected crack growth or not.

Further analysis is necessary to clarify whether this is SMDGC or mixed mode failure due to the complex stress state around the holes or deflection in the plane stress region due to the high stresses/ K in the area.

More detailed fractography of the planar and non-planar regions has been carried out on the first failure using the FEG-SEM in Figure 6-67 to Figure 6-71. Figure 6-66 shows the overall location for each image. The K levels of these locations are not known, but the crack growth mechanisms observed are again similar to those observed in the CNB samples tested in Chapter 5.

The large deflection from the top edge in Figure 6-67 and Figure 6-68 shows large secondary cracks. The slightly deflected region at the side edge in Figure 6-70 shows a transition between planar and deflected crack growth, but no obvious secondary cracks. The planar region in Figure 6-69 shows Stage II crack growth and secondary cracking, as does the region further ahead in Figure 6-71. More detail is given in the figure captions.

Figure 6-60: Deflected crack on disc air hole (number 2) failure initiated from the chamfer [101]

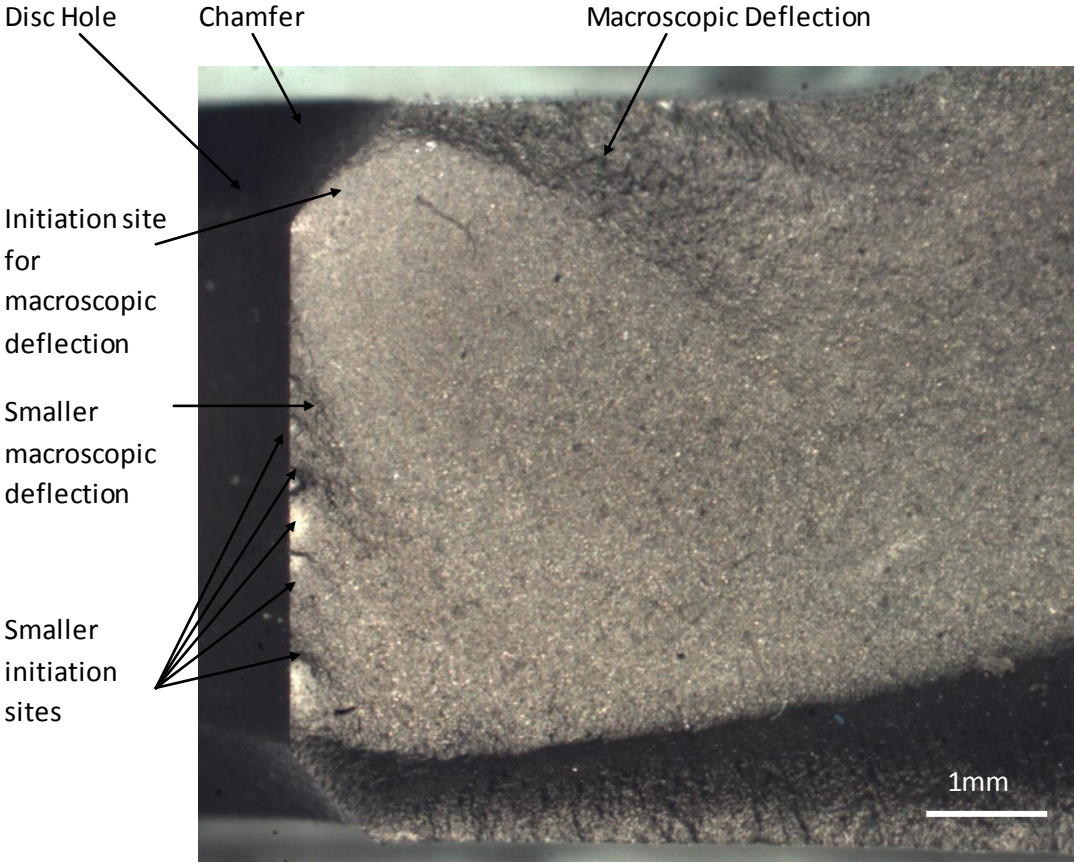

Figure 6-61: Fracture surface of disc air hole (number 2) failure initiated from the corner showing large deflection from the top surface and small deflections and initiation sites from the side surface

Figure 6-62: Deflected crack on disc air hole (number 14) failure initiated from the chamfer [101]

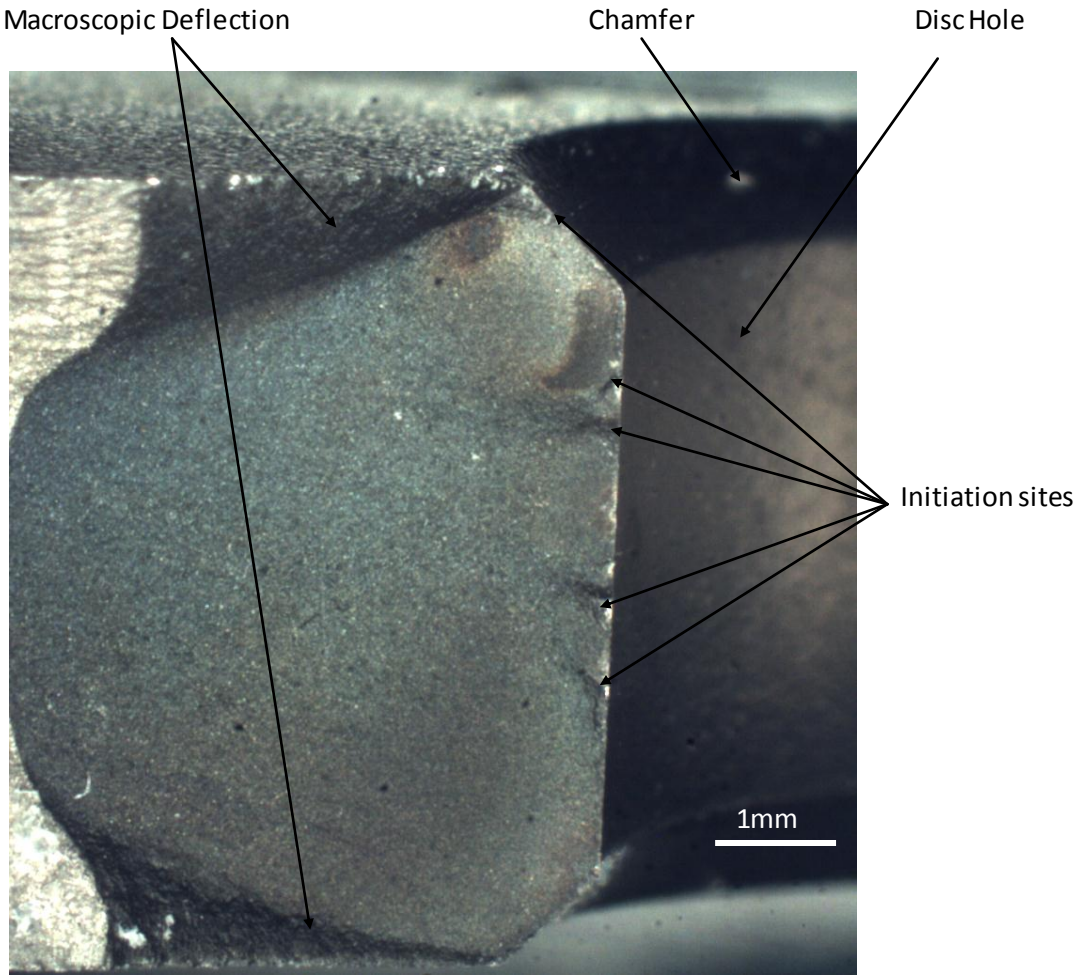

Figure 6-63: Fracture surface of disc air hole (number 14) failure initiated from the corner showing large deflection from the top surface initiated at the chamfer and several initiations sites at the side surface

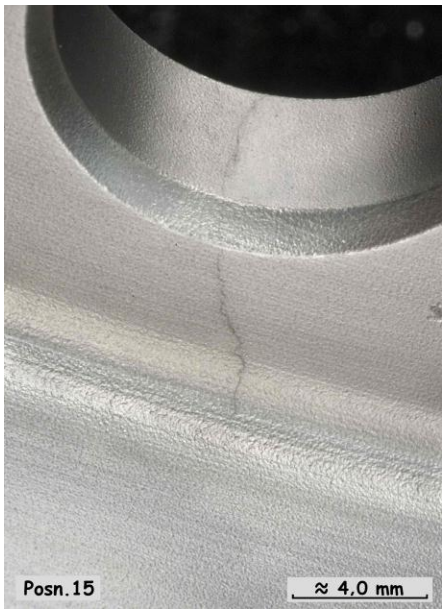

Figure 6-64: Deflected crack on disc air hole (number 15) failure initiated from the chamfer [101]

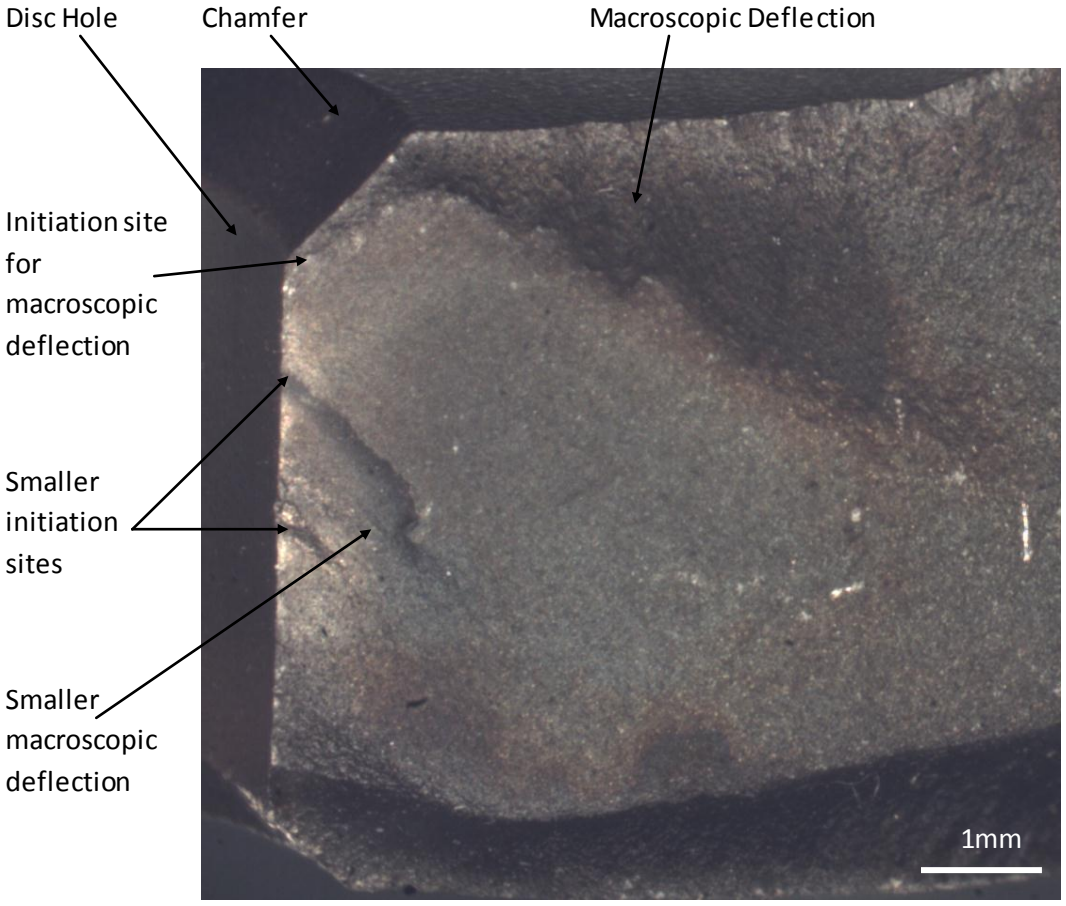

Figure 6-65: Fracture surface of disc air hole (number 15) failure initiated from the corner showing large deflection from the top surface and from the side surface

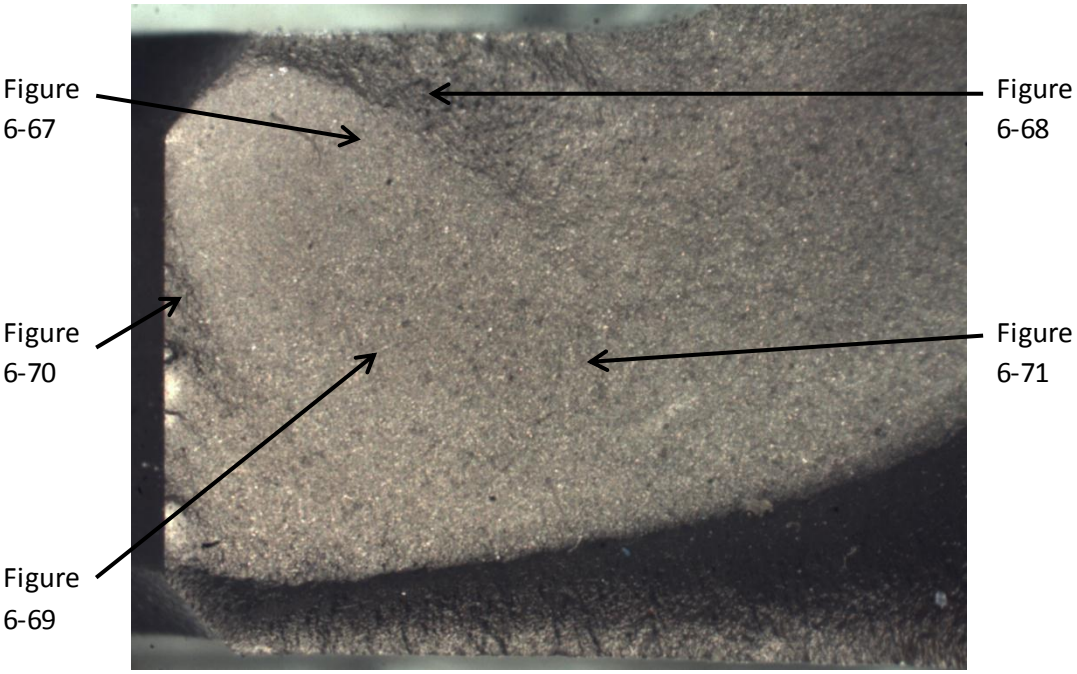

Figure 6-66: Location of SEM micrographs in air hole

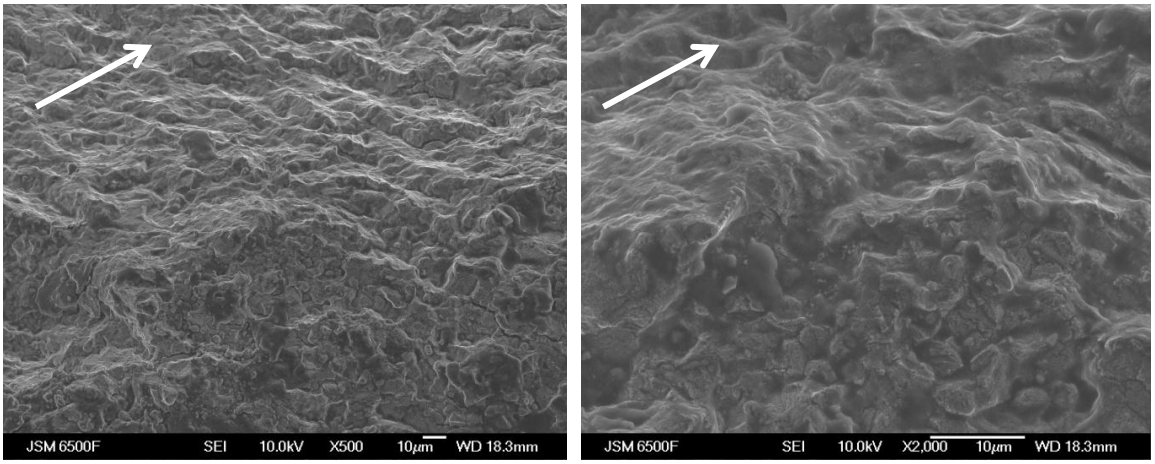

Figure 6-67: Fracture surface of the disc hole failure in U720Li C&W spin test at 600°C in air at the edge of the strongly deflected region at the top edge at *c*=1.34mm (Arrow indicates crack growth direction) a) at low magnification showing transition between planar and deflected crack growth (b) at high magnification showing slip traces

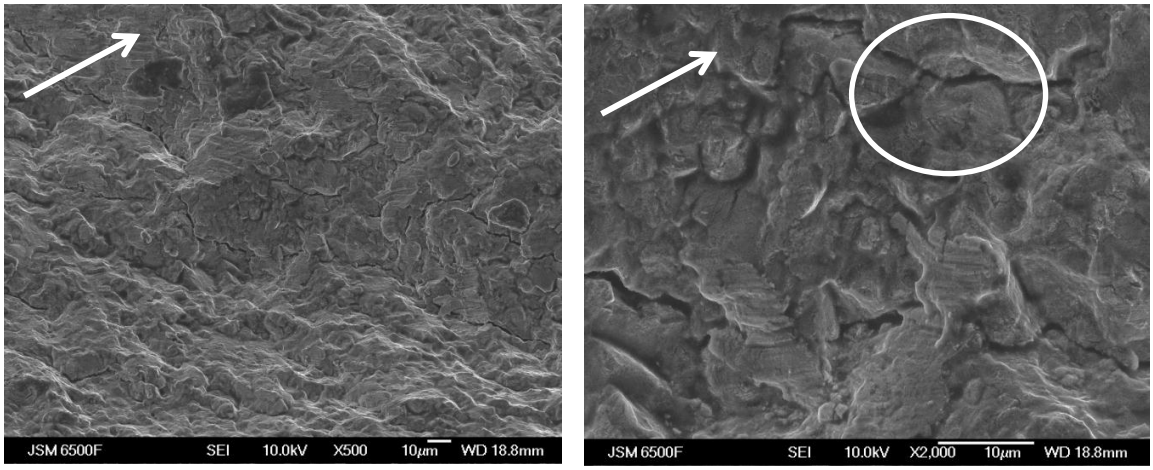

Figure 6-68: Fracture surface of the disc hole failure in U720Li C&W spin test at 600°C in air in the strongly deflected region at the top at *c*=1.30mm (Arrow indicates crack growth direction) a) at low magnification showing transition between planar and deflected crack growth (b) at high magnification showing slip traces and large secondary cracks (marked by circle)

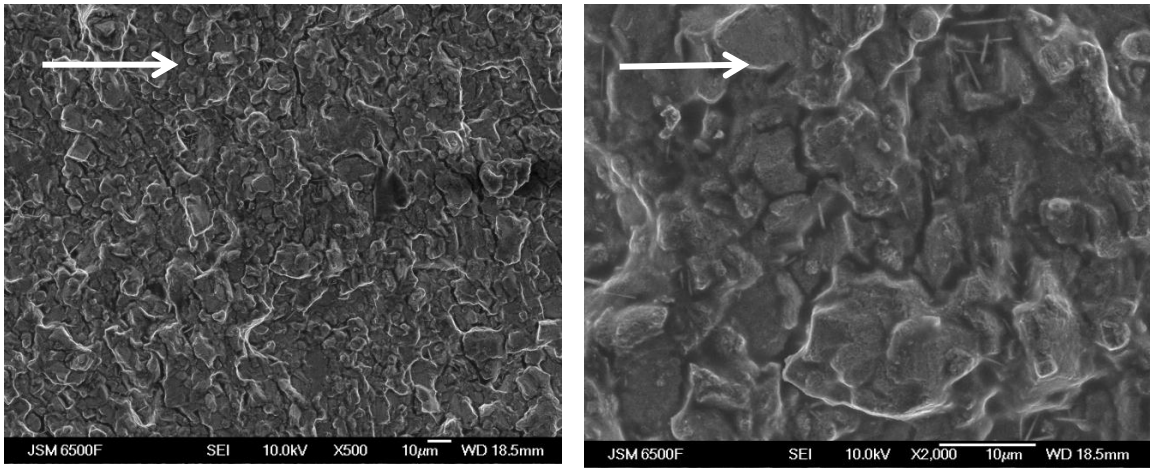

Figure 6-69: Fracture surface of the disc hole failure in U720Li C&W spin test at 600°C in air in the in the planar region in the centre at *c*=2.5mm (Arrow indicates crack growth direction) a) at low magnification showing transition stage II crack growth (b) at high magnification showing slip traces and large secondary cracks (marked by circle)

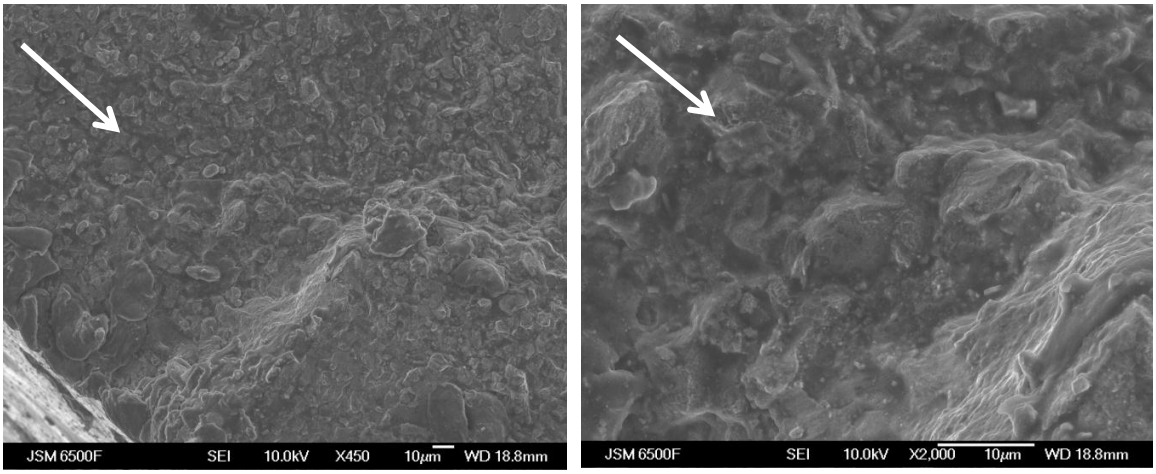

Figure 6-70: Fracture surface of the disc hole failure in U720Li C&W spin test at 600°C in air in the slightly deflected region at the side at *c*=4.5mm (Arrow indicates crack growth direction) a) at low magnification showing transition between planar and deflected crack growth (b) at high magnification not showing any obvious secondary cracks

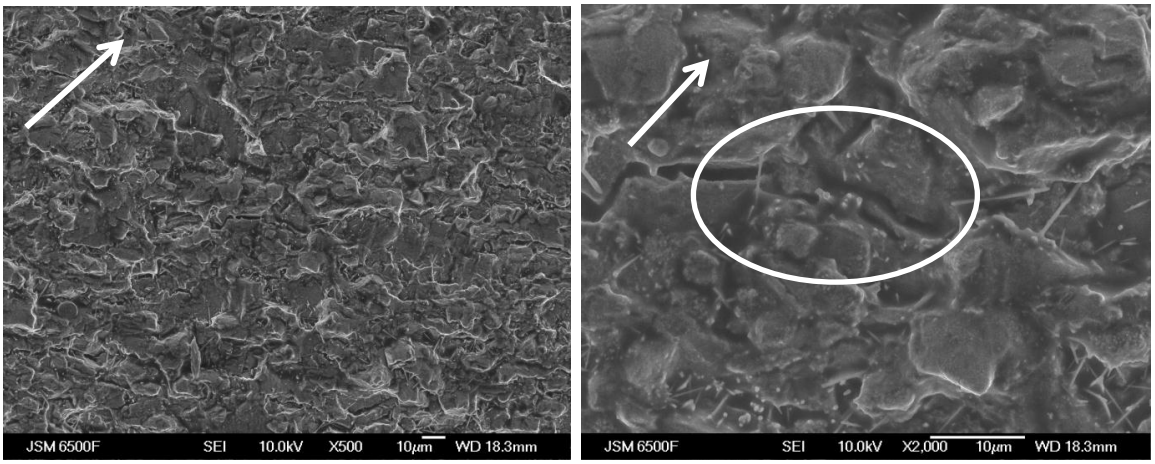

Figure 6-71: Fracture surface of the disc hole failure in U720Li C&W spin test at 600°C in air in the planar region further ahead at *c*=9.3mm (Arrow indicates crack growth direction) a) at low magnification showing stage II crack growth (b) at high magnification showing slip traces and secondary cracks (marked by circle)

6.4 Summary

A number of tests from other workers have been revisited, as well as some component failures from rig tests at Rolls Royce, which showed some deflection.

Crack deflection can also occur for a number of other reasons e.g. due to mixed mode loading, or tunnelling due to creep processes. These effects are however negligible under 600 °C [92]. Fracture surfaces have to be carefully analysed to confirm whether a deflection in a component failure can be classed as SMDCG, or whether it can be explained by a different mechanism.

A template has been produced based on the definition of SMDGC in Chapter 5; this can be used to quickly determine whether deflection can be considered to be SDMGC or whether they are deflection due to the plane stress region for a wider range of materials and test conditions.

The effect of temperature can be confirmed, SMDCG is observed at 300°C in air and vacuum, and is sustained in vacuum to 600°C. If we ignore two unexpected results, the results of Loo Morrey [50] confirm the results of this work for onset of deflection.

Moreover it was shown that R-ratio does not seem to have an effect, and the initial ΔK does not matter, the onset depends on the relevant ΔK, so deflection occurs earlier in a sample if ΔK_i is larger.

The effect of long dwell fatigue seems to reduce the effect at high temperature in vacuum. Deflection has been observed in some samples at high temperature (in vacuum), this could however be caused by creep.

Bithermal tests have shown that changing the temperature to and from a 'critical' temperature and 'switching' the mechanism on and off results in very little deflection (overall planar fatigue crack), possibly the low temperature crack does not have enough time to deflect, before turning back.

Furthermore a number of components from rig tests carried out at R-R have shown some sort of deflected crack growth, and have been studied in some detail, one on a firtree of an high pressure turbine disc and on a number of airholes in one high pressure turbine disc. Obviously components can have more complex geometry/ loading conditions than test specimens, this could give rise to more complex load states and mixed mode failure.

The firtree failure was in the critical temperature range (at 300°C) for SMDCG, however using the PZS template on the fracture surface showed that significant deflection could be expected there due to the plane stress region at the very high stresses in this region.

The airhole failure cannot be explained without further study of the stresses around the holes, but it is possible that it was also caused by the plane stress region if stresses are high enough or the complex stress state around the holes. It is also possible that it is SMDCG, as this test was at 600°C in a partial vacuum, but the level of the partial vacuum and its effect on the SMDCG is unknown.

Detailed fractography on samples and both components has also shown secondary cracking, as observed in the tested specimen both at deflection points and in 'ordinary' crack growth

These alloys are prone to secondary cracking anyway, however under some conditions (Intermediate Temperatures and higher temperature (600°C) in vacuum, but suppressed by room temperature or higher temperature in air) some of these secondary cracks get driven quite a long way. This can be linked to the plane stress state.

To understand whether a component is exhibiting SMDCG it is necessary to establish what the crack driving force is, that causes the crack to deflect and how this could be applied to the complex stress state in a component.

7 Lifetime predictions

The effect of sustained deflected macroscopic crack growth on the life should be determined to compare whether the crack growth rates of the complex crack path (with deflected and non-deflected regions) are slower (conservative) or faster (non-conservative) than the expected non-planar crack growth that models predict (e.g. SA16 at Rolls Royce plc. (R-R))

7.1 Lifing Methodology Comparison

7.1.1 $\Delta a/\Delta N$ approach from experimental data

The CNB samples to date have an experimentally determined lifetime, and also exhibit the sustained macroscopic deflected crack growth (SMDCG). In order to assess whether the current Stage II dominated *da/dN* data obtained from the SENB samples can be used to predict the lifetime for these samples a Paris law type incremental estimation has been adopted.

Initiation effects from the notches (which were not pre-cracked) might be expected to lead to conservative predictions using this approach, whereas any significant acceleration of effective *da/dN* due to SMDCG would make these predictions non-conservative.

A straightforward *da/dN* integration is difficult, as the *K* calibration for CNB (by Pickard [94]) is a very complex function of *a*, which also varies significantly (as a step function) at various *a/W* values, therefore an approach using an estimated $\Delta a/\Delta N$ was used over a certain Δa interval.

With the respective ΔK values (from the Pickard calibration) for two values: a_n and a_{n+1}, across a small crack growth increment:

$$\Delta a_i = a_{n+1} - a_n \qquad \text{Equation 7-1}$$

the average crack growth rate

$$(da/dN)_{average} = (da_{n+1}/dN_{n+1} + da_n/dN_n)/2 \qquad \text{Equation 7-2}$$

can be calculated using the Paris law (Equation 2-22) using *C* and *m* values for U720Li C&W obtained from the SENB tests and by Rolls Royce plc. from corner notch tests in tension (CNT) at 300, 600 and 650°C in air and vacuum [93]. Thus for each Δa_i a corresponding ΔN_i can be calculated from the $(da/dN)_{average}$.

Using an Excel spreadsheet the continuing sequence of Δa_i and their corresponding ΔN_i values were calculated. This was repeated up to a ΔK of 50MPa√m (as this value is close to the plastic collapse of the samples) and for 100MPa√m (the fracture toughness of the material) [13] for comparison. Then the total numbers of cycles to failure were calculated as the sum of all the ΔN values.

Initially a sensitivity study was performed to find the most appropriate value for the Δa intervals. An approach using an estimated $\Delta a/\Delta N$ was used over Δa intervals where *da/dN* varied by no more than a certain percentage. The respective number of cycles was calculated between these two *da/dN* values, by making an averaged *da/dN* assumption, and the *da/dN*

values compared to determine the next Δa interval. This meant that the Δa interval decreased as ΔK increased. This sensitivity evaluation has been carried out for a CNB sample of U720Li C&W tested at 300°C in air with an assumed ΔK_i=12MPa√m, using C and m data obtained from an SENB sample tested under the same conditions (see Table 18) up to a ΔK of 50MPa√m. The da/dN values across the Δa interval were allowed to vary between 1% and 100%. It can be seen in Figure 7-1, where the lifetime is predicted as a function of the allowed da/dN difference, that the predicted lifetime increases slightly for finer Δa intervals (i.e. where less da/dN difference is allowed) but the predicted lifetime value approaches a value of ~60815 cycles.

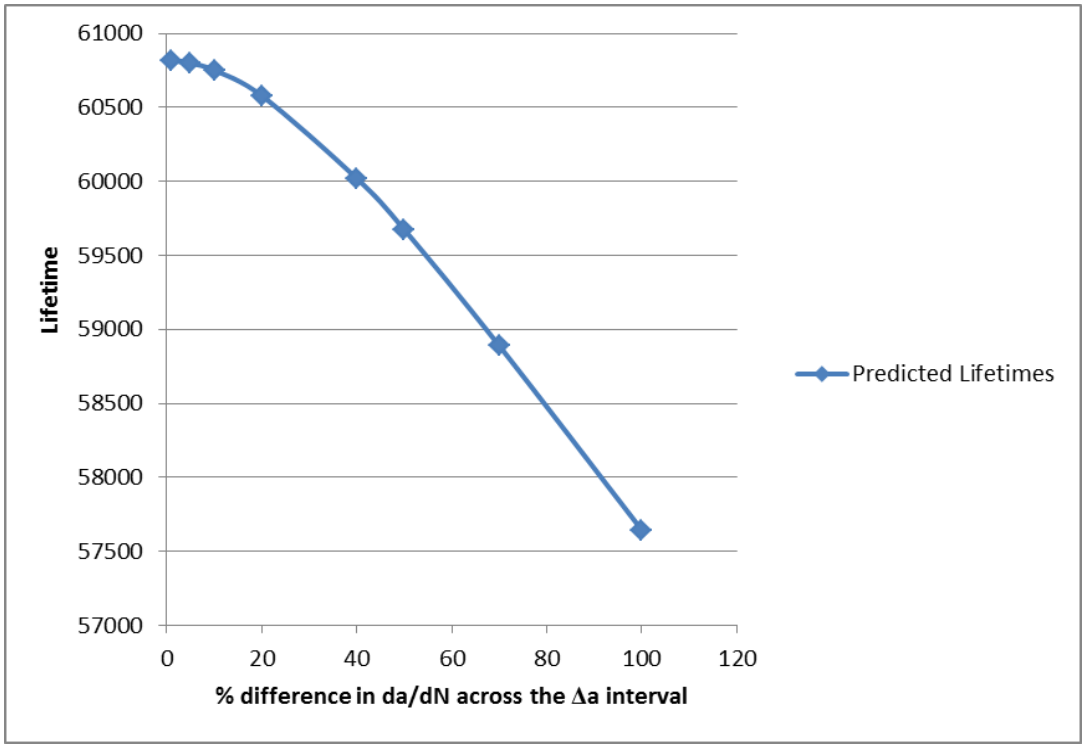

Figure 7-1: Lifetime prediction as a function of the allowed da/dN difference

Another approach using a constant Δa interval has also been tried, for Δa values of 0.01mm, 0.05mm and 0.1mm. These approaches achieved similar results also approaching a similar lifetime of ~60810 cycles, see Figure 7-2.

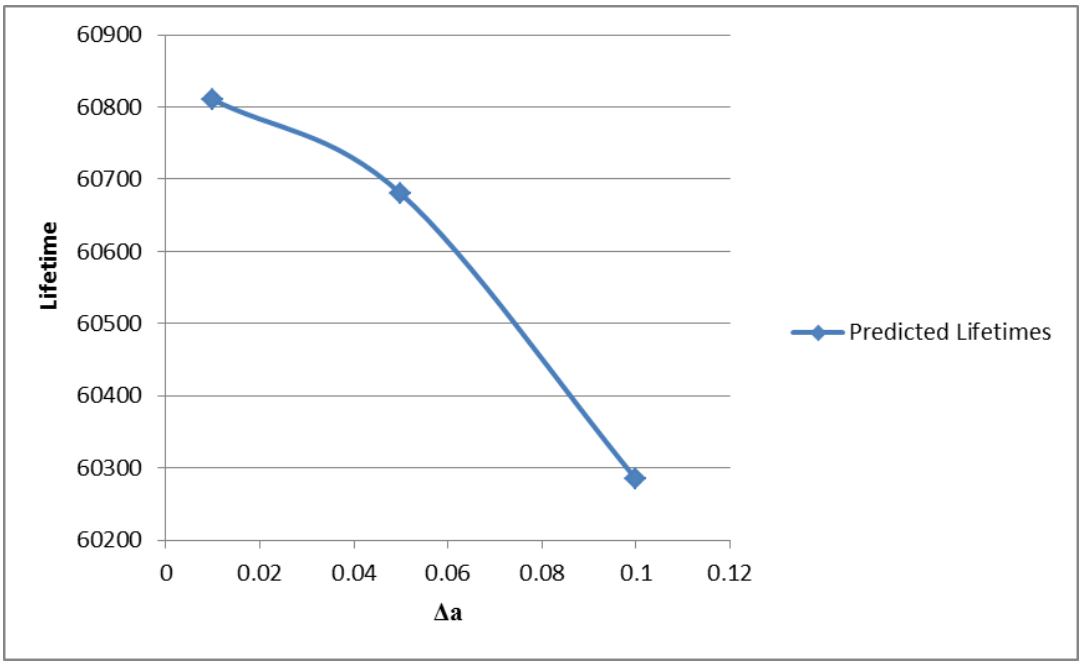

Figure 7-2: Lifetime prediction as a function of the different Δa

A *da/dN* difference of 1% has therefore been chosen to calculate the expected lifetime for all samples.

Lifetime calculations for the CNB samples were then carried out using the *C* and *m* values from the comparable SENB tests carried out at the University of Southampton on U720Li C&W. The SENB samples describe a more planar crack behaviour, as most of the fracture surface was not dominated by the sustained macroscopic deflection. These results are compared to lifetimes predicted using crack growth data given by Rolls Royce plc. (R-R) for U720Li (from the lifing database) [93]. These were determined from Corner Notch tests in tension (CNT) tested under a trapezoidal 1-1-1-1 waveform (0.25 Hz), which would be expected to have a larger proportion of deflected crack growth, and where more time-dependent crack growth processes are likely to occur. Figure 7-3 shows the relevant crack growth Paris plots for all tests and Table 18 summarises the crack growth law constants for the material at the temperatures.

Temperature/ Environment	*C* and *m* values (R-R) [93]	*C* and *m* values (SENB)
300°C air	$C = 4.55 \times 10^{-9}$ $m = 3.142$	$C = 7.801 \times 10^{-10}$ $m = 3.657$
600°C air	$C = 6.04 \times 10^{-8}$ $m = 2.656$	$C = 1.555 \times 10^{-8}$ $m = 2.922$
650°C air	$C = 6.89 \times 10^{-8}$ $m = 2.744$	$C = 1.557 \times 10^{-8}$ $m = 2.983$
300°C vacuum	$C = 7.57 \times 10^{-9}$ $m = 2.783$	$C = 6.063 \times 10^{-10}$ $m = 3.615$
600°C vacuum	$C = 2.52 \times 10^{-8}$ $m = 2.617$	$C = 9.274 \times 10^{-10}$ $m = 3.649$
650°C vacuum	$C = 2.46 \times 10^{-8}$ $m = 2.66$	$C = 1.662 \times 10^{-10}$ $m = 4.259$

Table 18: Crack growth law constants from R-R [93] and the SENB tests

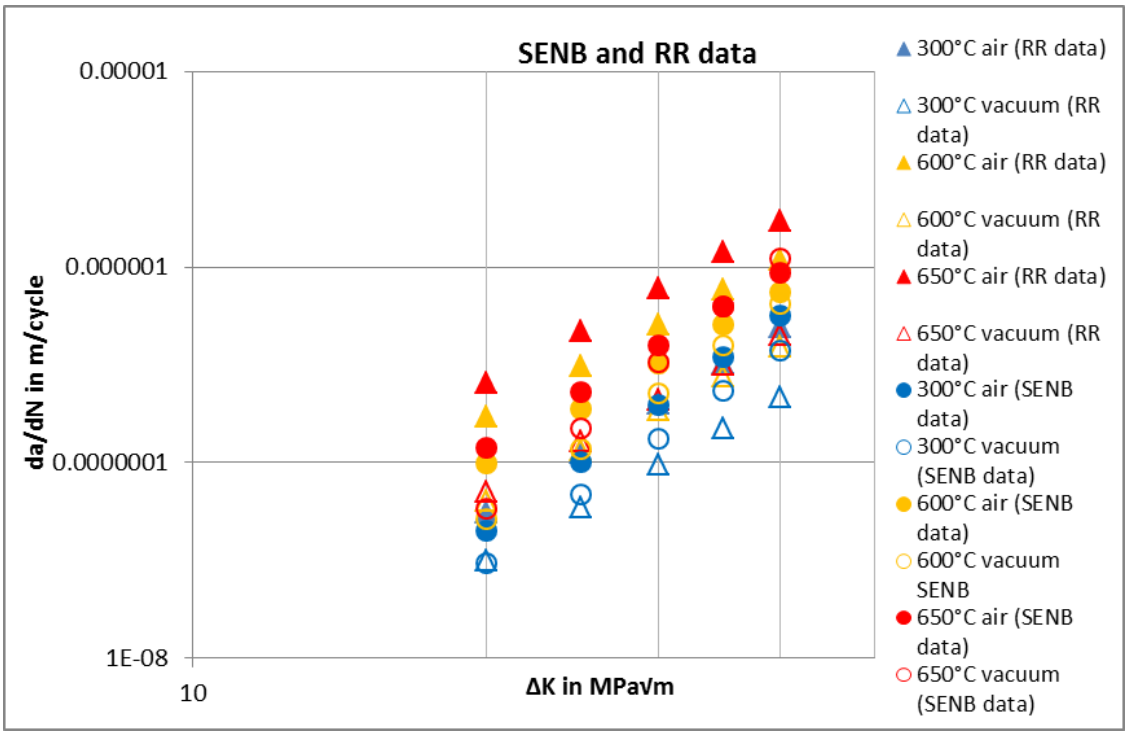

Figure 7-3: Crack growth rates from SENB tests and R-R database

7.1.2 Review of SA16: Rolls Royce lifing approach

A comparison was carried out with the automated lifetime prediction software SA16 that is used by Rolls Royce plc to predict the lifetimes of components.

SA16 is run as part of the SC03 Finite Element software at R-R. It takes the stress state calculated by SC03 for a 2D model of specific component. Usually for a turbine disk, the hoop stress (σ_z) and the radial stress (σ_y), and applies a simplified geometry (rectangle) with a specific defect (e.g. Corner notch). For this geometry and crack type and size the appropriate K calibration is chosen, which is the Pickard calibration for a corner crack of the size used.

A line section through the FE model of the sample (or component) defines the stress field for the maximum and minimum stress distance profile, which is then written as a polynomial function (with 9 coefficients). With the defined initial crack length, and the definition that it is a corner crack, SA16 uses the Pickard calibration to calculate the ΔK.

Based on this the lifetime of the component is calculated assuming a crack of defined size and position. It is not clearly documented within Rolls Royce what the software does in the background, it uses a Runge Kutta integration for the complex K calibration. The software iterates this until K_{max} reaches the defined Fracture toughness K_{IC} (usually defined as 100MPa√m for Nickel Superalloys) [13].

Values for the crack growth rate, usually the Paris regime, are chosen, with C and m values available from CNT tests at 1-1-1-1 or other dwell waveforms from the R-R database.

C and m values can also be defined manually; hence those from the SENB data have also been used in this work for direct comparison.

Modelling a CNB configuration is however rather difficult in SA16, as the Pickard solution used by the software does not consider how the growing crack affects the bend stress state and the simplistic loading assumptions for the sample means the crack stops growing as it reaches the notional neutral axis. But for this model the equivalent stress in tension has been calculated to be such that a Corner Notch sample with the same crack size would have achieved the same initial ΔK as for the bend case, see Figure 7-4. This should show equivalent behaviour for the crack growth behaviour on the top surface.

A Paris regime dominated crack growth is assumed from initiation to final failure. Thus as in the $\Delta a/\Delta N$ approximation approach, initiation and final failure processes are disregarded. However it should be noted that the C and m values for vacuum data from R-R values from tests are only valid from 19 to 40MPa√m. [93]

The calculations also consider values below 20MPa√m, but the C and m values from the SENB have been determined above this value, and may not be valid in this lower ΔK regime.

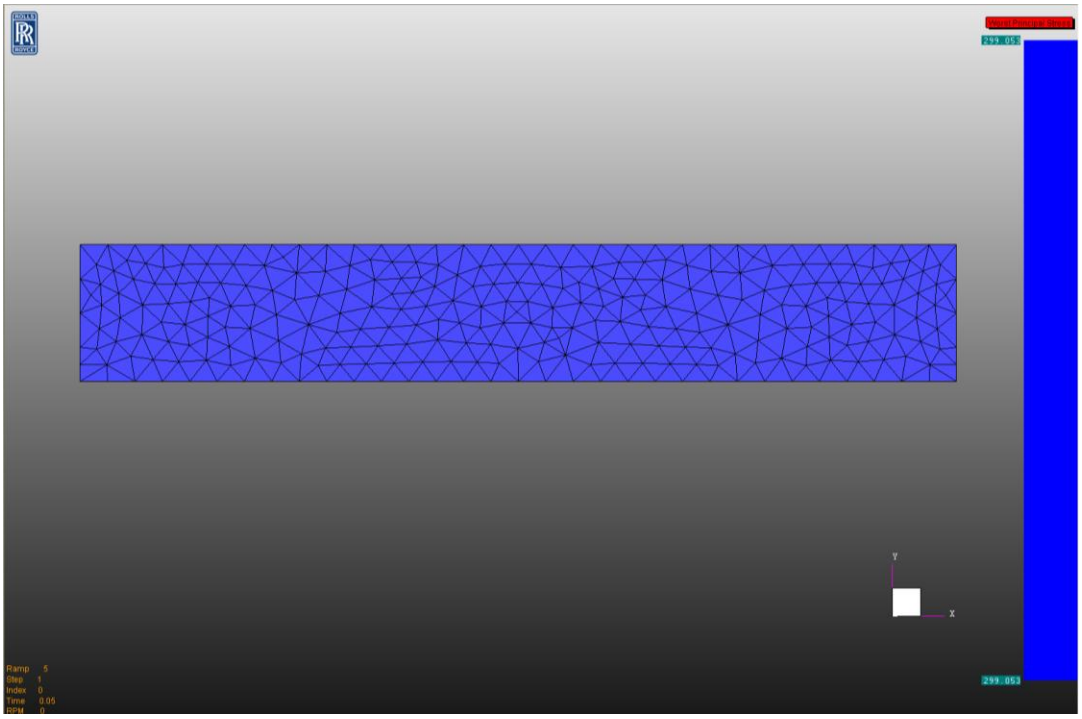

Figure 7-4: 2D model of a CNT sample in SC03 used for SA16 analysis of a corner notch defect

7.2 Results and Discussion

Table 19 summarizes the predicted and actual N_f for each test. All tests show much higher actual lifetimes than the predicted one, which indicates all lifing approaches are conservative. The ratio $N_{predicted}/N_{actual}$ shows a measure of conservatism for each prediction, where >1.0 is non-conservative and < 1.0 is conservative.

It is evident that using SENB crack growth rate data leads to between 3-114% longer predicted lifetimes for either calculation approach compared to the R-R data, but with increasing lifetime (of individual tests) values get more consistent.

Using the $\Delta a/\Delta N$ approach also predicts 8-37% longer lifetimes than the SA16 approach for both approaches calculated up to ΔK=100MPa√m (to be comparable).

Using 50 or 100MPa√m as the final value for the $\Delta a/\Delta N$ approach only increases lifetimes up to 10%, making 50MPa√m a reasonable assumption for final fracture of these specimens.

R-R data shows longer lifetimes only in the 300°C vacuum case cf. SENB data for the SA16 and the $\Delta a/\Delta N$ approach when calculating up to 100MPa√m. This is due to the crack growth rates for these conditions being lower from the SENB data for lower ΔK and exceeding the R-R rates as ΔK increases (i.e. a higher m-value means steeper slope, see Figure 7-3).

It should be noted when comparing the lifetime using the different C and m values from the SENB and the R-R data respectively, that the R-R data were produced in the CNT sample, which show more deflected crack growth. It would be expected that crack growth will be more retarded due to shielding compared to the SENB crack growth rates. They have however mostly higher crack growth rates in the air tests which could be explained by lower frequency (0.25Hz vs. 20Hz), which when tested in air might show accelerated crack growth rates due to additional oxidation fatigue effects. In vacuum crack growth rates are similar for the two specimen geometries, for the 300 and 600°C vacuum data the SENB even has higher crack growth rates for the higher K levels. Clavel and Pineau [102] have shown that higher strain rates (so higher frequencies) can promote more planar slip, thus may explain higher crack growth rates for the SENB vacuum tests (which were 20Hz).

Figure 7-5 a shows the lifetime of all tests using the SENB data and the $\Delta a/\Delta N$ approach. Figure 7-5 b excludes the U720Li C&W at 300°C in vacuum, as it is very far out. The line through this graph shows which conditions behave in a conservative or non-conservative manner. All predictions clearly behave very conservatively; showing actual lifetimes are much longer than the predicted ones. As these tests were not precracked, and it should be noted that initiation cycles might have had a significant effect on the observed lifetimes. But this might also be a reflection of intrinsic shielding, i.e. reduction of crack driving force, which has been observed to be caused by crack deflection itself, apart from any extrinsic shielding which may occur from closure effects [84].

The vacuum tests showed significantly higher experimentally determined lifetimes than any of the predictions, when compared to the tests performed in air; in particular the 300°C in vacuum test. The result from the test is an order of magnitude larger than the results from the

other tests. It is also the test that is expected to have the largest lifetime, however it is not clear why there is such a large difference compared to the tests in air. Delayed initiation effects might be more significant in vacuum; it is possibly linked to reduced slip band initiation due to enhanced reversibility of slip in vacuum.

The deflection sizes have been significantly larger in vacuum test, hence it is likely that shielding effects might be more pronounced, but it should also be noted that these deflections in the CNB samples started at a higher ΔK level.

Test condition	N_f measured	N_f calculated to ΔK= 50MPa√m	N_f calculated to ΔK= 100MPa√m	N_f calculated to ΔK= 50MPa√m	N_f calculated to ΔK= 100MPa√m	N_f calculated with SA 16 (CNT)	N_f calculated with SA 16 (CNT)
		R-R data	R-R data	SENB data	SENB data	R-R data	SENB data
300°C air	172000	48130	50862	60815	62702	43496	45749
	N_{pred}/N_{act}	0.28	0.30	0.35	0.36	0.25	0.27
600°C air	72656	13976	15494	24047	25995	14311	21164
	N_{pred}/N_{act}	0.19	0.21	0.33	0.36	0.20	0.29
650°C air	46626	10067	11000	21514	23043	9577	
	N_{pred}/N_{act}	0.22	0.24	0.46	0.49	0.21	
300°C vacuum	3332531	81359	88583	83666	86520	77388	66677
	N_{pred}/N_{act}	0.02	0.03	0.03	0.03	0.02	0.02
600°C vacuum	747409	37460	41725	45307	46899	38770	39404
	N_{pred}/N_{act}	0.05	0.06	0.06	0.06	0.05	0.05
650°C vacuum	256138	36562	40278	46921	47650	34817	
	N_{pred}/N_{act}	0.14	0.16	0.18	0.19	0.14	

Table 19: Numbers of cycles to failure for CNB tests and ratio of $N_{predicted}/N_{actual}$

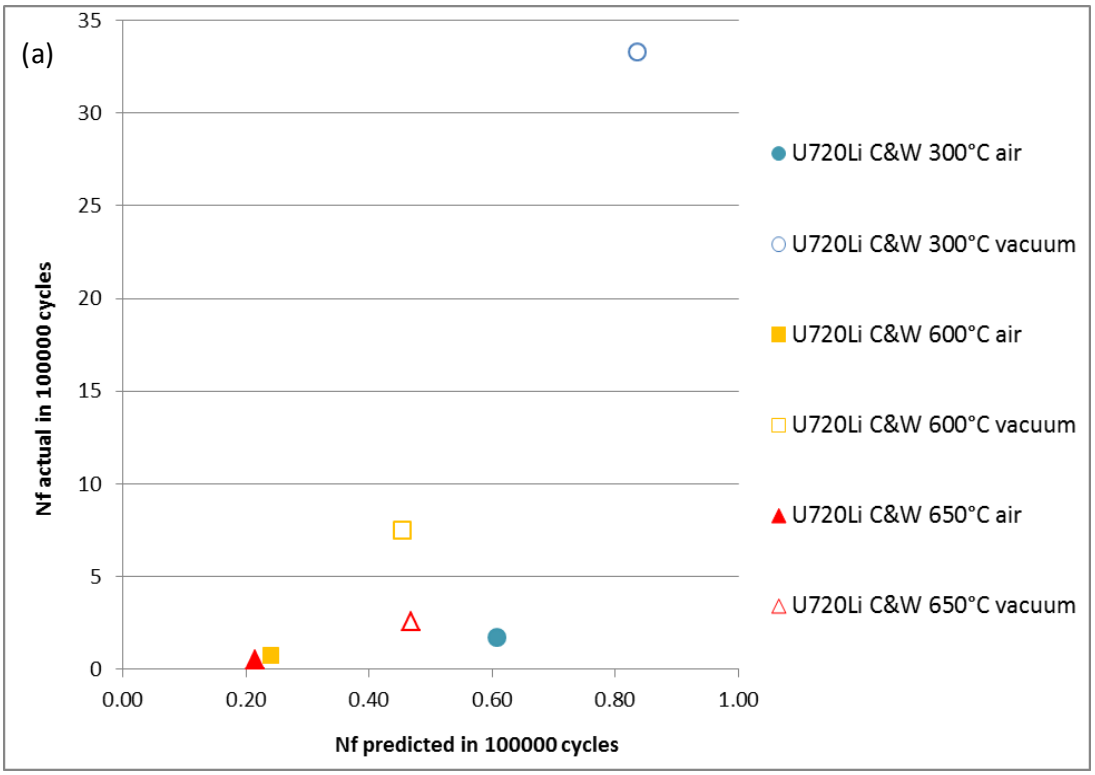

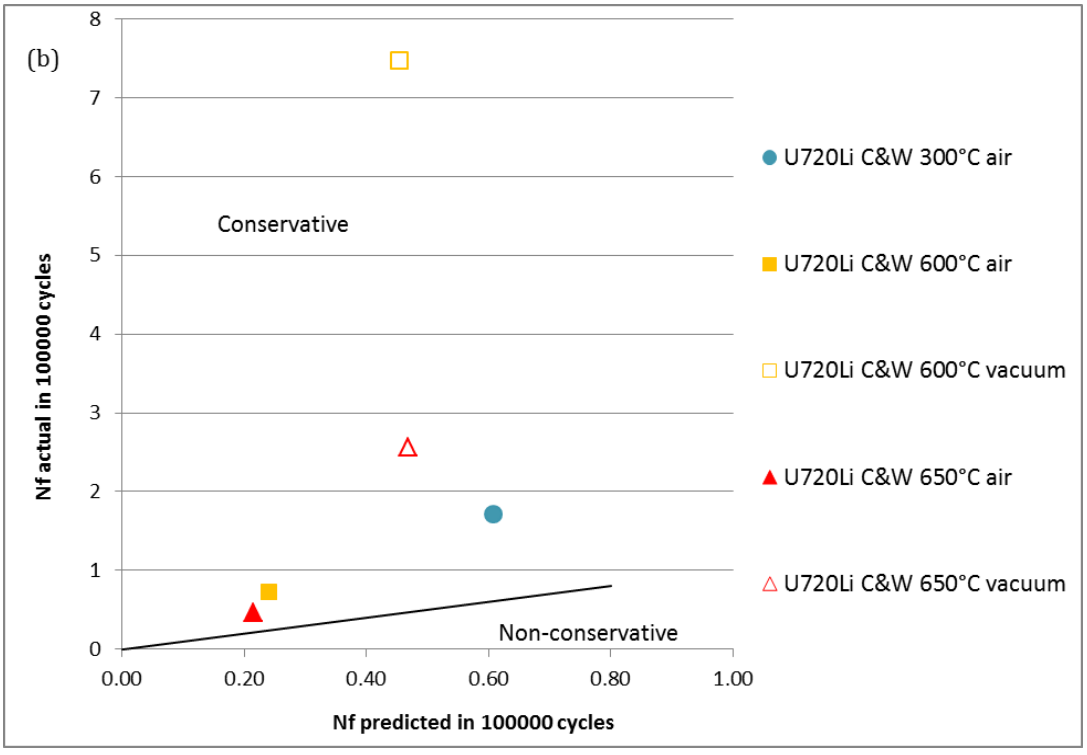

Figure 7-5: Number of cycles to failure N_f predicted against actual for each alloy and temperature using crack growth data from the SENB tests (a) for all test carried out (b) in more detail excluding extreme value (U720Li C&W at 300°C in vacuum) (Note different scale of axis)

7.3 Conclusion

Based on the lifetime assessments of CNB using a $\Delta a/\Delta N$ integration and the SA16 software, it can be seen that there is no indication from these test samples that the macroscopically deflected crack growth has led to decreased lifetimes (showing conservative behaviour). The effects of initiation cycles has not been evaluated, and may provide part of the explanation for the longer observed lifetimes, as all the lifetime predictions assume immediate growth. The expected decrease in crack driving force once the crack deflects has been assessed in greater detail in Chapter 8, but additional effects of crack closure as these macroscopically deflected crack surfaces start to contact may also lead to additional extrinsic shielding effects reducing the crack tip stress state and crack growth rates. It should be noted that this finding that lifetime predictions based on planar crack paths are still conservative is based on simple loading configurations. If the crack path deflected into a hoop stress field in a turbine disc component this might result in significant changes in crack propagation behaviour because of a change in the stress field experienced at the crack tip because it has moved into a different stress state in the component. Crack path direction still needs to be predicted to allow this scenario to be more fully explored.

8 Crack Path Prediction

8.1 Introduction

Clearly in terms of lifing the problem does not seem to be the lifetimes themselves, as shown in Chapter 7; however the crack path is important. In a turbine disc a deflected crack could grow into the hoop stress field and cause disc failure (discussed in more detail in Chapter 6). Understanding the path this sustained deflected crack follows, is therefore important.

As discussed in Chapter 5.5, the crack path does not follow any obvious microstructural features, nor does the deflection seem related to a change in micromechanism, hence this chapter concentrates on establishing the driving force that influences the sustained macroscopic deflected crack propagation portions of the complex crack front. The evolution of the opening and shear (and twist) components at the deflecting crack tip, in terms of the local stress intensity factors k_i and k_{ii} (and k_{iii}) needs to be determined. This should help to identify the crack tip stress state conditions required to produce sustained macroscopic deflected crack growth and to provide appropriate crack growth data.

8.2 Mixed Mode Testing

8.2.1 Methodology of mixed mode testing

The averaged crack growth data from SENB tests cannot fully describe the local crack growth behaviour in the terraced region as described in Chapter 5.2.2 and shown in Figure 5-49. This fatigue crack growth is occurring under mixed mode conditions, i.e. a combination of mode I (tensile) and II (shear) and mode III (twist) loading (which is ignored for the moment). In order to gain crack growth data for the deflected regions and to further quantify the crack driving force changes, a test under mixed mode conditions, (i.e. in an antisymmetric set up, see section 8.2.1), can be used to produce crack growth.

As the plane stress condition seems to be important to trigger the SMDCG, mixed mode tests have been carried out using thin SENB samples with a width of 2mm, to promote plane stress conditions in the specimen. The other specimen dimensions were as stated in Chapter 4.1.2.

To work out the mixed mode conditions (controlling the sustained deflected crack growth), the relationship between the mode I and mode II component of the local stress intensity factor can be calculated for a deflected crack tip, the angle of the deflection using Figure 8-1 shows the relationship between the local and global stress intensity factors and the deflected crack path according to Suresh [77].

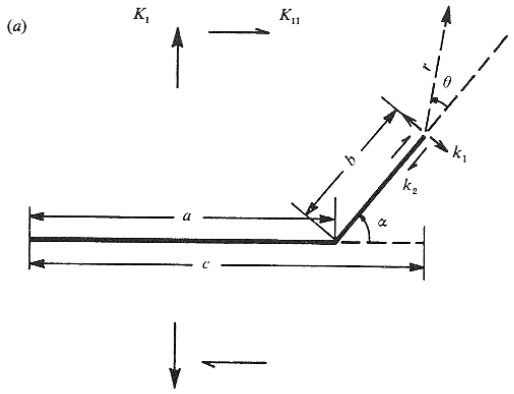

Figure 8-1: A schematic representation of kinked crack geometries and the associated nomenclature [77]

A range of typical values for the tilt angle α in the terraced region were measured in 3D maps created from the fracture surfaces of long crack tests with the Alicona Infinite Focus optical profilometer as discussed in 4.2.3.3 in different regions of the deflected regions of the 3D crack. Considering the highest and lowest angle a range of mixed mode conditions can be calculated.

Using stress intensity factor solutions for kinked cracks that could be extracted from Figure 8-2, adapted from [77], for the relationship between tilt angle α and k_i/K_I as well as k_{ii}/K_I the ratio k_i/k_{ii} can be calculated by fitting a polynomial function to the curves, where k_i and k_{ii} are the local mode I and II stress intensity factors and K_I is the overall Mode I stress intensity factor.

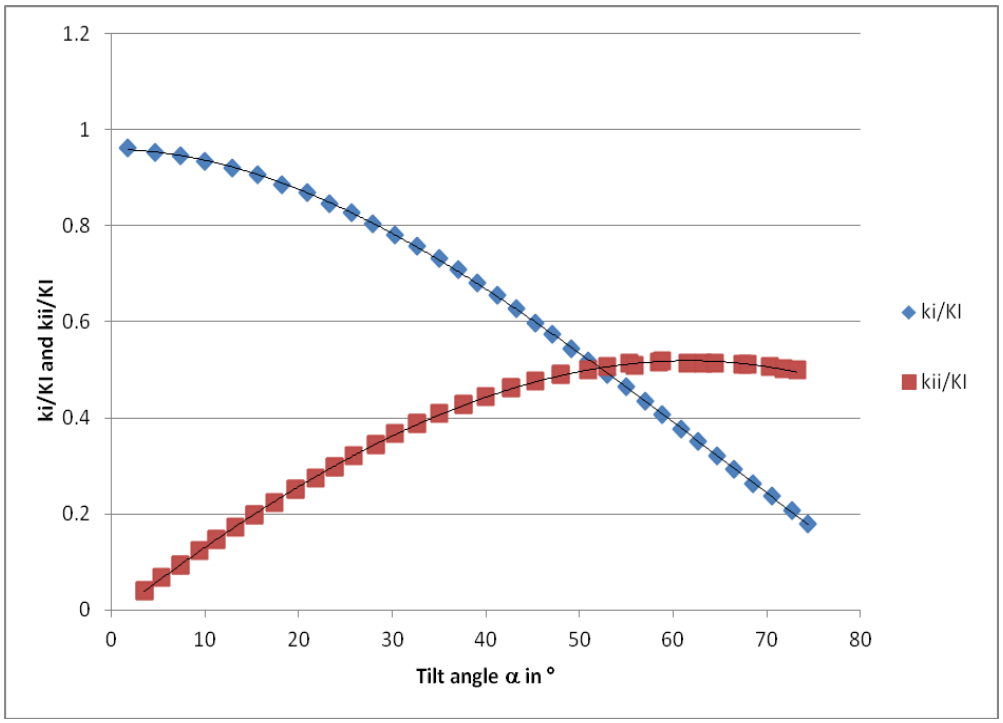

Figure 8-2: Variation of normalized k_1 and k_2 for b/a=0.1 as a function of α [77]

Using stress intensity factor solutions for kinked cracks that could be extracted from:

$$\frac{k_i}{K_I} = 10^{-6}\alpha^3 - 2*10^{-4}\alpha^2 - 0.0001\alpha + 0.959 \qquad \text{Equation 8-1}$$

$$\frac{k_{ii}}{K_I} = -5*10^{-7}\alpha^3 - 7*10^{-5}\alpha^2 + 0.0152\alpha - 0.0137 \qquad \text{Equation 8-2}$$

These ratios can be used to set up an antisymmetric 4 point bend, as shown in Figure 8-3.

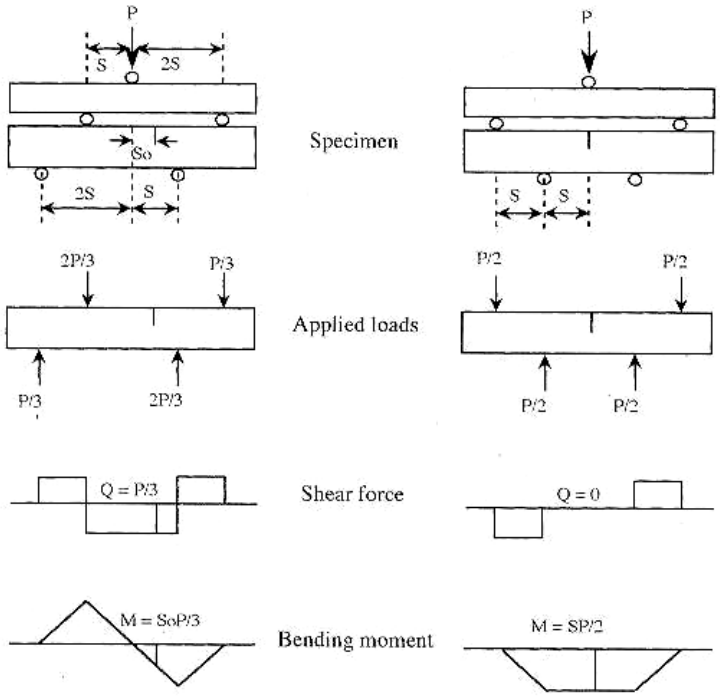

Figure 8-3: Antisymmetric 4 point SENB after Reed et al. [86]

In symmetric 4 point bend, as shown on the right hand side of Figure 8-3, with the notch in the centre, the crack experiences no shear force and a constant bending moment. In the antisymmetric 4 point bend (AS4P) the notch is offset from the centre by S_0. For S_0=0, the notch experiences pure shear, with increasing S_0 the bending moment increases, therefore the opening component increases.

In this set-up a normal Mode I crack would deflect away from the centre towards the increased opening moment. However for a sustained deflected crack, if the predicted opening to shear conditions are right, the crack would grow straight through the specimen, thus providing an opportunity to gain a simple assessment of crack tip stress state and crack growth rate for sustained macroscopic deflected crack growth.

According to Reed et al. [86] and with the geometrical relationship from Figure 8-3

$$K_I = \frac{Y_I M}{BW^{3/2}} = \frac{Y_I P S_0}{3BW^{3/2}}$$ Equation 8-3

$$K_{II} = \frac{Y_{II} Q}{BW^{1/2}} = \frac{Y_{II} P}{3BW^{1/2}}$$ Equation 8-4

where Q is the shear force, M is the bending moment, P is the applied load and S_0 is the distance that the notch is offset from the centre of the bend bar.

To calculate the load P Equation 8-4 can be transformed to:

$$P = \frac{3K_{II}BW^{1/2}}{Y_{II}}$$ Equation 8-5

S_0 can be calculated from Equation 8-3:

$$S_0 = \frac{3K_{I}BW^{3/2}}{Y_{I}P}$$ Equation 8-6

The compliance functions Y_1 and Y_2 for antisymmetric 4 point bend are given could be extracted from a diagram given by He et al. [103] and are shown in Figure 8-4.

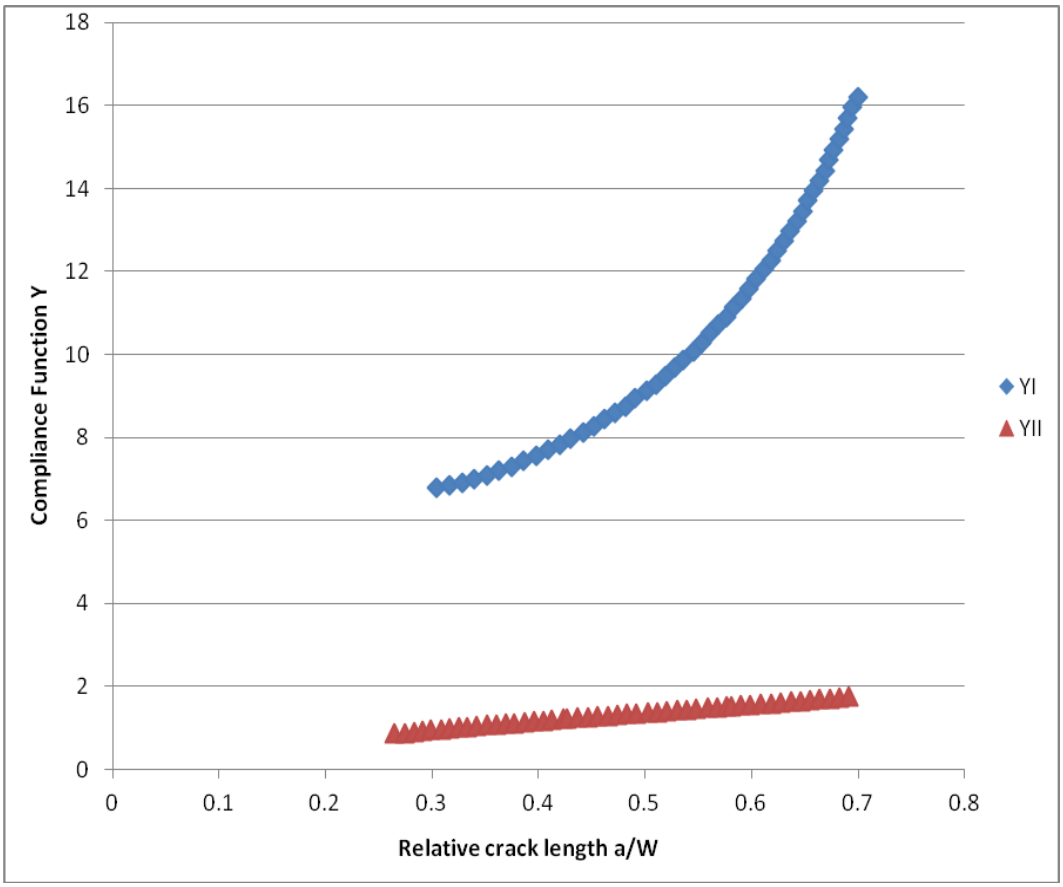

Figure 8-4: Compliance Function Y_1 and Y_2 as a function of a/W after He et al.

Polynomial trendlines have been fitted to the compliance functions Y_1 and Y_2 after He et. al [103] (Figure 8-4) and are described by the following functions:

$$Y_1 = 123.73\left(\frac{a}{W}\right)^3 - 127.06\left(\frac{a}{W}\right)^2 + 53.127\left(\frac{a}{W}\right) - 1.2044$$ Equation 8-7

$$Y_2 = 2.4906\left(\frac{a}{W}\right)^3 - 4.045\left(\frac{a}{W}\right)^2 + 4.1157\left(\frac{a}{W}\right) + 0.0125$$ Equation 8-8

Also from He et al. [103]

$$K_I = Y_1 \eta Q \sqrt{\frac{\pi a}{W}} = Y_1 \frac{S_o P}{3W^{\frac{3}{2}} B} \sqrt{\frac{\pi a}{W}} \qquad \text{Equation 8-9}$$

Therefore the compliance function Y_I as used in Equation 8-3 (by Reed et al. [86]) is

$$Y_I = Y_1 \sqrt{\frac{\pi a}{W}} \qquad \text{Equation 8-10}$$

and that corresponding to Y_{II} as used in Equation 8-4:

$$Y_{II} = Y_2 \sqrt{\frac{\pi a}{W}} \qquad \text{Equation 8-11}$$

K_{eff} can be calculated based on a simple strain energy release criterion [104]

$$K_{eff} = \sqrt{K_I^{\,2} + K_{II}^{\,2}} \qquad \text{Equation 8-12}$$

Based on the range of deflection angles and using the calculations derived and the angles measured on the SENB sample in Chapter 5.4.3 we can assess some k_i/k_{ii} representative ratios. For the lower end of the measured angle range (i.e. an angle of 30°) the local stress intensity factor has a low shear component, with k_i/k_{ii} of 2.2. At the top of the range (50°) opening and shear stress intensity factors are almost the same, with k_i/k_{ii} of 1.14. Two tests have therefore been carried out in AS4P using the above equation, one for the high shear condition and one for the low shear condition. The crack path under these loading conditions would be expected not to deflect if the K_I and K_{II} are chosen appropriately to reproduce the loading conditions and overall driving force that promote sustained deflected crack growth. On the other hand, if stage II type fatigue occurs then the crack would be expected to deflect to experience the maximum opening load.

Two symmetric 3 point bend tests have been carried out previously on thin SENBs which are described section 5.2.

All tests have been performed at 300 °C in air on a thin SENB sample with an R ratio of 0.1 with an initial notch size of circa a/W = 0.25, that has been precracked in symmetrical 3 point bend in air at room temperature at a constant ΔK of 20MPa√m. Tests and precracking were both done at a frequency of 20Hz. For the initial ΔK_{eff} for the test of 25 MPa√m was chosen, as it was assumed this was after the onset of the deflection based on CNB and SENB test observation, as discussed in Section 5.3.

8.2.2 Mixed Mode Testing Results

Two tests have been carried out in AS4P using the above equation, one for the high shear condition and one for the low shear condition. For a ΔK_{eff} =25MPa√m, at which the deflection is expected to have started already, according to the measurements for the ΔK onset.

8.2.2.1 Low shear

The first mixed mode test was carried out with a K_I/K_{II} = 2.2. Figure 8-5 shows how the crack deflected through the sample. The crack has clearly deflected away from the centre towards the increased bending moment. Figure 8-6 shows the fracture surface with the notch and precrack and then the crack grow-out that shows a planar Stage II region and deflected terraces that join in the centre. When observing the fracture surface directly from the top of the Stage II region (Figure 8-7), it is similar to the mode I test in the thin sample.

8.2.2.2 High Shear

For the mixed mode test with a higher shear component (K_I/K_{II} = 1.14), a similar result can be observed. Figure 8-8 shows how the crack deflected through the sample, from the side. The crack has clearly deflected away from the centre towards the increased bending moment. Figure 8-9 shows the fracture surface with the notch and precrack and then the crack grow-out that shows a planar Stage II region and deflected terraces that join in the centre. When observing the fracture surface directly from the top of the Stage II region (Figure 8-10), it is similar to the mode I test in the thin sample.

8.2.2.3 Fractography

The mixed mode sample with high shear condition has been observed in the FEG-SEM under a tilted angle so that the flat stage I region could be seen. Figure 8-13 shows the positions where SEM pictures were taken. The SEM fractography of the 'Stage II' region shows similar behaviour as in the Mode I samples, slip traces and corresponding secondary cracks. With increase in crack length, i.e. increase in ΔK, the slip traces get deeper and secondary cracks get larger and merge, as observed in the mode I samples. In the terraced region after the deflected crack growth regions have met, the same phenomenon can be observed. Estimations for the ΔK levels were difficult to make for the deflected crack length.

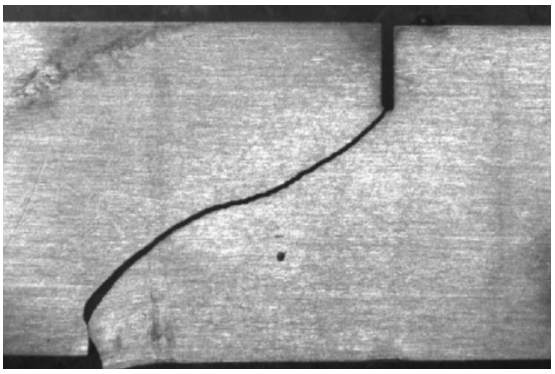

Figure 8-5: Low shear mixed mode fracture from the side

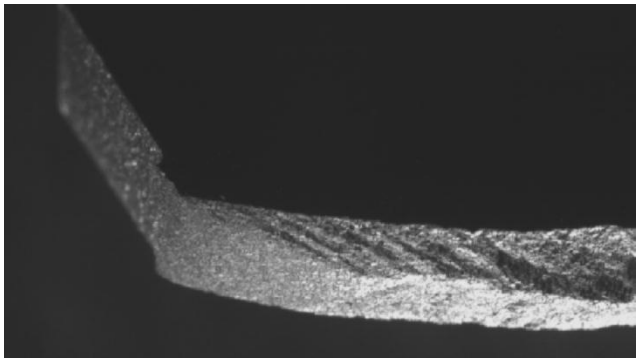

Figure 8-6: Low shear mixed mode fracture surface showing the Stage II region

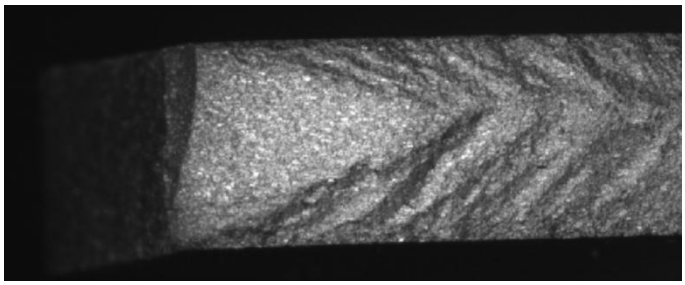

Figure 8-7: Low shear mixed mode fracture surface showing the stage II region

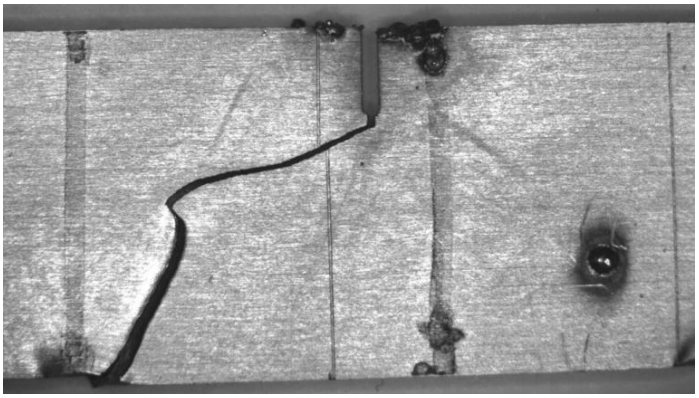

Figure 8-8: High shear mixed mode fracture from the side

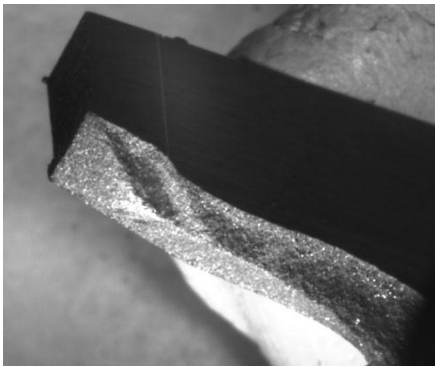

Figure 8-9: High shear mixed mode fracture surface showing the Stage II region

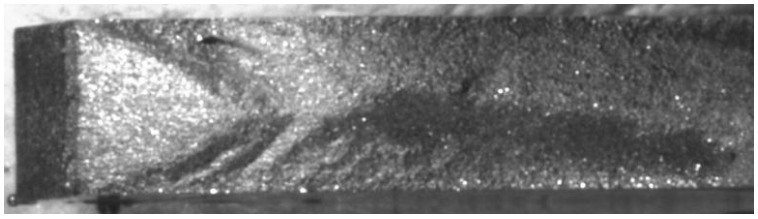

Figure 8-10: High shear mixed mode fracture surface showing the Stage II region

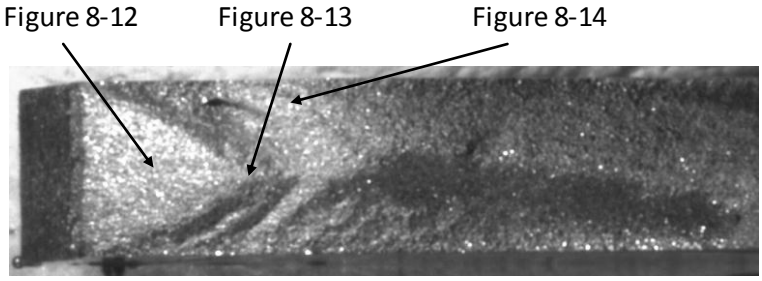

Figure 8-11: High shear mixed mode fracture surface

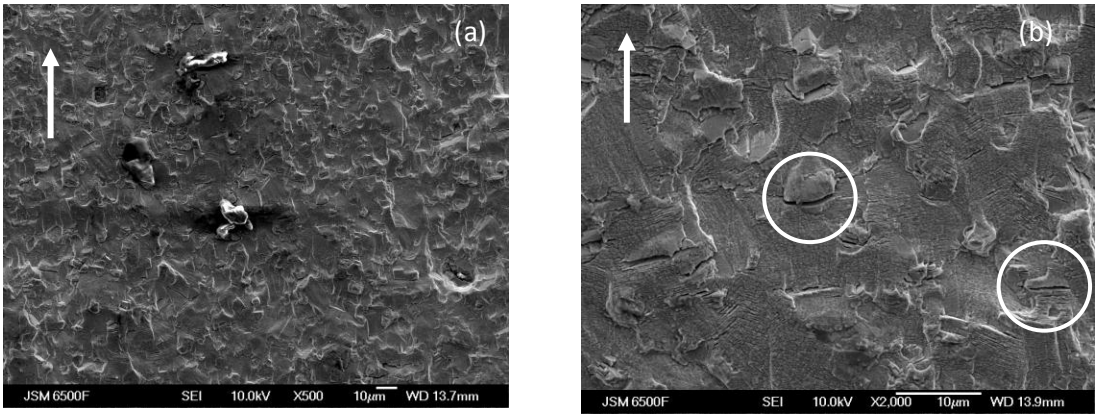

Figure 8-12: Fracture surface of U720Li C&W in AS4P thin SENB at 300°C in air in the centre of the sample in the region before terracing at a distance from precrack of 0.24mm (Arrow indicates crack growth direction) (a) at low magnification showing stage II growth (b) at high magnification showing slip traces and secondary cracks

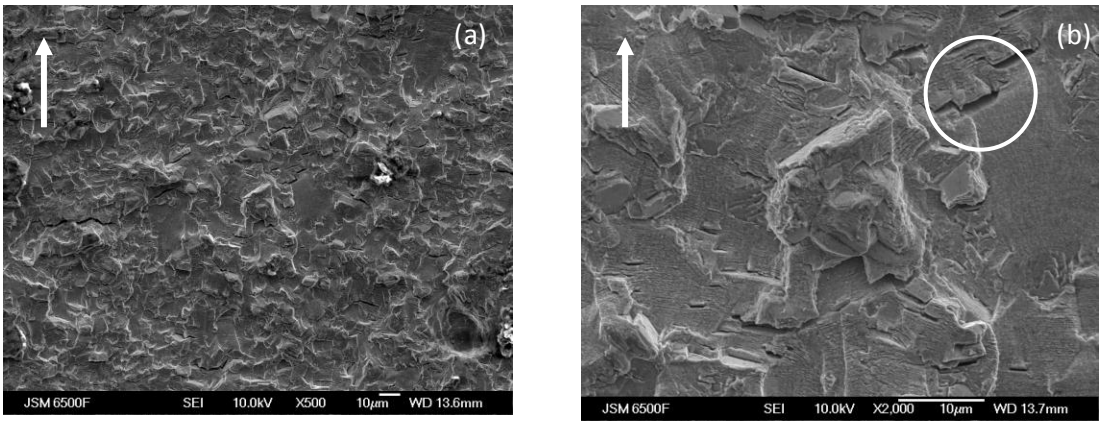

Figure 8-13: Fracture surface of U720Li C&W in AS4P thin SENB at 300°C in air in the centre of the sample in the region before terracing at a distance from precrack of 1.54mm (Arrow indicates crack growth direction) at low magnification showing stage II growth (b) at high magnification showing slip traces and larger secondary cracks merging over several grain size

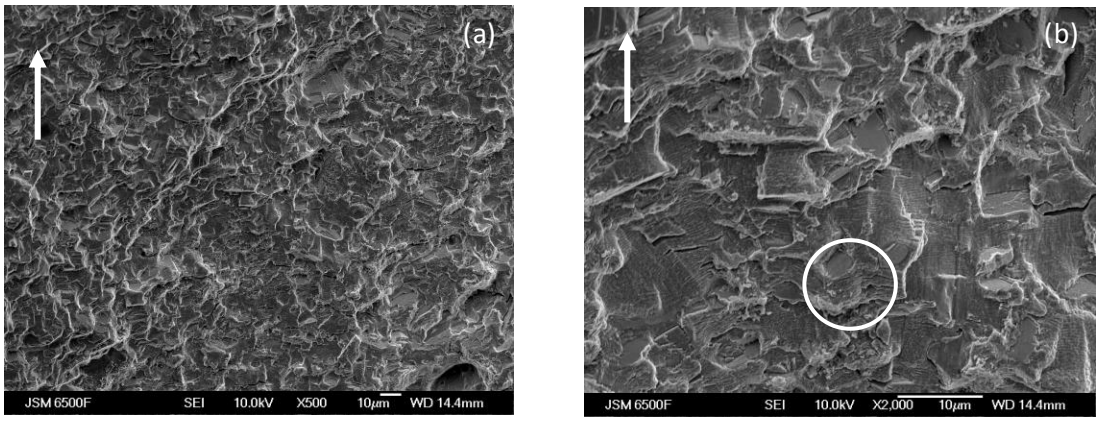

Figure 8-14: Fracture surface of U720Li C&W in AS4P thin SENB at 300°C in air in the terraced region at a distance from the precrack of 2.12mm (Arrow indicates crack growth direction) (a) at low magnification showing stage II growth (b) at high magnification showing slip traces and secondary cracks

8.2.3 Discussion

The causes of crack deflection can be described by deflection mechanics in three stages (or at three different scales), which are schematically presented in Figure 8-15. (a) Firstly in a crack under mode I loading a small local deflection can emerge caused by planar slip processes or other local deflections triggered by the microstructure. (b) Secondly this small deflection from the parent crack can develop more significantly, but still be contained within the crack tip plastic zone. (c) Finally the crack could deflect to become a macroscopic mixed mode crack, which can be described by linear elastic fracture mechanics (LEFM) (with a local k_1 and k_2 controlling the crack propagation). The two first cases occur regularly during the growth of a crack, but do not necessarily develop into a macroscopically deflected crack.

The prior crack morphology determines the near-tip conditions, and mixity and net driving force evolve rapidly at deflecting tip, therefore the failure processes become path dependent, hence the k_1 and k_2 evolution need to be assessed by extracting crack path features. These can be taken from the profilometry results.

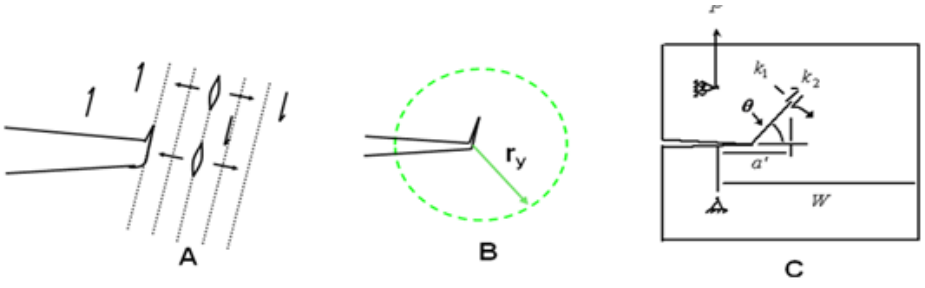

Figure 8-15: Stages of crack deflection

Based on assessment of the k_1/k_2 levels at the deflected crack growth areas seen in the SENB samples tested, two mixed mode test conditions were also defined with K_I/K_{II} = 1.14 and 2.2 respectively and were carried out in thin samples (to promote plane stress conditions)

In a successful mixed mode test, a sustained deflected crack would have grown straight through the sample (assuming the correct K_I/K_{II} conditions were achieved) as shown by the yellow line in Figure 8-16 and Figure 8-17, where it can be seen how the crack deflected during growth through the low shear and high shear sample, respectively. Sustained deflection has clearly not been achieved. A pure Mode I crack would be expected to grow along the estimated Maximum Tangential Stress (MTS) fracture angle, based on Figure 2-7 in Section 2.3.1, which in this case is estimated to be 41° in the low shear case and 53° in the high shear case, as shown by the red line in Figure 8-16 and Figure 8-17, respectively. This crack has however gone off at an even higher angle.

The point where the shear lips meet in the centre is also of interest, the opening to shear ratio is now estimated to have changed to K_I/K_{II}=3.6 in the low shear sample and K_I/K_{II}=2.2 in the high shear sample, so there is much more opening than shear in this position. The ΔK_{eff} at this point (and the k_i/k_{ii} ratio) can be estimated by assuming the crack had grown straight down from a crack in this position with an initial crack and precrack of the same projected perpendicular length as the actual crack, indicated by the green line. The estimated ΔK_{eff} is approximately 49 MPa√m for the low shear and 48 MPa√m for the high shear, which is similar to the ΔK of 45 MPa√m in the thin Mode I sample where the shear crack regions were found to meet.

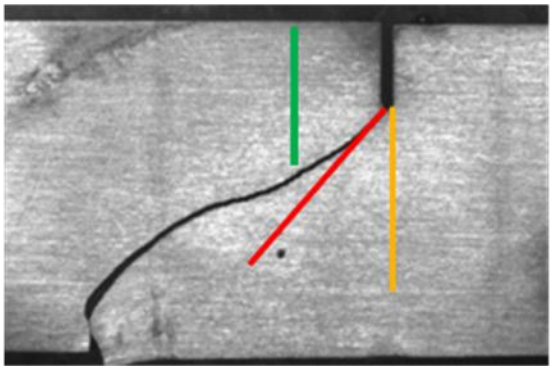

Figure 8-16: Low shear mixed mode fracture from the side

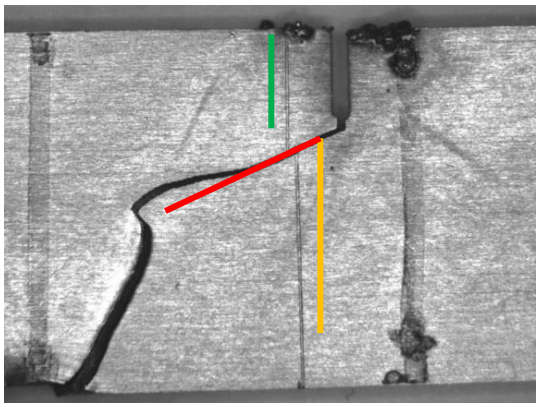

Figure 8-17: High shear mixed mode fracture from the side

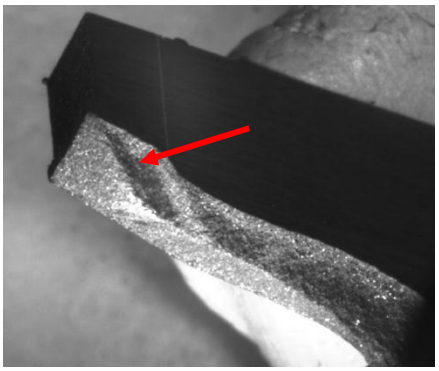

Figure 8-18: High shear mixed mode fracture surface view on the teardrop region with the red arrow indicating a turn back into the shear direction

Figure 8-18 shows the fracture surface of the high shear test with the notch and precrack and then the crack growout that shows a planar Stage II region and deflected terraces that join in the centre. A slight turn down into the higher shear direction can be observed, where the shear lips meet, as indicated by the red arrow. It seems that that crack started to try to grow in the self-sustained direction at this ΔK_{eff}, however it might not have the required self-sustaining K_I/K_{II} ratio.

At this point the shear component was too low to achieve sustained deflected crack for a high enough ΔK level (for overall deflection). Since both mixed mode tests did not achieve sustained shear deflection, it is possible that a higher ΔK_{eff} is needed. As suggested by the onset of terracing for U720Li C&W at 300 in air the ΔK value is between 25-28 MPa√m, so slightly higher than the value used in these tests. However the value where total deflection has been observed in a thin sample is about 45 MPa√m, this is however already near the level for final fracture.

It seems therefore higher ΔK levels are required for these tests; however the necessary loads were too high for such a thin specimen geometry to remain stable during set up in bend.

It is also possible that the twist component (mode III) which has been ignored in these tests may play an important role for the sustained macroscopic deflection, considering the tilted and twisted shape of the deflection. The SEM fractography showed the same competition between two cracking modes in both the deflected and Stage II region, that had been observed in the mode I samples.

8.3 Crack Path Modelling

8.3.1 Introduction

As described in section 8.2.3, the K_I/K_{II} conditions used to set up a mixed mode test did not produce a simple sustained deflected crack growth behaviour under well-defined K_I/K_{II} conditions to allow unambiguous crack growth rate determination. The hope was that this approach might both help to clearly identify the crack tip stress state conditions required to produce sustained macroscopic deflected crack growth and to provide appropriate crack growth data. This approach had been successful in previous work in analysing the factors controlling extended 'simple' Stage I crack growth in Ni-base single crystals along particular slip systems [86]. Clearly the conditions controlling sustained macroscopic deflected crack growth in this polycrystalline system are not simply controlled by the rather simplistic 2D analysis of the stress state conducted thus far, hence a finite element modelling approach has been used to characterise the crack path observed. It is necessary to run a 3D model, as the 2D analysis from Suresh does not consider the twist element of this 3D deflection. In addition the plane stress state (which appears to play a critical triggering role) is hard to replicate throughout an entire specimen.

This section concentrates on establishing the driving force that influences the sustained macroscopic deflection and the planar crack propagation portions of the complex crack front. The evolution of the opening, shear and twist components at the deflecting crack tip, in terms of the local stress intensity factors k_i, k_{ii} and k_{iii}, needs to be determined.

8.3.2 Methodology

A decision has been made to represent this behaviour as a simple overall deflection at the appropriate angle at the specimen sides, rather than reproducing each individual angle and terrace, in defining the overall crack path.

To determine this crack growth driving force, the 3D crack surface data points from the Alicona Infinite Focus map of the Single Edge Notch Bend sample tested at 300°C in air (see Figure 8-28) have been used to create a simplified 3D Finite Element Model in ABAQUS. A simpler 3D model based on the measurements of the deflection on the side of the sample has also been created.

Zencrack has then been used to model the deflected crack growth stages and extract the relevant k_i, k_{ii} and k_{iii} components. Zencrack is a software that can easily create a crack by replacing the elements in the location of the crack tip by a predefined crack block. The results have been benchmarked against simpler approaches in 2D (using Franc2D) where simplifications of the observed crack deflections have been examined and compared with the 3D results.

8.3.2.1 Franc2D Methodology

Franc2D is a free two dimensional FE software for fracture mechanics evaluations developed by Cornell University [105]. A crack of a specific length and direction can be inserted, after we have defined an uncracked mesh, and is automatically remeshed as the crack extends. Figure 8-19 shows the uncracked mesh and how the crack tip is remeshed after the crack length has been defined for an SENB sample with a planar crack. All units had to be converted into imperial units in, ksi and ksi√in for Franc2D. The plane stress condition was defined, as we wished to consider the behaviour of the free surface (from where the deflected behaviour appears to be triggered). Δk_i and Δk_{ii} values can be calculated at the crack tip using a displacement correlation technique, a J-integral technique or a modified crack closure integral technique. These methods are all described in more detail in Wawrzynek and Ingraffea [105]. These all showed similar results for the *K*-levels as shown in Table 20, where they are compared for a planar crack in an SENB sample, and have also been compared to the *K* calibration from the British Standard (BS) and the results from a planar crack in Zencrack (for the edge and the centre of the sample) . Although the Franc2D analysis was carried out under plane stress conditions, they vary significantly from the values from the edge of the 3D Zencrack model, while they are similar to the centre of the Zencrack model (which should be more plane strain dominated) and the analytical solution from the BS (again plane strain dominated). The results for the J-integral method match most consistently with the analytical *K* calibration from the BS; hence this value has subsequently been used.

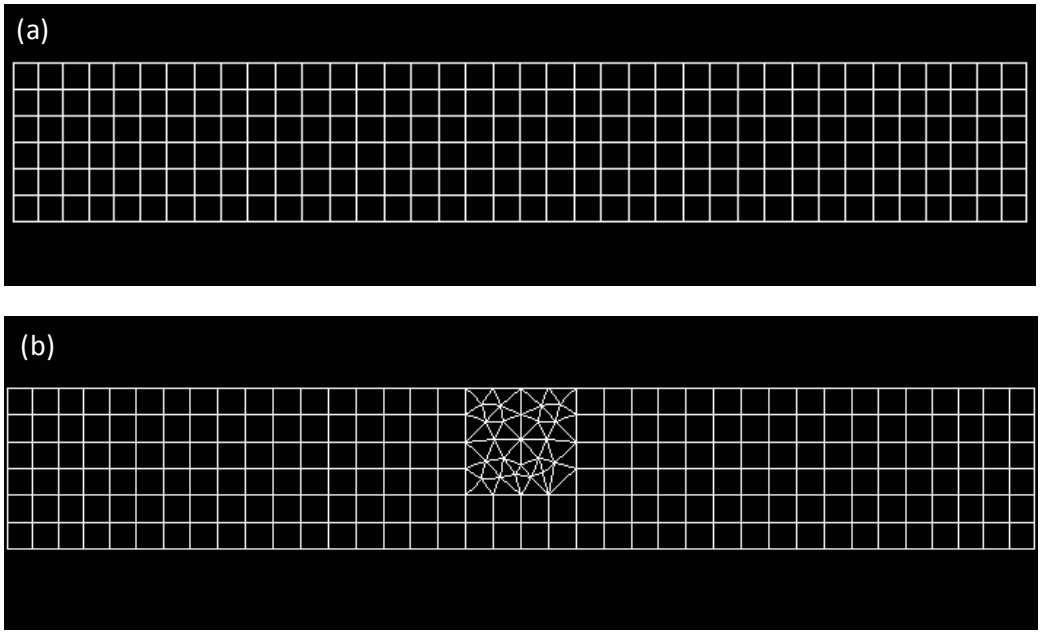

Figure 8-19: Franc2D model of an SENB sample (a) uncracked (b) with remeshed crack tip

	Franc2D: Displacement Correlation (plane stress)		Franc2D: J-Integral (plane stress)		Franc2D: Modified Crack Closure (plane stress)		Zencrack (Edge) (plane stress)		Zencrack (Centre) (plane strain)		BS (plane strain)
A	Δk_i	Δk_{ii}	Δk_i	Δk_{ii}	Δk_i	Δk_{ii}	Δk_i	Δk_{ii}	Δk_i	Δk_{ii}	ΔK
Mm	MPa√m	MPa√m	MPa√m	MPa√m	MPa√m	MPa√m	MPa√m	MPa√m	MPa√m	MPa√m	MPa√m
4	18.1	0.0	20.4	0.0	20.1	-0.3	17.4	0.0	20.7	0.0	19.9
5	25.6	0.6	25.5	0.5	25.1	0.3	21.0	0.0	25.4	0.0	24.6
6	30.5	0.2	31.3	0.4	31.3	1.4	25.7	0.0	31.5	0.0	31.0
7	39.3	0.3	40.9	-0.7	40.8	0.7	33.1	0.0	40.9	0.0	40.3
8	52.3	1.0	54.8	0.8	54.9	2.1	43.8	0.0	54.4	0.0	54.9

Table 20: Δk_i and Δk_{ii} for different crack lengths in model of a planar crack in SENB sample from Franc2D (using different methods), Zencrack (for the edge and the centre) and ΔK from BS

8.3.2.2 Zen Crack Methodology

The 3D model has been developed using Abaqus and Zencrack. The ZenCrack software works within Abaqus FE software, and is a tool that remeshes the crack tip automatically, by replacing individual elements in the defined mesh at the crack tip location by a crack block, which is a defined meshed crack tip from the Zencrack crack block library. [106]

These crack blocks can be specified with different refinement levels of the mesh, i.e. different numbers of elements and for different crack geometries e.g. corner and though thickness cracks, as in our test samples. The direction of the crack is defined using the node numbers and the crack length is defined for two sides of the crack block as described in Figure 8-21.

There are two types of crack blocks in Zencrack, standard and large, where a large element has to be linked to the surrounding mesh using surface ties in Abaqus to be replaced by a large crack block. Figure 8-22 show a model of a CNB sample, where large elements have been linked to the surrounding mesh with surface ties, and been replaced by a 'large' crack block.

Figure 8-20 shows examples of the 4 different crack block types. Using the large crack blocks is an easier way of creating (and growing out) a crack, however a deflected crack front near the surface cannot be created using these.

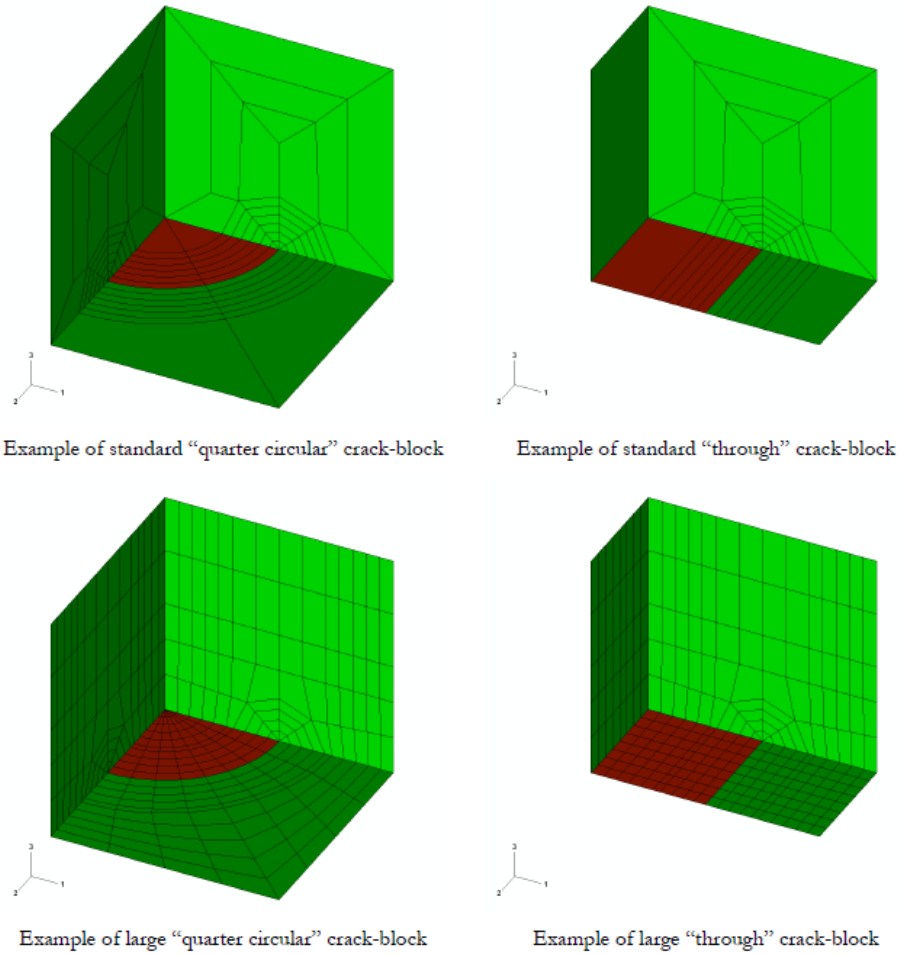

Figure 8-20: Examples of the different Types of crack blocks in Zencrack [106]

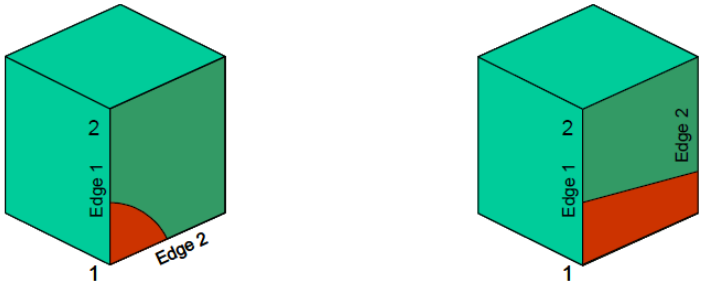

Figure 8-21: Corner and through thickness crack, the direction of the crack is defined by the numbers of the nodes from 1 to 2 as marked, and the size of the crack is defined for edge 1 and 2 [106]

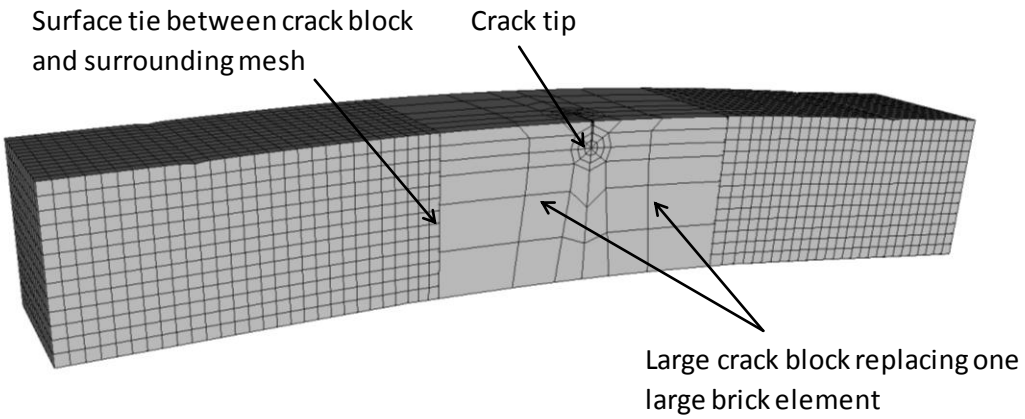

Figure 8-22: Large crack blocks in Zencrack in model of CNB sample

Zencrack has been chosen as remeshing the crack tip manually (as we extend the crack) would be very time consuming and also difficult to do in any other FE software.

For longer cracks, as in the SENB case, the SPLIT function in Zencrack [106] can be used to separate the elements behind the crack tip, to create a deep crack or the crack wake. Figure 8-23 shows an SENB sample with such a crack block. Arrows show how crack blocks are used on either side of the crack and replacing each element along the crack front and how SPLIT elements are used to create the crack wake.

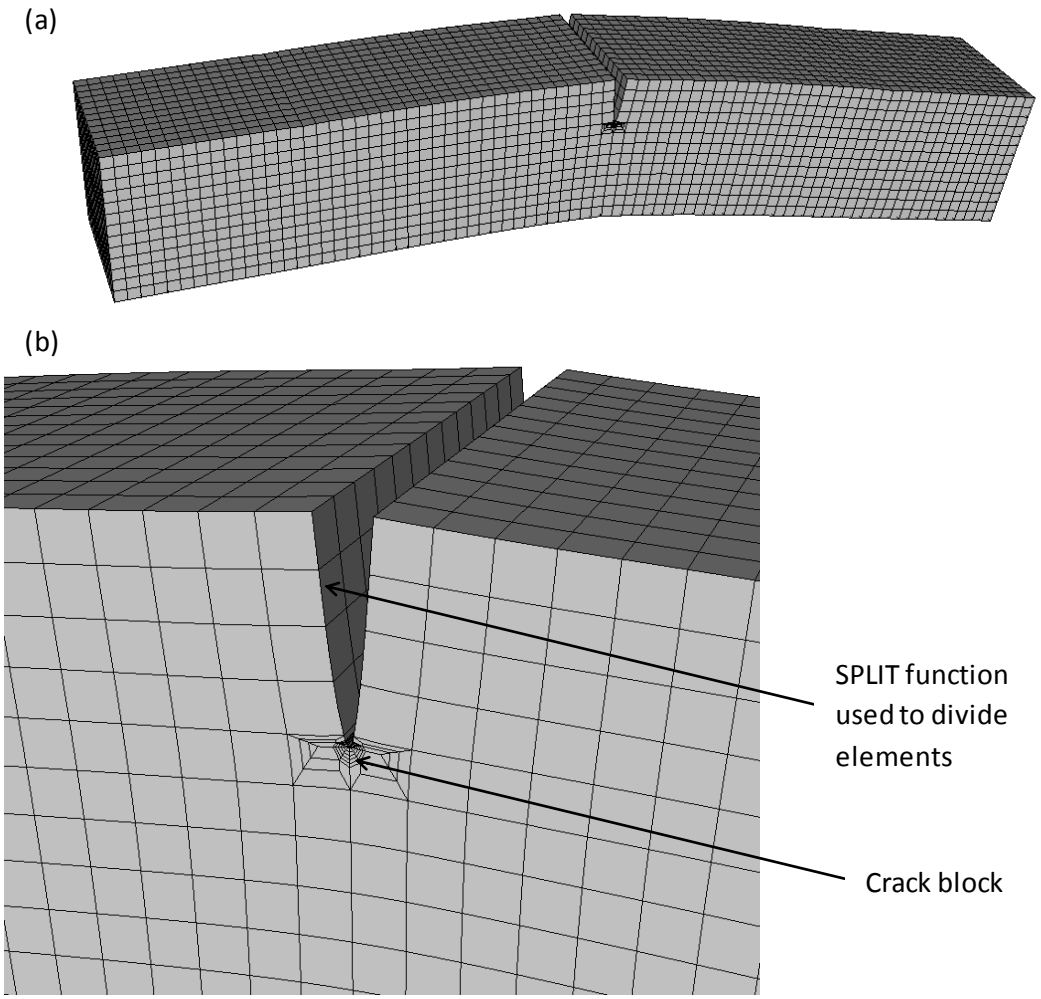

Figure 8-23: Zencrack model of SENB sample using crack blocks on either side of the crack and split elements for a deep crack (a) whole model (b) detailed view of crack tip

Zencrack uses a simple code in which the crack tip is specified in terms of size and direction. It opens the Abaqus file, inserts the crack block in the mesh, and then runs Abaqus for the analysis.

K values are calculated using from relative crack tip opening displacements V_i, V_{ii}, V_{iii} for the opening, tilting and twisting using Westergaard equations (valid for linear elastic isotropic materials) [106]

$$K_I = \frac{EV_i}{4B}\sqrt{\frac{2\pi}{r}}$$ Equation 8-13

$$K_{II} = \frac{EV_{ii}}{4B}\sqrt{\frac{2\pi}{r}}$$ Equation 8-14

$$K_{III} = \frac{EV_{iii}}{2(1+v)}\sqrt{\frac{\pi}{2r}}$$ Equation 8-15

where *r* is the distance from the crack front and *v* is the Poisson's ratio and:

$B = 1 - v^2$ for plane strain Equation 8-16

$B = 1$ for plane stress Equation 8-17

From this the equivalent energy release rate *G* is calculated with

$$G = \frac{B}{E}(K_I^2 + K_{II}^2) + \frac{1+v}{E}K_{III}^2$$ Equation 8-18

which can be used grow the fatigue crack, and hence calculate the lifetime of the model using an integration of *dG/da*. This can however only be used for a model of a planar crack, as discussed below.

Appropriate *C* and *m* values from the SENB tests have been used as well as data from the Rolls Royce database (from CNT tests), as described in Chapter 6. The load ratio is defined as 0.1.

The integration scheme assumes that the rate of change in energy release rate *dG/da* is constant as the crack grows. At the end of each load block the estimate of *dG/da* and the crack growth are used to update the base value for *G* for integration of the next load block.

$$G_{final} = G_{initial} + \left(\frac{dG}{da}\right)da$$ Equation 8-19

The crack growth direction is determined by assessing the local out of plane angle with respect to the maximum opening stress, which is calculated using the Maximum Tangential Stress criterion, hence growing out a sustained macroscopic deflected crack is not possible using Zencrack as it will always deviate back to experience the maximum opening mode direction (i.e. it is growing the crack as if it were propagating in normal Stage II fashion) Hence for this study the use of Zencrack to predict the crack growth behaviour is not the aim, rather we can use the Zencrack capability to reproduce the observed experimental crack path trajectory (including the regions of sustained macroscopic crack deflection) and assess how the local components of the stress intensity factors k_i, k_{ii} and k_{iii}, evolve.

However we can predict the lifetime for a planar crack. Zencrack has a function for Boundary transfer, which allows the crack tip to be moved to the next element, if it cannot grow any further. This allows the crack to grow through most of the SENB model. The sample fails in Zencrack, when da exceeds the maximum allowed value between two analysis steps. This is the size of the smallest crack block.

8.3.2.3 Specimen and crack path modelling in Franc 2D

A 12.5 by 80mm rectangle was created and meshed with square elements of 2.083 mm length in Franc2D. Young's modulus was set to 214.7GPa and Poisson's ratio was set to 0.281 representing U720Li C&W at 300°C in air [93].

A P_{mean} of 2.646kN for the SENB and of 13.144kN for the CNB was distributed equally in the positions of the top two rollers, representing idealised specimen dimensions for the tested conditions. At the position of the bottom rollers constraints were set in the *X* and *Y* direction, with a central roller to represent 3 point bend for the SENB, and two inner rollers to represent 4 point bend for the CNB. All units had to be converted into imperial units in, ksi and ksi √in for Franc2D. The plane stress condition was defined, as we wished to consider the behaviour of the free surface.

From the initial crack length 5 different crack fronts are modelled for both deflected and non-deflected crack and for each Δk_i and Δk_{ii} are calculated, modelled for a simplified crack front without any terraces using a measured angle of 20° for the SENB and 15° for the CNB samples, as measured on the free surface of each sample at 300°C in air from the onset of deflection to the maximum deflection before plastic collapse. Figure 8-24 shows the SENB sample with a deflected crack for the final crack front calculated. The results for the 2D case are used for benchmarking of the ZenCrack 3D results (and to compare to Suresh's analytical models [77] as discussed in section 8.2).

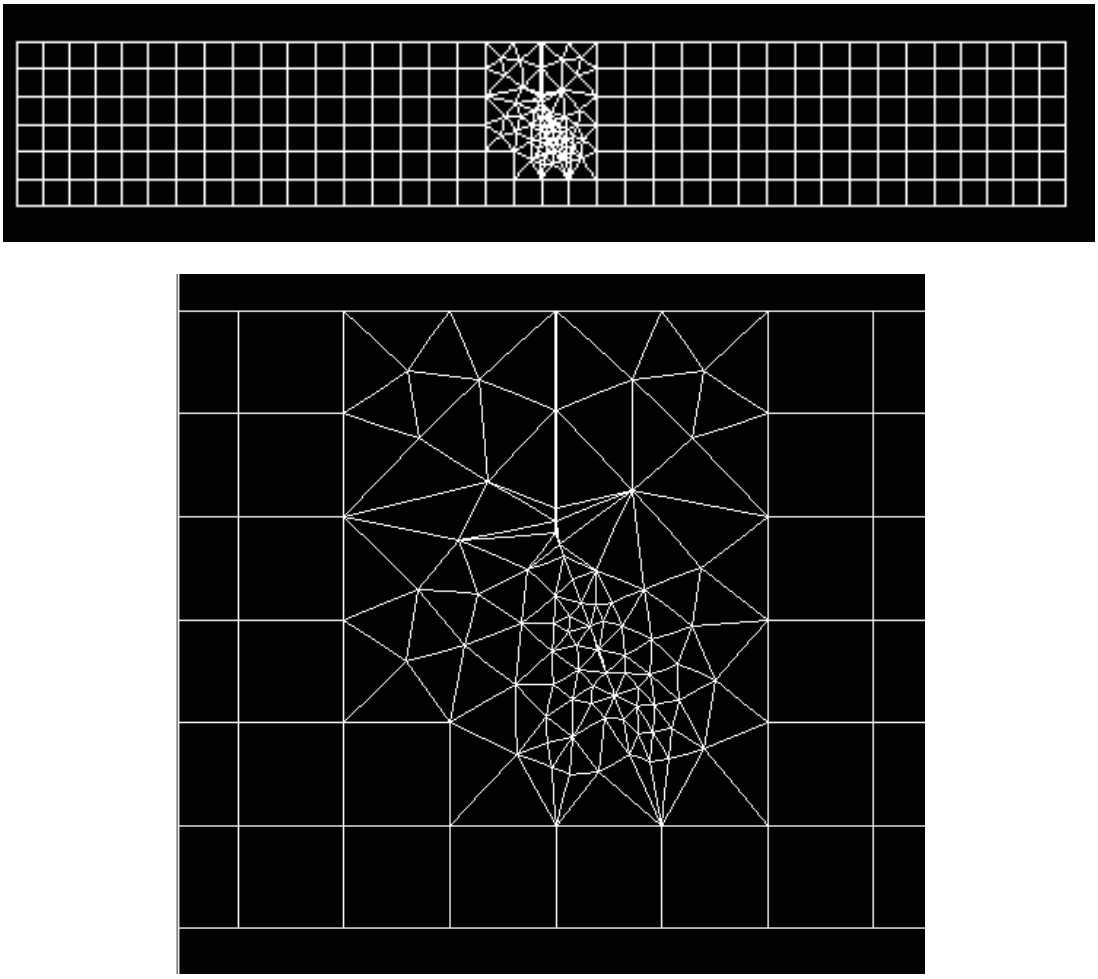

Figure 8-24: Franc2D mesh for an SENB specimen with a deflected crack for crack length a=8mm

8.3.2.4 Specimen modelling in Zencrack

To develop the models for SENB and CNB in the first instance 3D models of the bend bar specimens have been created and meshed using PATRAN to create a 12.5x12.5x80mm specimen. 20-noded brick elements have been used with a length of 0.962 mm. 20-noded brick elements are needed for the elements to be replaced by Zencrack crack blocks.

For the Corner Notch sample in 4 point bend the applied P_{mean} was 13269.6N for a sample with a notch of 0.35mm and a ΔK_i of 12 MPa√m based on Pickard's calibration [94]. This load was distributed on all the nodes in the positions of the two top rollers, and constraints set at the location of the two inner bottom rollers in the Z direction.

For CNB a large crack block model has been used, which is relatively easy to model compared to using standard crack blocks, however this does not allow for more complex 3D deflected crack growth to be modelled, so a simple deflection of the entire crack plane has been used. A model with a planar crack has also been modelled for comparison. On either side of the crack plane a large element (with dimensions of 12.5x12.5x12.5mm) for the crack block has been linked to the rest of the mesh using a surface tie, which is the suggested method [106]. This may have an effect on the results of the stress analysis to some extent, but might not affect

the crack tip stress so much, as it is 12.5mm away from the crack plane, where the maximum crack deflection from this plane is 1mm.

For the SENB the plain rectangular bend bar is then loaded in 3 point bend (the same loading condition as in the tests for an idealised crack length of 4mm), using a P_{mean} of 2646N with the load distributed on all the nodes in the positions of the two top rollers and constraints in the *Z* direction set at the location of central bottom roller.

Both models have been constrained in the *X* and *Y* directions at a single node (in the location of the bottom roller) to avoid the model moving unrealistically.

An ABAQUS input file was created from this mesh (without the notch) and the material properties from the Rolls Royce data base for Alloy 720Li were added. An analysis was run in ABAQUS for the uncracked models and Figure 8-25 shows the meshed CNB model and Figure 8-26 shows the meshed SENB sample, with the FE results for the maximum principal stress, showing the maximum tensile stress on the surface.

The results of the Abaqus stress analysis of the plain rectangular uncracked sample for the tensile stresses on the top surface are again similar (within ~10%) to the calculated values based on simple beam theory, based on

$$\sigma = \frac{3PS}{BW^2}$$

Equation 8-20

For 4 Point bend set up 565.6MPa was predicted with FE and 555.8MPa for beam theory for maximum stress (dependent on specimen geometry, not material properties) and for the 3 Point bend configuration 177.5MPa was calculated from the FE and 184.8MPa for simple beam theory for the maximum surface stress.

Stresses around the rollers are expected to be large (and cause local deformation on the actual samples), but can be ignored, as crack growth always initiated from the defects in the centre region. Based on this initial evaluation the far-field loading in the FE simulation was considered a reasonable approximation to what is assumed in simple beam theory.

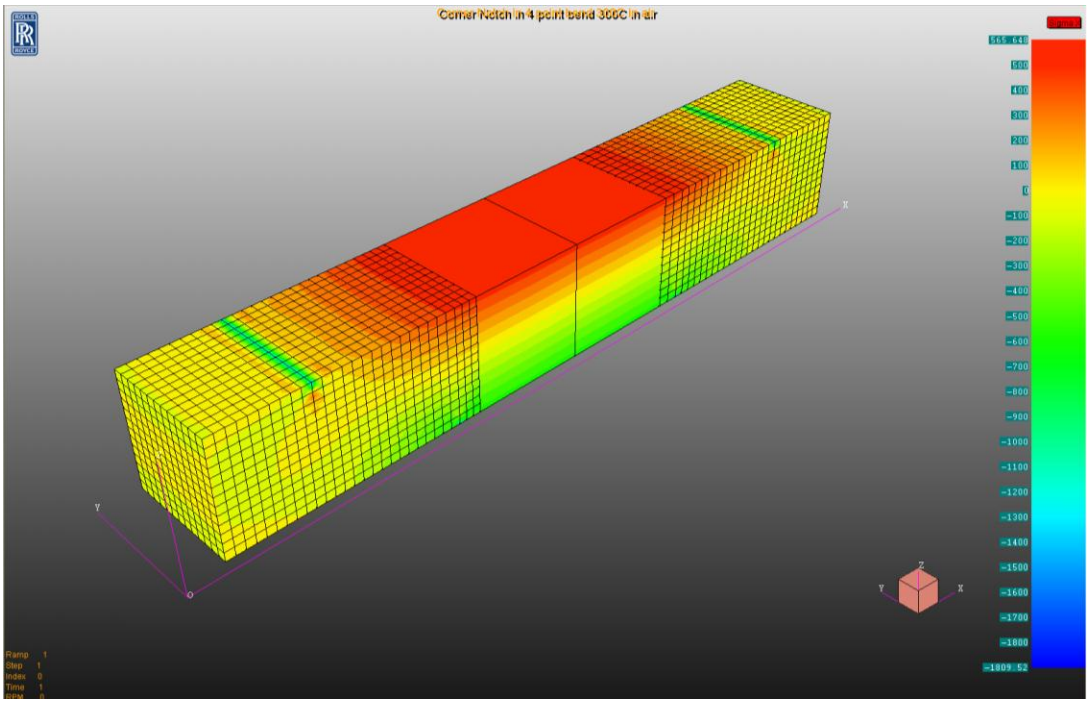

Figure 8-25: Abaqus model of CNB sample with 2 large elements showing maximum principal stress

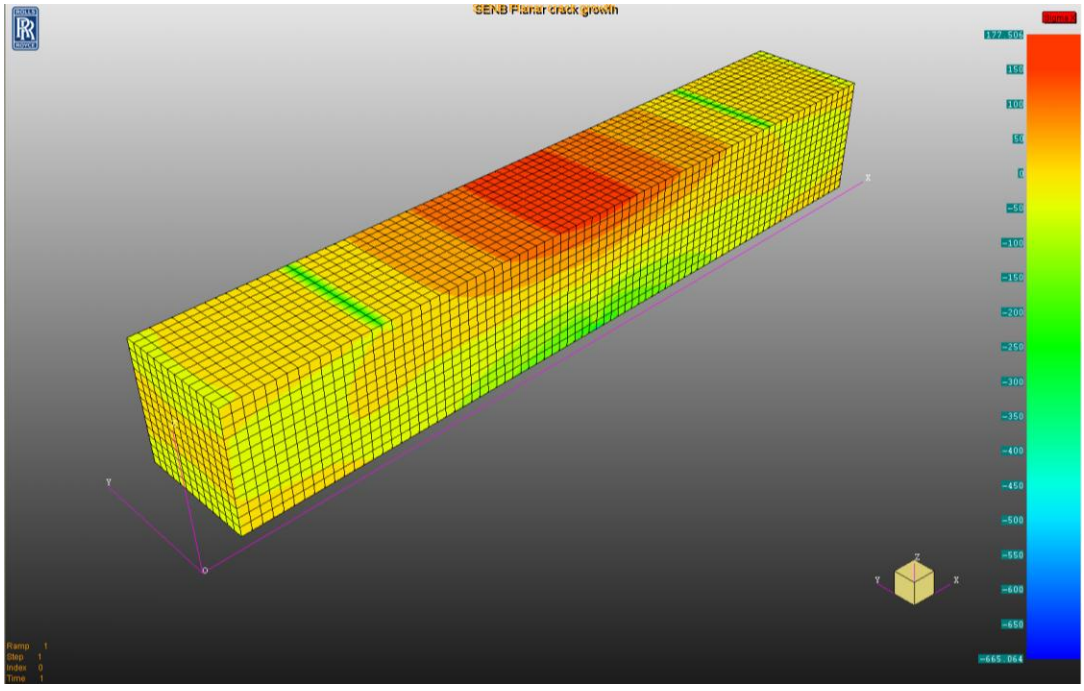

Figure 8-26: Abaqus model of SENB sample showing maximum principal stress

8.3.2.5 Crack path modelling in Zencrack

To create a crack in the CNB model, a crack block l03_q112x4 was used from the Zencrack crack block library [106], see Figure 8-27, to replace the large elements. ΔK levels at 7 different crack fronts have been calculated, starting with an initial crack of 0.35mm (corresponding to the initial notch), and then in intervals of approximately 1mm. For the deflected model a single deflection of 15° has been used for the entire crack plane. This is representative of the angle measured at the sample edge between onset of deflection and the final deflection from the CNB sample tested at 300°C in air. As this is not representative for the planar behaviour in the centre and the 'shear lip' near the edge, which will also have twist component, only the edge of the sample has been considered in analysis.

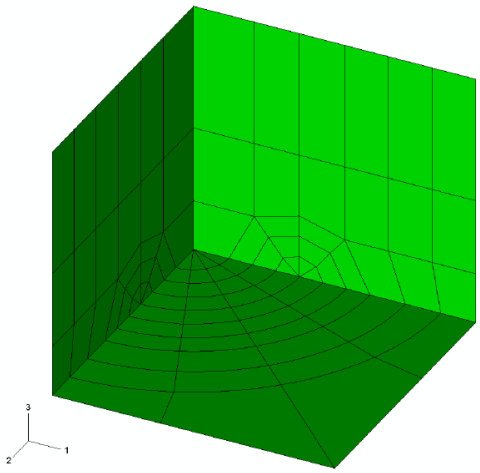

Figure 8-27: Zencrack large crack block l03_q112x4 used for model of CNB [106]

For the SENB configuration a planar crack has been created and also two deflected crack paths, by offsetting nodes from their original position in the first two element rows next to the edge in PATRAN, to recreate and simplify the observed deflection in the SENB sample based on coordinates measured in the Alicona infinite focus map for the 300°C air SENB test (as described in Chapter 5.4.3), see Figure 8-29 and Figure 8-30. The adjacent nodes were moved as well to stop the nodes overlapping.

Two deflected models have been created. Model A is most simplified showing a single deflection (that is in the same direction on both edges), based on the measurements of 3 coordinates from the 3D map, as marked in Figure 8-28 in red. Model B is an asymmetric model, one edge deflects to a particular point, and then the deflection goes in the opposite direction, while on the second edge it is the same as model A. This is based on coordinates measured from the other side of the 3D map, marked in blue in Figure 8-28.

The deflections have been modelled from the sample up to a crack length of 9mm, and then they are set back to the original centre line to allow for the constraints to be fixed in the position of the bottom roller. In the original sample the deflection would further increase from this point on, but the ΔK levels above 9 mm are close to plastic collapse ($\Delta K \approx 80$MPa$\sqrt{m}$), so this area is not considered in the crack path analysis.

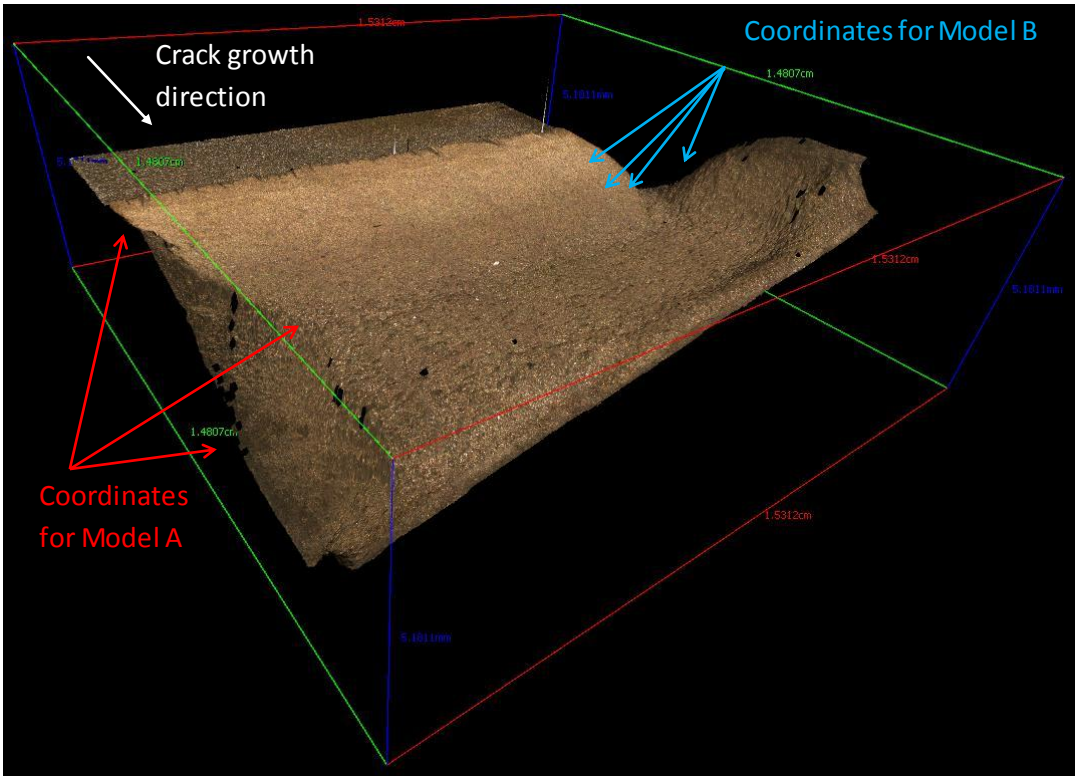

Figure 8-28: 3D map of SENB fracture surface indicating the positions measured to define the simplified deflected crack shapes in model A and B

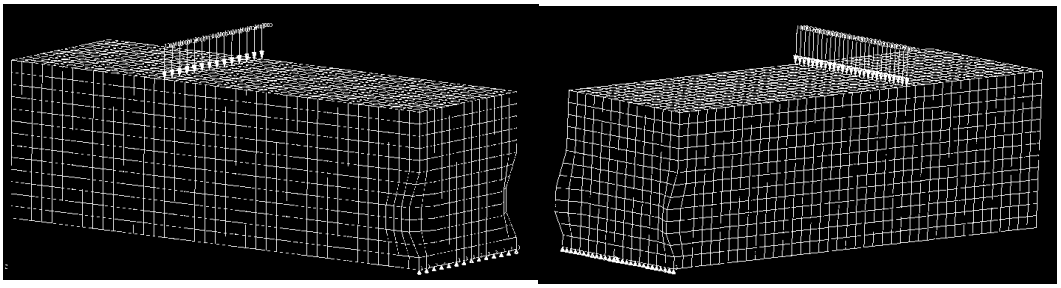

Figure 8-29: PATRAN model of SENB sample showing both halfs of the deflected crack plane (model A) and also the force representing the upper roller applied loads and constraints representing the bottom roller

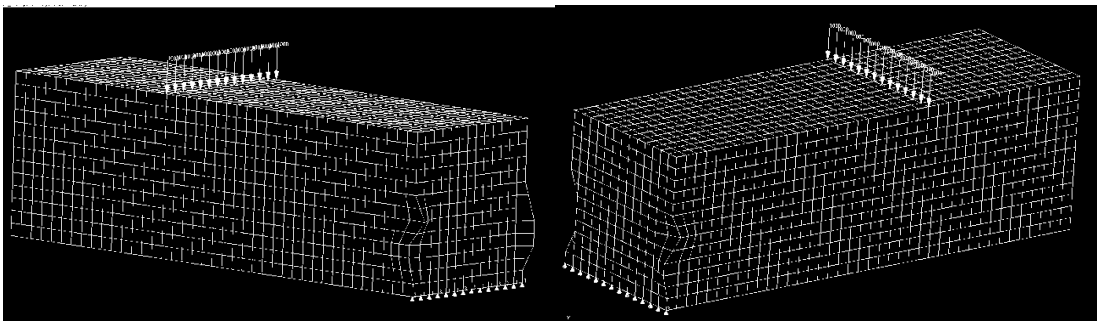

Figure 8-30: PATRAN model of SENB sample showing both halfs of the deflected crack plane (model B) and also the force representing the upper roller applied loads and constraints representing the bottom roller

Zencrack was then used for remeshing of the crack tip for 10 different progressive crack-fronts every 0.5mm, starting from a=4mm, the length of the precrack. K levels were calculated for each of these crack fronts. The standard crack block s04_t35x1 from the Zencrack library was chosen [106], see Figure 8-31. It is a crack block with a relatively coarse mesh, which seems appropriate as the elements are relatively small and there are 14 of them along each crack front. The crack fronts were assumed to progress as projected straight lines on the fracture surface based on the results of Loo-Morrey's beachmark test [50] that showed that planar and non-planar cracking occurs along one projected crack front (i.e. the shear lip region is part of the crack growth process). The edge of the smallest element at the crack tip was measured to be circa 40μm. This measure might decrease if the crack tip mesh is getting deformed. This size is similar to the larger grain size of the material, which has a mean of 16.4μm, but a range of 4.5 - 45.3μm.

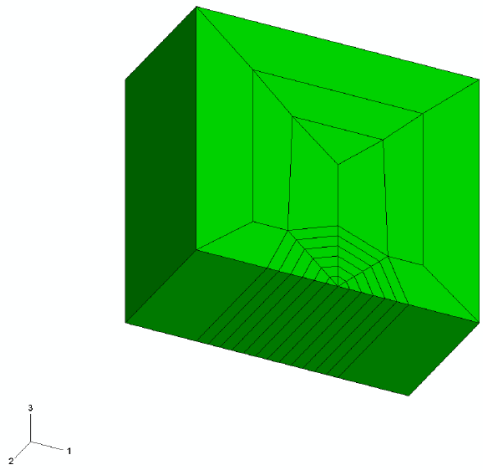

Figure 8-31: Zencrack crack block s04_t35x1 used for model of SENB [106]

The analysis was run for maximum and minimum load from the defined load case, and the ΔK values were calculated from $\Delta K = K_{max} - K_{min}$ for each case. Results of the ΔK values were combined in a spreadsheet for all crack fronts, which each consisted of 13 elements, providing 14 results across the crack front (taken at the edge of each element).

As already mentioned, Zencrack also offers the possibility to grow a crack and calculate the lifetime, assuming mode I crack growth. This has been done for the 300°C in air CNB and SENB model, to compare the predicted lifetimes with the test results. C and m values from both the SENB results and the Rolls Royce database were used, at an R-ratio of 0.1 and this is compared later with the simple lifing approaches discussed in Chapter 6.

8.3.3 Results and Discussion of Modelling

Comparison for the different specimen types and 2D and 3D models for planar and deflected regions are made, in terms of local stress intensity factors Δk_i, Δk_{ii} and Δk_{iii} and the effective stress intensity factors Δk_{eff}. In the following the Δk_{eff} used is based on a coplanar strain energy release rate criterion [104]

$$\Delta k_{eff} = \sqrt{\Delta k_i^{\,2} + \Delta k_{ii}^{\,2} + \Delta k_{iii}^{\,2}} \qquad \text{Equation 8-21}$$

8.3.3.1 Results of the CNB model

A CNB sample has also been modelled in Zencrack and Franc2D.

A Franc2D model has been created for the planar and deflected crack and compared to the analytical model from Suresh. For both the onset of deflection at about 25MPa√m, i.e. a crack length of 1.5mm, was chosen. The results for Δk_i and Δk_{ii} are compared in Figure 8-32. Δk_{ii} for deflected Franc 2D and Suresh analyses are very close together, however Δk_i is significantly larger for the Franc2D model. The deflected Franc2D model is slightly below the planar one. As expected the Δk_{ii} for the planar Franc2D model is 0.

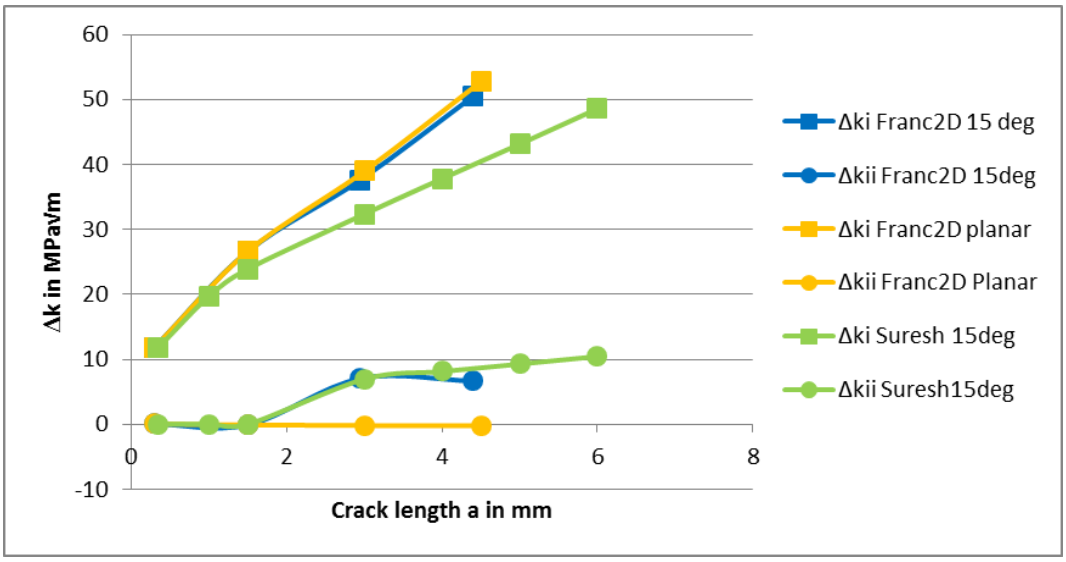

Figure 8-32: Results of $\Delta k_{i,ii}$ vs a from the Franc2D and analytical anlysis after Suresh for the CNB

A 3D model of a planar crack has also been modelled with Zencrack and Abaqus and has been used for comparison. Figure 8-33 and Figure 8-34 show the model of the planar crack in the CNB sample, for the first and the final (6th) crack front, respectively. Then the crack in this sample was deflected at an angle of 15°. Figure 8-35 and Figure 8-36 show the model of the deflected crack in the CNB sample, for the first and the final (6th) crack front, respectively.

For the initial very small notch in the first crack front it can be seen that the mesh is deformed strongly, so initial K values might be inaccurate, however the mesh improves for the larger crack length. They are lower than the Pickard K calibration predicts; when comparing the CNB results for the 3D case with Pickard's calibration, it can be seen that the initial ΔK is 10.1MPa√m, where we would expect it to be 12MPa√m.

In the CNB 3D models only the values at the top edge are describing the actual crack as the entire crack plane is deflected at the angle measured from the surface, so only this position has been evaluated.

(a)

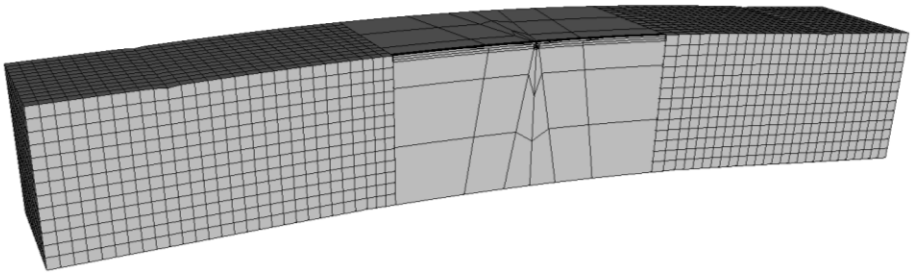

(b)

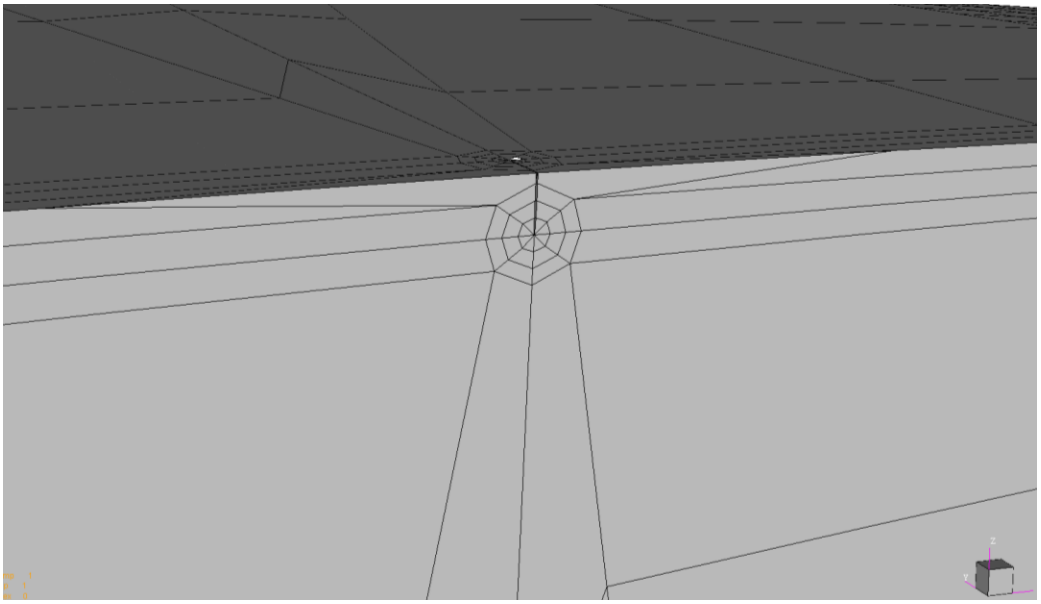

Figure 8-33: Zencrack model of CNB sample with planar crack using large crack blocks on either side of the crack for crack front 1 (a) whole model (b) detailed view of the crack

(a)

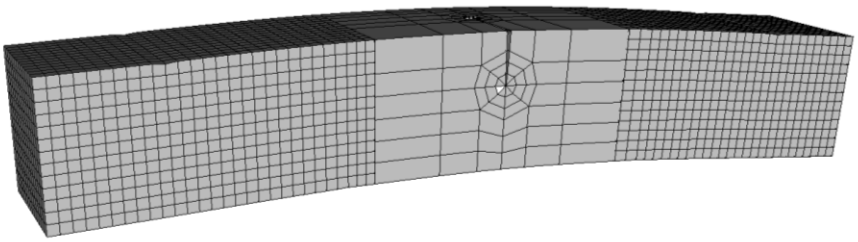

(b)

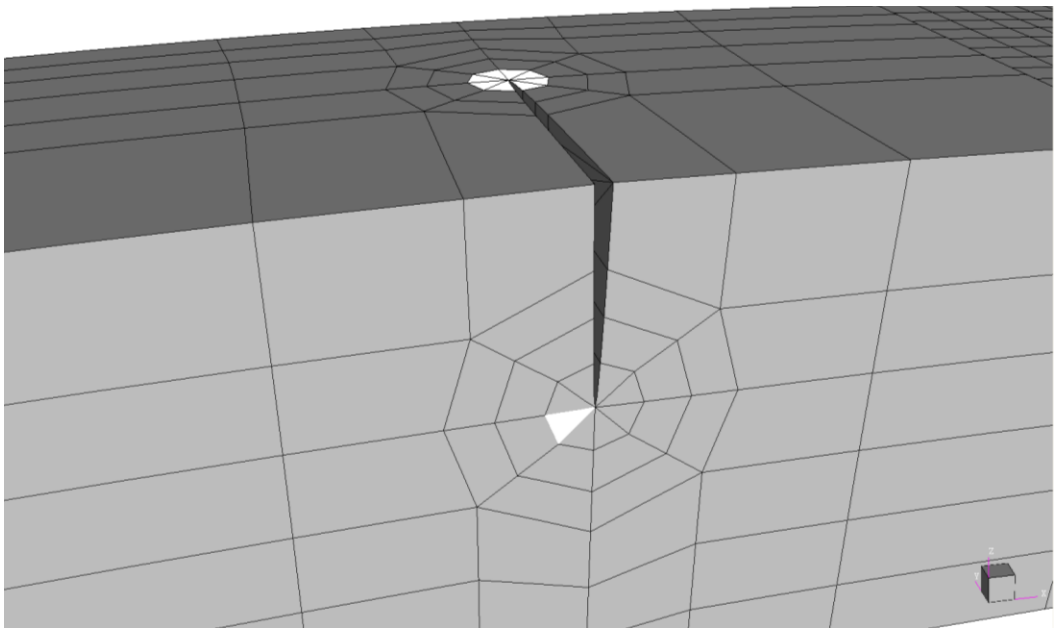

Figure 8-34: Zencrack model of CNB sample with planar crack using large crack blocks on either side of the crack for crack front 6 (a) whole model (b) detailed view of the crack

(a)

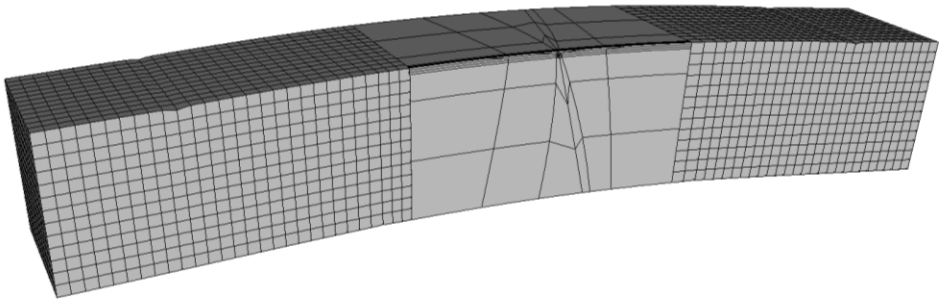

(b)

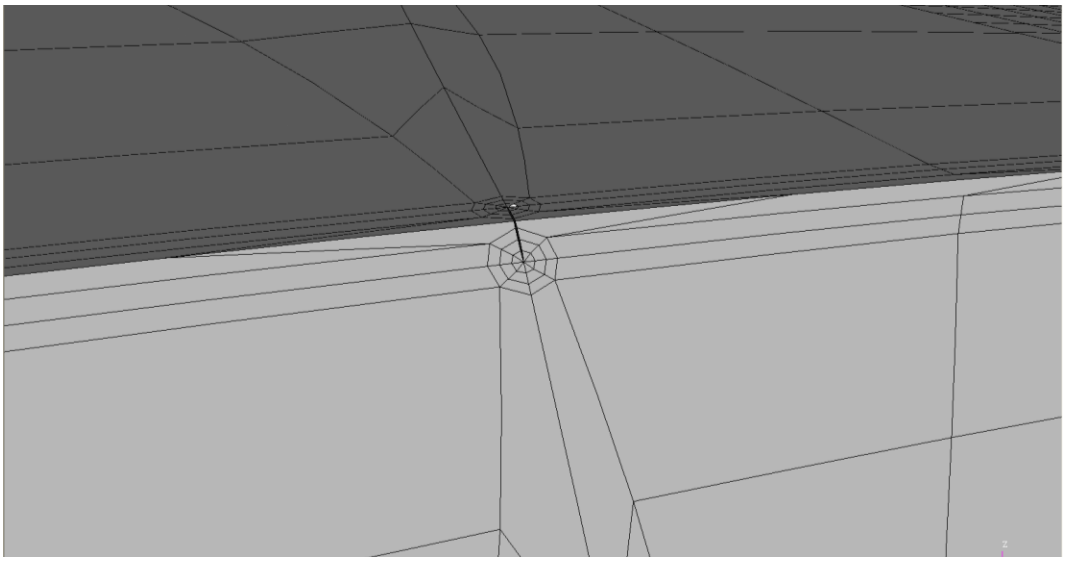

Figure 8-35: Zencrack model of CNB sample with deflected crack using large crack blocks on either side of the crack for crack front 1 (a) whole model (b) detailed view of the crack

(a)

(b)

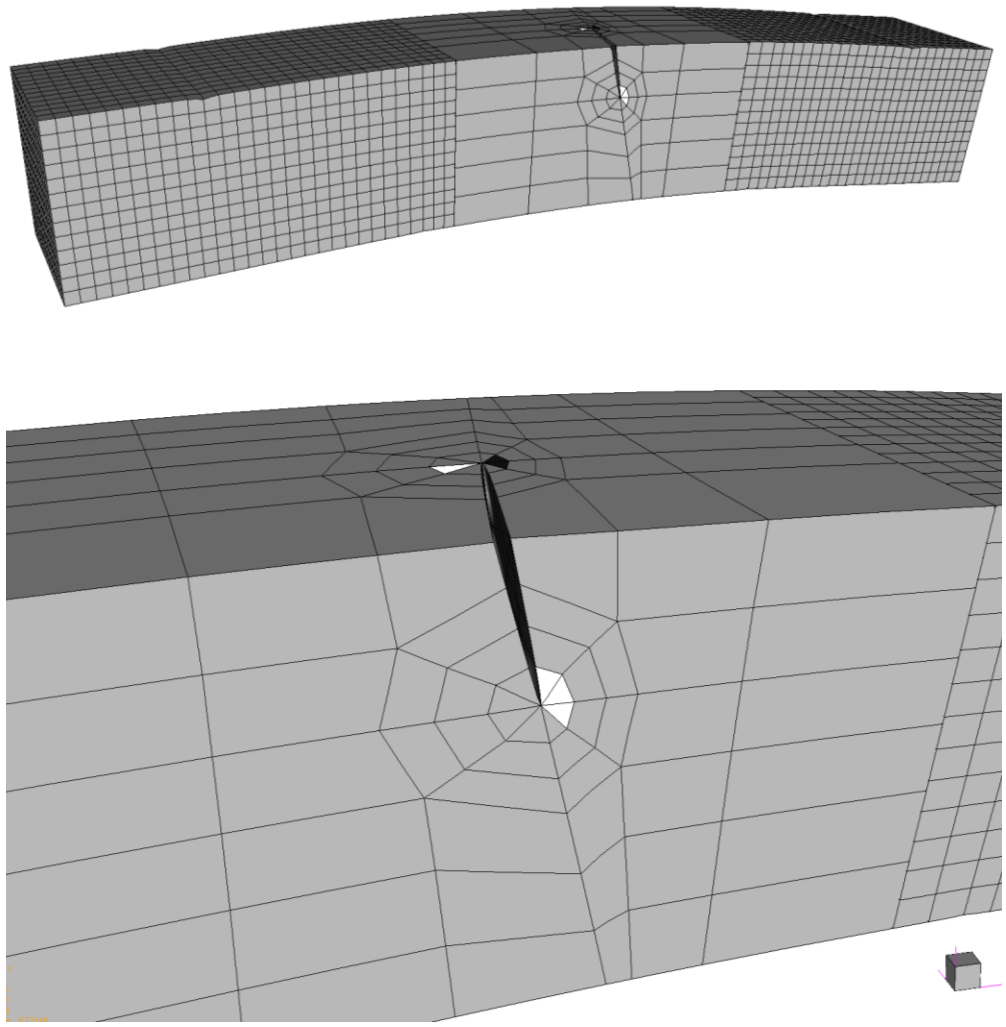

Figure 8-36: Zencrack model of CNB sample with deflected crack using large crack blocks on either side of the crack for crack front 6 (a) whole model (b) detailed view of the crack

The results of $\Delta k_{i,ii,iii}$ for the edges of both the deflected and the planar crack are shown in Figure 8-37, and they are compared with the nominal ΔK from the Pickard calibration. As defined the deflection started immediately not only after the measured onset ΔK (circa 25 MPa√m)

As expected for the planar crack the Δk_{ii} and Δk_{iii} components are 0, while they increase with crack length for the deflected crack. As this model does not represent the 3D shaped crack deflection, the Δk_{iii} component does not describe the real twisting of the crack. For the planar crack the Δk_i is identical to the Δk_{eff}, while for the deflected crack the Δk_i is below the Δk_{eff}. It can be seen that the Δk_{eff} for planar and deflected crack are both below the Pickard calibration. The deflected crack has a slightly smaller Δk_{eff} than the planar crack, indicating that the driving force is lower in the deflected region. This could be a reflection of intrinsic shielding, i.e. reduction of crack driving force, which has been observed to be caused by crack deflection itself, apart from any extrinsic shielding which may occur from closure effects (in an actual fatigue test) [84].

Figure 8-38 shows the evolution of $\Delta k_{ii}/\Delta k_i$ and $\Delta k_{iii}/\Delta k_i$ over Δk_{eff}. Again the twist component Δk_{iii} might not represent the actual crack very well. $\Delta k_{ii}/\Delta k_i$ decreases, before it increases almost linearly again, after circa 24MPavm, which is about the measured level of onset of deflection.

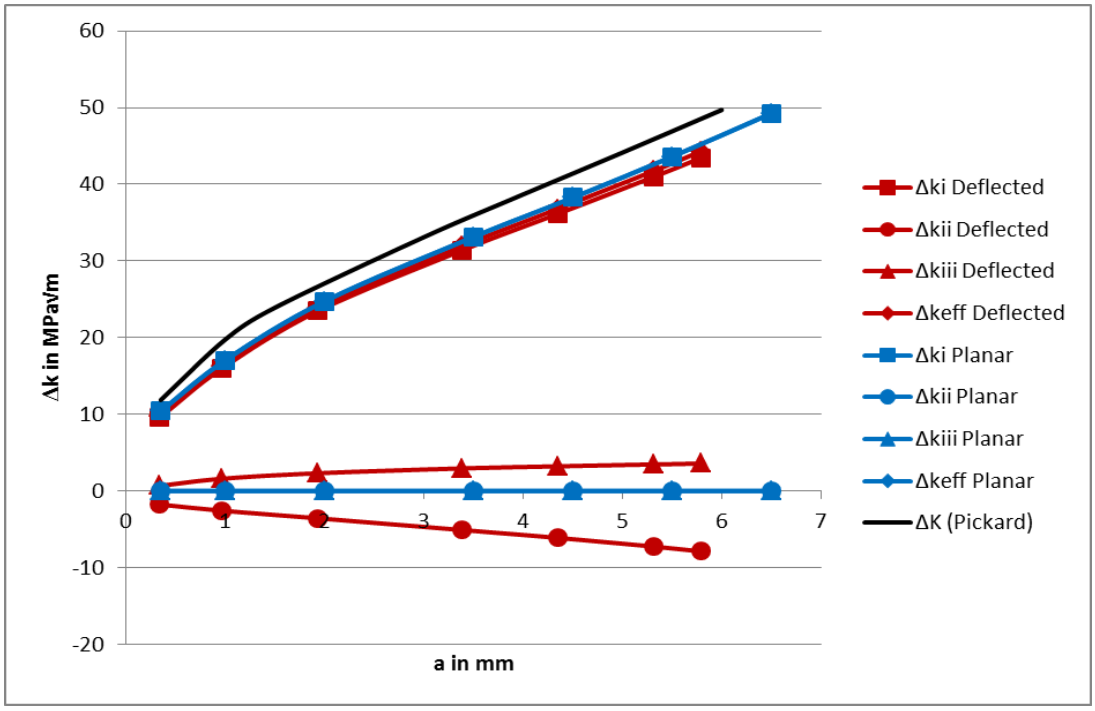

Figure 8-37: Results of $\Delta k_{i,\,ii,iii}$ vs a from the Zencrack 3D analysis for the CNB for the planar and deflected crack, compared with the ΔK from the Pickard calibration

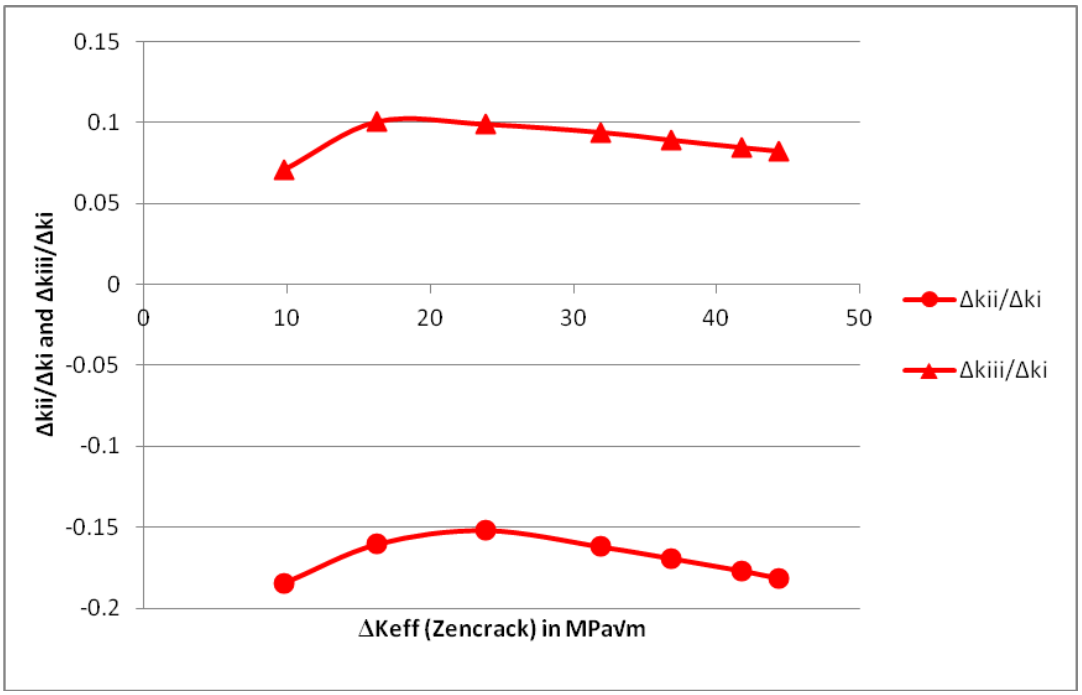

Figure 8-38: ΔK_{eff} vs $\Delta k_{ii}/\Delta k_i$ and $\Delta k_{iii}/\Delta k_i$ for deflected CNB sample

8.3.3.2 Comparison of 2D and 3D CNB models

Figure 8-39 compares the results for the deflected cracks from the Franc 2D and Zencrack for the CNB with the analytical solution after Suresh and the Pickard K calibration. The Δk_{ii} for the Zencrack does start immediately, not only after the onset of deflection level, which was defined for the others, and it is negative, i.e. the shear is in the opposite direction, but it increases to a similar level (below 10MPa√m), even though the others achieve this value at a shorter crack length. The Δk_i is below the Pickard derived ΔK, Δk_i from the Suresh analysis is slightly below this curve, and the Δk_i from the Franc2D is initially similar, but then increases faster.

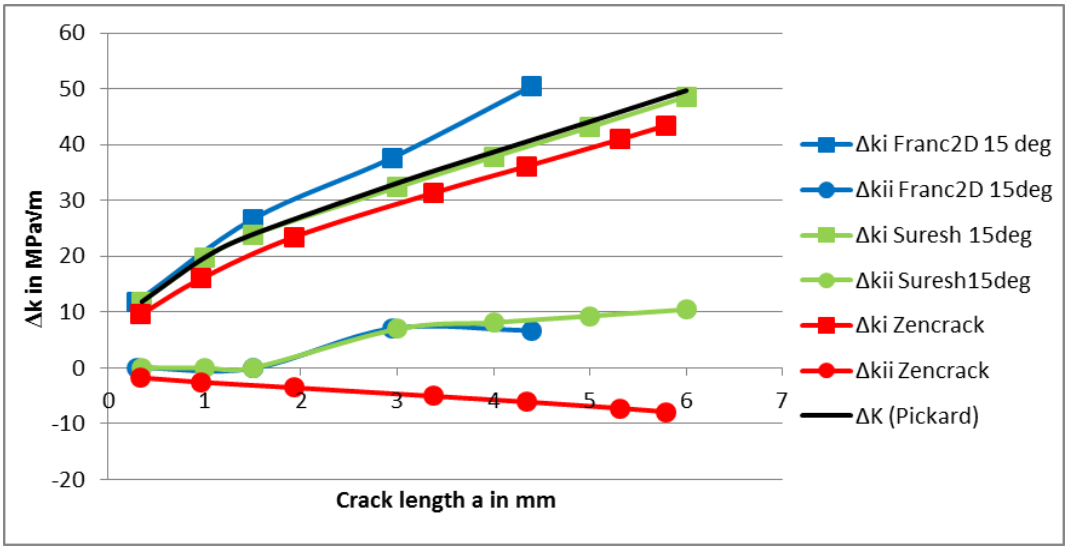

Figure 8-39: Results of $\Delta k_{i,ii}$ vs a from the deflected Franc2D and the Zencrack 3D analysis and analytical anlysis after Suresh for the CNB, compared with the ΔK from the Pickard calibration

Figure 8-40 shows the Δk_{eff} from the Zencrack, Franc2D and Suresh analysis compared with the Pickard ΔK. The Δk_{eff} of the analysis after Suresh is identical to the Pickard calibration, as the Δk_i and Δk_{ii} were calculated using the ΔK from Pickard.

The Δk_{eff} from the Zencrack analysis of the deflected crack is always below the Pickard value, indicating a reduced driving force, possibly due to shielding, however the Δk_{eff} from the Franc2D analysis is initially identical with Pickard's calibration, but for ΔK above circa 20MPa√m, in the region of the onset of terracing, it is above the Pickard value, indicating a higher crack driving force. However it should be noted that the corner notch is less well established in terms of K calibration as the SENB, and that the 3 different analyses show very different results independent of any deflection, and it is hence not straightforward to compare them to each other.

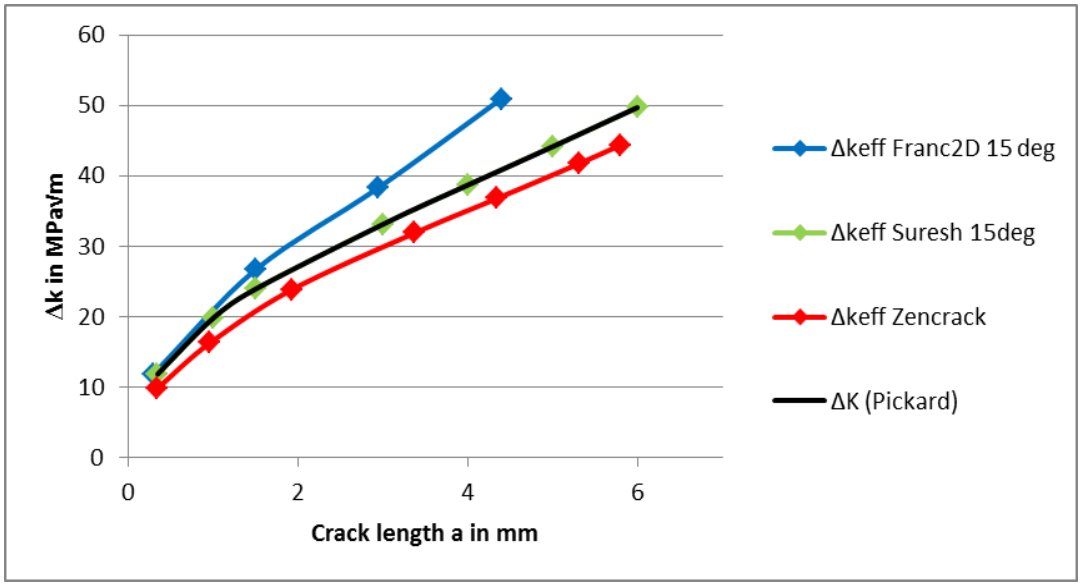

Figure 8-40: Results of Δk_{eff} vs a from the Franc2D and analytical anlysis after Suresh and the Zencrack 3D analysis for the CNB, compared with the ΔK from the Pickard calibration

To get more accurate results and to model the deflection in the near surface region, it would be necessary to use standard crack blocks and hence to build up a circular mesh, in which they can replace the elements. This might improve the crack tip mesh by creating less deformed elements, and could hence lead to better results for the *K* levels. The deflected planar regions could also be modelled by moving individual nodes, so comparison to the SENB samples could be made.

8.3.4 SENB 2D results

The results of the Franc2D model of the SENB have been compared with results from the analytical solution in Suresh's work [77] for a measured overall angle of 20°, which is equivalent to the angle on the free surface in the 3D model and the observations of the SENB test specimen. Both Franc 2D and Suresh's analytical approach show similar results for Δk_i to the nominal ΔK_i predicted from the BS standard. The Δk_{ii} values have similar behaviour after the onset crack length, but Suresh's solution is always slightly higher, see Figure 8-41.

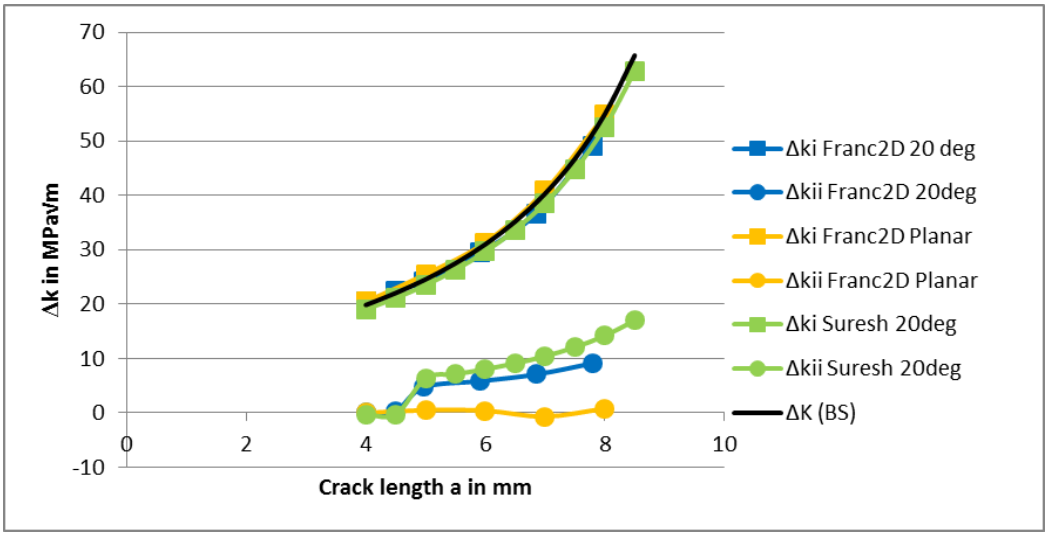

Figure 8-41: Results of $\Delta k_{i,ii}$ vs a from the Franc2D and analytical anlysis after Suresh, compared with the ΔK from BS ISO 12108

8.3.5 Analysis of the 3D Zencrack model of the SENB

At first a planar crack was modelled. The Zencrack analysis gives the Δk_i, Δk_{ii} and Δk_{iii} levels as outputs for each node position spaced along the crack front i.e. going through the specimen thickness (this is represented as a variation in b, the specimen thickness, which varies from 0 (indicating one edge) to 12.5 indicating the other edge). A series of crack fronts are also defined, from Crack front 1 to Crack front 10 as the crack is progressively lengthened.

Figure 8-42 shows the relationship between Δk_i, Δk_{ii} and Δk_{iii} and Δk_{eff} for alternate Crack fronts (i.e. Crack fronts 1,3,5,7,9) to show the evolution of the stress state as the crack propagates.

As expected for all crack fronts Δk_{ii} and Δk_{iii} are 0, and Δk_{eff} is equal to Δk_i. A lower driving force can be observed in the near the surface again, indicating that it is not necessarily caused by shielding due to the deflected crack growth.

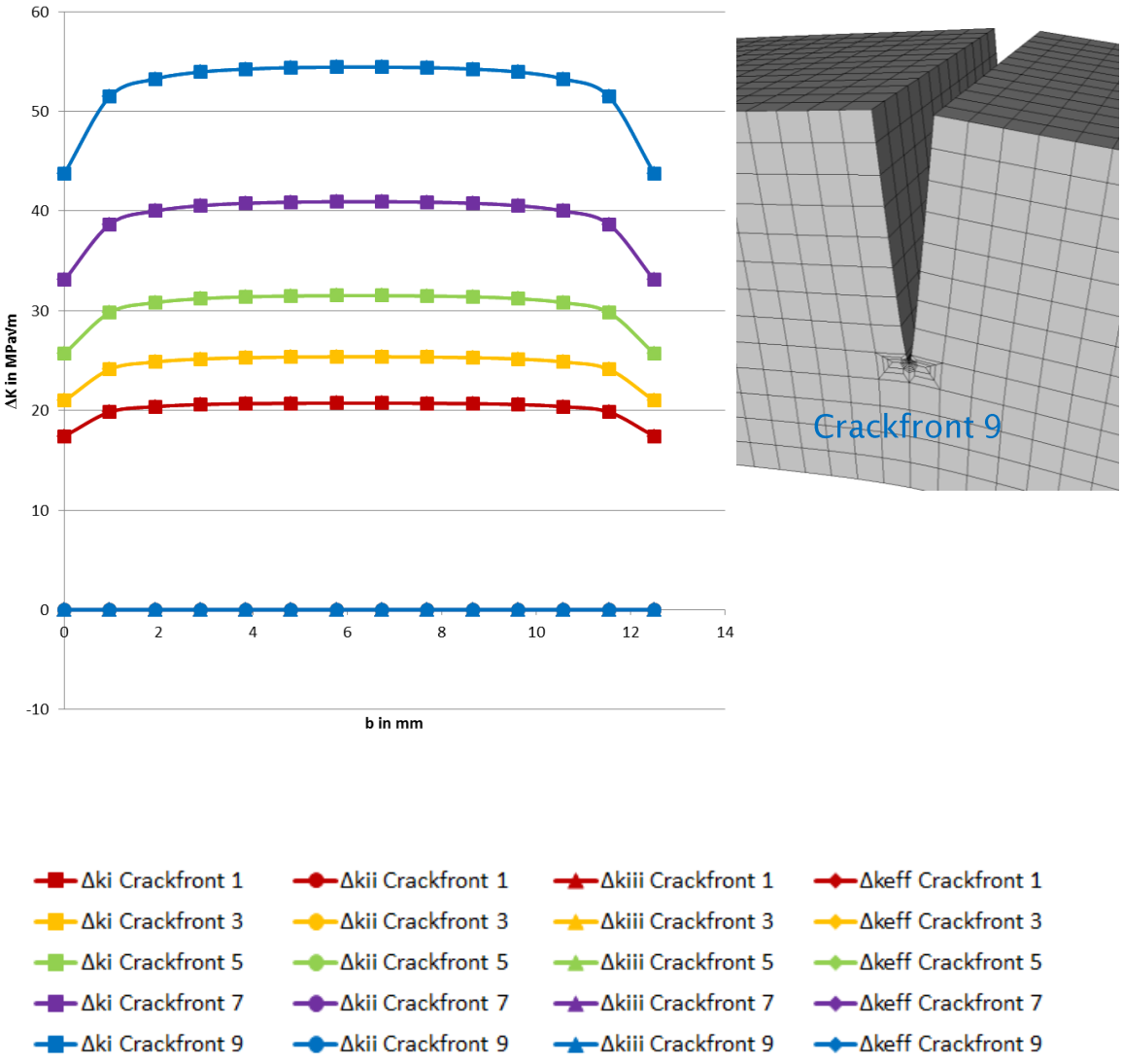

Figure 8-42: Δk_i, Δk_{ii}, Δk_{iii} and Δk_{eff} along 5 different crack fronts in the planar SENB, and the respective mesh (the deflection is scaled to ca. 20x)

The results of the analysis for different progressive crack fronts are shown schematically in Figure 8-43 for the symmetric deflected SENB Model A. The deflection has been exaggerated in this representation, by scaling any deformation up by a factor of circa 30, in this figure to better show the crack and deflection.

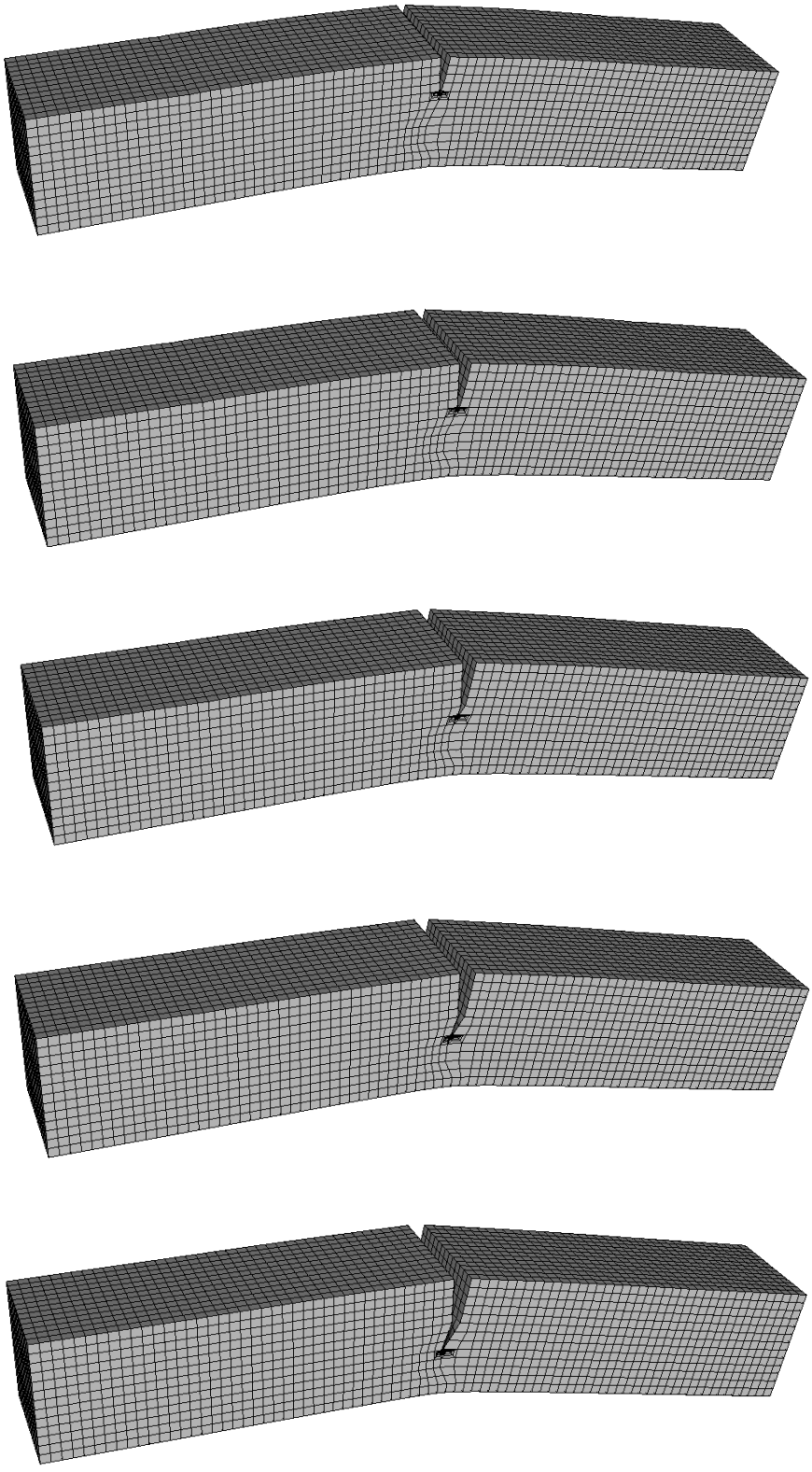

Figure 8-43: Zencrack model of SENB sample using crack blocks on either side of the crack and split elements for a deep crack using a scaling factor of 30x for the deflection

Figure 8-44 shows the relationship between Δk_i, Δk_{ii} and Δk_{iii} and Δk_{eff} for alternate Crack fronts (i.e. Crack fronts 1,3,5,7,9) building up progressively to show the evolution of the stress state as deflection increases as the crack propagates.

For Crackfront 1 there is no deflection yet, hence Δk_{ii} and Δk_{iii} are 0 and hence Δk_i and Δk_{eff} are the same. The driving force is lower in the plane stress area (near the free surface, as would be expected). The deflection starts at crack front 3, where the Δk_{eff} is about 25MPa√m.

At longer crack lengths and with a developing larger deflection, Δk_{ii} and Δk_{iii} values are seen to increase in the deflected region, whilst remaining negligible in the (planar) centre.

However the Δk_{eff} is still lower at the edges than in the centre, possibly due to intrinsic shielding, or extrinsic shielding due to closure effects. It should be noted that the plane stress state at the specimen surface itself will still give a reduction in crack driving force for a planar crack.

However by the 9th crackfront, the Δk_{eff} of the edge has increased to the same value as in the centre, due to the larger Δk_{ii} and Δk_{iii} at this deflection contributing to the proposed crack driving force. This may indicate why the deflection becomes sustained.

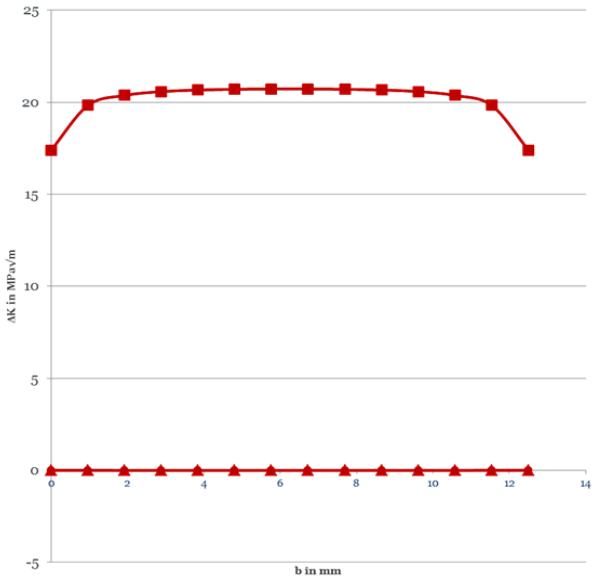
ΔK in MPa√m
b in mm

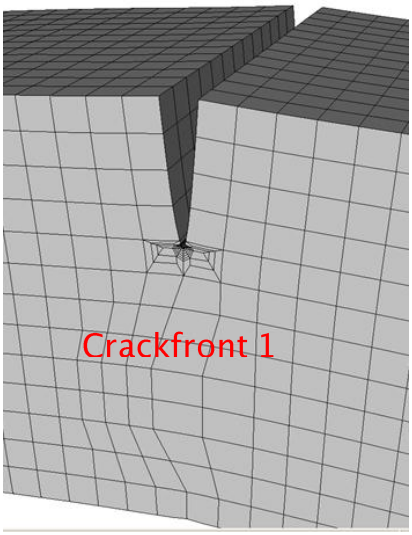
Crackfront 1

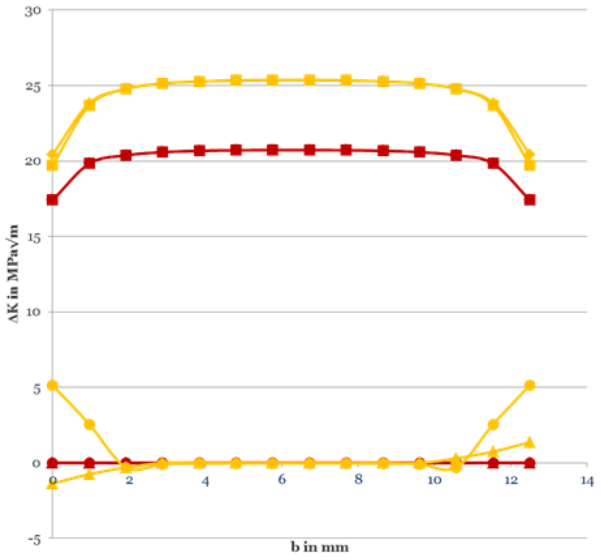
ΔK in MPa√m
b in mm

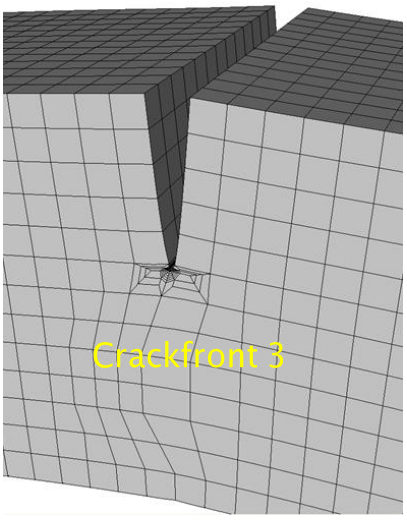
Crackfront 3

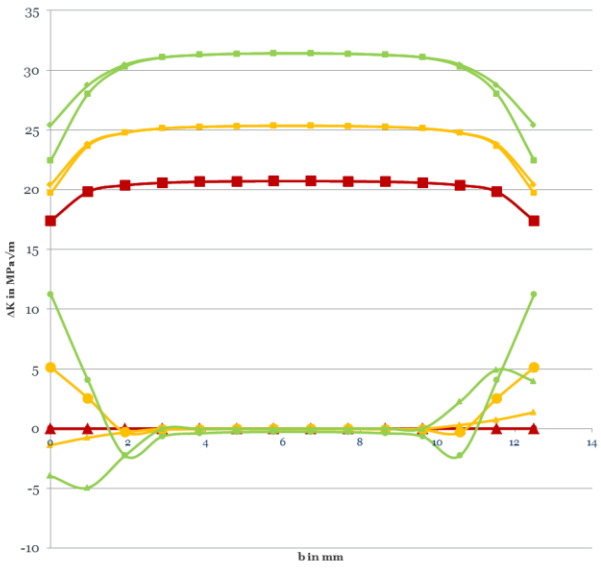
ΔK in MPa√m
b in mm

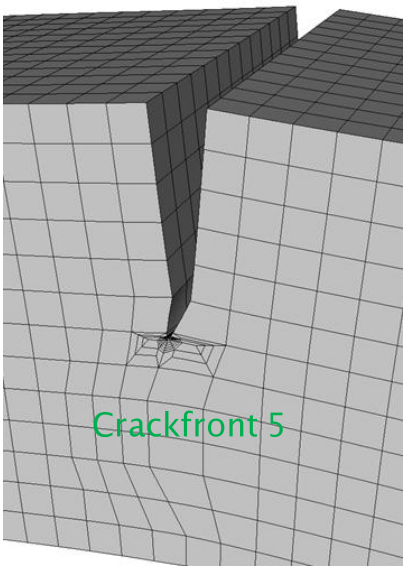
Crackfront 5

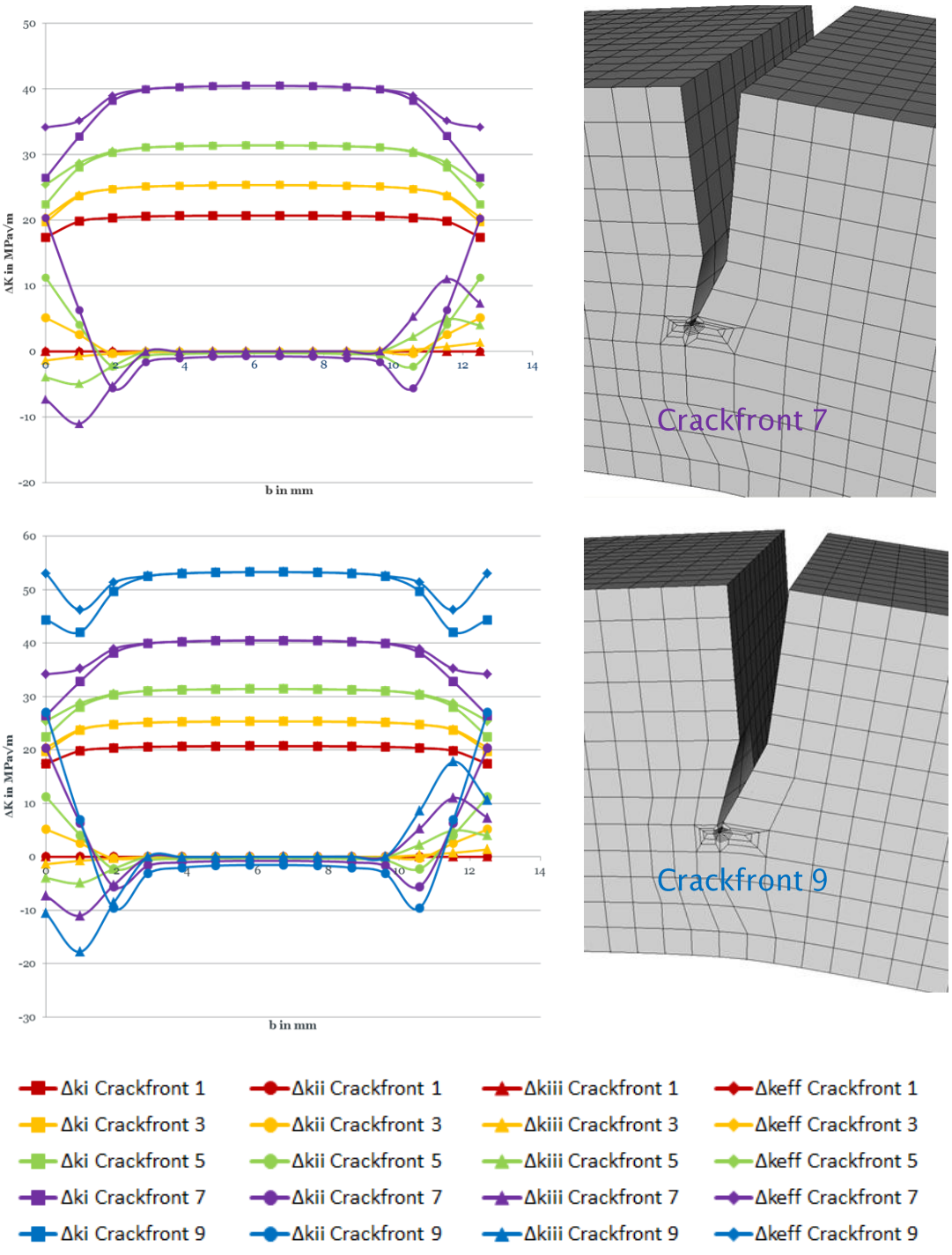

Figure 8-44: Δk_i, Δk_{ii}, Δk_{iii} and Δk_{eff} along 5 different crack fronts in the first symmetric deflected SENB, and the respective mesh (the deflection is scaled to ca. 30x)

Figure 8-45 compares the Δk_{eff} for these crackfronts in the planar and deflected model A. According to this there is not so much influence of shielding on the driving force at the edge, but the effect seems to be caused mainly by the plane stress region. The deflected edge had an even higher driving force than the planar one for high *K* levels, while for the second position, which might be more effected by the twisting component, shielding may have a larger effect, as for the deflected model the driving force always seems to be below the same position for the planar sample.

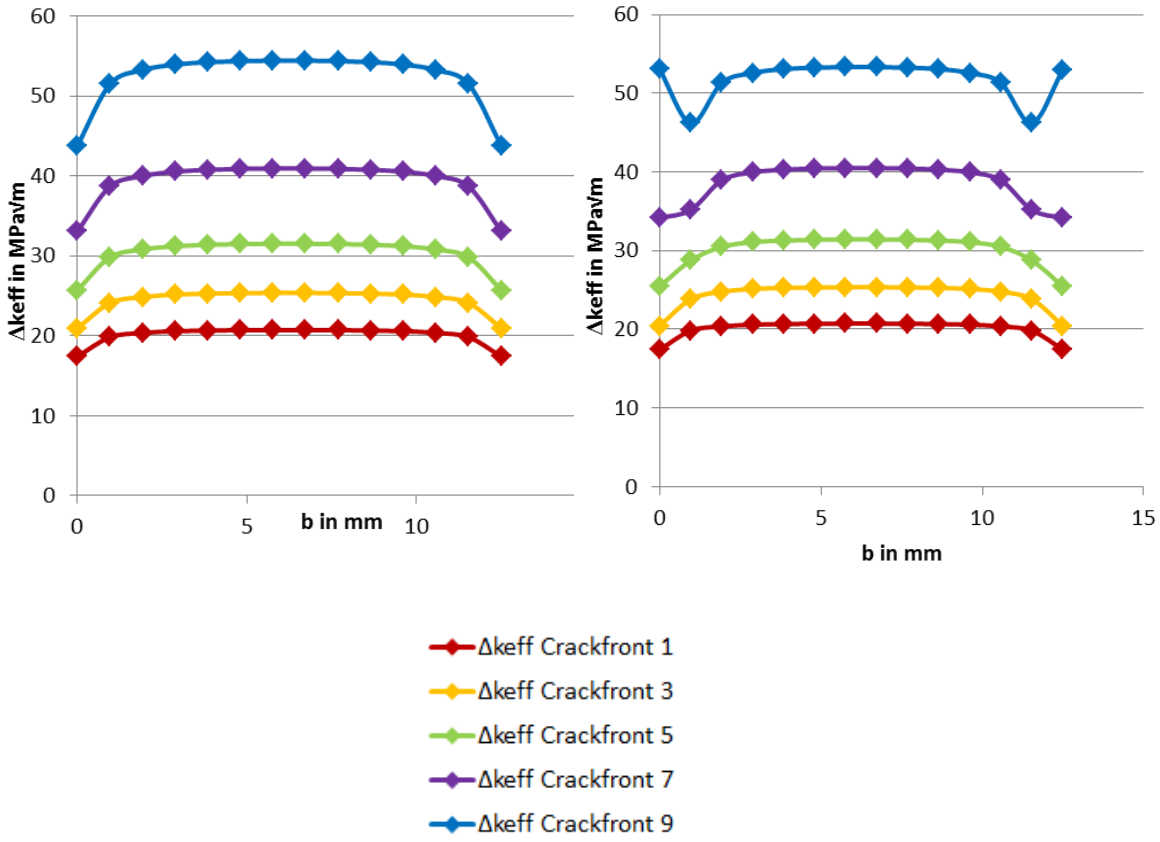

Figure 8-45: Δk_{eff} for planar and deflected model A for different crack fronts

In the next representation of the evolution of crack driving force for model A we can evaluate how the ΔK values develop as the crack grows, considering different positions along the crack front. Figure 8-46 shows these positions along the crack-front, Position 1 was measured directly on the edge, where there is the largest deflection, Position 2 is the second row of elements, the next set of measurements is taken in Position 7, in the centre of the sample, where crack growth is planar. Figure 8-47 shows the variation in Δk_i, Δk_{ii}, Δk_{iii} and Δk_{eff} against the projected crack length *a* for each crack position.

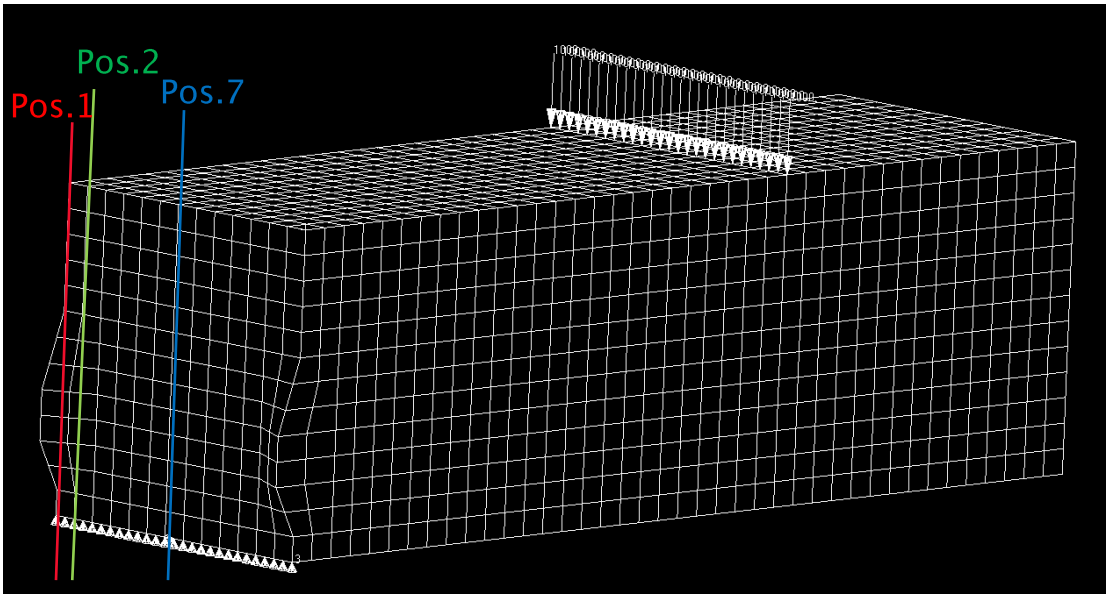

Figure 8-46: Deflected crack plane of SENB model A showing 3 crack front positions

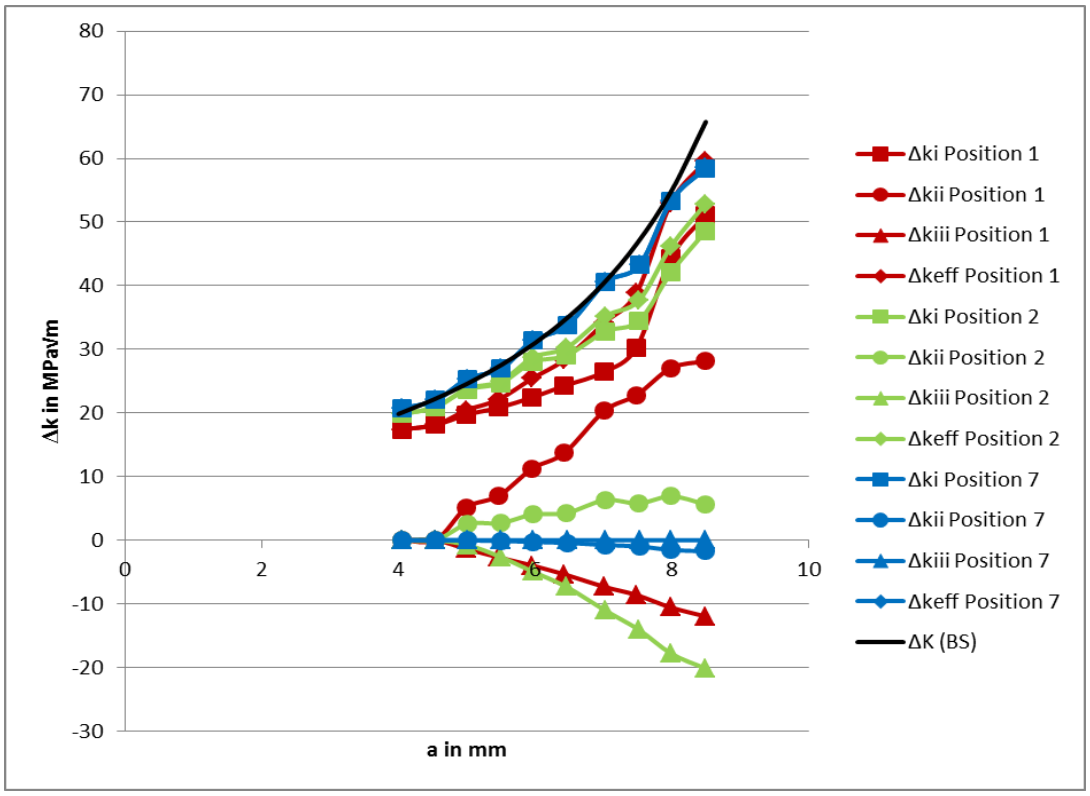

Figure 8-47: Results of $\Delta k_{i,ii,iii}$ vs a for the different Positions 1, 2 and 7 in model A and the ΔK from BS ISO 12108

The *K* calibration for the projected crack length from British Standard BS ISO 12108 has also been plotted in Figure 8-47. The planar crack growth (position 7) in the centre of the sample is very consistent with this (until significant deflection is established at crackfront 3). This gives confidence that the results of the FE model are correct. The Δk_{eff} of Position 1 (surface) and position 2 (near-surface) are lower than in the centre (position 7), again showing a lower driving force in the deflected region, as mentioned earlier.

In Position 1 Δk_{ii} increases significantly to more than 75% of the respective Δk_i, while in Position 2 it is significantly smaller, less than 20% of the respective Δk_i. However Δk_{iii} can be seen to be even higher in Position 2 than in Position 1, ~40% of the respective Δk_i. Position 7 has almost no Δk_{ii} and Δk_{iii} components as expected for planar crack growth. It can be seen that the Δk_{eff} of Position 1 (surface) and position 7 (centre) become equivalent at the longer projected crack lengths.

Figure 8-48 describes the evolution of $\Delta k_{ii}/\Delta k_i$ and $\Delta k_{iii}/\Delta k_i$ with the nominal ΔK (calculated for the equivalent projected crack length) for the surface position (Position 1). Such ratios could potentially be used to predict the crack path in a component (if we can make crack path iterations follow such pre-defined ratios). It can be seen that both $\Delta k_{ii}/\Delta k_i$ and $\Delta k_{iii}/\Delta k_i$ increase up to circa 40 MPa√m, from where they start decreasing again. It should be noted that crack growth rates at ΔK levels above 40 MPa√m are very fast and in these specimens such ΔK levels are near the plastic collapse point of these samples.

When we compare this to Figure 8-38, which shows the evolution of $\Delta k_{ii}/\Delta k_i$ and $\Delta k_{iii}/\Delta k_i$ over ΔK_{eff} for the CNB Zencrack model, ignoring the twist component Δk_{iii} which might not represent the actual crack in CNB very well. $\Delta k_{ii}/\Delta k_i$ shows very different behaviour from the SENB sample. Its value decreases, before it increases almost linearly again, after circa 24MPa√m, which is about the measured level of onset of deflection. It should be mentioned that the SENB model only started at a ΔK of 20MPa√m. However the maximum value is much lower than for the SENB samples which showed almost 80% for the $\Delta k_{ii}/\Delta k_i$, while it is between 15-20% for the CNB, as shown in Figure 8-38.

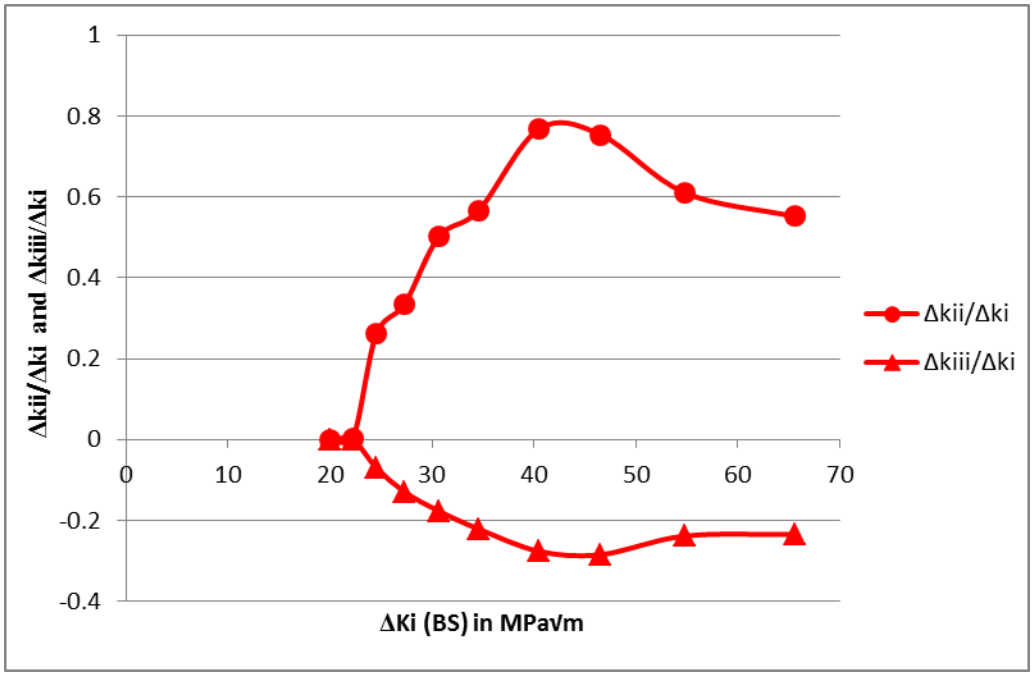

Figure 8-48: ΔK vs $\Delta k_{ii}/\Delta k_i$ and $\Delta k_{iii}/\Delta k_i$ for SENB model A for Position 1

For the asymmetric model B the same comparisons have been carried out, as shown in Figure 8-49 to Figure 8-52. This model has a more complex crack shape on one side of the sample at b = 0mm, where the crack changes direction (thus showing a simplified version of the terracing observed in the actual specimens). Accordingly at this position, where the crack changes direction, k_{ii} decreases as the crack path moves back towards experiencing more mode I, k_i also increases and the overall crack driving force is clearly higher on this side.

The main differences we can see compared to model A are as follows:

Before the turn (crack front 7) the Δk_{ii} is almost equivalent to Δk_i at b= 0 mm. And for the 9th crackfront the Δk_{eff} at the edge is higher than in the centre, indicating a higher driving force at the edge after the crack has turned, this provides an explanation for why the terracing is promoted in these samples.

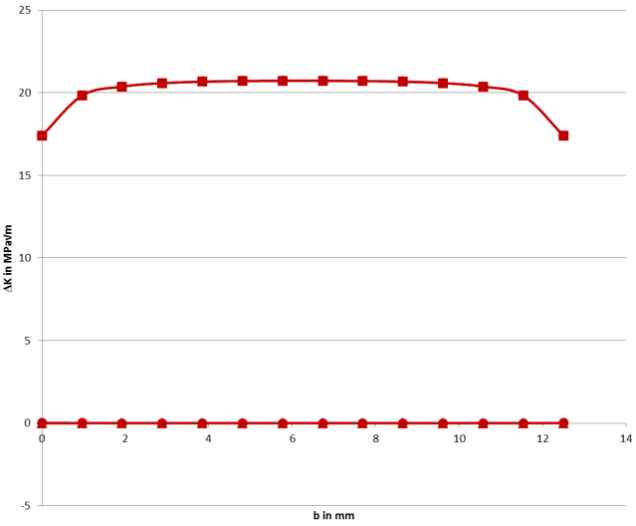

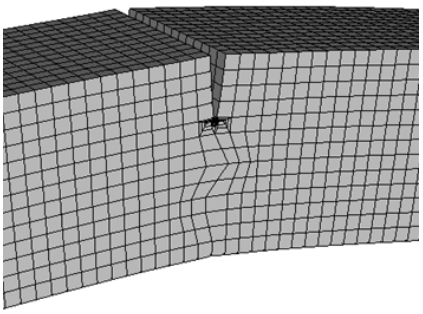

Crackfront 1

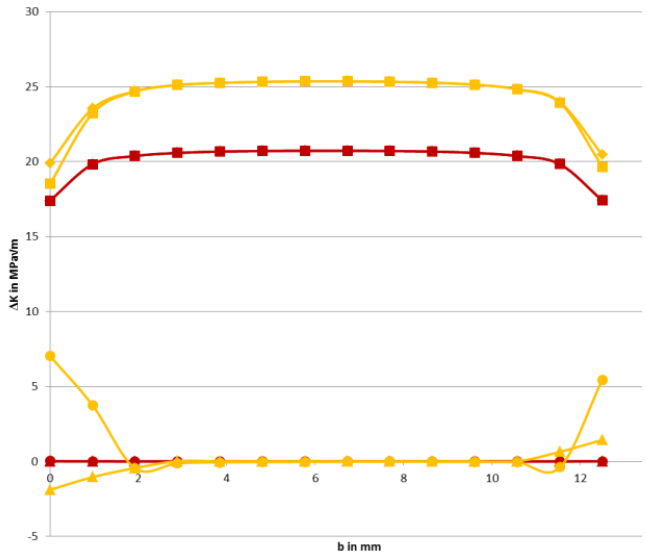

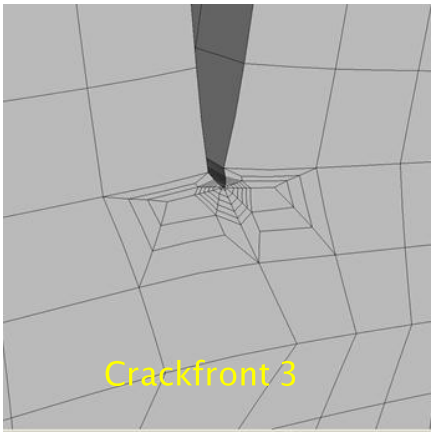

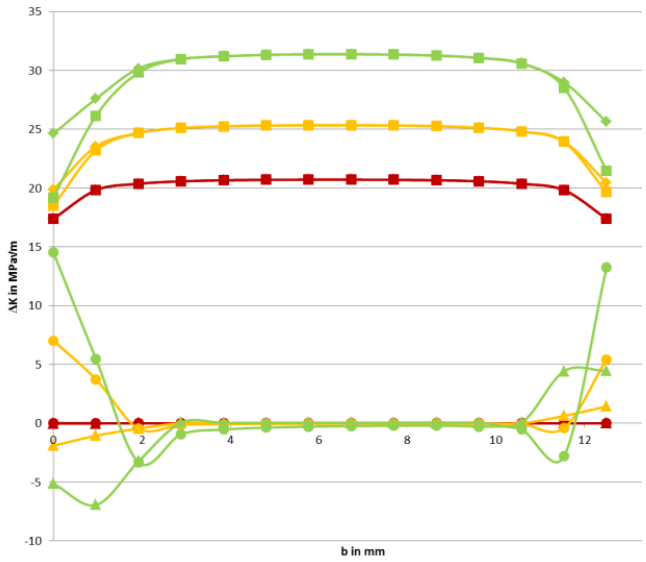

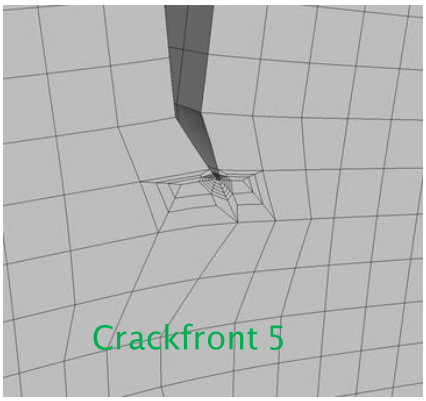

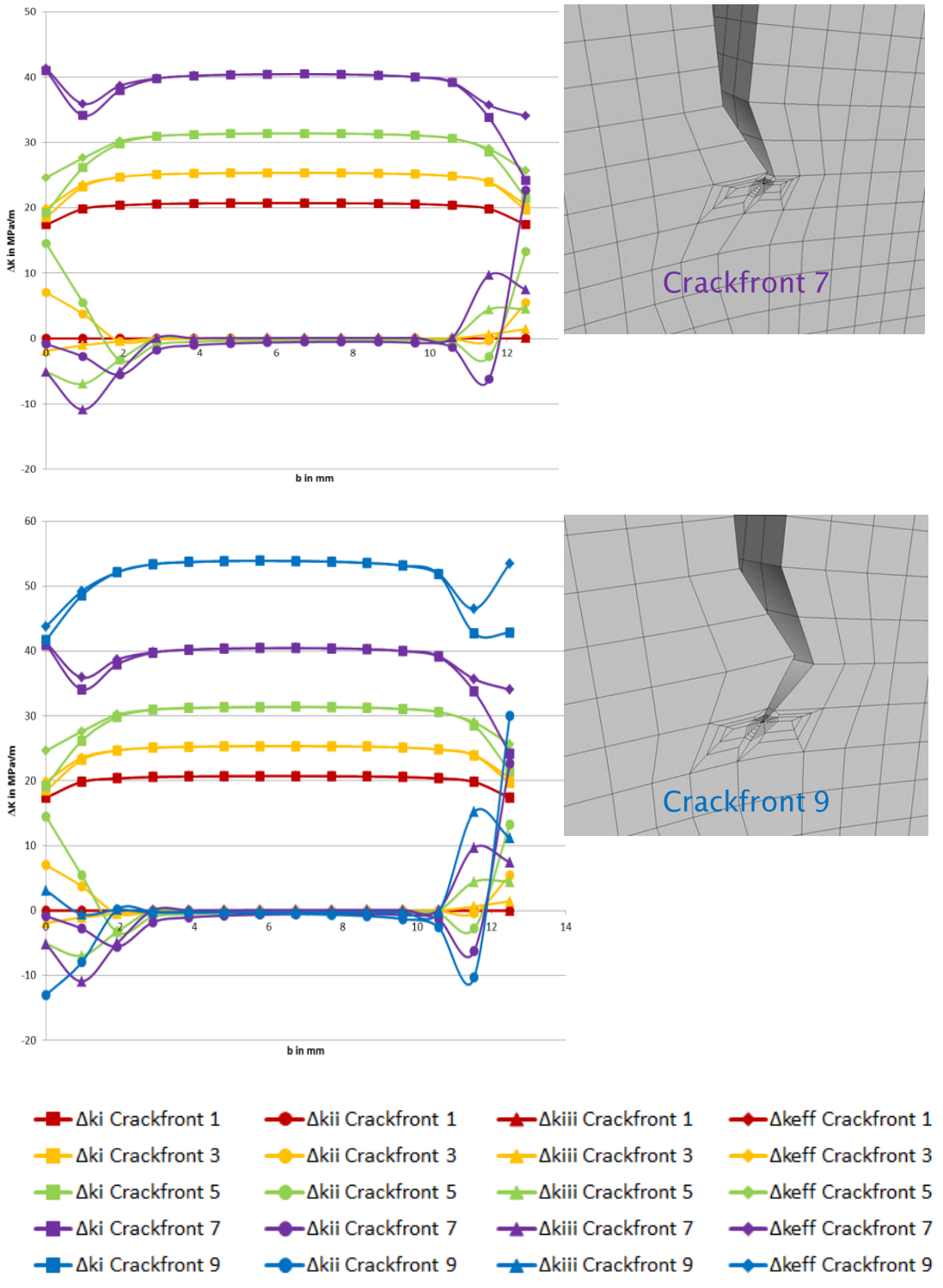

Figure 8-49: Δk_i, Δk_{ii}, Δk_{iii} and Δk_{eff} along 5 different crack fronts in the second deflected SENB, and the respective mesh (the deflection is scaled to ca. 20x)

In the next representation of the evolution of crack driving force for model B we can evaluate how the ΔK values develop as the crack grows, considering different positions along the crack front. Figure 8-50 shows these positions along the crack-front, Position 1 was measured directly on the edge, where there is the largest deflection, Position 2 is the second row of elements, the next set of measurements is taken in Position 7, in the centre of the sample, where crack growth is planar. Figure 8-51 shows the variation in Δk_i, Δk_{ii}, Δk_{iii} and Δk_{eff} against the projected crack length a for each crack position. At the edge of the sample, we can see an increase of deflected Δk_{eff} over planar as Δk_i increases strongly as Δk_{ii} drops.

Figure 8-52 describes the evolution of $\Delta k_{ii}/\Delta k_i$ and $\Delta k_{iii}/\Delta k_i$ with the nominal ΔK (calculated for the equivalent projected crack length) for the surface position (Position 1). It shows stronger increase of $\Delta k_{ii}/\Delta k_i$ compared to model A, and then the change in direction causing a sudden drop.

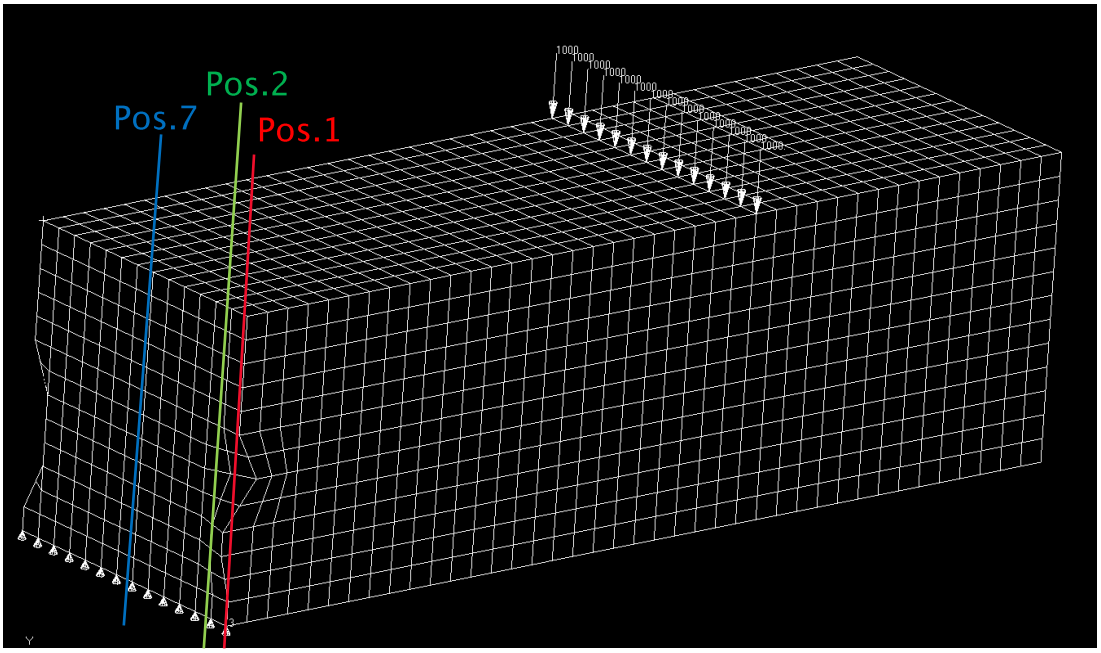

Figure 8-50: Deflected crack plane of SENB model B showing 3 positions

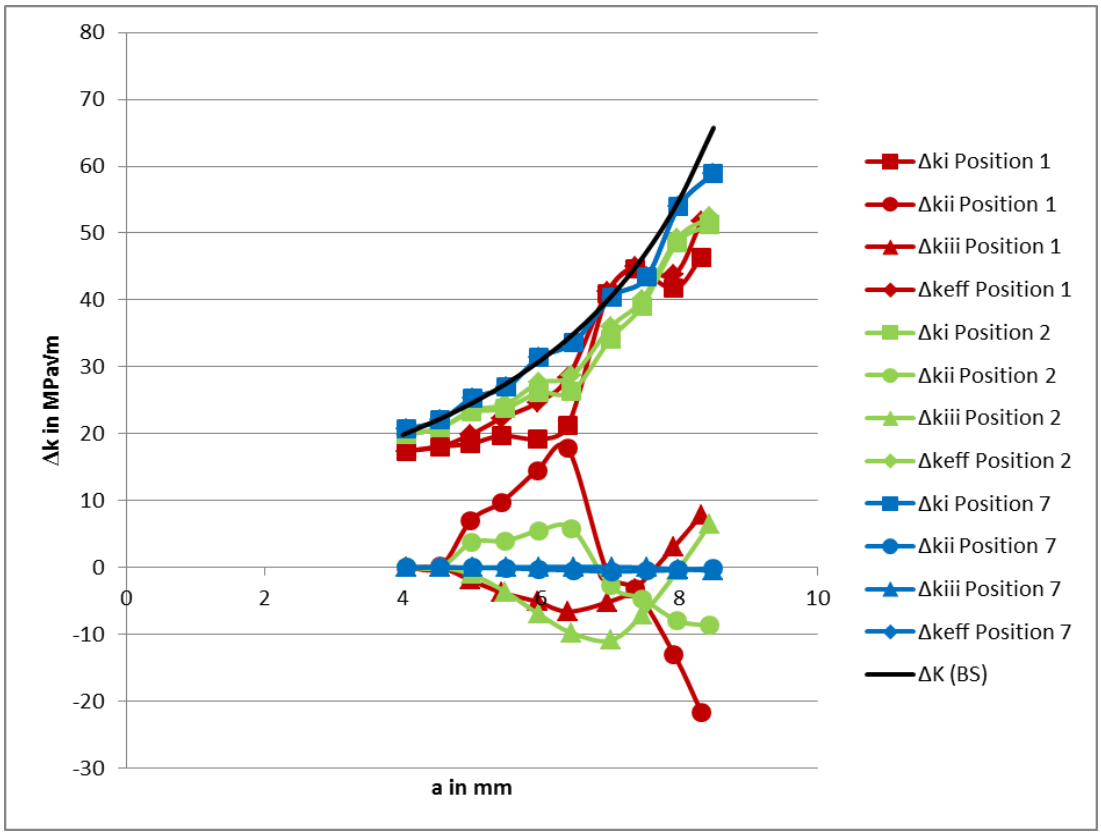

Figure 8-51: Results of $\Delta k_{i,\,ii,\,iii}$ vs a for the different Positions 1, 2 and 7 (for second SENB) and the ΔK from BS ISO 12108

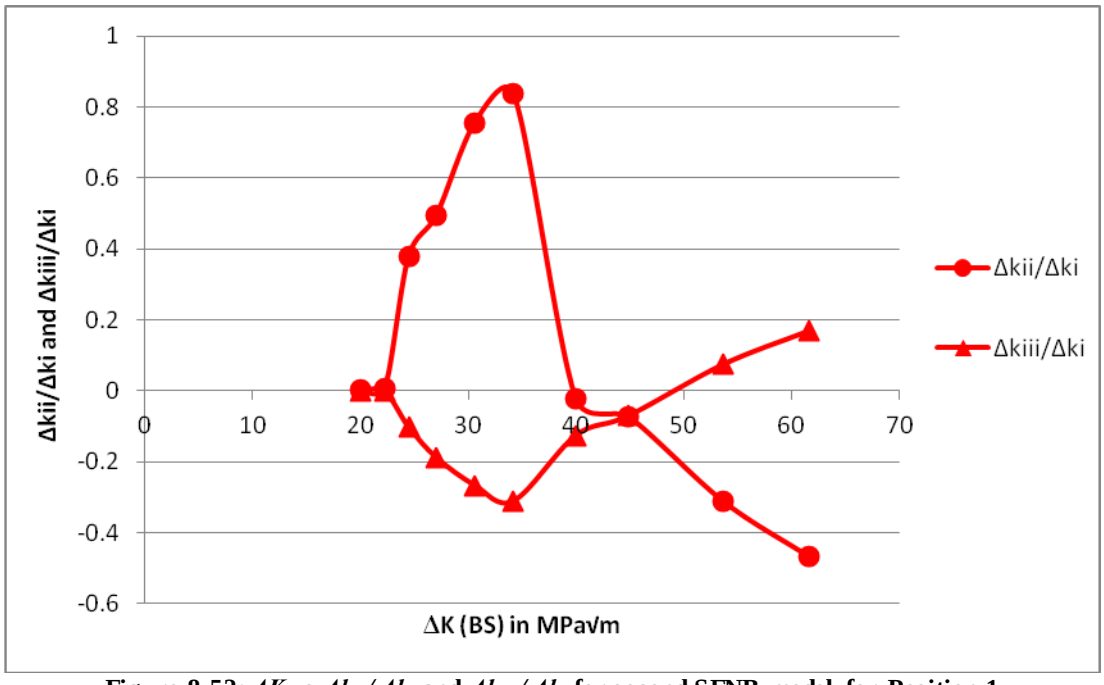

Figure 8-52: ΔK vs $\Delta k_{ii}/\Delta k_i$ and $\Delta k_{iii}/\Delta k_i$ for second SENB model for Position 1

8.3.6 Comparison 2D and 3D SENB models

Δk_i and Δk_{ii} results have been compared from the 2D models and from the 3D models on the specimen surface in Figure 8-53. It can be seen that Δk_{ii} is significantly larger in the 3D case than in the 2D case, while Δk_i is always lower.

The Δk_{eff} combining Δk_i and Δk_{ii} in these two calculations also behave similarly to the nominal K_i, so the mode II deflection does not seem to have produced a significant shielding effect for the 2D case. Ritchie [84] mentions that the twisting in the deflection could possibly increase the shielding effect. The overall lower Δk_{eff} for the 3D case can be explained by a more significant shielding effect caused by the twist component required to maintain crack front continuity c.f. the assumption in the 2D case that the deflection continues throughout the specimen thickness.

This lower overall driving force would indicate a lower crack growth rate for the 3D deflected crack which would be expected for such a crack (in the deflected region at the sample edge).

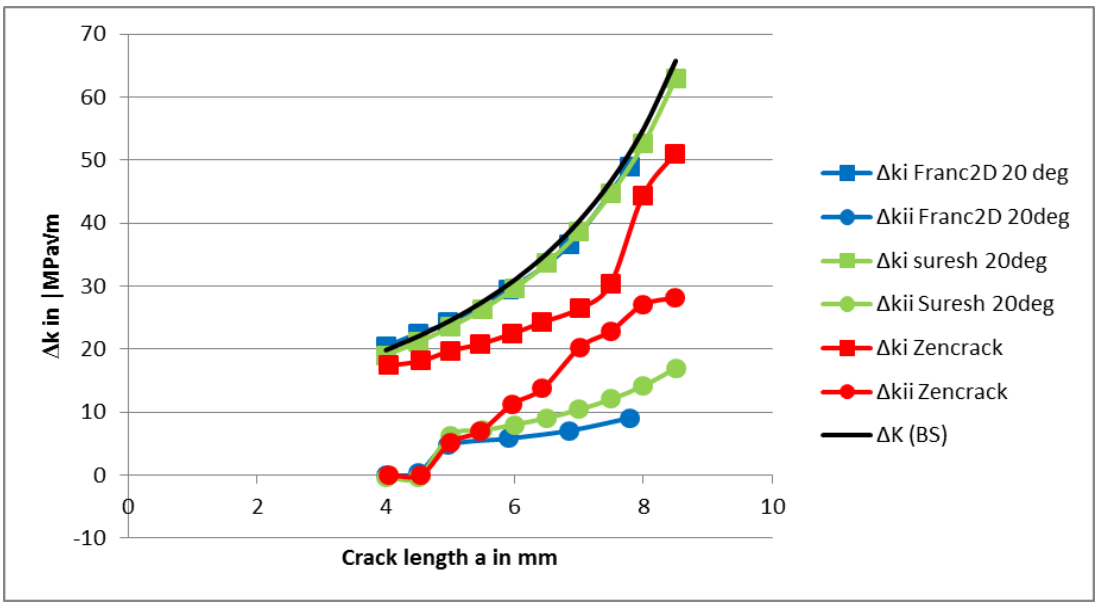

Figure 8-53: Results of $\Delta k_{i,ii}$ vs a from the Franc2D and analytical anlysis after Suresh and the Zencrack 3D analysis, compared with the ΔK from BS ISO

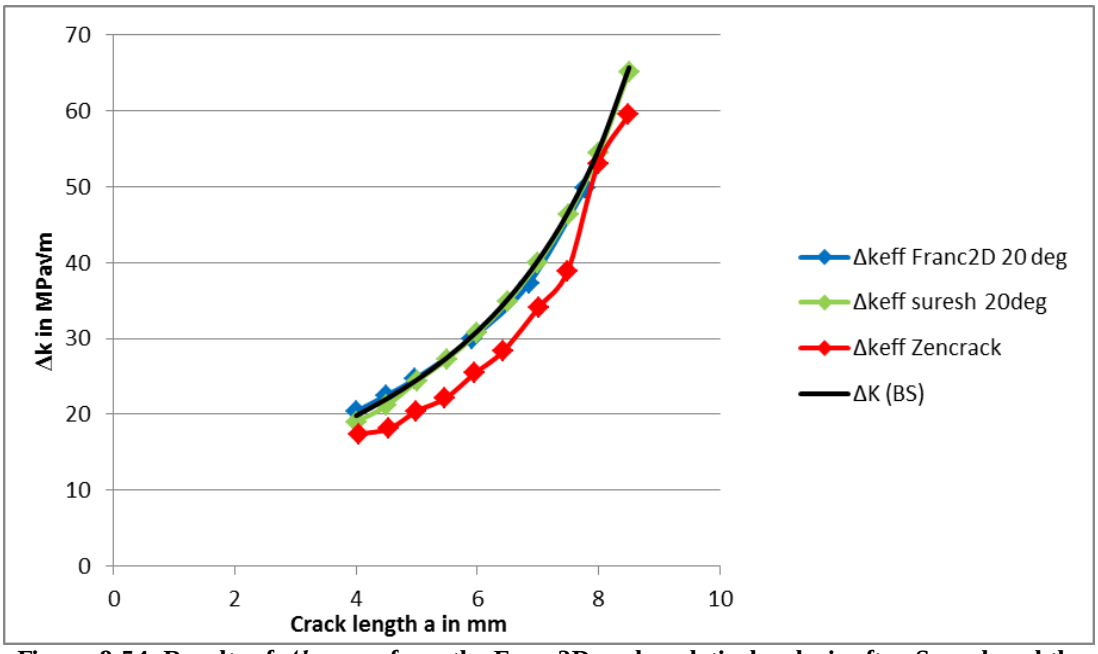

Figure 8-54: Results of Δk_{eff} vs a from the Franc2D and analytical anlysis after Suresh and the Zencrack 3D analysis, compared with the ΔK from BS ISO 12108

Comparison of the BS *K*-calibration with the planar crack in 3D and the planar crack in 2D are in good agreement as shown in Figure 8-54. Again the deflected crack in 3D shows a lower overall driving force.

8.3.7 Lifetime prediction

A planar crack has been grown out in the SENB and CNB using Zencrack, using the *C* and *m* values from both the SENB test and the R-R lifing programme values (as shown in chapter 6) for 300°C in air.

The lifetimes from the Zencrack grow out for the CNB are 89135 when using the R-R *C* and *m* values, failing at about 84MPa√m and 122465 cycles; when using the *C* and *m* values from the SENB tests, failing at about 88MPa√m, compared to the 172000 cycles for the lifetime from the actual test.

As in Chapter 6 the predicted N_f is much lower than the actual, which is possibly due to initiation or due to shielding effects. However the values predicted by Zencrack are higher, i.e. less conservative, than by the other methods used previously, namely $\Delta a/\Delta N$ approach and SA16.

Table 19 revisits the lifetime prediction for 300° in air calculated by $\Delta a/\Delta N$ approach and SA16, showing that the Zencrack values are in some cases 2x as large as for the other approaches using the same crack growth rates. This could be because Zencrack allows for a plane stress (lower) *K*, while the analytical solution does not.

N_f measured	N_f calculated to ΔK= 50MPa√m		N_f calculated to ΔK= 100MPa√m		N_f calculated with SA 16 (CNT)		N_f calculated with Zencrack	
	R-R data	SENB data	R-R data	SENB data	R-R data	SENB data	R-R data	SENB data
172000	48130	60815	50862	62702	43496	45749	89135	122465

Table 21: Numbers of cycles to failure for CNB test at 300 °C in air

For the SENB the Zencrack approach predicted that the sample failed after 30019 cycles at a crack length of 8.8mm, that is at a ΔK_i of ~70MPa√m, for the crack growth data from the SENB tests. When the lifing was repeated using the R-R data the lifetime was predicted to be 26851 cycles (failing at a ΔK_i of 64MPa√m at 8.6mm)

The results for the SENB compare well with the actual lifetime from the test at 300°C in air of 29318 cycles, in particular with the SENB crack growth rate data which makes sense as they come from this exact same sample (with some deflection). However the amount of deflected crack growth in the SENB set-up is relatively limited and so unlikely to affect lifetimes much.

8.4 Summary

Fracture surfaces have previously been shown to exhibit a competition between opening and shear modes of crack growth, with macroscopic deflection being initiated from the free surface; however no clear underlying microstructural or micromechanistic differences have been found to explain this. Hence an attempt has been made to more fully characterise the stress state at the crack tip, which the complex crack path follows.

In the first instance two mixed mode tests have been carried out in antisymmetric 4 point bend on thin plane stress SENB samples, to attempt to replicate the stress state of the deflected crack and to gain crack growth data for deflected regions. The local shear to opening ratio (one higher and one lower) that may promote prolonged deflection were identified near the surface from the range of tilt angles measured in optical profilometry.

The initial ΔK_{eff} in the mixed mode tests used to try to replicate this local stress state in a specimen (which had been chosen based on the onset of deflection measured for this temperature), seems not to have been high enough to achieve sufficient sustained deflection immediately, to gain crack growth data for these deflected regions. At higher ΔK_{eff} a slight growth in the 'deflected' mixed mode direction could be observed, however the overall K_I/K_{II} was likely to be too high for the deflection to be sustained. Tests with higher initial ΔK levels could not be performed in the set up with thin samples. This also provides an important indication that the ΔK levels at which such macroscopic deflection is produced throughout an entire sample are very close to the final stages of fatigue crack growth before failure .

Fractography of the mixed mode samples showed the same competition between the two modes as observed in the mode I samples.

After the mixed mode testing did not achieve full macroscopic deflected crack growth and so did not clearly identify the complex stress state controlling the sustained deflected crack growth, the evolving crack-tip stress state as the complex 3D crack path develops was further evaluated. To understand this further 2D and 3D Finite Element Models were used to assess local crack tip Δk evolution.

Crack tip modelling has been carried out using: (1) 2D FE models in Franc2D for CNB and SENB based on the angle at the free surface (2) 3D FE models in Zencrack/Abaqus for CNB based on the 2D angle measured on the free surface (and then applied through the entire 3D sample as a deflected plane) and (3) Fully 3D models based on a simplified 3D crack path from actual crack shape of SENB sample based on angles measured from the Alicona Infinite focus maps.

The deflection at the surface in the SENB 3D analysis has been shown to generate an increased local Δk_{eff} at the surface compared to a planar crack, although the opening component reduces. Modelling a simple terracing (switch back in crack growth direction at the surface deflected crack) shows higher Δk_{eff} than the simple deflection.

Looking at overall driving forces at the deflected crack tip, a 2D assumption (where the crack is deflected throughout the specimen) in Franc2D and the CNB Zencrack model shows no intrinsic shielding (neither does the Suresh 2D analysis used for comparison), whereas the 3D

case for the SENB in Zencrack(with deflection confined to the surface region) shows some shielding, indicating that the twist (mode III) component has significant influence on shielding .

Evaluating the local crack tip driving forces has shed some light on why these macroscopic deflections become self-sustaining, but not what triggers them. This could be used as an input into a more sophisticated lifing model for a representative component. The relationship of ΔK_i: ΔK_{ii}: ΔK_{iii} could be applied to a more complex component and stress state to evaluate the crack path, and whether the crack might grow into a e.g. hoop stress field.

Lifetime prediction for planar cracks with Zencrack approaches shows approximately twice as high lives for CNB than the analyses carried out in Chapter 6, but these are still below the lifetime for the actual (deflected) CNB sample (these could however have a long initiation life, as they had no precrack). Comparison with SENB planar cracks in Zencrack is however in good agreement with lifetime of the actual sample; this sample is however much more dominated by planar crack growth.

8.4.1 Potential Applications to Lifing Methodologies

To use the outcomes of this work in future component lifing it is suggested that R-R need to develop a Lifing Toolkit. This could initially define when deflection starts, based on the definition of onset of terracing as the ΔK range, as described in Chapter 5.3.

Then following a conservative approach, a 'deflected crack growth calculator' can be developed that, based on the FE results for a simplified crack shape, defines crack path to follow typical ΔK_i: ΔK_{ii}: ΔK_{iii} ratios. This will start to grow the angle under a suitable deflection. ΔK_{eff} will be used to calculate *da/dN* either in terms of a relative *da/dN* for various specific positions (which will have to be defined and cross-checked) or a simpler approximation of an overall *da/dN*. After a certain growth interval, the crack path and overall applied stress state should be checked to see if it is going towards any hoop stress region.

8.5 Crack growth rate for deflected crack

After establishing the Δk_i, Δk_{ii},Δk_{iii} and Δk_{eff}, a crack growth rate *da/dN* can be calculated, using the measured *da/dN* (assuming planar crack growth is dominant). Considering that beachmarking has shown in Loo-Morrey's samples, that the deflected crack grows along a circular crackfront, as one would expect from a planar crack, the actual crack length can be calculated, using the angle for the deflection measured, at first instance in 2D for the edge.

Projected $da/dN = \Delta K_I$ controlled *da/dN* (from SENB tests) Equation 8-22

Actual *da* = projected *da* * cos α Equation 8-23

assuming a single deflection angle from 2D (ca. 20° for SENB)

The actual *da/dN* vs ΔK (nominal), cf. projected *da/dN* vs K_I can then be calculated.

A 3D approach is more complicated, therefore the same approach has been used in the first SENB model for the edge Position (Position 1) and for the 2nd row element (Position 2). Position 7 is the planar crack growth in the centre.

The crack growth data is slightly lower the more deflected the sample is, but the difference is very small, see Figure 8-55.

It would be possible to recalculate lifetimes based on these crack growth rates (using *da/dN* vs K_{eff}), but it will not make a significant difference, as the rates are very similar, and it would only represent the deflected or planar region, not a combination of both. It should also be noted that this does not consider the twist component, so might not describe the shielding caused by the 3D crack growth, but it shows that crack growth at the edges will be slowed down.

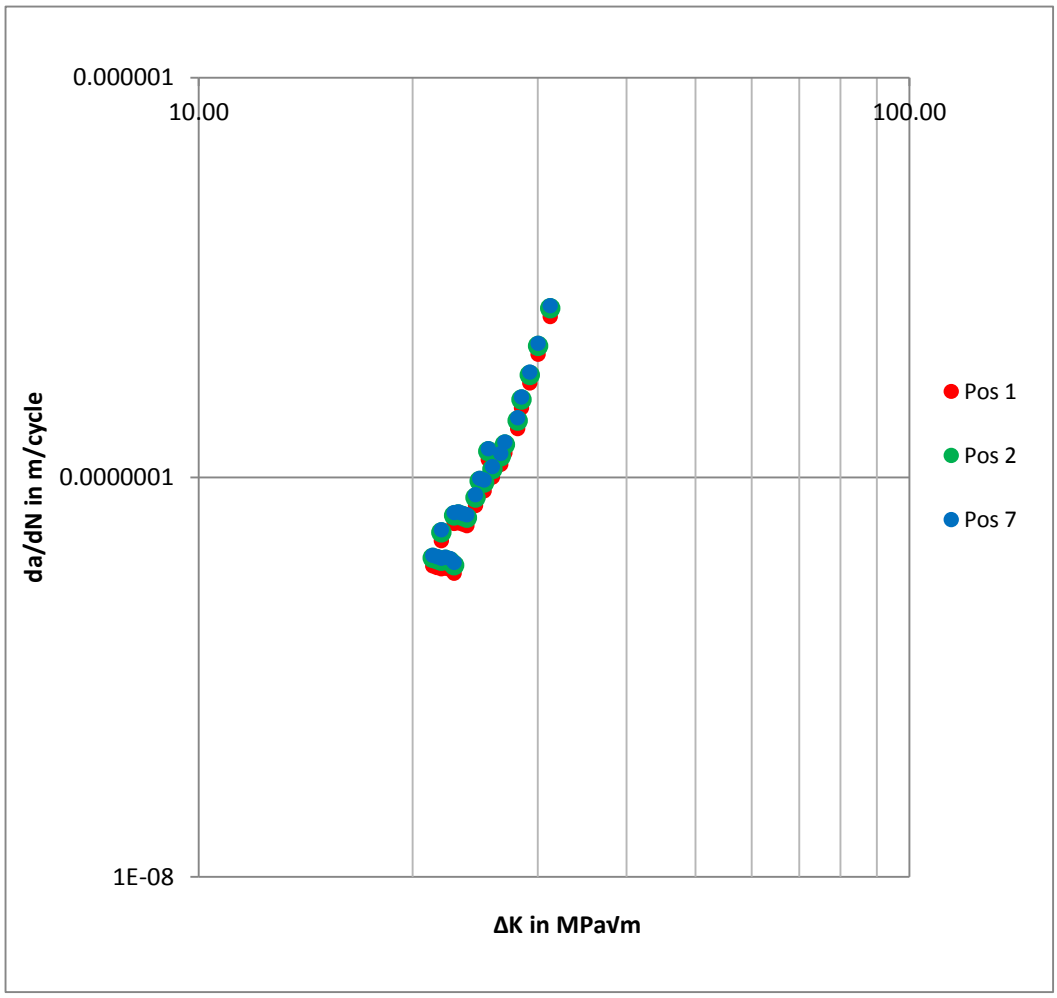

Figure 8-55: Crack growth rates for deflected crack, at Position 1, 2 and 7 in the first SENB

9 Discussion

SMDCG has been observed in fine grained superalloy U720Li at intermediate temperatures (200-500°C) in air and vacuum, but not at room temperature. In air it was not observed above 600°C, whilst in vacuum it was observed at 600 and 650°C. The local crack tip driving forces of the resultant complex crack shape have been evaluated via 3D FEA and this has shed some light on why these macroscopic deflections become self-sustaining, but it is still not clear what triggers the initial deflections.

This material is clearly prone to secondary cracking, as the slip traces and secondary cracks observed in the FEG-SEM suggest, this can be linked to planar slip in this material at these temperature ranges, which is promoted by the shearable γ' precipitate.

As discussed in section 2.3.5, the Aluminium alloys AA7050 and AA2297 showed similar deflected crack growth behaviour in fatigue. The deflection from the expected nominal crack plane has been linked there to either strongly textured alloys with high volume fractions of shearable δ' (Al_3Li) precipitates where slip band crack growth has been promoted or specific alignments where grain boundary failure processes (principally shear controlled) have dominated fatigue failure. [90]

These alloys are however highly textured while the variants of U720Li in this work did not show any texture, so clearly planar slip processes cannot be the only explanation for this deflection.

In addition, planar slip processes would be expected to operate at room temperature as well as between 200-500°C, and previous work showed SMDCG only occurred above 200°C. This influence of temperature could be explained by increased diffusion of interstitial atoms (boron and carbon) in the alloy. Increased ease of diffusion of interstitial atoms in these alloys may result in Dynamic Strain Ageing (DSA), as mentioned in section 2.1.4.4, which is commonly assumed to be caused when solute interstitial atoms are able to diffuse faster than dislocations travel through the lattice and are hence able to catch up with them and repeatedly pin them. The stress must increase to tear the dislocations away from the pinning atoms, and subsequently the dislocations can move at a lower stress, until a solute atom catches up again. This occurs many times, which results in a serrated stress-strain curve during plastic deformation. [36] DSA is common in Nickel based superalloys at intermediate temperatures and was observed in U720 at temperatures above 300°C, but was most intense at temperatures between 500 and 600 °C, and it is therefore somewhat unclear how it contributes to the observed deflected crack growth at intermediate temperatures.

SMDCG has been seen in U720 and the low interstitial variant U720Li, which raises the question whether diffusion of interstitial atoms could be an explanation for this effect. However when comparing the content of interstitial atoms, this version of U720Li may not be in fact a very low interstitial alloy. Table 22 shows the sum of the contents in weight % of the interstitial atoms Carbon and Boron, which indicates that it is slightly lower than for the normal variant, however there is still a significant amount of interstitial atoms in the alloys. Pang's U720Li PM alloy still has 3.9%, the alloy U720Li C&W from this work still 3%, while the content in the 'normal' variants exhibiting SMDCG is about 5%. This means that there are still

interstitial atoms in the U720Li alloy that could diffuse through the alloy at increased temperatures, potentially enabling DSA effects which may contribute to the deflecting cracks becoming self-sustaining.

To study this further, future work could include tests using a model alloy that has minimal interstitial atoms (C and B), to study in greater detail what the effect of these elements is on the deflected crack growth, and whether their absence would suppress SMDCG.

Diffusion would still be expected at higher temperature, an explanation of the difference between air and vacuum at higher temperature (600°C and above) could be that in a high temperature test in air the effect of oxidation during fatigue could become more dominant over the sustained deflected crack growth, and the deflection could be suppressed, while in vacuum only SMDCG would be present without any oxidation effects.

	Alloy	B	C	Sum of interstials
U720 'Normal' variants	U720 PM (as tested by M. Loo Morrey [49])	3.0	2.0	5.0
	U720 PM FG (as tested by R.R. Brooks [90])	3.1	2.2	5.3
	U720 PM CG (as tested by R.R. Brooks [90]) (SHOWS NO SMDCG)	2.0	1.9	3.9
U720Li Low interstial variant	**U720Li PM FG and LG ([22])**	**1.6**	**2.3**	**3.9**
	U720Li C&W (as tested by R.R. Brooks [90])	1.1	2.1	3.2
	U720Li C&W [92]	**1.6**	**1.4**	**3.0**

Table 22: Contents of interstial elements in wt.% in different variants of U720Li and U720 (materials in bold have been tested in this work)

10 Summary and Conclusions

In this thesis the phenomenon of sustained macroscopic deflected crack growth (SMDCG) during fatigue in Nickel based Superalloys is discussed, this has also been referred to as 'teardrop' cracking in previous work. In a corner notched specimen a fatigue crack usually grows in a quarter-circular plane perpendicular to the stress axis, the sustained deflected crack however exhibits considerable deflection from this plane at the free surfaces, so that a central planar region is enclosed by large shear terraces. This raises concerns about the lifing methodology for aeroengine components based on assumptions of planar fatigue crack growth. A deviation from the expected crack path in a component could result in significant changes in crack propagation behaviour because of a change in the stress field experienced. Hence the aim of this work is to develop an understanding of the mechanism and develop assessment methodologies for component lifing.

Microstructural characterisation (using image analysis and also EBSD) has revealed grain size, primary and secondary γ' size and volume fraction of U720Li C&W, and U720Li PM in a fine grain (FG) and a large grain (LG) variant, which have been used in this work and U720PM, which has been used in previous work on sustained deflected crack growth.

The measured grain size for the U720 PM and the U720Li C&W were similar to the U720Li PM LG, but significantly larger than U720Li PM FG, however their solution heat treatment temperature was below or the same as the one of the FG material. While the U720Li PM FG showed consistent grain sizes, the other alloys showed a greater variation in grain size, this potentially has implications on the range of microstructure/grain sizes sampled by a fatigue crack tip. Some variation between the EBSD and Image analysis measurements for grain size has been observed. Studies with EBSD on all the materials considered have shown that none of the materials studied show any significant texture.

Initial fatigue testing has been carried out on Corner Notch samples in bend (CNB) on U720Li PM FG and LG at 300°C in air. Further CNB and Single Etch Notched Bend (SENB) testing have been performed on U720Li C&W at 300, 600 and 650°C in air and vacuum. All testing in this project was performed at 20Hz with a sinusoidal waveform and at an R-ratio of 0.1. Two thin (plane stress dominated) SENB samples were also tested for comparison at 300°C in air.

All tests showed some deflected crack growth at the free surface. The fracture surfaces of the CNB showed a central flat 'teardrop' region and terraced regions starting from the top and side surface, where flat and deflected crack growth mode were alternating. Teardrop cracking really only describes the particular geometry produced in a CNB sample and also refers to the planar region, which is the region where the crack growth is behaving as expected. Since this deflection was also clearly seen at the free surfaces of SENB samples, the phenomenon is better described as sustained macroscopic deflected crack growth (SMDCG).

A method has been proposed to characterise the onset of this deflection in a systematic manner, independent of sample size or type, notch size and initial ΔK levels. The onset of deflection has been given as a range of nominal ΔK values where the deflection exceeds the monotonic plane stress plastic zone size distance from the free surface (defined as the range between Rice and Dugdale approximation). This is believed to represent the plane stress

dominated region in which some deflection (typical shear lip formation) might be expected. In the C&W material an increase in onset ΔK values can be seen with increased temperature in air tests for both CNB and SENB tests, indicating the SMDCG effect is reduced at higher temperature or completely suppressed. In vacuum testing onset ΔK values are relatively independent of the test temperature assessed in this study. The ΔK_{Onset} ranges in vacuum for the CNB samples are however higher than those observed in air, but exist over a similar range as seen for the SENB.

A number of tests from other workers and some aeroengine component failures from rig tests at Rolls Royce plc., showing some deflection, have been assessed in terms of this ΔK_{Onset} approach. An Excel template has been developed to calculate the variation in monotonic plane stress plastic zone distance from all free surfaces and to overlay this on the fracture surface. This template can then be used to determine whether deflection can be considered to be SMDGC (i.e. exceeding the monotonic plane stress plastic zone at a relatively low ΔK_{Onset} range) or whether the deflections observed are simply due to shear lip formation in the expected plane stress region or a result of complex loading conditions for a wider range of materials and test conditions. The effect of temperature has been confirmed, SMDCG is observed at 300°C in air and vacuum, and is sustained in vacuum to 600°C. The results of Loo Morrey [50] confirm the results of this work for a consistent onset ΔK for deflection. R-ratio does not seem to have an effect, and the initial ΔK does not matter, the onset occurs at the relevant ΔK, so for example deflection occurs earlier in a sample where the initial ΔK_i is higher.

Assessing the results of other researchers: The effect of long dwells in fatigue seems to reduce the effect at high temperature in vacuum. Deflection has been observed in some (but not all) samples with very long dwells at high temperature (in vacuum), deflection (or tunnelling) could however also be caused by creep (a quite different mechanism). Bithermal tests have shown that changing the temperature to and from a 'critical' SMDCG temperature and 'switching' the mechanism on and off results in very little deflection (overall planar fatigue crack), possibly the low temperature crack does not have enough time to macroscopically deflect, before turning back. Given that this alternation in temperature is closer to the expected "peanut" temperature and stress cycle typically seen in turbine disc service conditions this may indicate the SMDCG will not occur to any significant extent in a turbine disc.

In terms of components: cracks which had initiated from a firtree root in a high pressure turbine disc had occurred in the critical temperature range (at 300°C) where SMDCG might have been expected, however using the monotonic plastic zone size template on the fracture surface showed that significant deflection could be expected there anyway due to the expected extent of the plane stress region for the very high stresses in this region. Deflected fatigue failure in airholes in a high pressure turbine disc therefore needs further elucidation of the stresses around the holes before an assessment can be made as to whether SMDCG is being observed.

Detailed fractography with FEG-SEM on tested specimens from the different test geometries, test conditions and components has also shown slip traces and secondary cracking, in both the macroscopically deflected and planar crack growth regions. This could be evidence of local

competition between opening and shear crack growth modes, and the shear crack growth predominating may then trigger the macroscopic deflection.

The predominance of shear crack growth modes could be linked to planar slip processes, which are more pronounced in vacuum, as slip becomes more reversible, whilst they are suppressed at 600°C in air, where usually wavy slip would be promoted. However in previous work the SMDCG effect has not been seen at room temperature, where planar slip would be more prevalent, so the origin of SMDCG cannot be solely due to an increase in planar slip processes.

Further detailed analysis of secondary deflected crack tips with focussed ion beam (FIB) serial sectioning combined with EBSD analysis has allowed a detailed 3D reconstruction of the SMDCG crack tip interaction with local microstructure. This, together with TEM foils extracted via FIB in the same region, have confirmed that the SMDCG in these systems is not linked to any local texture effects or surface microstructural differences. The deflected (secondary) crack behaves similarly to a planar crack growing both transgranularly and occasionally intergranularly through γ and γ'. There is also no observed texture/grain orientation effect that influences the deflection.

These alloys seem prone to secondary cracking, however under specific stress state and temperature conditions some of these secondary cracks become quite self-sustaining. This appears to be triggered by the plane stress state, but clearly deflects beyond the plane stress region.

In the SENB tests PD measurements were used to gain Paris law crack growth data. The crack growth rates from these tests compare well to the crack growth data obtained by Rolls Royce plc. from Corner Notch tests in tension (CNT). A lifetime prediction has been carried out for the CNB samples (which showed the most significant SMDCG due to the higher ΔK levels achieved in the test), using a $\Delta a/\Delta N$ integration approach and the SA16 software at R-R, based on the C and m values from the SENB and CNT test respectively. Comparing these predictions, which are based on assumptions of planar crack paths, to the observed lifetimes of the deflected test samples, there is no indication that the macroscopically deflected crack growth has led to shorter lifetimes. It should be noted that there may be some effect of initiation cycles, that may provide part of the explanation for the longer observed lifetimes, as all the lifetime predictions assume immediate growth. Moreover additional effects of crack closure (from macroscopically deflected crack surfaces contacting) may also lead to additional extrinsic shielding effects reducing the crack tip stress state and crack growth rates. Thus it appears that for these test specimen geometries SMDCG has not reduced lifetimes.

To be able to predict crack paths in components, it is necessary to establish what the crack driving force is, what causes the crack to deflect and how this could be applied to predict lifetimes for the complex stress state in a component.

3D maps of some CNB and SENB fracture surfaces have been created using an Alicona Infinite Focus profilometre. The system is a microscope that scans over the fracture surface and automatically focuses on the height of the sample, and works out a 3D height profile. From the 3D map tilt angles in the deflected areas could be measured, and from the range of tilt angles

measured the opening to shear ratio that is assumed to promote prolonged sustained deflected crack growth was calculated.

Mixed mode tests have been carried out on thin SENB samples for two opening to shear ratios (K_I/K_{II}) in antisymmetric four point bend. The aim was to replicate the stress state of the deflected crack in a specimen and get crack growth data for SMDCG. If the K_I/K_{II} was chosen correctly the sustained deflected crack would be expected to grow straight through the sample, which would allow explicit measurement of crack growth rates with PD. However both mixed mode tests did not achieve full scale deflection, the crack deflected towards the mode I (opening) direction. ΔK_{eff} seemed to be too low to trigger the deflection and as the crack grew towards the mode I direction, the ΔK_{eff} increased, however the shear component decreased, so that sustained deflection could not be achieved, as the complex stress state controlling the sustained deflected crack growth could not be replicated in such a simple specimen set-up.

To further understand the evolving crack-tip stress state as the complex 3D crack path develops, Finite Element Models were used to assess local crack tip Δk evolution. Crack tip modelling has been carried out using: (1) 2D FE models in Franc2D for CNB and SENB based on the angle at the free surface (2) 3D FE models in Zencrack/Abaqus for CNB based on the 2D angle measured on the free surface (and then applied through the entire 3D sample as a deflected plane) and (3) Fully 3D models based on simplified 3D crack path from actual crack shape of the SENB sample based on angles measured from the Alicona Infinite Focus 3D map.

Looking at overall driving forces at the deflected crack tip, a 2D assumption in Franc2D and the CNB Zencrack model shows no intrinsic shielding, whereas the 3D case for the SENB in Zencrack shows some shielding, indicating that the twist (mode III) component has a significant influence on shielding. Evaluating the local crack tip driving forces has shed some light on why these macroscopic deflections become self-sustaining, but not what triggers them. The outcomes of this work could be used as an input into a more sophisticated lifing model for an aeroengine component, using the relationship of ΔK_i: ΔK_{ii}: ΔK_{iii} from the 3D FE analysis. This could be applied to a more complex component and stress state to predict the deflected crack path.

The factors that influence the SMDCG are summarised in Figure 10-1.

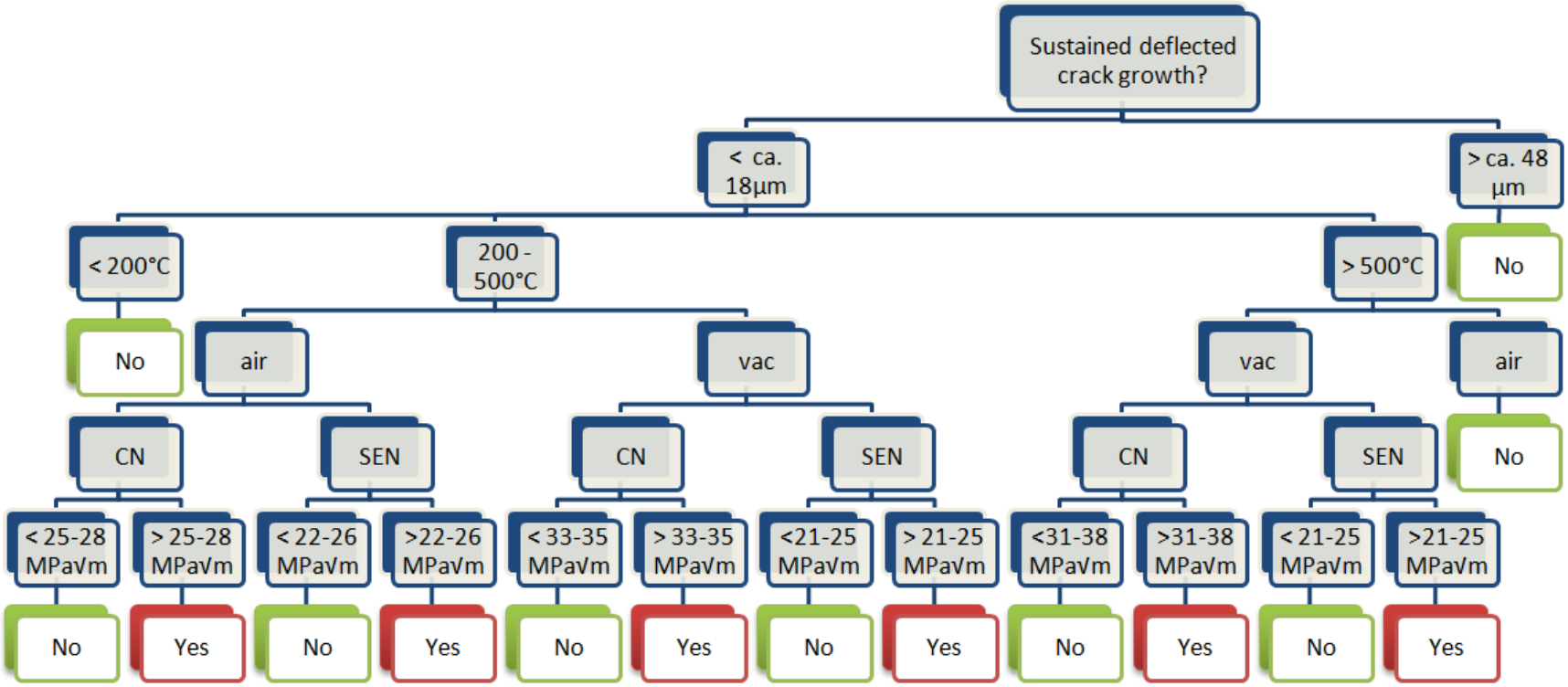

Figure 10-1: Factors influencing sustained macroscopic deflected crack growth, based on current and previous work [4, 5]

11 Future Work

Evaluating the local crack tip driving forces has shed some light on why these macroscopic deflections become self-sustaining, but not what triggers them.

The outcomes of this work could be used as an input into a more sophisticated lifing model for an aeroengine component, such as a turbine disc. The relationship of ΔK_i: ΔK_{ii}: ΔK_{iii} could be applied to a more complex component and stress state to evaluate the crack path, and whether the crack might grow into e.g. a hoop stress field.

In the first instance a manual approach could use the decision flow chart in Figure 10-1 in Chapter 9 and a simple rule of thumb approach to work out how far it will grow.

To develop this further, a Lifing Toolkit could be developed, that at first defines when deflection starts, based on the definition of onset of terracing from the ΔK range, as described in Chapter 5.3. Then following a conservative approach, a 'deflected crack growth calculator' can be developed that based on the FE results for a simplified crack shape, defines crack path to follow typical ΔK_i: ΔK_{ii}: ΔK_{iii} ratios. This will start to grow the angle under a deflection. ΔK_{eff} will be used to calculate da/dN either the relative da/dN for each specific position or the overall da/dN. After a certain growth interval, the crack path and overall applied stress state should be assessed to see if it is growing towards a higher hoop stress region.

The model could be further advanced by considering the effect of changing temperature in components, based on the work with bithermal testing, and how such changes may reduce the effect of deflection.

Further work to improve the understanding of SMDCG, should involve studying any further component failures and specimens, that are showing deflected crack growth, in the same manner (using ΔK_{Onset} template and fractography using SEM). This would allow creation of a fuller database of failures to be complied for better characterisation and to build confidence in the ΔK onset values.

To identify the crack growth rates of a deflected crack, further analysis of the existing PD data from the mixed mode tests could be performed by cutting the observed deflected crack shape (from the side of the mixed mode samples) in a foil analogue to scale, and measuring the PD readings to get a better PD calibration, as shown in Figure 11-1. 3D analogues could also be replicated in a conducting medium, but this would have to be done on a specimen by specimen basis.

These crack growth rates could then be compared to the ones estimated in section 8.5, to further study the influence of shielding from the deflection on the crack growth rates under a more complex applied loading state.

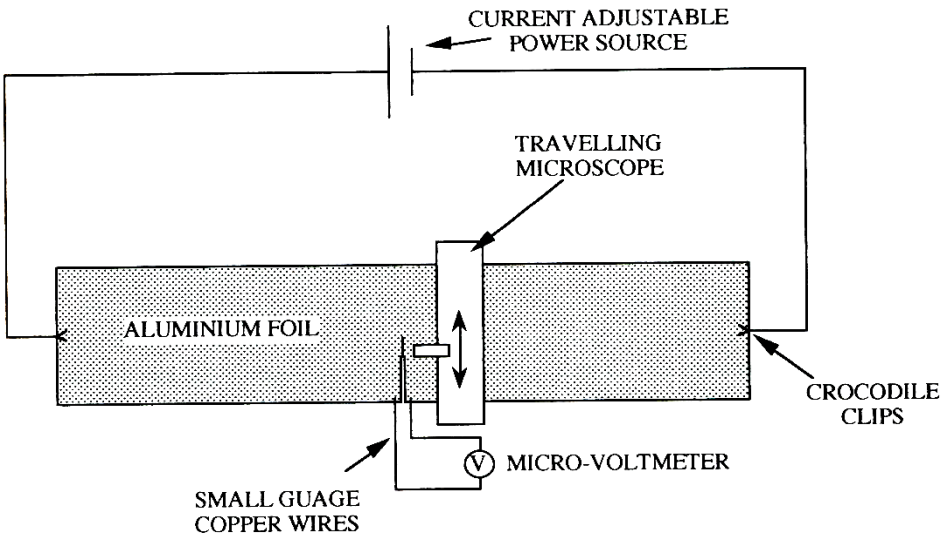

Figure 11-1: Schematic of apparatus arrangement for foil analogue calibration of voltage to crack length [107]

Further investigation on the effect of vacuum on the onset in CNB/SENB could be confirmed and further studied by additional vacuum testing over a greater number of temperatures to more precisely identify the temperature regime where SMDCG is dominant, and the effect of the stress state in the different specimen on the onset of deflection.

Moreover the effect of grain size and γ' size distribution on the occurrence and the onset of SMDCG could be studied in more detail, using various heat treatments of the material to achieve varying grain sizes and γ' size distributions and fatigue these variants to identify whether there is a threshold grain size for SMDGC, and how the degree of slip planarity (altered via γ' size distributions) affects SMDCG.

References

1. Schoettle, C., Reed, PAS, Starink, MJ, Sinclair, I, Child, D, West, GD, Thomson, RC. *Mechanism of Sustained Macroscopic Deflected Fatigue Crack Growth in the Nickel Based Superalloy Udimet 720*. in *Materials Science and Technology Conference and Exhibition 2011, MS and T'11*. 2011. Columbus, Ohio: TMS.
2. Schoettle, C., Sinclair, I., Starink, M.J., Reed, P.A.S. , *Deflected 'Teardrop Cracking' in Nickel based Superalloys: Sustained Macroscopic Deflected Fatigue Crack Growth.* International Journal of Fatigue, 2012. **44**: p. 188-201.
3. Schoettle, C., Reed, P.A.S., Starink, M.J., Sinclair, I., Child, D.J., West, G.D.,Thomson, R.C. *Sustained Macroscopic Deflected Fatigue Crack Growth in Nickel Based Superalloy 720Li*. in *Superalloys 2012*. 2012. Seven Springs, PA, USA: John Wiley & Sons, Inc., Hoboken, NJ, USA.
4. Loo-Morrey, M., Reed, PAS, *Anomalous crack shape development (tear drop cracking) in turbine disc material Udimet 720.* Material Science and Technology, 2000. **16**: p. 133-146.
5. Brooks, R., Rainforth, WM, *Fatigue damage mechanisms associated with 'tear-drop' cracking in UDIMET 720.* 1999.
6. Betteridge, W., Heslop, J *The Nimonic Alloys and Other Nickel Base High-Temperature Alloys*1974, London, UK: Edward Arnold.
7. King, J., *Fatigue crack propagation in nickel-base superalloys-effects of microstructure, load ratio, and temperature.* Materials Science and Technology, 1987. **3**: p. 750-764.
8. Sims, C., Stoloff, NS, Hagel, WC, ed. *Superalloy II*. 1987, John Wiley and Sons.
9. Hessell, S., Voice, W, James, AW, Blackham, SA, Small, CJ, Winstone, MR *United States Patent: Nickel Alloy for Turbine Engine Components*, 1999: United States.
10. Chakravorty, S. and D.R.F. West, *NI3AL-NI3CR-NI3TA SECTION OF NI-CR-AL-TA SYSTEM.* Materials Science and Technology, 1985. **1**(11): p. 978-985.
11. Polvani, R., Ruff, AW, Strutt, PR *A mechanism for metalloid strengthening of Udimet-700.* Journal of Materials Science Letters, 1983. **3**: p. 287-290.
12. Kear, B.H., Wilsdorf, H.G.F., *Dislocation configuration in plastically deformed CU_3Au alloys.* Transaction of the Metallurgical Society of AIME, 1962. **224**: p. 382-386.
13. Reed, R.C., *The Superalloys - Fundamentals and Applications*2006, Cambridge, UK: Cambridge University Press.
14. Ricks, R., Porter, AJ, Ecob, RC *The growth of γ' precipitates in nickel-base superalloys.* Acta Metallurgica, 1983. **31**: p. 43-53.
15. Burke, M., Greggi, J Jr., Whitlow, GA *The effects of Boron and Carbon on the microstructural chemistries of two wrought nickel base superalloys.* Scripta Metallurgica, 1984. **18**: p. 91-94.
16. Connolley, T., *Initiation and Growth of short cracks in U-notch bend specimens of superalloy IN718 during high temperature low cycle fatigue*, in *School of Engineering and Applied Sciences*2001, University of Southampton: Southampton.
17. Jackson, M., Reed, RC *Heat treatment of UDIMET 720Li: the effect of microstructure on properties.* Materials Science and Engineering, 1999. **A259**: p. 85-97.
18. Mao, J., Chang, KM, Yang, W, Ray, K, Vase, SP, Furrer, DU *Cooling precipitation and strengthening study in powder metallurgy superalloy U720Li.* Metallurgical and Materials Transactions A, 2001. **32A**(2441-2452).
19. Tawancy, H.M., et al., *THERMAL-STABILITY OF ADVANCED NI-BASE SUPERALLOYS.* Journal of Materials Science, 1994. **29**(9): p. 2445-2458.
20. Antolovich, S., Rosa, E, Pineau, A, *Low cycle fatigue of Rene 77 at elevated temperatures.* Materials Science and Engineering, 1981. **47**: p. 47-57.

21. Antolovich, S., Jayaraman, N, *Metallurgical instabilities during the high temperature low cycle fatigue of nickel-base superalloys.* Material Science and Engineering, 1982. **57**: p. L9-L12.
22. Brooks, R., Rainforth, WM, *The effect of microstructure on the morphology of fatigue cracks in UDIMET 720.* 2000.
23. Pang, H.T., *Effect Of Microstructure Variation On Turbine Disc Fatigue Lives*, in *School of Engineering Sciences*2003, University of Southampton: Southampton.
24. Cadek, J., Pahutova, M, Sustek, V, Dlouhy, A *On the role of recovery in creep of precipitation-strengthened polycrystalline nickel-base alloys.* Materials Science and Engineering, 1997. **A238**: p. 391-398.
25. Lerch, B., Jayaraman, N, Antolovich, SD *A study of fatigue damage mechanism in Waspaloy from 25 to 800°C.* Material Science and Engineering, 1984. **66**: p. 151-166.
26. Subramanya Sarma, V., Sundararaman, M, Padmanabhan, KA, *Effect of γ' size on room temperature low cycle fatigue behaviour of a nickel base superalloy.* Materials Science and Technology, 1998. **14**: p. 669-675.
27. Valsan, M., Sastry, DH, Bhanu Sankara Rao, K, Mannan, SL, *Effect of strain rate on the high-temperature low-cycle fatigue properties of a Nimonic PE-16 superalloy.* Metallurgical and Materials Transactions A, 1994. **25A**: p. 159-171.
28. Grabowski, L., King, JE *Modelling short crack growth behaviour in nickel-base superalloys.* Fatigue and Fracture of Engineering Materials and Structures 1992. **15**: p. 595-606.
29. Reed, P., Gale, WF, King, JE, *Intrinsic threshold in polycrystalline Udimet 720.* Materials Science and Technology, 1993. **9**: p. 281-287.
30. Blankenship, C.J., Hornbogen, E, Starke, EA Jr. , *Predicting slip behaviour in alloys containing shearable and strong particles.* Materials Science and Engineering, 1993. **A169**(33-41).
31. Blankenship, C.J., Starke, EA Jr *Mechanical behavior of double-aged AA8090.* Metallurgical Transactions A, 1993. **24A**: p. 833-841.
32. Jata, K., Starke, EA Jr *Fatigue crack growth and fracture toughness behaviour of an Al-Li-Cu alloy.* Metallurgical Transactions A, 1986. **17A**: p. 1011-1026.
33. Duva, J., Daeubler, MA, Starke, EA Jr, Luetjering, G *Large shearable particles lead to coarse slip in particle reinforced alloys.* Acta Metallurgica, 1988. **36**: p. 585-589.
34. Zheng, D., Ghonem, H *Influence of prolonged thermal exposure on intergranular fatigue crack growth behavior in alloy 718 at 650°C.* Metallurgical Transactions A, 1992. **23A**: p. 3169-3171.
35. Hale, C.L., W.S. Rollings, and M.L. Weaver, *Activation energy calculations for discontinuous yielding in Inconel 718SPF.* Materials Science and Engineering a-Structural Materials Properties Microstructure and Processing, 2001. **300**(1-2): p. 153-164.
36. Dieter, G., *Mechanical Metallurgy*1988, Singapore: McGraw-Hill.
37. Hayes, R.W., Hayes, W.C., *On the Mechanism of Delayed Discontinous Plastic Flow in an Age-Hardened Nickel Alloy.* Acta Metallurgica, 1982. **30**: p. 1295.
38. Koul, A.K., Pickering, F.B., *Serrated Yielding in Ni-Fe Base Superalloys at 700^{O}C.* Scripta Metallurgica, 1982. **16**: p. 119.
39. Nahm, H., Moteff, J. , *Second Phase Formation and its Influence on the Fatigue Properties of Incoloy 800 at Elevated Temperatures.* Metallurgical Transactions, 1979. **2**: p. 943.
40. Miner, R.V., Castelli, M.G. , *Hardening Mechanism in a Dynamic Strain Ageing Alloy, HASTELLOY X, during Isothermal and Thermomechanical Cycle Deformation.* Metallurgical Transactions A, 1992. **23A**: p. 551.
41. Jenkins, C.F., Smith G.V., Trans AIME, 1969. **245**: p. 2149.

42. Callister, W., *Material Science and Engineering: An introduction* 2000, New York, USA: John Wiley and Sons.
43. Smith, R., Liu, Y, Grabowski, L, *Short fatigue crack growth behaviour in Waspaloy at room and elevated temperatures.* Fatigue and Fracture of Engineering Materials and Structures 1996. **19**: p. 1505-1514.
44. Suresh, S., *Fatigue of Materials*. Second Edition ed1998: Cambridge University Press.
45. Anderson, T., *Fracture Mechanics - Fundamentals and Applications* 2005, Boca Raton: CRC Press Taylor and Francis Group.
46. Griffith, A.A., *The Phenomena of Rupture and Flow in Solids.* Philosophical Transactions Series A, 1920. **221**: p. 587-603.
47. Pang, H.T., *PhD Thesis: Effect Of Microstructure Variation On Turbine Disc Fatigue Lives*, in *School of Engineering Sciences* 2003, University of Southampton.
48. Irwin, G.R. *Onset of Fast Crack Propagation in High Strength Steel and Aluminium Alloys*. in *Sagamore Research Conference Proceedings*. 1956.
49. Sadananda, K., Shahinian, P *A fracture mechanics approach to high temperature fatigue crack growth in Udimet 700.* Engineering Fracture Mechanics, 1979. **11**: p. 73-86.
50. Loo-Morrey, M., *Crack Growth Transitions in Udimet 720*, in *Faculty of Engineering and Applied Science* 1997, University of Southampton: Southampton.
51. Rice, J., *Mechanics of crack tip deformation by extension of fatigue.* Fatigue Crack Propagation, Special Technical Publication 415, American Society for Testing anf Materials, 1967: p. 247-309.
52. Irwin, G., *Plastic zone near a crack and fracture toughness*, in *The seventh Sagamore Ordnance Materials Conference* 1960: New York: Syracuse University. p. 63-78.
53. Dugdale, D., *Yielding of steel sheets containing slits.* Journal of the Mechnics and Physics of Solids, 1960. **8**: p. 100-108.
54. Miller, K., *The short crack problem.* Fatigue of Engineering Materials and Structures 1982. **5**: p. 223-232.
55. Wu, Z., Sun, X, *Multiple fatigue crack initiation, coalescence and growth in blunt notched specimens.* Engineering Fracture Mechanics, 1998. **59**: p. 353-359.
56. Fournier, D., Pineau, A, *Low cycle fatigue behavior of Inconel 718 at 298K and 823K.* Metallurgical Transactions A, 1977. **8A**: p. 1095-1105.
57. Goto, M., Knowles, DM, *Initiation and propagation behaviour of microcracks in Ni-base superalloy Udimet 720Li.* Engineering Fracture Mechanics, 1998. **60**: p. 1-18.
58. Hicks, M., Brown, CW *A comparison of short crack growth behaviour in engineering alloys.* Fatigue, 1984.
59. Stephens, R., Grabowski, L, Hoeppner, D W *In-situ/SEM fatigue studies of short crack behaviour at ambient and elevated temperature in a nickel-base superalloy*. in *Short Fatigue Cracks*. 1990. Sheffield: Mechanical Engineering Publications Limited
60. Yates, J., Zhang, W, Miller, KJ, *The initiation and propagation behaviour of short cracks in Waspaloy subjected to bending.* Fatigue and Fracture of Engineering Materials and Structures 1993. **16**: p. 351-362.
61. Mei, Z., Krenn, CR, Morris, J W Jr. , *Initiation and growth of small fatigue cracks in a Ni-base superalloy.* Metallurgical and Materials Transactions A, 1995. **26A**: p. 2063-2073.
62. Healy, J., Grabowski, L, Beevers, CJ *Short-fatigue crack growth behaviours of alloy 718.* International Journal of Fatigue, 1991. **13**: p. 133-138.
63. Reger, M., Remy, L, *High temperature, low cycle fatigue of IN100 superalloy I: influence of temperature on the low cycle fatigue behaviour.* Material Science and Engineering A, 1988. **101**: p. 47-54.
64. Gayda, J., Miner, R V *Fatigue crack initiation and propagation in several nickel-base superalloys at 650°C.* International Journal of Fatigue, 1983. **5**: p. 135-143.

65. Vecchio, R.S., Hertzberg, R W, *A rationale for the 'apparent anomalous' growth behaviour of short fatigue cracks.* Engineering Fracture Mechanics, 1985. **22**: p. 1049-1060.
66. Zhang, Y.H., Edwards, L *The development of plastic zones ahead of small fatigue cracks and their consequences for crack growth rate.* Aluminium alloys, 1992. **2**: p. 563-568.
67. Toh, S.F., Rainforth, W M *Fatigue of a nickel base superalloy with bimodal grain size.* Materials Science and Technology, 1996. **12**: p. 1007-1014.
68. Isomoto, T., Stoloff, N S *Effect of microstructure and temperature on high cycle fatigue of powder metallurgy Astroloy.* Materials Science and Engineering, 1990. **A124**: p. 171-181.
69. King, J.E., *Surface damage and near-threshold fatigue crack growth in a Ni-base superalloy in vacuum.* Fatigue and Fracture of Engineering Materials and Structures (UK), 1982. **5**: p. 177-188.
70. Sadananda, K., Shahinian, P *Effect of environment on high temperature crack growth behaviour of several nickel-base alloys*. in *Proc. Int. Conf. on Corrosion of Nickel-Base Alloys*. 1985. *Cincinnati, Ohio, USA*: American Society for Metals,.
71. Nikbin, K.M., Webster, G A. *Creep-fatigue crack growth in a nickel-base superalloy*. in *Proceedings 2nd International Conference on Creep and Fracture of Engineering Materials and Structures*. 1984. Swansea, UK: Pineridge Press Ltd.
72. James, L. *Fatigue crack propagation in alloy 718: A review*. in *Superalloy 718 - Metallurgy and Applications*. 1989. Pittsburgh, Pennsylvania, USA: TMS.
73. Gayda, J., Gabb, T P, Miner, R V. *Fatigue crack propagation of nickel-base superalloys at 650 C*. in *Low Cycle Fatigue*. 1988. Bolton Landing, New York, USA: ASTM STP 942.
74. Byrne, J., Hall, R, Grabowski L, *Elevated temperature fatigue crack growth under dwell conditions in Waspaloy.* International Journal of Fatigue, 1997. **19**: p. 359-367.
75. Hide, N.J., Henderson, M B, Reed, P A S *Effects of grain and precipitate size variation on creep-fatigue behaviour of Udimet 720 in both air and vacuum*. in *Ninth International Symposium on Superalloys*. 2000. Seven Springs, PA, USA: Minerals, Metals and Materials Society/AIME.
76. Carbou, C., Mendez, J, Violan, P *Factors influencing creep-fatigue crack propagation in P/M Astroloy at 650°C and 750°C*. in *Mechanisms and Mechanics of Damage and Failure, Proc. of 11th Biennial European Conf. on Fracture (ECF11)*. 1996. Poitiers-Futuroscope, France.
77. Suresh, S., Shih, CF, *Plastic near-tip fileds for branched cracks.* International Journal of Fracture, 1986. **30**: p. 237-259.
78. Erdogan, F., Sih, GC, Trans ASME J. Basic Eng., 1963. **85**: p. 519-527.
79. Sih, G.C., *Energy-density concept in fracture mechanics.* Eng. Fract. Mech., 1973. **5**: p. 1037-1040.
80. Reed, P.A.S., *Effects of warm prestressing on A533B weld metal*, 1990, University of Cambridge: Cambridge.
81. Chang, K.J., Trans. ASME J. App. Mech., 1982. **49**: p. 377-385.
82. Maiti, S.K., Smith, R.A., *Criteria for brittle fracture in biaxial tension.* Eng. Fract. Mech., 1984. **19**: p. 793-804.
83. Smith, R.N.L., *Second-order terms and strain energy density for the angled crack problem.* Eng. Fract. Mech. , 1987. **26**: p. 463-469.
84. Ritchie, R.O., *Mechanism of Fatigue Crack Propagation in Metals, Ceramics and Composites: Role of Crack Tip Shielding.* Material Science and Engineering, 1988. **A103**: p. 15-28.
85. Suresh, S., *Fatigue Crack Deflection And Fracture Surface-Contact - Micromechanical Models.* Metallurgical Transactions A-Physical Metallurgy And Materials Science, 1985. **16**: p. 249.

86. Reed, P., Wu, XD, Sinclair, I, *Fatigue Crack Path Prediction in UDIMET 720 Nickel-Based Ally Single Crystals.* Metallurgical and Materials Transactions A, 2000. **31A**: p. 109-123.
87. Tong, J., *Mixed-mode crack growth from an unusual source.* Fatigue Fract Engng Mater Struct, 2001. **24**: p. 771-775.
88. Cotterell, B., *Notes on the paths and stability of cracks in alloys.* Int. J. Fracture Mech., 1966. **2**: p. 526-533.
89. Pook, L.P., *On fatigue crack paths.* International Journal of Fatigue, 1995. **17**: p. 5-13.
90. Joyce, M., Sinclair, I *Experimental assessment of mixed mode loading effects on macroscopic fatigue crack paths in thick sections AL-Cu-Li alloy plate*, in *Materials Research Group Report*2004, University of Southampton: Southampton, UK.
91. Brooks, R., *Fatigue Damage Mechanism in the Nickel-Based Superalloy Udimet720*, in *Department of Engineering Materials*1996, University of Sheffield: Sheffield.
92. Antunes, F., Ferreira, JM, Branco, CM, Byrne, J, *Influence of stress state on high temperature fatigue crack growth in Inconel 718.* Fatigue Fract Engng Mater Struct, 2001(24): p. 127-135.
93. Ganesan, M., *Rolls Royce Private Communication*, 2010.
94. Pickard, A., *The application of 3-dimensional finite element methods to fracture mechanics and fatigue life prediction*1986, UK: EMAS.
95. BSI, *BS ISO 12108:2002 Metallic Materials – Fatigue Testing – Fatigue Crack Growth Method*, 2002.
96. Everitt, S., *Developments in advanced high temperature disc and blade materials for aero-engine gas turbine applications*, in *Faculty of Engineering and the Environment*2012, University of Southampton: Southampton, UK.
97. Child, D., West, GD, Thomson, RC, *The Use of Combined Three-Dimensional Electron Back Scatter Diffraction and Energy Dispersive X-Ray Analysis to Assess the Characteristics of the Gamma/Gamma-Prime Microstructure in Alloy 720Li™.* Ultramicroscopy.
98. West, G., Thomson, R.C., *Combined EBSD/EDS Tomography in a Dual-Beam FIB/FEG-SEM.* Journal of Microscopy, 2009. **233**(3): p. 442-450.
99. Bowen, D.C., *T500: Damage Tolerance in HPT Firtree Disc Posts Fatigue Crack Propagation in Alloy 720Li Corner Crack Specimens: The Effect Of Temperature On Non-Planar Crack Morphology*, 2009, Rolls Royce plc: Derby, UK.
100. Saunders, E.A., *HP Turbine Disc (PFR) Serial No. EKC 93 Part No. NN11888 Ex-Cyclic Spin Test MRD 806*, in *Failure Investigation Report*1994, Rolls Royce plc: Bristol, UK.
101. Andrews, S., *DHC336790, Examination Of The Trent 900 HPT Disc, Serial Number LDRPP00172, From Spin Test MRA 44665*, in *Rolls Royce materials report*2010.
102. Clavel, M., Pineau, A, *Frequency and waveform effects on the fatigue crack growth behavior of alloy 718 at 298K and 823K.* Metallurgical Transactions A, 1978. **9A**: p. 471-480.
103. He, M., Cao, HC, Evans, AG, *Mixed-Mode Fracture: The Four-Point Bend Shear Specimen.* acta metall mater, 1990. **38**(5): p. 839-846.
104. Reed, P.A.S., King, J.E., *Mixed-Mode Fatigue Effects In Ni-Base Single-Crystals - Preliminary-Results.* Scripta Metallurgica Et Materialia 1992. **26**(12): p. 1829-1834.
105. Wawrzynek, P., Ingrafea, A. . *Franc2D User guide*. 1994; Available from: http://www.cfg.cornell.edu/.
106. Zentech, *Zencrack User Manual Version 7.6*, Zentech International Ltd. : London, UK.
107. Tucker, P., *Mixed-Mode Creep Fatigue Interactions in SRR99*, in *Department of Engineering Materials* 1998, University of Southampton: Southampton.